

AEROSOL and CLOUD ENVIRONMENTAL DATA RECORDS

AEROSOL POLARIMETRY SENSOR ALGORITHM THEORETIC BASIS DOCUMENT

SDRL 020

Version 1.0: January 2003

Brian Cairns
NASA GISS

Jacek Chowdhary
Columbia University

TABLE OF CONTENTS

LIST OF FIGURES	III
LIST OF TABLES	III
GLOSSARY OF ACRONYMS.....	III
ABSTRACT	IV
1. INTRODUCTION	1
1.1. PURPOSE	1
1.2. SCOPE.....	1
1.3. APS DOCUMENTS	2
1.4. REVISIONS	2
2. OVERVIEW AND BACKGROUND INFORMATION	2
2.1. HISTORICAL PERSPECTIVE	3
2.2. EXPERIMENTAL THRESHOLDS AND OBJECTIVES	4
3. SCIENTIFIC BASIS.....	7
3.1. BASIC CONCEPTS AND DEFINITIONS	8
3.2. PHYSICAL BASIS FOR AEROSOL RETRIEVALS	11
3.2.1. OVER OCEANS AND LARGE LAKES	13
3.2.2. OVER LAND.....	14
3.3. PHYSICAL BASIS FOR CLOUD PARTICLE SIZE RETRIEVALS	16
3.3.1. WATER CLOUDS.....	16
3.3.2. ICE CLOUDS	18
3.3.2.1. CIRRUS CLOUDS	18
POLAR STRATOSPHERIC CLOUDS	20
3.4. RADIATIVE TRANSFER MODELING	21
3.4.1. SINGLE-SCATTERING PROPERTIES AND SIZE DISTRIBUTIONS.....	22
3.4.2. MULTIPLE SCATTERING MODELING	28
3.4.3. OCEAN MODELING.....	33
3.4.3.1. BIO-OPTICAL MODEL.....	34
3.4.3.2. HYDROSOL COMPONENTS.....	35
3.4.3.3. POLARIZATION CONSTRAINTS	36
3.4.3.4. MIXING RATIOS	37
3.4.4. LAND SURFACE MODELS	37
3.4.5. SPECTRAL INTEGRATIONS AND THE CORRELATED K DISTRIBUTION	39
3.5. MATHEMATICAL IMPLEMENTATION OF ALGORITHM	41
3.6. ROBUSTNESS AND FLEXIBILITY	45
4. SENSOR DESCRIPTION AND REQUIREMENTS.....	45
4.1. SIMULTANEOUS MEASUREMENTS	46
4.1.1. TEMPORAL SIMULTANEITY	47
4.1.2. SPATIAL SIMULTANEITY (IFOV MATCHING).....	47
4.1.2.1. INTRA-TELESCOPE IFOV UNIFORMITY	47
4.1.2.2. INTER-TELESCOPE BORESIGHT ALIGNMENT	48
4.2. SPECTRAL BAND SELECTION	48

4.2.1.	NUMBER OF SPECTRAL BANDS	49
4.2.2.	CIRRUS CLOUD SCREEN.....	50
4.2.3.	RAYLEIGH MEASUREMENTS	53
4.2.4.	WATER VAPOR ESTIMATION	54
4.2.5.	SPECTRAL BAND CENTERS AND WIDTHS	56
4.3.	CALIBRATION.....	56
4.3.1.	POLARIMETRIC CALIBRATION	57
4.3.1.1.	ONBOARD POLARIMETRIC CALIBRATOR (OPC–PRIMARY)	58
4.3.1.2.	ONBOARD POLARIMETRIC CALIBRATOR (OPC)– SECONDARY	59
4.3.2.	RADIOMETRIC CALIBRATION	61
4.3.2.1.	ONBOARD RADIOMETRIC CALIBRATOR (ORC)	61
4.3.2.2.	ONBOARD CHECKOUT SOURCE (OCS)	63
4.3.3.	REDUNDANCY OF MEASUREMENTS.....	63
4.4.	DYNAMIC RANGE	63
4.4.1.	PRIMARY DRIVER - MINIMUM DETECTABLE SIGNAL AT 2250 NM.....	64
4.4.2.	SECONDARY DRIVER - EFFECT OF QUANTIZATION NOISE ON POLARIZATION	67
4.5.	SIGNAL-TO-NOISE.....	68
4.5.1.	INTENSITY MEASUREMENTS	68
4.5.2.	Q AND U MEASUREMENTS	69
4.5.3.	RELATIVE Q (=Q/I) AND U(=U/I) MEASUREMENTS	69
4.6.	FIELD OF VIEW	70
5.	SDR (RDR TO SDR) ALGORITHM DESCRIPTION	70
5.1.	PROCESSING OUTLINE	70
5.1.1.	NEAR REAL-TIME PROCESSING	71
5.1.2.	OFFLINE PROCESSING	72
5.2.	ALGORITHM INPUTS	73
5.2.1.	APS DATA.....	73
5.2.2.	NON-APS DATA.....	74
5.2.2.1.	SPACECRAFT EPHEMERIS.....	74
5.2.2.2.	SURFACE ELLIPSOID/DIGITAL ELEVATION MODEL	74
5.3.	THEORETICAL DESCRIPTION	74
5.4.	EVALUATION AND TESTING	76
5.5.	PRACTICAL CONSIDERATIONS.....	76
5.6.	SDR ALGORITHM DEVELOPMENT SCHEDULE	77
6.	EDR (SDR TO EDR) ALGORITHM DESCRIPTION	77
6.1.	PROCESSING OUTLINE	80
6.2.	ALGORITHM INPUT	83
6.2.1.	APS DATA.....	83
6.2.2.	NON-APS DATA	83
6.3.	APS CLOUD MASK GENERATION.....	84
6.4.	AEROSOL EDR IMPLEMENTATION.....	85
6.4.1.	CONFIDENT CLEAR SKY	86
6.4.2.	CIRRUS CONTAMINATION.....	86
6.4.3.	PROBABLY CLEAR SKY	87
6.5.	CLOUD EDR PRODUCTION	87
6.5.1.	CLOUDY SKY	88
6.5.2.	PROBABLY CLOUDY SKY	88
6.6.	WATER VAPOR ESTIMATION.....	88
6.7.	STRATOSPHERIC AEROSOLS.....	89
6.8.	CALIBRATION ANALYSIS AND SYNTHESIS	89
6.9.	EVALUATION AND TESTING	90
6.10.	PRACTICAL CONSIDERATIONS	90

6.11.	EDR ALGORITHM DEVELOPMENT SCHEDULE	91
7.	RETRIEVAL CHARACTERIZATION AND ERROR ANALYSIS	91
7.1.	ACCURACY AND PRECISION.....	93
7.1.1.	AEROSOL EDR ACCURACY	94
7.1.2.	AEROSOL EDR PRECISION	95
7.1.3.	CLOUD EDR ACCURACY AND PRECISION	96
7.2.	FORWARD MODEL UNCERTAINTIES – OCEAN SURFACE	97
8.	CONSTRAINTS, LIMITATIONS AND ASSUMPTIONS	101
8.1.	SPECTRAL REFRACTIVE INDEX	101
8.2.	SPECIFICATION OF UNCERTAINTY	102
8.3.	SOLAR ZENITH ANGLE	103
8.4.	NEGLECT OF CIRCULAR POLARIZATION	104
9.	CALIBRATION AND VALIDATION	104
10.	POTENTIAL SCIENCE OPPORTUNITIES	105
10.1.	AEROSOL MIXED LAYER DEPTH AND CLOUD TOP HEIGHT	106
10.2.	IDENTIFY PREDOMINANT ICE CRYSTAL SHAPES	106
10.3.	IN CLOUD ABSORPTION	106
10.4.	SURFACE POLARIZED BRDF.....	106
10.5.	WATER VAPOR COLUMN.....	106
11.	REFERENCES	107
APPENDIX A – EVALUATION OF REQUIRED TOLERANCES ON SPECTRAL BANDS IN ORDER TO LIMIT CONTAMINATION BY GASEOUS ABSORPTION.....		115

LIST OF FIGURES

LIST OF TABLES

GLOSSARY OF ACRONYMS

ABSTRACT

In this document we describe the scientific basis of the algorithms to be used for the Aerosol Polarimetry Sensor (APS) that is planned to fly on the 21:30 NPOESS satellite platforms. These algorithms convert the APS data from Raw Data Records to calibrated Sensor Data Records and then retrieve the aerosol and cloud Environmental Data Records (EDRs) assigned to the APS sensor. The APS instrument is a nine spectral band instrument designed to measure the first three Stokes vector elements simultaneously in all nine spectral bands and to view earth scenes from multiple angles. The EDRs assigned to the APS instrument will provide an estimate of the radiative forcing of the climate of the Earth by aerosols with the accuracy required to constrain and evaluate these effects in climate models and will provide an accurate global aerosol climatology that can be used to improve the retrieval of aerosols by other instruments such as VIIRS.

1. INTRODUCTION

As our understanding of the range of natural and anthropogenic processes that are relevant to climate improves, general circulation models (GCMs) have tried to represent these processes in their calculations leading to increasingly complex models. If these models are to credibly address the important question of *climate variability and prediction* in the next millennium and the impacts of climate change at a regional level, then it is crucial that the processes included in GCMs are tested for their accuracy and realism. A significant uncertainty in understanding the current climate state is knowledge of the distribution and optical properties of aerosols. Aerosols cause a direct climate forcing by reflecting sunlight to space and an indirect climate forcing by altering cloud properties. The nature and magnitude of *both* these effects depends strongly on the aerosol characteristics including their concentration, size distribution and chemical composition. When GCMs are used to simulate changes in temperature over the past century they can be made to match observed changes quite well if the aerosol radiative properties are suitably chosen. These aerosol radiative properties are however poorly known and getting the right answer for the wrong reason is not acceptable if our aim is to produce skillful predictions of future climate variability and change. The importance of aerosols to understanding climate has become even more apparent in recent years. The INDOEX experiment (Meywerk and Ramanathan 1999) measured aerosol radiative forcings far in excess of those predicted by existing aerosol climatologies. It has also been demonstrated that not only may aerosols have a significant climate impact, but that their impact may be more susceptible to mitigation than reducing CO₂ emissions (Hansen *et al.* 2000). Thus, accurately determining the concentration (optical depth), size distribution and chemical composition (refractive index) of aerosols in the atmosphere is necessary both for evaluating the state of the current climate and to understanding the best strategies for mitigating anthropogenic effects on the climate.

1.1. Purpose

This Algorithm Theoretic Basis Document (ATBD) describes the Raw Data Records (RDRs), the process by which the RDRs are transformed into Sensor Data Records (SDRs) and the algorithms used to analyze the SDRs into the required aerosol and cloud Environmental Data Records (EDRs) for the Aerosol Polarimetry Sensor on the National Polar-Orbiting Operational Environmental Satellite System (NPOESS). Specifically this document outlines the data flow, illustrating and explaining the relationships between the data collected by the sensor and the final EDR product. The science algorithms used to produce the required EDRs are discussed including the physical theory and mathematical background together with relevant equations and analyses. Data from other sources required to produce the EDRs are identified along with required levels of performance. Practical considerations in the implementation of the algorithms are described and approaches to testing and validating the algorithms are outlined.

1.2. Scope

This document covers the algorithm theoretic basis for the aerosol and cloud parameters to be included in the APS aerosol and clouds EDRs. Only parameters that

are to be operationally retrieved are discussed. In its present release this ATBD is a "living document" in that not all aspects of the algorithms have been finalized and processing constraints that may restrict, or expand, algorithm capability are still not well defined.

Section 1 describes the purpose and scope of this document. Section 2 provides a historical background and summarizes the EDR performance that the polarimetric measurements must meet. The physical basis for using polarization measurements to retrieve the specified aerosol and cloud EDRs, together with the required radiative modeling, the mathematical implementation and issues regarding robustness and flexibility against APS channel loss and external data loss are described in Section 3. A basic description of the APS sensor that summarizes those aspects that are directly relevant to the algorithmic approach to aerosol and clouds EDRs are described in Section 4. The transformation of RDRs to SDRs is described in Section 5 and the analysis of SDRs into EDRs is described in Section 6. These sections (5 and 6) include discussions of practical considerations in algorithm implementation, approaches to evaluation and testing and development schedules. Section 7 uses the mathematical formalism presented in Section 3 to characterize uncertainties in the EDR products and provide error budgets for APS sensor and algorithm. Constraints, limitations and assumptions, including those limiting the solar zenith angle range over which operational EDR products are produced, are described in Section 8. A process for calibrating APS prior to launch and calibrating and validating APS RDR, SDR and EDR products after launch is presented in Section 9. Section 10 identifies two additional products that will be generated as a necessary adjunct to EDR production and a product that represents a potential science opportunity. References to publications cited in the text are given in Section 11.

1.3. APS Documents

Reference to APS project or reference documents is indicated by a number in italicized brackets, e.g. [SDRL-1].

[EM 17-0014] Mission Specification for the Aerosol Polarimetry Sensor (APS).

[SDRL 012] APS Performance Specification

[SDRL 021] APS Algorithm Performance Specification

1.4. Revisions

This is release 1 of this document. Revisions in future versions will be denoted by change bars and/or revision control documentation of line changes.

2. OVERVIEW AND BACKGROUND INFORMATION

In order to improve our knowledge of the role of aerosols in the global climate system for the purposes of long-term climate predictability, it is necessary to accurately estimate the aerosol radiative forcing and also diagnose the type and size distribution of the aerosols that are causing the radiative forcing globally. The spatial and temporal

heterogeneity of aerosols means that realistically this can only be done from a satellite platform.

The remote sensing of tropospheric aerosols from satellite relies on reflected solar radiation that is, in general, polarized and contains embedded information about the intrinsic nature of aerosol particles as well as the underlying surface. Some of this information is accessible through standard remote sensing techniques that utilize changes in the intensity of reflected solar radiation with wavelength and viewing geometry. However, more detailed physical information, e.g., aerosol particle size distribution, aerosol composition based on the spectral signature of refractive indices, number concentration and particle shape, is only available through the measurement and analysis of the spectral and angular polarization signature of the reflected radiation. The absence of sensitivity of intensity measurements to the detailed particle size distribution and refractive index of particles means that these properties cannot be retrieved from such measurements. This means that these properties need to be assigned values based on other measurements. Any errors in this assignment will then propagate into errors in the other aerosol properties that are being retrieved, such as the aerosol optical depth and Angstrom parameters retrieved from VIIRS measurements. Thus, the measurements made by the APS sensor not only provide a more accurate and complete picture of the types and amounts of aerosols in the atmosphere, but can also reduce errors in retrievals from instruments such as VIIRS by improving the realism of the aerosol models that are assumed in those retrievals.

2.1. Historical Perspective

Space-borne remote sensing of tropospheric aerosols dates back to the 1970s with the advent of visible and near-infrared radiance measurements by the Multi-Scanner Subsystem (MMS) on Landsat since 1971 (Griggs, 1975, 1977; Fraser, 1976; Mekler et al., 1977), the Advanced Very High Resolution Radiometer (AVHRR) on the NOAA-platforms since 1973 (Carlson and Wendling, 1977; Carlson, 1979), the Visible Infrared SpinScan Radiometer (VISSR) on GOES since 1975 (Griggs, 1979; Norton et al., 1980), and the sensors on Meteosat since 1978 (Kästner et al., 1983). The science behind these early observations was mostly driven by studies of large-scale outbreaks of Saharan dust across the Atlantic ocean (Carlson and Prospero, 1972; Prospero and Carlson, 1972), and resulted in the only standard aerosol product available for the last two decades: a weekly, global composite of equivalent aerosol optical thickness over the ocean retrieved from AVHRR channel-1 radiance measurements (Rao et al., 1989).

During the same period, extensive research on polarimetric observations of Venus (Coffeen and Gehrels, 1969; Hansen and Arkin, 1971; Hansen and Travis, 1974; Santer and Herman, 1979; Kawabata et al., 1980; Esposito and Travis, 1982; Sato et al., 1996; Knibbe et al., 1997, 1998) demonstrated that cloud droplet properties such as size, phase, and composition can be accurately retrieved from polarization. Polarimetry was also successfully used to study haze and cloud properties of Jupiter (Tomasko et al., 1978; Carlson and Lutz, 1989; Mishchenko, 1990) and Titan (Tomasko and Smith, 1982; West et al., 1983), and also to retrieve aerosol properties of dust veils on Mars

(Dolfus et al., 1984a, 1984b, Santer et al., 1985, 1986; De Haan, 1987). It is therefore probably the case that remote sensing of aerosols on other planets has been more accurate than the measurements made of the Earth until recently.

The new generation of Earth observing satellite instruments do make measurements that are more sensitive to aerosol properties than previous instruments. Particularly noteworthy are the Multi-angle Imaging SpectroRadiometer (MISR) (Diner et al., 1991) instrument, the MODerate-resolution Imaging Spectroradiometer (MODIS) instrument (King et al., 1992), and the POLarization and Directionality of the Earth Reflectance (POLDER) instrument (Goloub et al., 1999). These instruments measure the radiance emerging from the top of the atmosphere in more wavelengths (MISR, MODIS, POLDER), more viewing angles (MISR, POLDER) than the AVHRR instrument, and monitor the linear polarization of this field too (POLDER). While these measurements provide more data to constrain properties of aerosol particles, they are unable to resolve the non-uniqueness problem of aerosol retrieval with accuracies necessary for long-term climate monitoring of climate forcings and feedbacks (Hansen et al., 1995). For example, instruments like MODIS and MISR are unlikely to provide sufficiently accurate information on the aerosol composition, size distribution, and column density number because of their lack of polarization measurements (Mishchenko et al., 1997). And the lack of channels at wavelengths longer than one micron limits the ability of the POLDER instrument to constrain the properties of coarse mode particles (Chowdhary et al., 2001, 2002). We therefore conclude that to retrieve aerosol properties for studies in climate research requires accurate multiangle photo-polarimetric measurements over the full range of the solar spectrum reflected by the Earth's atmosphere.

2.2. Experimental Thresholds and Objectives

The provision of an Aerosol Polarimetry Sensor is based on the need to quantify climate change by tropospheric aerosols. There are three aspects to this task. Firstly, to monitor changes in the background level of tropospheric aerosols that are significant in terms of long-term climate forcing one needs to retrieve their optical thickness to an accuracy of better than 10% (DeLGenio et al., 1993). Secondly, it is necessary to provide information on the chemical composition of aerosol particles in order to (i) distinguish anthropogenic (industry, agriculture) and natural (deserts, biogenic, volcanic) sources and trends (Andrea, 1995; Jacob et al., 1995); (ii) to study aerosol evolution such as gas-to-particle conversion, formation of cloud condensation nuclei, and in-cloud processing (Hobbs, 1993; Raes et al., 1995), and to (iii) compute single scattering properties for modeling climate change (Lacis and Mishchenko, 1995; Toon, 1995). Thirdly, to evaluate or study direct and indirect effects of aerosols one needs to retrieve the aerosol size distribution parameters r_{eff} and v_{eff} (defined in Section 3.4.1) for at least two aerosol modes. Variance analyses performed by Pan et al. (1998) for several aerosol-cloud models suggest for example that the uncertainty in indirect forcing by aerosol particles derives mostly from the uncertainty in the aerosol size distribution. Lacis and Mishchenko (1995) also demonstrated how the size distribution defines the spectral behavior of aerosol scattering properties and consequently the spectral variation of the radiative forcing.

These climate change measurement needs have been captured in the performance requirements for the APS sensor that are described in the MISSION SPECIFICATION FOR THE AEROSOL POLARIMETRY SENSOR (APS) which is TRW Document EM17-0014). The aerosol algorithm is to retrieve an aerosol model consisting of optical thickness, size, real part of refractive index, single-scattering albedo and detection of whether particles are spherical, or non-spherical for an accumulation mode and a coarse mode. For ease of reference the descriptions of aerosol properties and the EDR requirements for range, accuracy, precision and long-term stability are repeated here with reference to the relevant tables in EM17-0014 included below each table. In all of the following tables “#” applies to the total column.

Aerosol Optical Thickness (AOT) is defined as the extinction (scattering + absorption) vertical optical thickness of modes 1 (~ 0.1 µm) and 2 (~ 1.0 µm) of a bimodal aerosol size distribution at multiple wavelengths within the 0.4 – 2.4 micron spectral range..

Table 2.2-1. Aerosol optical thickness EDR requirements abstracted from Table 3.1.4.1.1-1.

Req. No.		Threshold	Objective
40.3.1.1-18	g. Measurement Range #	0.0 to 5.0	0.0 to 10.0
	h. Measurement Accuracy		
40.3.1.1-19	1. Over ocean	Greater of 0.02 or 7%	Greater of 0.01 or 5%
40.3.1.1-20	2. Over land	Greater of 0.04 or 10%	Greater of 0.03 or 7%
	i. Measurement Precision #		
40.3.1.1-21	1. Over ocean	0.01	0.005
40.3.1.1-22	2. Over land	0.03	0.02
40.3.1.1-14	j. Long-term Stability	0.01	0.005

The size denotes a measurement of the bimodal size distribution of the aerosol population in terms of the effective radius r_{eff} and effective variance v_{eff} of each mode. The effective radius is the ratio of the third moment of the aerosol size distribution to the second moment. The effective variance, v_{eff} , characterizes the width of the size distribution, $n(r)$, and is calculated as an area weighted average of the normalized variance as given by the following expression:

$$v_{\text{eff}} = [\int (r - r_{\text{eff}})^2 \pi r^2 n(r) dr] / [r_{\text{eff}}^2 \int \pi r^2 n(r) dr] \quad 2.2-1$$

It also can be expressed in terms of the second, third, and fourth moments of the size distributions:

$$v_{\text{eff}} = [(m_4 m_2) / m_3^2] - 1 \quad 2.2-2$$

Where m_n denotes the moment of the size distribution.

Table 2.2-2. Aerosol particle size EDR requirements abstracted from Table 3.1.4.1.2-1.

Req. No.		Threshold	Objective
	g. Measurement Range		
40.3.1.2-17a	2. Climate, effective radius	0 to 5 µm	0 to 10 µm

40.3.1.2-17b	3. Climate, effective variance	0 to 3	0 to 5
	h. Measurement Accuracy		
40.3.1.2-19a	4. Climate, Effective Radius	Greater of 0.1 μm or 10%	Greater of 0.05 μm or 5%
40.3.1.2-19b	5. Climate, Effective Variance	Greater of 0.3 or 50%	Greater of 0.2 or 30%
	i. Measurement Precision		
40.3.1.2-18a	4. Climate, Effective Radius	Greater of 0.05 μm or 10%	Greater of 0.05 μm or 5%
40.3.1.2-18b	5. Climate, Effective Variance		
	j. Long Term Stability		
40.3.1.2-13a	1. Effective Radius	Greater of 0.05 μm or 10%	Greater of 0.05 μm or 5%
40.3.1.2-13b	2. Effective Variance	Greater of 0.2 or 40%	Greater of 0.1 or 20%

Measurement of the real part of the refractive index m , and the single-scattering albedo ω , of each mode of the bimodal aerosol size distribution at multiple wavelengths within the 0.4-2.4 micron spectral range; and determination of whether aerosol particles are spherical or non-spherical. Non-sphericity is detected when the value $S = (L_{\text{max}}/L_{\text{min}} - 1) > 0.3$, where L_{max} is the maximum dimension of the particle and L_{min} is the minimum dimension of the particle. The value of S can be inferred from multi-angular measurements of the departure of scattered radiation from that expected from spherical aerosol particles. The refresh requirement is to provide observations from the satellite nadir-track of any satellite carrying the APS. The requirements below apply only under clear conditions and are only applicable to sub-satellite pixels.

Table 2.2-3. Aerosol real refractive index, single scattering albedo and particle shape EDR requirements abstracted from Table 3.1.4.1.3-1.

Req. No.		Threshold	Objective
40.3.1.4-7	g. Measurement Range #		
	1. Refractive Index	1.3 to 1.7	1.3 to 1.8
	2. Albedo	0 to 1	0 to 1
40.3.1.4-10	h. Measurement Accuracy #		
	1. Refractive Index	0.02	0.01
	2. Albedo	0.03	0.01
40.3.1.4-8	i. Measurement Precision #		
	1. Refractive Index	0.01	0.005
	2. Albedo	0.02	0.01
40.3.1.4-13	j. Long Term Stability		
	1. Refractive Index	0.01	0.005
	2. Albedo	0.02	0.01
	k. Sphericity	Spherical/Non-spherical	Spherical/Non-spherical
	l. Probability of Correct Typing	90% (TBR)	95%

The cloud algorithm is to retrieve the clouds particle size distribution defined here as the effective radius r_{eff} and effective variance v_{eff} of a single mode particle size distribution. The effective radius is the ratio of the third moment of the size distribution to the second moment. The effective variance characterizes the width of the size distribution and is defined in Eq. 2.2-2 above.

Req. No.		Threshold	Objective
----------	--	-----------	-----------

40.4.10-3	g. Measurement Range		
	1. Radius	0 to 50 μm	0 to 80 μm
	2. Variance	0 to 2	0 to 3
40.4.10-6	h. Measurement Accuracy		
	1. Radius	Greater of 1 μm or 10%	Greater of 0.5 μm or 5%
	2. Variance	Greater of 0.05 or 50%	Greater of 0.04 or 40 %
-6	i. Measurement Precision		
	1. Radius	Greater of 0.5 μm or 5%	Greater of 0.3 μm or 3%
	2. Variance	Greater of 0.04 or 40%	Greater of 0.03 or 30 %
40.4.10-9	j. Long Term Stability		
	1. Radius	Greater of 0.5 μm or 5%	Greater of 0.3 μm or 3%
	2. Variance	Greater of 0.04 or 40%	Greater of 0.03 or 30

For completeness the guidance regarding the definition of “clear” and “cloudy” skies that is provided in *EM 17-0014* is repeated here. **Detectable Cloud:** An aqueous aerosol having a vertical extinction optical depth exceeding 0.03 (*TBR*) in the visible or a contrast with the background exceeding 0.02 (*TBR*) in the visible. Contrast with the background is defined as the difference between the cloud and adjacent background radiance divided by the sum of these two radiances. “Cloud” is always to be interpreted to mean “detectable cloud.” **Clear:** A given area is classified as “clear” if there are no detectable clouds, as defined above, overlying the area and if the average vertical LOS extinction optical thickness of the atmosphere overlying the area is < 0.03 in the 0.4-0.7 μm band.

3. SCIENTIFIC BASIS

The scientific basis for retrieving aerosol and cloud microphysical properties from photopolarimetry of light scattered by aerosol and cloud particles derives from the following four observations. First, polarimetry senses the nature of transverse electromagnetic waves that make up light and provides more information than a photometric measurement only. In what follows, we will refer to this nature of electromagnetic waves as the *state of polarization*. Secondly, the state of polarization of light scattered once by an aerosol or cloud particle contains more and geometrically sharper features as a function of scattering angle (i.e., angle between incident and scattered light) than features in the total intensity of this light. The implication is that such features in the state of polarization can be distinguished more easily from one another than those in the total intensity. Thirdly, these features in the state of polarization are much more sensitive to the microphysical properties of particles (shape, size, and composition) than corresponding features in total intensity. This significantly reduces the uniqueness problem often encountered when inverting total intensity measurements. And fourthly, single-scattering sensitivities of the state of polarization to particle properties are much better preserved in the presence of multiply scattered light than corresponding sensitivities of the total intensity. There are, in addition, instrumental design and calibration advantages to making measurements of polarization. The accuracy of aerosol retrievals using intensity-only measurements is largely determined by the absolute radiometric calibration. In contrast, the transverse state of electromagnetic waves can be expressed in terms of dimensionless intensity *ratios* which can be

determined with much higher accuracies because such ratios are independent of absolute calibration. The conclusion that we draw is that polarimetric observations have a very high information content regarding aerosol properties, and that polarimetric measurements can be made with an accuracy that allows this information content to be realized (Mishchenko and Travis 1997a, 1997b, Chowdhary *et al.* 2001, 2002).

3.1. Basic concepts and definitions

To describe the total intensity and state of polarization, we use the *Stokes vector* I defined to be

$$I = \begin{pmatrix} I \\ Q \\ U \\ V \end{pmatrix} = \{I, Q, U, V\} \quad 3.1-1$$

which has as its components the *Stokes parameters* I , Q , U , and V . These parameters relate to the electrical field of light as follows. Let the direction of light propagation be denoted by the real unit vector \mathbf{k} and let us choose an arbitrary reference plane \mathbf{S} containing \mathbf{k} . Furthermore, let \mathbf{r} and \mathbf{l} be unit vectors parallel and perpendicular to this plane, respectively, such that $\mathbf{k} = \mathbf{r} \times \mathbf{l}$. Following Hansen and Travis (1974), we define I , Q , U , and V for transverse electromagnetic waves as the real, time-averaged quantities

$$\begin{aligned} I &= \langle E_l E_l^* + E_r E_r^* \rangle, \\ Q &= \langle E_l E_l^* - E_r E_r^* \rangle, \\ U &= -\langle E_l E_r^* + E_r E_l^* \rangle, \\ V &= i \langle E_r E_l^* - E_l E_r^* \rangle, \end{aligned} \quad 3.1-2$$

where E_l and E_r are the l - and r -components of the electric field, respectively, and the asterisk denotes the complex-conjugate. Stokes parameters Q and U describe the component of this light whose electrical field oscillations are confined to a plane called the *linear polarization plane*. The angle χ between this plane and reference plane \mathbf{S} can be found from

$$\tan 2\chi = \frac{U}{Q} \quad 3.1-3$$

while the intensity I_p of this so-called *linear polarized light* is given by

$$I_p = \sqrt{Q^2 + U^2}. \quad 3.1-4$$

Stokes parameter V describes the component of light, called *circular polarized light*, whose electrical field rotates in a plane perpendicular to \mathbf{k} . A more detailed discussion on I , Q , U , and V is provided by Hovenier and van der Mee (1983). For future reference, we define further the *relative Stokes parameters* i , q , and v as

$$\begin{aligned}
q &= Q/I, \\
u &= U/I, \\
v &= V/I,
\end{aligned}
\tag{3.1-5}$$

respectively. Note that the absolute calibration is the same for I , Q , U , and V , and hence that q , u , and v are independent of this calibration. Substituting q and u for Q and U , respectively, in the definition for I_P leads to the *degree of linear polarization* p :

$$p = \sqrt{q^2 + u^2}. \tag{3.1-6}$$

Consider now a beam of light with Stokes vector \mathbf{I}_{in} propagating in a direction denoted by the unit vector \mathbf{s}_{in} , and let this beam of light illuminate a volume-element containing particles. Let \mathbf{I}_{sca} denote the Stokes vector of a beam of light scattered by the volume element through an angle Θ ($0 \leq \Theta \leq 2\pi$) into the direction specified by unit vector \mathbf{s}_{sca} . If we choose the plane containing \mathbf{I}_{in} and \mathbf{I}_{sca} , i.e., the scattering plane, as the reference plane for the Stokes parameters, then the scattering process can be described by means of a (4x4) matrix called the *scattering matrix* $\mathbf{P}(\Theta)$ which transforms \mathbf{I}_{in} into \mathbf{I}_{sca} according to

$$\mathbf{I}_{\text{sca}} \propto \varpi_0 \mathbf{P}(\Theta) \mathbf{I}_{\text{in}}, \tag{3.1-7}$$

where ϖ_0 is the single-scattering albedo, and where Θ is the *scattering angle* between the direction of incidence, \mathbf{s}_{in} , and the direction of scattering, \mathbf{s}_{sca} :

$$\cos \Theta = \mathbf{s}_{\text{in}} \cdot \mathbf{s}_{\text{sca}}. \tag{3.1-8}$$

The variation of $\mathbf{P}(\Theta)$ with Θ depends strongly on the microphysical properties of the scatterer(s). Note that we assume \mathbf{P} to depend on Θ only, which is true for randomly oriented particles. If, in addition, the process of scattering occurs by

- (i) an assembly of randomly oriented particles each having a plane of symmetry (e.g., homogeneous spheres or spheroids),
- (ii) an assembly containing particles and their mirror particles in equal number and with random orientation,
- (iii) an assembly of particles whose size is much smaller than the wavelength of incident light such that \mathbf{P} can be approximated by Rayleigh scattering

then $\mathbf{P}(\Theta)$ takes the form (Van de Hulst, 1957; Mishchenko, Travis and Lacis, 2002)

$$\mathbf{P}(\Theta) = \begin{pmatrix} a_1(\Theta) & b_1(\Theta) & 0 & 0 \\ b_1(\Theta) & a_2(\Theta) & 0 & 0 \\ 0 & 0 & a_3(\Theta) & b_2(\Theta) \\ 0 & 0 & -b_2(\Theta) & a_4(\Theta) \end{pmatrix}. \tag{3.1-9}$$

While the choice of scattering plane as reference plane for Stokes parameters is logical when describing single scattering in an arbitrary medium, we are interested in a general description of multiple scattering in plane-parallel atmospheres. To describe such scattering it is convenient to use coordinates and reference planes that are related to

the atmospheric geometry. That is, let z be the height in the atmosphere measured from the lower boundary of the atmosphere. A direction s in the atmosphere may then be specified by the pair of coordinates (θ, ϕ) , where θ is the polar angle measured from the positive z direction ($0 \leq \theta \leq \pi$) and ϕ is the azimuth angle measured clockwise from a plane containing the z -axis when looking upwards ($0 \leq \phi \leq 2\pi$). The xyz coordinates of s in terms of θ and ϕ are given by

$$\mathbf{s} = \mathbf{x} \sin \theta \cos \phi + \mathbf{y} \sin \theta \sin \phi + \mathbf{z} \cos \theta \quad 3.1-10$$

It is further useful in radiative transfer theory to employ the direction cosine $u = -\cos \theta$, or its absolute value $\mu = |u|$ if the sign of u is not important, or is specified explicitly. The plane containing s and the z -axis is the meridional plane for the propagation direction s and it is the Stokes vector specified in this plane that we will use to describe multiple scattering. Employing such *meridional planes* as reference planes for Stokes parameters requires the use of the *phase matrix* \mathbf{Z} instead of the scattering matrix \mathbf{P} to describe single scattering. The relation between \mathbf{Z} and \mathbf{P} is given by (Hovenier, 1969)

$$\mathbf{Z}(u_{\text{sca}}, u_{\text{in}}, \varphi_{\text{sca}} - \varphi_{\text{in}}) = \mathbf{L}(\pi - i_2) \mathbf{P}(\Theta) \mathbf{L}(-i_1) \quad 3.1-11$$

where \mathbf{L} is a rotation matrix used to rotate reference planes, and i_1 and i_2 are angles between the scattering plane and the local meridional plane for incident and scattered light, respectively. We refer to Hovenier (1969, 1971) for how i_1 and i_2 are related to s_{in} , and s_{sca} . The relationship between the scattering angle and the (θ, ϕ) coordinate representation can be obtained by substitution into expression 3.1-8

$$\cos \Theta = \mathbf{s}_{\text{in}} \cdot \mathbf{s}_{\text{sca}} = u_{\text{in}} u_{\text{sca}} + \sqrt{1 - u_{\text{in}}^2} \sqrt{1 - u_{\text{sca}}^2} \cos(\varphi_{\text{sca}} - \varphi_{\text{in}}). \quad 3.1-12$$

It follows that one needs only to be concerned with differences in azimuth angles for the description of scattering because of rotational symmetry with respect to the z -axis.

The phase matrix describes scattering by a volume element in the atmosphere. However, our interest lies with the study of sunlight reflected by an atmospheric column of the Earth. To describe this light, we introduce the reflection matrix \mathbf{R}_E as follows. Let \mathbf{I}_0 denote the Stokes vector of sunlight illuminating the Earth in the direction of $s_0 = (\theta_0, \phi_0)$, i.e., θ_0 is the solar zenith angle and ϕ_0 the solar azimuth angle. Using F_0 for the extra-terrestrial solar flux through a unit area perpendicular to s_0 at 1 AU from the sun one can write for \mathbf{I}_0 :

$$\mathbf{I}_0 = \frac{F_0 \delta(\mu - \mu_0) \delta(\varphi - \varphi_0) \{1, 0, 0, 0\}}{r_E^2} \quad 3.1-13$$

where $\mu_0 = |\cos \theta_0|$, δ is the Dirac delta function and r_E is the distance of the earth from the sun in AU. Note that this light is unidirectional and unpolarized. Let \mathbf{I}_E denote the Stokes vector of sunlight reflected by the Earth in the direction of $s_E = (\theta_E, \phi_E)$. Following Hansen and Travis (1974), we define the (4x4) reflection matrix \mathbf{R}_E of the Earth such that

$$\mathbf{I}_E = \frac{\mu_0 \mathbf{R}_E(\mu_E, \mu_0, \varphi_E - \varphi_0) \mathbf{F}_0}{\pi r_E^2} \quad 3.1-14$$

where $\mu_E = |\cos \theta_E|$ and

$$\mathbf{F}_0 = F_0 \{1, 0, 0, 0\}. \quad 3.1-15$$

In Sec. 3.3, we discuss how to obtain the reflection matrix \mathbf{R}_E from the phase matrices \mathbf{Z} of volume elements in the atmosphere. Finally, we remark that, when analyzing \mathbf{I}_E within the context of remote sensing, a useful quantity is the normalized Stokes vector $\bar{\mathbf{I}}_E$ defined as

$$\bar{\mathbf{I}}_E = \frac{\pi r_E^2 \mathbf{I}_E}{F_0} = \mu_0 \mathbf{R}_E(\mu_E, \mu_0, \varphi_E - \varphi_0) \equiv \{\bar{I}_E, \bar{Q}_E, \bar{U}_E, \bar{V}_E\}. \quad 3.1-16$$

This is because the spectral variation of $\bar{\mathbf{I}}_E$ is independent of the solar spectrum and so all channels can be treated uniformly while still preserving the effects of the scattering geometry.

3.2. Physical Basis for Aerosol Retrievals

The scientific basis for using polarimetric measurements to retrieve aerosol and cloud properties has been evaluated using an airborne instrument, the Research Scanning Polarimeter, that has similar functional capabilities to the APS instrument. In Figure 3.2-1 is shown a best fit to RSP observations for both intensity and polarization that was obtained using an iterative search similar to that which is used in the aerosol APS EDR algorithm. The iterative search incorporates the relative uncertainties of the calibration of the intensity and polarization. The spectral aerosol optical depth retrieved (red line in right hand panel below) had an optical depth at 555 nm of 0.102, and a bimodal size distribution with modes of effective radius 0.35 μm (water soluble) and 1.01 μm (sea salt). The spectral optical depths measured by a sunphotometer (symbols in right hand panel below) indicate that both the retrieved optical depth and size distribution are realistic since the agreement is within 0.01 in optical depth over the entire spectral range. Similar agreement was achieved over the Santa Barbara channel on another

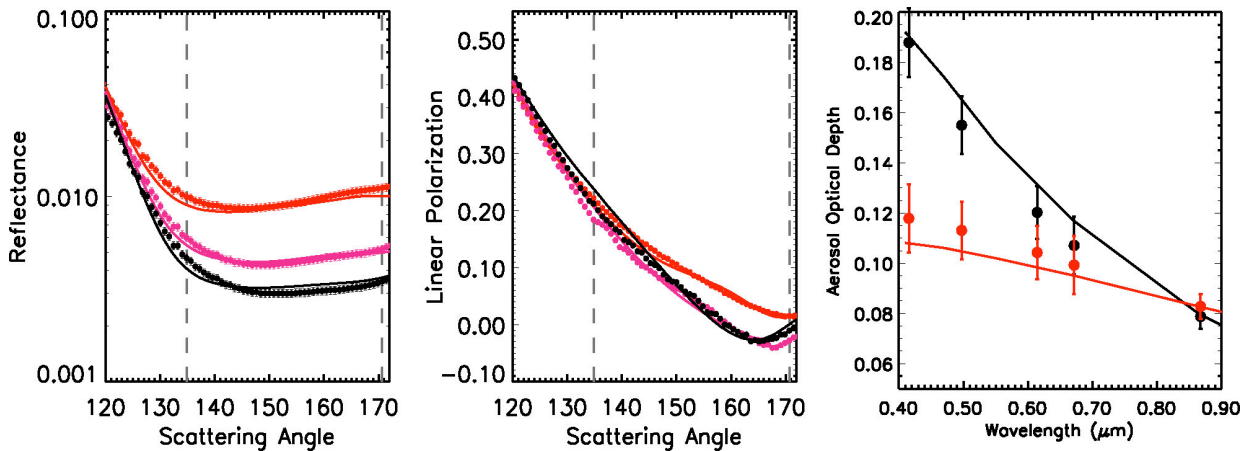


Figure 3.2-1 Demonstration of fitting theoretical model to RSP data (intensity and linear polarization in the plane of scattering, left and center panels respectively) and consequent accuracy of retrieved parameters evaluated against independent sunphotometer measurements (right-hand panel). The RSP data shown here is in spectral bands at 865, 1590 and 2250 nm (red, purple and black respectively).

day (black lines and symbols). It is the spectral and angular variation of the radiance and polarization that provides the information that is used to determine the aerosol optical depth and size distribution parameters. For example the linear polarization shown in this figure is the relative Stokes parameter q in the plane of scattering, which is why it is a signed quantity. The zero crossing in the 1590 and 2250 nm measurements provides a very strong constraint on the coarse mode size distribution and refractive index. The fine mode size distribution is constrained by the spectral variation of the radiances and linear polarization in all the spectral bands and the optical depth is constrained by the magnitude of the linear polarization in all the spectral bands.

More recently for a higher aerosol optical depth (0.3 at 555 nm), during the CLAMS field experiment over the Chesapeake Bay, similar agreement was achieved between an advanced airborne sunphotometer (AATS-14) and polarimetric aerosol retrievals using RSP data. This data set also demonstrated the capability of APS-type measurements to retrieve aerosol vertical distribution information.

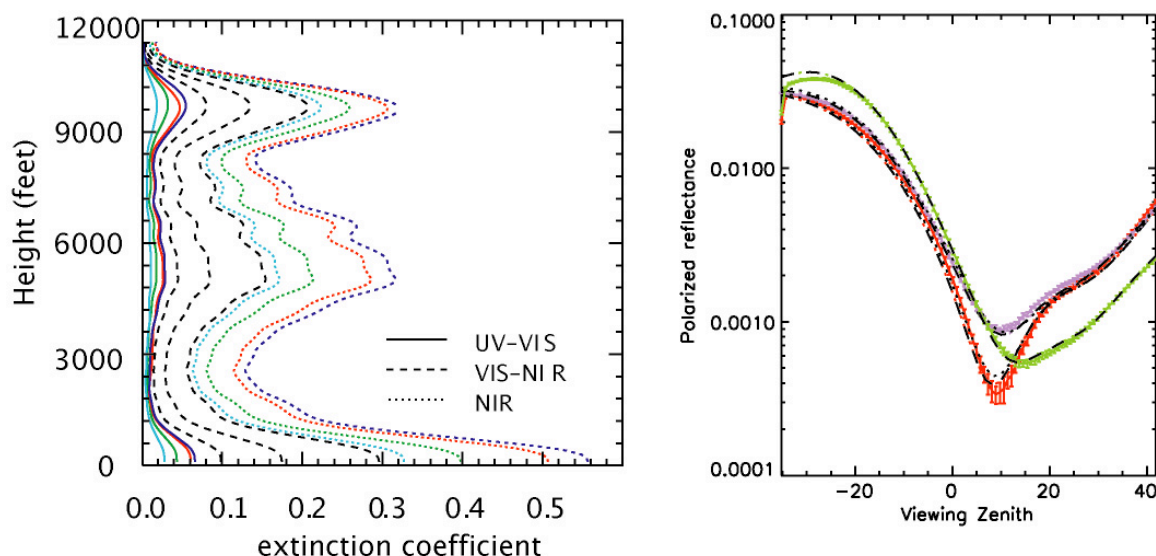


Figure 3.2-2 The vertical distribution of aerosol extinction derived from AATS-14 data in a range of spectral bands is shown in the left hand panel. The right-hand panel shows the polarized reflectance at 410, 470 and 555 nm observed by the RSP instrument.

In Figure 3.2-2 data from the AATS-14 instrument (shown courtesy of Dr. Philip Russell of NASA Ames Research Center) and the RSP instrument are shown. The dip in the polarized reflectance at 10° view zenith in the right hand panel and the reflectance can only **both** be matched by theoretical calculations that have an absorbing layer of fine mode aerosol particles between 9000 and 12000 feet. This theoretical analysis is corroborated by the AATS measurement shown in the left hand panel. Again, the information that allows for a detailed aerosol retrieval including sensitivity to vertical distribution is contained in the spectral and angular variation of the reflectance and polarized reflectance. In particular it can be seen that the dip in the polarized reflectance at 10° view zenith in the right hand panel is only apparent in the 410 and 470 nm observations and not the 555 nm observations, because of the lower Rayleigh

optical depth at 555 nm and consequent reduced sensitivity to vertical distribution of aerosols.

3.2.1. Over oceans and large lakes

A major issue for aerosol retrievals is proper characterization and modeling of the surface contribution to the observed radiances and polarization. Over the ocean at wavelengths less than 865 nm the contribution of upwelling radiation from the ocean body must be known, or retrieved simultaneously with the aerosol retrieval (see Section 7.2). In the case of APS retrievals theoretical analyses shown in Figure 3.2.1-1 indicate that polarized radiances are less sensitive to ocean color than radiances. The theoretical analyses are shown by dashed and solid lines that span the range of possible ocean conditions. It is clear that this range is smaller for the polarized reflectance than the reflectance.

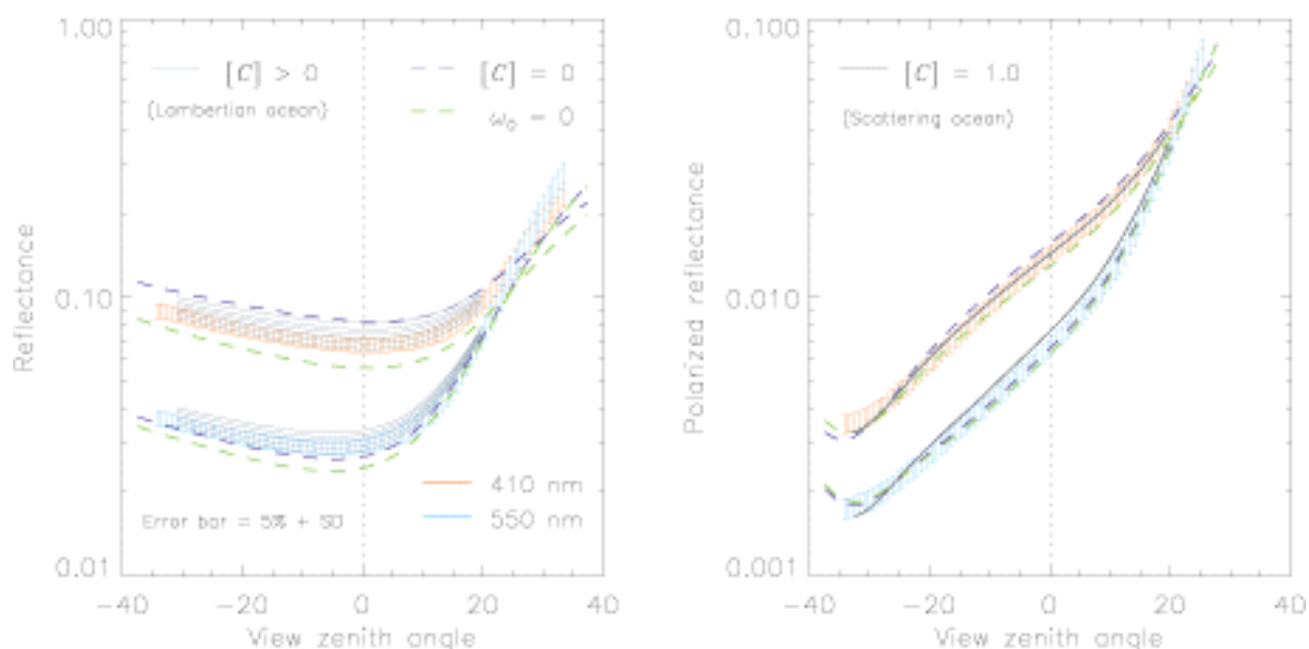


Figure 3.2.1-1 Examples of reflectance and polarized reflectance data at 410 and 550 nm taken from RSP acquisitions together with theoretical analysis of the sensitivity to ocean state (Chlorophyll concentration and absorption by Dissolved Organic Matter [DOM]).

This theoretical analysis is born out by data taken during the CLAMS field campaign. Figure 3.2.1-2 shows RSP data taken at 150 m above sea level, with reflectances on the left and polarized reflectances on the right. The clustering of the 410, 470 and 555 nm (blue, mauve, turquoise) reflectances is typical of what one expects when the ocean is bright in the coastal zone. This is because the observed reflectances are a combination of the ocean body reflectance that peaks at 550 nm and for which the dominant source of illumination is the direct solar beam and the reflectance of diffuse skylight (which decreases monotonically with wavelength) on the roughened ocean surface. The net combination of these two contributions to the observed reflectance is to yield similar reflectances at 410, 470 and 555 nm when there is significant scattering

within the ocean body. In contrast, the polarized reflectances show the monotonic decrease with wavelength that is expected if the signal is dominated by scattering of diffuse skylight off the roughened ocean surface and is not significantly affected by scattering from the ocean body.

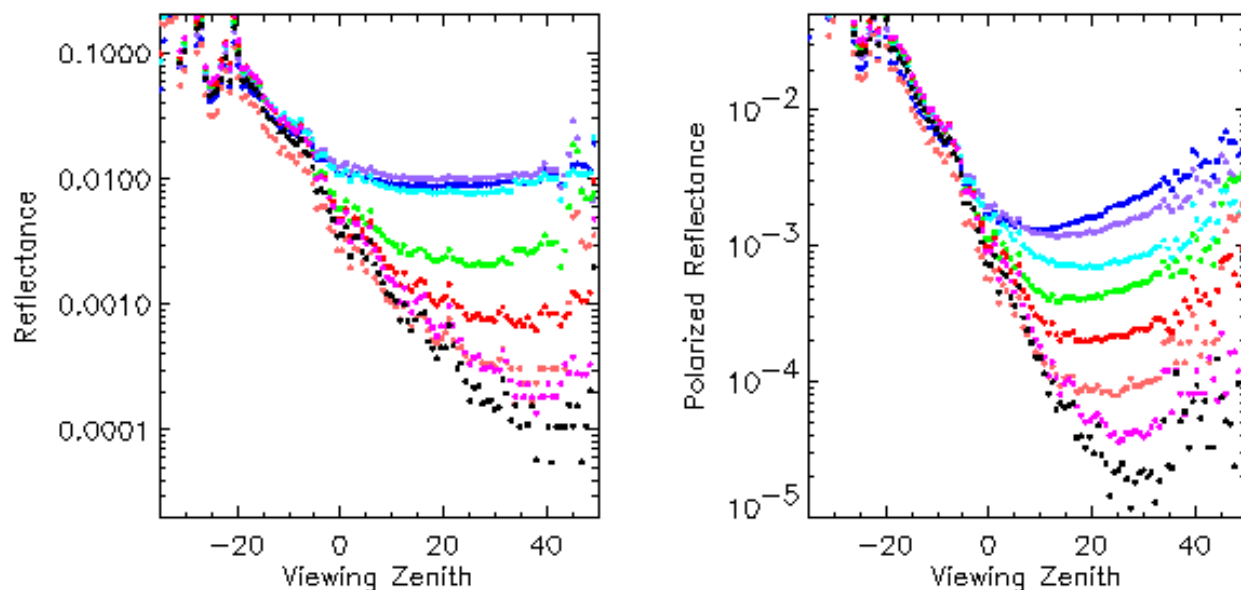


Figure 3.2.1-2 RSP data taken at 150 m above sea level in bands at 410, 470, 555, 670, 865, 960, 1590 and 2250 nm.

3.2.2. Over land

Over land the variability of the surface spectral albedo makes the retrieval of aerosol properties using intensity only measurements problematic. Commonly one empirical regression relationships to link the reflectance observed at 2250 nm with the surface reflectances at 410, 440, 470 and 670 nm. The scatter in these regression relationships is large and depends on scene type, season and viewing angle because these variables are dependent on the mixture of vegetation and soil in a scene (Remer *et al.* 2001, Gatebe *et al.* 2001). In contrast, the physical mechanism for the generation of surface polarization is Fresnel reflection from the front facet of the surfaces, whether they are vegetated or bare soils. Since the behavior of this surface interaction is determined by the real refractive index of the material, which typically has a weak spectral variation, the spectral variation of surface polarization is expected to be weak. This means that the surface polarized reflectance is expected to be “grey” for any given scene, although there may be contrast variations as function of scene, e.g., soils and vegetation. The behavior of the empirical models that must be used for aerosol retrievals over land from reflectance only measurements (such as VIIRS) and of the physically based Fresnel model of the surface that will be used for APS aerosol retrievals over land are shown in Figure 3.2.2-1. It is clear that the scatter in the regression relationship used for characterizing the land surface albedo is large, whereas the scatter of the observations about a physically based (Fresnel) model of the surface polarized reflectance is much

smaller. Furthermore, the surface polarized reflectance model has the significant advantage of being physically (not empirically) based.

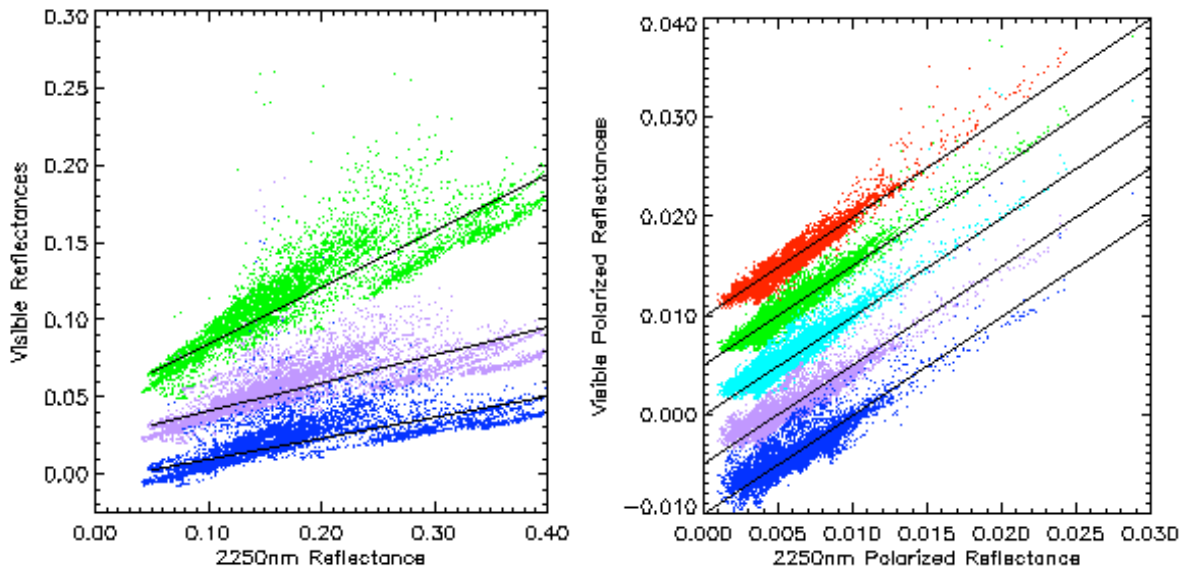


Figure 3.2.2-1 The left hand figure shows the surface reflectance in shorter wavelength bands as a function of reflectance at 2250nm. The right hand figure shows the measured surface polarized reflectance in shorter wavelength bands as a function of surface polarized reflectance at 2250nm. Offsets have been applied to the respective visible and near infrared band data of: -0.025, 0.000, 0.025 in the left panel; and of -0.010, -0.005, 0.000, 0.005 and 0.010 in the right panel.

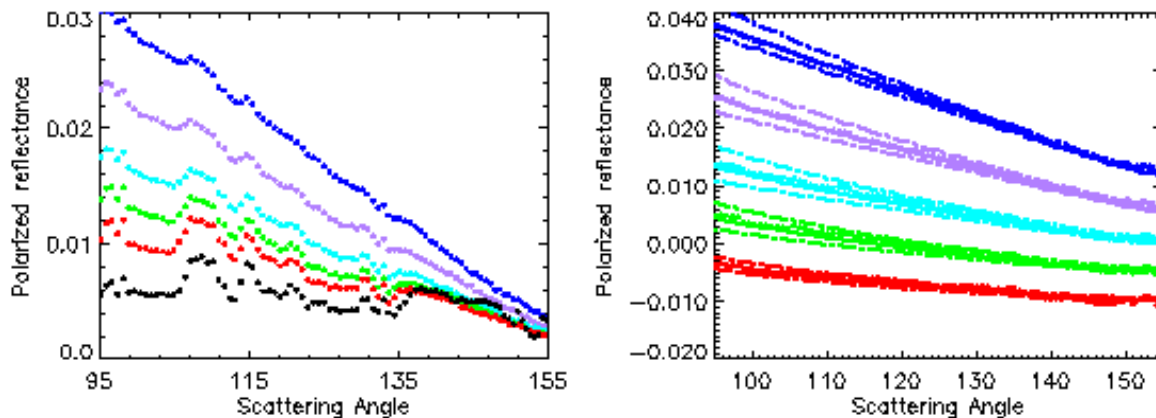


Figure 3.2.2-2 Left hand panel: Polarized reflectance for multiple views of the "same" scene. Non-ideal aircraft orientation causes scene to be a mixture of two different surfaces. Right hand panel: Atmospheric polarized reflectance after the surface polarization is corrected using the polarized reflectance at 2250nm as a proxy for surface polarized reflectance. RSP measurements at 410, 470, 555, 670, 865 and 2250 nm are shown as blue, purple, turquoise, green, red and black filled dots. The solid line is the polarized atmospheric reflectance derived from radiative transfer calculations that use an atmospheric model defined by sunphotometer measurements.

The consequent capability to retrieve aerosol properties over land that this simple surface polarized reflectance model provides is demonstrated in figure 3.2.2-2. The solid line that represents the polarized atmospheric reflectance derived from radiative transfer calculations that use an atmospheric model defined by sunphotometer measurements is indistinguishable from the RSP measurements (symbols). The dot-dashed lines demonstrate the sensitivity ($\pm 0.05\mu\text{m}$) of the polarized reflectance to perturbations in the accumulation mode effective radius.

3.3. Physical Basis for Cloud Particle Size Retrievals

A natural corollary of making measurements that provide accurate aerosol retrievals is the ability to retrieve cloud properties. In a certain sense, for an instrument like APS, a cloud is just a distribution of large aerosol particles with the refractive index of liquid or ice water. Operationally, this simply means that radiance and polarization “clues” need to be determined that allow for retrieval algorithms oriented specifically towards clouds to be applied to a particular scene, rather than aerosol retrieval algorithms. The behavior of polarization in the longest wavelength channels, where aerosol opacity is minimal, and higher radiance levels at visible wavelengths are used as cloud detection criteria. The angular variation of polarization in the visible channels of APS provides a direct indication of cloud thermodynamic phase (i.e. no rainbows for ice clouds) and is sensitive to cloud optical depth. Sensitivity to particle size is provided by measurements in spectral bands (1610 and 2250nm) where ice and liquid water absorb radiation, because larger particles absorb radiation more efficiently than smaller particles. For liquid water clouds this method of retrieving cloud particle size (Nakajima and King 1990), that is currently being used by MODIS and AVHRR, is supplemented by using the sensitivity of polarization in the rainbow and glory scattering angles to size particles.

3.3.1. Water Clouds

In figure 3.3.1-1 we show a model fit to measurements made over a thin, broken stratus cloud deck. The model used was a simple single layer cloud with a constant particle size throughout the cloud layer. A better fit can be obtained by adding complexity to the model, such as allowing a vertical profile of particle size and haze both within and above the cloud. However it is difficult to assess whether such additional complexity is justified when the cloud layer is heterogeneous as in this case.

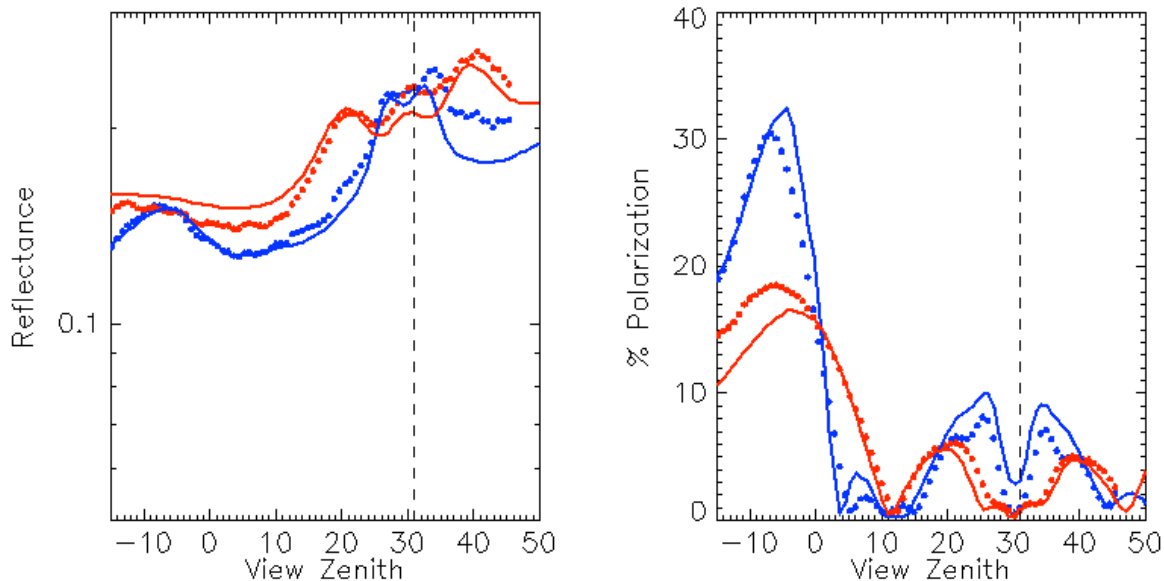


Figure 3.3.1-1 RSP measurements at 865nm (blue dots) and 2250nm (red dots) of the intensity and polarization of sunlight reflected from clouds, averaged over five pixels to mitigate the small scale effects of cloud inhomogeneity. The solid lines are model calculations for a cloud layer with an optical depth at 550nm of 2.0 and water droplets with an effective radius of $5.5\mu\text{m}$ (effective variance is 0.07).

Nonetheless although the cloud field is quite broken the polarization unambiguously limits the droplet effective radius to $5.5\mu\text{m} \pm 0.5\mu\text{m}$ and the effective variance to 0.07 ± 0.02 .

The simple use of single view angle radiances at absorbing and non-absorbing wavelengths is principally sensitive to the effective radius of the particles (Nakajima and King 1990) and it is the use of multiple angles and polarization that allows for a robust retrieval of the effective variance of the particle size distribution. This is shown in Figure

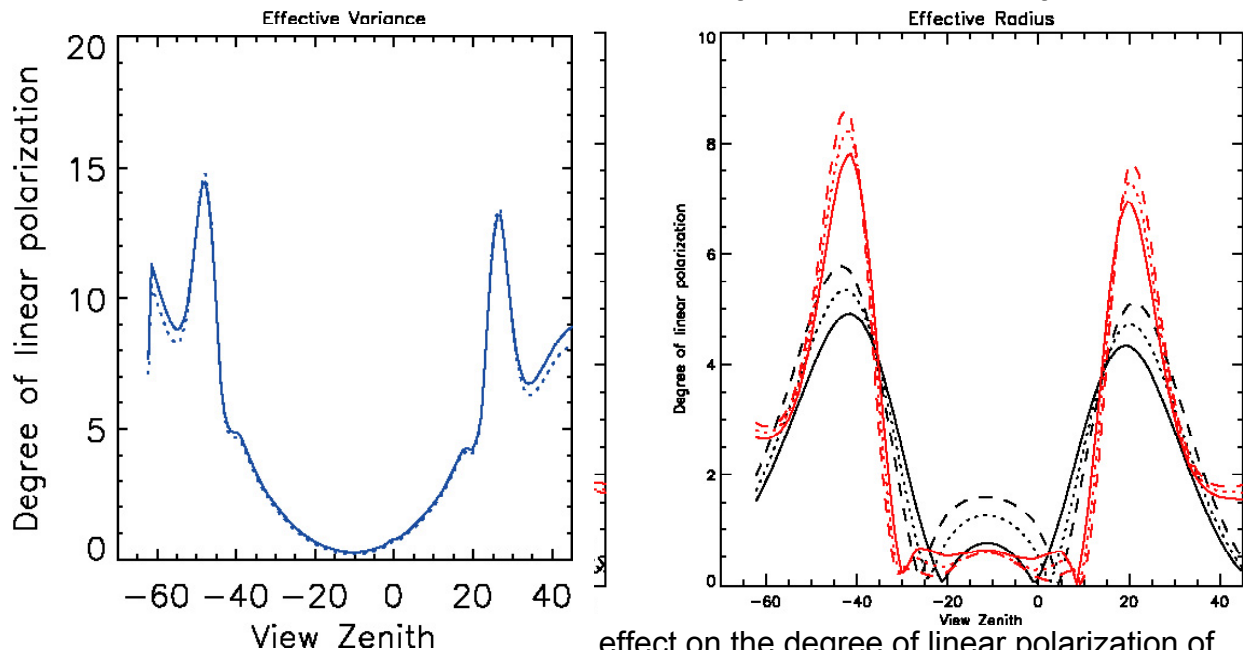


Figure 3.3.1-3. Calculations of the degree of linear polarization at 410 nm for a cloud with its top at 500 (solid) or 600 (dashed) mbar

effect on the degree of linear polarization of 0.05, 0.1) and increasing the effective radius for the 865 (red) and the 2250 nm

3.3.2. Ice Clouds

In the following two sections we discuss the properties of cirrus and polar stratospheric clouds (PSCs). Although PSCs may be liquid, their typical optical depths mean that a discussion of the retrieval of their properties falls into the same category as thin cirrus clouds.

3.3.2.1. Cirrus Clouds

The scattering of visible radiation by cirrus clouds depends principally on the optical depth of the clouds and on the shape of the ice crystals composing the clouds. This is because ice crystals are generally much larger than the dominant solar wavelengths, and the variation of their microphysical properties as a function of crystal size and wavelength is therefore quite weak. The integrated effect of cirrus clouds on the solar spectrum also depends on the size of the ice-crystals, because large (small) particles are more (less) efficient absorbers in the near infrared (NIR) regions of the spectrum where there is substantial ice absorption. The value of the asymmetry parameter for visible scattering by ice crystals is a major determinant of the radiative impact of cirrus clouds [Stephens *et al.* 1990, Wielicki *et al.* 1990] and is directly related to ice crystal habit and size. The thermal effects of cirrus clouds are also strongly dependent on the microphysical properties of the ice crystals [Takano *et al.* 1992], as well as the cloud optical depth and temperature.

The inference of cirrus properties from the remote sensing measurements by instruments such as VIIRS requires that either assumptions about the crystal habit must be made, or the crystal habit must be retrieved in order to have robust estimates of the required quantities, i.e., the particle size, optical depth and Ice Water Path (IWP). Incorrect assumptions about the crystal habit can cause large errors in the optical depth retrieved from solar reflectance measurements [Minnis *et al.* 1993, Mishchenko *et al.* 1996], errors in the estimated particle size [Rolland *et al.* 2000] and erroneous angular variations in the inferred albedo of the cirrus clouds [C.-Labonnote *et al.* 2001].

The RSP instrument recently took part in the CRYSTAL-FACE field experiment. One type of cloud that was wide-spread and frequently observed during CRYSTAL-FACE was thin cirrus clouds. For RSP observations this type of cirrus is identified by a negligible variation in the visible radiances and an order of magnitude increase in radiance in the band located at 1880 nm. At 1880 nm there is a strong water vapor band that ensures that surface features, low level clouds and boundary layer aerosols are not observed by the RSP. An example of this behavior is presented in Figure 3.3.2.1-1 where clear skies and some boundary layer clouds are apparent between scans 0 and 200. From scan 200 to 400 thin cirrus clouds increase the brightness in

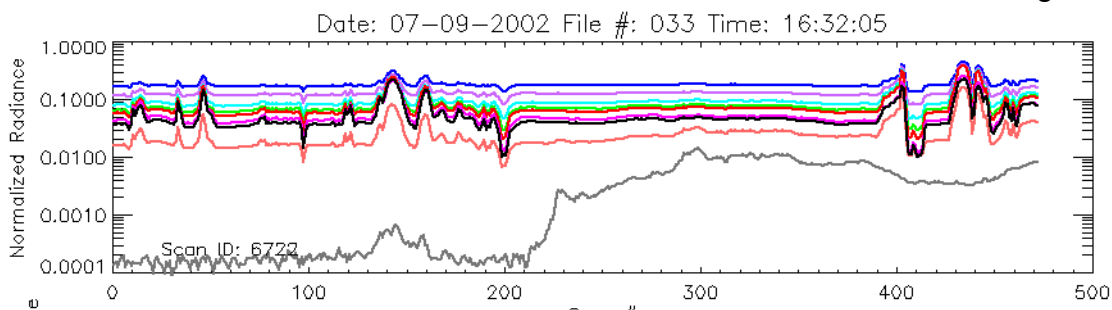


Figure 3.3.2.1-1 Variation of RSP radiance measurements at 410, 470, 555, 670, 865, 960, 1590, 1880 and 2250 shown as blue, mauve, turquoise, green, red, orange, fuschia, grey and black lines respectively as a function of scan number.

the 1880 nm spectral band, while the visible bands remain at a constant value close to the clear sky values.

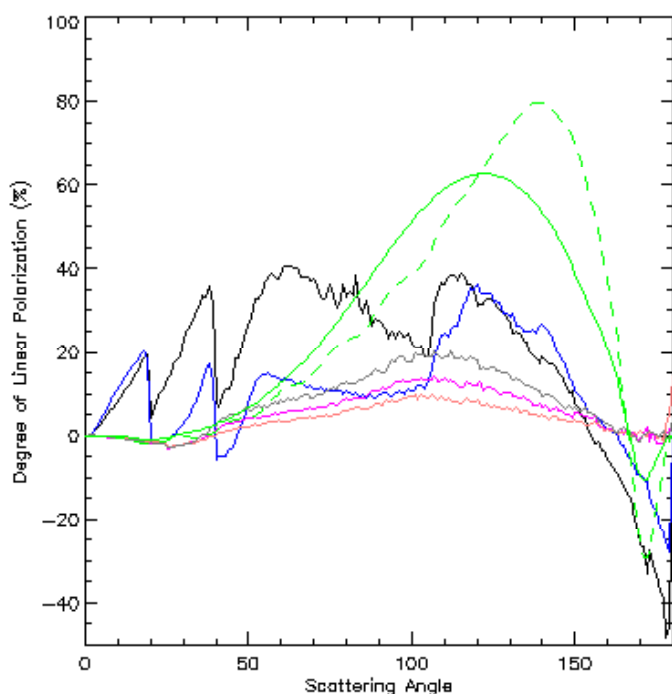


Figure 3.3.2.1-2 Degree of linear polarization for single scattering by ice crystal plates (black), columns (blue) and polycrystals (fuschia) that have a 200 μm surface equivalent sphere radius. The effect of size on the fractal polycrystal polarization signature is shown for 450 (grey) and 10 (orange) μm particles.

The polarimetric signature of these thin cirrus clouds is typically featureless and the polarization is low. In order to provide a comparison with the type of polarization signatures expected from cirrus clouds Figure 3.3.2.1 shows the degree of linear polarization for single scattering from different ice crystals. For comparison, calculations for a coarse mode (effective radius 2.3 μm , effective variance 0.17) dust aerosol modeled as a size-shape distribution of spheroids (green solid) and as a size distribution of spheres (green dashed) are also shown. In modeling the polarization behavior in the 1880 nm band we found that the best fit is obtained using a polycrystal particle model and a power law size distribution with an exponent of between -2 and -3. The

type of fit obtained is shown in Figure 3.3.2-3 where the jagged solid line is the theoretical calculation and the symbols are the RSP measurements. (The noise in the theoretical calculations is caused by using too few rays in the geometrical optics calculations.) The left hand figure shows data from 7/9/2002 near the Yucatan peninsula, while the right hand figure shows data from 7/21/2002 over Florida. The same size distribution is used in both cases and is broadly consistent with coincident size distribution measurements from the CPI and SPP-100 instruments.

This preliminary result suggests that thin cirrus clouds are dominated by small particles and are composed of aged crystals with distorted, or roughened facets and possibly air bubble inclusions that yield a generic scattering behavior with featureless phase

matrices and low polarization. This can be reasonably well modeled by a polycrystal shape and a power law size distribution. In contrast the polarization signatures of thick cirrus clouds are much more variable, but do generally show polarization inversions near backscatter indicating that although the shape and/or size distributions of these clouds are highly variable more pristine crystalline habits than those present in thin cirrus clouds are relevant to their scattering properties.

The cloud EDR retrieval algorithm will take this behavior into account by allowing for a set shape mixtures that can be selected using the measurements at 1378 nm where single scattering calculations provide an acceptable tool for selecting the shape mixture.

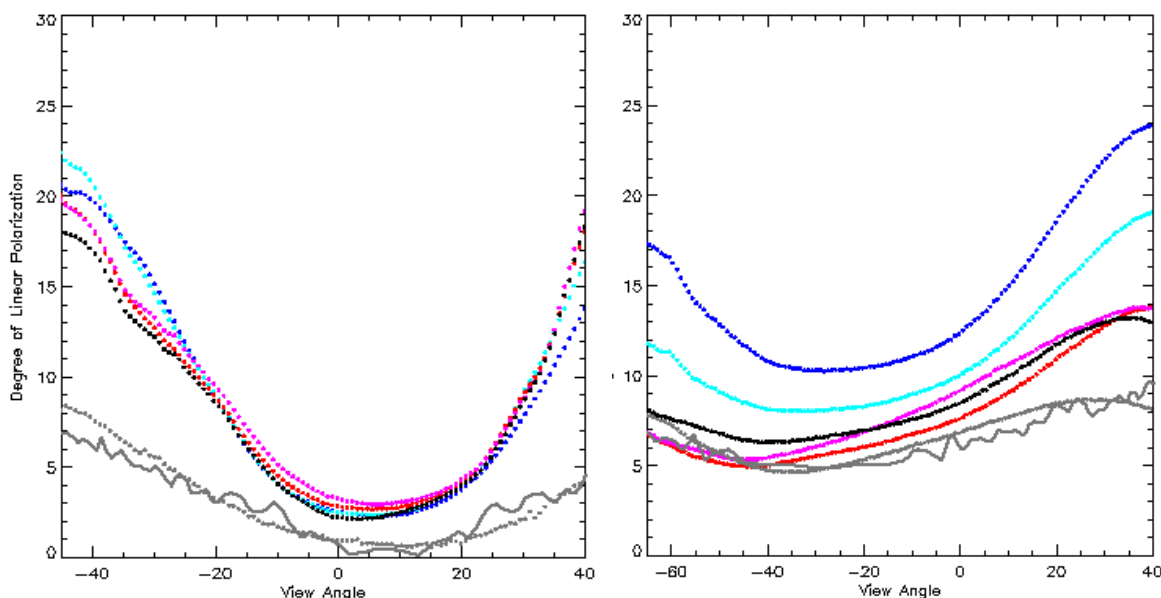


Figure 3.3.2-3. Fit for the 1880 nm band (grey) between observations (symbols) and fractal polycrystal ice particles (solid line).

3.3.2.2. Polar Stratospheric Clouds

High Altitude Mother of pearl clouds have been observed in the Arctic for years. In the late '70s solar occultation measurements by the SAM II instruments showed that these tenuous clouds were observed at altitudes between about 14-25 km above both poles in the winter and were frequently seen in the proximity of orographic features. The term "polar stratospheric clouds" was coined (McCormick *et al.*, 1982). The height, frequency of occurrence, formation temperature and extinction characteristics were measured, but the clouds were regarded as a curiosity of minimal scientific interest until the Antarctic "ozone hole" was revealed in 1984 (Farman *et al.*, 1984). Investigations of Antarctic ozone depletion showed that PSCs were important because they provide surfaces for reactions that convert "reservoir" chlorine compounds into "active" compounds that participate in ozone destruction. This discovery gave new importance to PSCs intensifying research of their properties.

Since the SAM II observations PSC data sets have been acquired by several solar occultation instruments (SAGE I-III, HALOE, POAM and ILAS), IR thermal emission instruments (CRISTA, MIPAS, ISAMS and CLAES), numerous ground-based lidars, balloon-borne particle counters, aircraft measurements and ground observations of scattered light.

PSCs have been classified according to formation temperature into Type I which form below about 195 K and Type II which form below about 187K. Type I is further divided into Type 1a – which is crystalline, predominantly nitric acid trihydrate or NAT and Type 1b which is liquid and is a ternary solution $\text{HNO}_3/\text{H}_2\text{O}/\text{H}_2\text{SO}_4$. Type II is water ice and rarely found in the Arctic but is widespread in the Antarctic winter. Other $\text{H}_2\text{O}/\text{H}_2\text{NO}_3$ compounds e.g. NAD and metastable compounds have been proposed as well. The indices of refraction for many of these compounds are included in the HITRAN 2000 database and will be used in the construction of set of tables for the retrieval of PSC properties.

The liquid or crystalline nature of PSCs has been determined largely from lidar depolarization measurements. Type 1 particles are fairly small 0.5-1 μm . Type II particles (5-20 μm) which form below the frost point are larger and have sedimentation velocities that facilitate denitrification and consequently ozone destruction over Antarctica. Larger Type 1 particles with significant fall velocities have been cited as a route to denitrification without dehydration so “small” Type 1 particles is not always the case and the retrieval approach takes this into account by allowing particle sizes to vary freely from 0.5-20 μm .

The mean and standard deviation of the optical depth at a wavelength of $1\mu\text{m}$ for Type I PSCs in Antarctica during 1987 was $9.55\text{e-}04$ and $7.10\text{e-}04$, respectively (Lin and Saxena 1992). SAM II data from 1992 indicates that the extinction coefficient goes above 0.02/km when temperatures indicate that Type II PSCs are present. With cloud optical thicknesses of 2-4 km the optical depths of Type II PSCs are between 0.04 and 0.08 (Mergenthaler *et al.*, 1997) Type I PSCs are therefore near the detection limit of the APS measurements at 1378 nm, but Type II PSCs should be readily detectable when present and given the small size of the particles compared to snow measurements at 1610 nm should be usable in the analysis of these clouds.

Polar mesospheric clouds which exist at altitudes of 80-90 km will not typically be detectable using the APS instrument since their typical optical depths are 0.001, or less, with particle sizes of 70 nm (Debrestian *et al.*, 1997). The highest altitude from which a measurable signal will be obtained in the APS observations is around 25 km when PSCs of sufficient optical depth are present.

3.4. Radiative Transfer Modeling

The quantities that are required before the polarized reflectance of a surface-atmosphere system can be calculated are the single scattering properties of the constituent particles. In section 3.4.1 we define the required single scattering properties, their size distribution averaged values, the types of size distribution that are

used herein and briefly review the techniques that are available for the calculation of single scattering properties.

There are a number of methods available for the calculation of reflection from a vertically inhomogeneous multiple scattering atmosphere above a reflective surface. Both invariant imbedding (Mishchenko and Travis 1997) and doubling/adding (Cairns *et al.* 1997, Chowdhary *et al.* 2000) have been successfully used in the analysis of polarimetric remote sensing. Other methods that have been developed for calculating the Stokes vector of radiation reflected from an atmosphere are vector discrete ordinates (VDISORT, Schulz *et al.* 1999), a successive order of scattering method (Chami *et al.* 2001) the Monte Carlo method and hybrid methods (Hatcher Tynes *et al.* 2001). In section 3.4.2 we describe the doubling/adding method since this method is simple, flexible, fast and accurate and allows accuracy and speed to be traded off in a straightforward and controllable manner (de Haan *et al.* 1986, Cairns *et al.* 1997).

If the lower boundary of the atmosphere consists of an ocean, then one needs to compute also the bidirectional and spectral properties of the water-leaving radiation. Underwater light multiple scattering computations can be performed using the same radiative transfer methods as those used for the atmosphere. However, the scarce information on single scattering properties of hydrosols particles necessitates using a multitude of constraints obtained from in-situ measurements of physical properties as well as from the remote sensing of ocean color. In section 3.4.3 we review these constraints and use them to construct a hydrosol model that leads to realistic variations of total and polarized water-leaving radiances as a function of wavelength and biomass concentration. A similar description of modeling the lower boundary condition for land surfaces is provided in Section 3.4.4.

The APS instrument has bands with finite spectral bandwidths and so the reflectances that are calculated for use in the APS EDR algorithm are integrated over wavelength and weighted by the band's spectral response in order to be directly comparable with the APS measurements. The spectral averages are defined in section 3.4.5 and the use of the correlated k distribution (Lacis and Oinas, 1990) to provide an accurate integration over very rapid spectral variations such as those caused by line absorption is explained.

3.4.1. Single-scattering properties and size distributions

Consider a small volume element dV enclosing an ensemble of particles such as molecules, aerosols, and/or cloud droplets. Let us concentrate first on the case in which the particles contained by dV have the same composition and the same size. Light propagating through this volume element may be *absorbed* and/or *scattered* by these particles, the combined sum of which is called *extinction* of light. To describe these processes, we introduce first the *scattering cross section* C_{sca} (m^2), the *absorption cross section* C_{abs} (m^2) and the *extinction cross section* C_{ext} (m^2) of a particle. Cross section C_{sca} is an area such that the total energy scattered by this particle is equal to the energy of incident radiation falling on a cross sectional area C_{sca} . Cross sections C_{abs} and C_{ext} are defined similarly except for absorption and extinction of light, respectively. If G

denotes the geometrical cross section of this particle, then one can further define the *scattering efficiency* Q_{sca} as

$$Q_{\text{sca}} = \frac{C_{\text{sca}}}{G} \quad 3.4.1-1$$

and similarly for the *absorption efficiency* Q_{abs} and *extinction efficiency* Q_{ext} . Then, let dV contain N_p identical particles per unit volume, and let $I_{\text{in}}(s)$ denote the intensity of a beam of light illuminating dV in the direction of s . The loss of intensity $-dI(s)$ due to extinction over a distance of ds through the volume element is given by *Beer's law*

$$-dI(s) = k_{\text{ext}} I_{\text{in}}(s) ds \quad 3.4.1-2$$

where

$$k_{\text{ext}} = N_p C_{\text{ext}} \quad 3.4.1-3$$

is the *extinction coefficient* (m^{-1}). Similarly, one can use the *scattering coefficient* $k_{\text{sca}} = N_p C_{\text{sca}}$ (m^{-1}) and *absorption coefficient* $k_{\text{abs}} = N_p C_{\text{abs}}$ (m^{-1}) to obtain the intensity lost due to scattering and absorption over a distance ds , respectively. It follows from the definition of extinction that

$$C_{\text{ext}} = C_{\text{sca}} + C_{\text{abs}} \quad 3.4.1-4$$

$$Q_{\text{ext}} = Q_{\text{sca}} + Q_{\text{abs}} \quad 3.4.1-5$$

$$k_{\text{ext}} = k_{\text{sca}} + k_{\text{abs}} \quad 3.4.1-6$$

From these quantities, one can further define the *single scattering albedo* ϖ as

$$\varpi = \frac{C_{\text{sca}}}{C_{\text{ext}}} = \frac{Q_{\text{sca}}}{Q_{\text{ext}}} = \frac{k_{\text{sca}}}{k_{\text{ext}}} \quad 3.4.1-7$$

That is, ϖ is the fraction of the loss of energy in the direction of s due to scattering. Finally, we remark that the angular distribution of light scattered away from s is described by the scattering function P introduced in Section 3.1. Alternatively, if $I_{\text{sca}}(s')$ denotes the intensity of light scattered by dV in the direction of s' , then from Beer's law one can define P as

$$I_{\text{sca}}(s') \propto k_{\text{sca}} P(\Theta) I_{\text{in}}(s) ds \quad 3.4.1-8$$

where Θ is the angle between s and s' . Introducing further the *optical thickness* $d\tau$ from

$$d\tau \equiv k_{\text{ext}} dz = k_{\text{ext}} (\cos \theta) ds \quad 3.4.1-9$$

in which θ is the polar zenith angle between s and the z -axis, we obtain for $I_{\text{sca}}(s')$:

$$I_{\text{sca}}(s') \propto \frac{k_{\text{sca}}}{k_{\text{ext}}} P(\Theta) I_{\text{in}}(s) k_{\text{ext}} ds \equiv \varpi P(\Theta) I_{\text{in}}(\hat{s}) \frac{d\tau}{\cos \theta} \quad 3.4.1-10$$

A discussion of methods for the determination of $P(\Theta)$, C_{sca} , C_{ext} and C_{abs} is given at the end of this section.

Thus far, we assumed the particles contained by dV to all have the same size and composition. However, in most practical cases one will encounter dispersion of sizes even if the particles are chemically the same. Let $n(r)$ denote such a particle size distribution, i.e., $n(r)$ is the number of particles per unit volume with radius between r and $r+dr$. We shall see later that it is straightforward to compute single-scattering properties similar to those introduced above for arbitrary $n(r)$. However, our ultimate aim is to invert scattering properties back to particle properties; hence, it is desirable to describe particle size distributions by a minimum number of parameters that can be retrieved from remote sensing data. Hansen and Travis (1974) demonstrated that different size distributions of spherical particles lead to essentially identical scattering properties if these distributions have the same *effective radius* r_{eff} and *effective variance* v_{eff} defined as

$$r_{\text{eff}} = \frac{\int_{r_1}^{r_2} r \left\{ \pi r^2 n(r) \right\} dr}{\int_{r_1}^{r_2} \left\{ \pi r^2 n(r) \right\} dr} = \langle G \rangle^{-1} \int_{r_1}^{r_2} r \left\{ \pi r^2 n(r) \right\} dr \quad 3.4.1-11$$

and

$$v_{\text{eff}} = \left(\langle G \rangle r_{\text{eff}}^2 \right)^{-1} \int_{r_1}^{r_2} (r - r_{\text{eff}})^2 \left\{ \pi r^2 n(r) \right\} dr \quad 3.4.1-12$$

respectively, where $\langle G \rangle$ is the size-averaged geometrical area of the particles. Their conclusions have recently be extended by Mishchenko and Travis (1994) to polydispersions of randomly oriented spheroids. In what follows, we therefore employ parameters r_{eff} and v_{eff} to describe particle size distributions. Among the most widely used of these distributions are the *gamma distribution*

$$n_{\text{gam}}(r) = \text{constant} \times \left(r^{\frac{1-3b}{b}} e^{\frac{-r}{ab}} \right) \quad 3.4.1-13$$

where

$$r_{\text{eff}} = a, \quad v_{\text{eff}} = b \quad 3.4.1-14$$

and which is often used for cloud and haze water droplets; the *log-normal distribution*

$$n_{\text{log}}(r) = \text{constant} \times \frac{1}{s_g r} \exp \left[-(\ln r - \ln r_g)^2 / (2s_g^2) \right] \quad 3.4.1-15$$

where

$$r_{\text{eff}} = r_g (1 + v_{\text{eff}})^{5/2}, \quad v_{\text{eff}} = \exp(s_g^2) - 1 \quad 3.4.1-16$$

and which is often used for aerosol particles; and the *power law distribution*

$$n_{\text{pwr}}(r) = \begin{cases} \text{constant} \times r^{-l} & r_1 \leq r \leq r_2 \\ 0 & \text{otherwise} \end{cases} \quad 3.4.1-17$$

where for $l \neq 3$

$$r_{\text{eff}} = \left(\frac{3-l}{4-l} \right) \left(\frac{r_2^{4-l} - r_1^{4-l}}{r_2^{3-l} - r_1^{3-l}} \right), \quad v_{\text{eff}} = \left(\frac{3-l}{5-l} \right) \left(\frac{r_2^{5-l} - r_1^{5-l}}{r_2^{3-l} - r_1^{3-l}} \right) \left(\frac{3-l}{5-l} \right)^2 \left(\frac{r_2^{5-l} - r_1^{5-l}}{r_2^{3-l} - r_1^{3-l}} \right)^2 - 1 \quad 3.4.1-18$$

while for $l = 3$

$$r_{\text{eff}} = \frac{r_2 - r_1}{\ln(r_2/r_1)}, \quad v_{\text{eff}} = \frac{r_2 + r_1}{2(r_2 - r_1)} \ln(r_2/r_1) - 1 \quad 3.4.1-19$$

The advantage of using a power law size distribution is that once r_1 and r_2 are fixed, one needs only one parameter (the exponent l) to describe or retrieve $n_{\text{pwr}}(r)$. Another advantage is that the extinction efficiency Q_{ext} can for such size distributions be approximated by

$$Q_{\text{ext}}(\lambda) \propto \lambda^{3-l} \equiv \lambda^{-\gamma} \quad 3.4.1-20$$

where γ is the so-called *Ångström coefficient*. For terrestrial aerosols, γ varies in general between 0.5 and 2.0. We remark finally that the constants appearing in $n_{\text{pwr}}(r)$, $n_{\text{gam}}(r)$ and $n_{\text{pwr}}(r)$ are chosen such that the corresponding size distribution satisfies

$$\int_0^{\infty} n(r) dr = 1 \quad 3.4.1-21$$

That is, $n(r)$ is here the *fraction* of particles per unit volume with radius between r and $r+dr$.

For a size distribution $n(r)$ specified by r_{eff} and v_{eff} , the size-averaged efficiency factors for scattering, absorption, and extinction are given by

$$\langle Q_{\text{sca}} \rangle = \langle G \rangle^{-1} \langle C_{\text{sca}} \rangle = \langle G \rangle^{-1} \int_{r_1}^{r_2} C_{\text{sca}}(r) n(r) dr = \langle G \rangle^{-1} \int_{r_1}^{r_2} \pi r^2 Q_{\text{sca}}(r) n(r) dr \quad 3.4.1-22$$

$$\langle Q_{\text{abs}} \rangle = \langle G \rangle^{-1} \langle C_{\text{abs}} \rangle = \langle G \rangle^{-1} \int_{r_1}^{r_2} C_{\text{abs}}(r) n(r) dr = \langle G \rangle^{-1} \int_{r_1}^{r_2} \pi r^2 Q_{\text{abs}}(r) n(r) dr, \quad 3.4.1-23$$

$$\langle Q_{\text{ext}} \rangle = \langle G \rangle^{-1} \langle C_{\text{ext}} \rangle = \langle G \rangle^{-1} \int_{r_1}^{r_2} C_{\text{ext}}(r) n(r) dr = \langle G \rangle^{-1} \int_{r_1}^{r_2} \pi r^2 Q_{\text{ext}}(r) n(r) dr, \quad 3.4.1-24$$

respectively. Similarly, the size-averaged scattering matrix $\langle \mathbf{P}(\Theta) \rangle$ is given by

$$\langle \mathbf{P}(\Theta) \rangle = \int_{r_1}^{r_2} \mathbf{P}(\Theta) n(r) dr \quad 3.4.1-25$$

If the volume element dV contains several types of size-averaged particles, e.g., cloud and aerosol particles, then one should weight their respective contributions to the bulk scattering properties of dV by their number fraction of particles per unit volume. That is,

let subscript ' i ' denote quantities belonging to particle type i (where $i \geq 1$). If f_i is the number fraction of type i particles per unit volume, then

$$\langle C_{\text{sca}} \rangle = \sum_i f_i \langle C_{\text{sca}} \rangle_i \quad 3.4.1-26$$

$$\langle C_{\text{abs}} \rangle = \sum_i f_i \langle C_{\text{abs}} \rangle_i \quad 3.4.1-27$$

$$\langle C_{\text{ext}} \rangle = \sum_i f_i \langle C_{\text{ext}} \rangle_i \quad 3.4.1-28$$

for the bulk cross sections, and

$$\langle G \rangle = \sum_i f_i \langle G \rangle_i \quad 3.4.1-29$$

for the bulk geometrical particle area. The bulk efficiency factors are still given by the corresponding size-averaged equations except for including averaging for the number fractions. Note further that the bulk single scattering coefficient is given by

$$\langle \varpi \rangle = \frac{\langle C_{\text{sca}} \rangle}{\langle C_{\text{ext}} \rangle} = \frac{\langle Q_{\text{sca}} \rangle}{\langle Q_{\text{ext}} \rangle} \quad 3.4.1-30$$

while for the bulk scattering matrix one has to include multiplication by the bulk scattering cross section for each type of particle

$$\langle \mathbf{P}(\Theta) \rangle = \frac{\sum_i f_i \langle C_{\text{sca}} \rangle_i \langle \mathbf{P}(\Theta) \rangle_i}{\sum_i f_i \langle C_{\text{sca}} \rangle_i} \quad 3.4.1-31$$

If particles are spherical and if their composition can be represented by a single value of complex refractive index, then one can obtain $\mathbf{P}(\Theta)$ using the standard Mie-theory (van de Hulst, 1957; de Rooij and van der Stap, 1984). A discussion of methods for calculating the scattering properties of non-spherical particles, which is relevant to the remote sensing of both dust aerosols and ice clouds concludes this section.

The ability to calculate the radiative properties of cirrus ice particles has often been a limiting factor in the interpretation of remote sensing data because of the large uncertainties regarding the nature of ice particle shapes and the difficulty of calculating scattering properties for nonspherical particles. As a result of recent advances in the calculation of scattering by nonspherical particles [Mishchenko *et al.* 2000], the principal remaining problem appears to be the uncertain shape distributions of cirrus clouds.

The molecular structure of atmospheric ice water enforces hexagonal symmetries [Strauss *et al.* 1997]. However, inhomogeneous growth conditions, splitting and aggregation can lead to the formation of complicated particles like bullet rosettes, dendrites, aggregates etc. Air bubbles may be trapped inside rapidly growing ice particles or inside suddenly frozen supercooled droplets [Hallet, 1994]. Moreover measurements performed by the Counterflow Virtual Impactor (CVI) [Noone *et al.* 1993]

have shown that mineral or soot impurities are sometimes trapped in ice crystals due to the presence of aerosols in the upper troposphere acting as ice nuclei, although only a small number of impurities per crystal is generally found. The absence of strong halo and backscattering features in recent ground-based, *in situ* nephelometer and airborne radiance measurements of cirrus clouds [Foot 1988, Francis 1995, Gayet *et al.* 1995, Posse and Von Hoyningen-Huene 1995, Spinhirne *et al.* 1996, C.-Labonnote *et al.* 2001] indicate that pure hexagonal monocrystals are not in general a realistic model for crystals in cirrus clouds. Indeed, ice particle replicas with high spatial resolution show that ice crystals often have much more complicated shapes than solid hexagonal cylinders [Sassen *et al.* 1994, Heymsfield and Iaquinta 2000]. It can also be seen that the crystal habits depend on temperature which, together with the dependence of ice water content on temperature [Heymsfield and Platt 1984], further complicates the possible range of cirrus radiative feedbacks.

However there are now a number of methods that appear to provide useful approaches for calculating the scattering properties of imperfect hexagonal particles and obtaining good matches with both remote sensing and *in situ* data. Liou *et al.* [2000] have shown that the remote sensing measurements made by Spinhirne *et al.* [1996] are well matched by model calculations using the scattering properties of ice crystal aggregates with rough surfaces. A similar effect on the scattering properties of ice crystals to that of the rough surfaces used by Liou *et al.* can be obtained by a method that was developed by Macke *et al.* [1996a]. In this approach the surfaces of hexagonal particles are randomly distorted. In both cases the effect of the roughness, or distortion, is to reduce the magnitude of halo features as shown in Figure 3.4.1-1.

A second approach for deriving ice crystal scattering phase functions which match observations is to include small trapped air bubbles inside hexagonal particles where the ray tracing approach is coupled with a Monte Carlo technique for calculating the scattering on the trapped bubbles [Macke *et al.* 1996b, C.-Labonnote *et al.* 2001].

A third approach, which may be combined with the previous two approaches, is to perform calculations for more realistic irregular crystal shapes such as hollow columns, bullet rosettes, dendrites and capped columns [Takano and Liou 1995]. A mixture of bullet rosettes, plates and dendrites was successfully used by Liou *et al.* [2000] to model the polarization features of a cirrus cloud observed by Coffeen [1979] at a wavelength of 2.2 μm which is in an ice water absorption feature.

The scattering properties of artificial particles, such as Koch fractals and stochastically deformed ice spheres, have also been used as an analog for scattering by dendritic ice crystals, disordered polycrystals and graupel [Macke *et al.* 1996a, Muinonen 2000]. The use of such particle shapes was motivated in part by observations that indicated the need for ice crystal phase functions with asymmetry parameters that were smaller than those possible for pure hexagonal monocrystals [Kinne *et al.* 1991]. More recent analyses of the 1986 FIRE IFO case suggest that these results may have been affected by inhomogeneities in the cirrus cloud field [Kinne 2000]. Other measurements made during EUCREX '94 also indicate that the apparent need for very low asymmetry

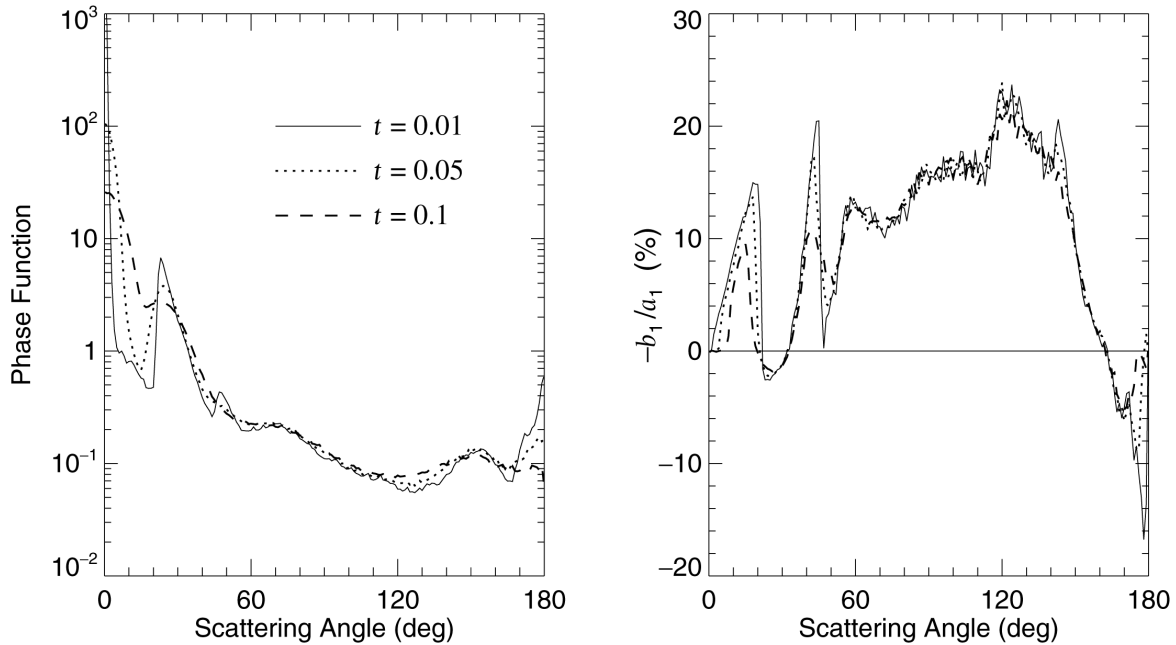


Figure 3.4.1-1. Ray-tracing phase function and the degree of linear polarization, $-b_1(\Theta)/a_1(\Theta)$, versus scattering angle for randomly oriented hexagonal ice columns with a length-to-diameter ratio of 6.2 and distortion parameters $t = 0.01, 0.05$, and 0.1 . The relative refractive index is $m = 1.311$.

parameter values to reconcile IR emissivity and solar reflectance measurements is associated with thin inhomogeneous cirrus clouds [Chepfer *et al.* 1999b].

A separate effect that can impact the scattering properties of cirrus clouds is the orientation of crystals as they fall. This can have a significant effect on PDL returns [Platt 1978, Sassen *et al.* 2001] and has also been observed in POLDER aircraft data [Chepfer 1999a] in the form of enhanced intensity in the specular reflection direction. By pointing lidars away from zenith it has been shown that when this occurs these particles tend to be strongly oriented, to within less than $2\text{-}3^\circ$ of horizontal. Thus, a few crystals can have a large effect in the specular scattering direction, even though they may not dominate the scattering properties of the cloud in other directions [Sassen 2000].

3.4.2. Multiple scattering modeling

The essence of the doubling or adding method is simple: if the reflection and transmission properties are known for each of two atmospheric layers, then one can obtain the reflection and transmission properties of the combined layer by computing the reflections back and forth between the two layers. Consider for this purpose the two plan-parallel layers placed on top of one another in figure 3.4.2-1.

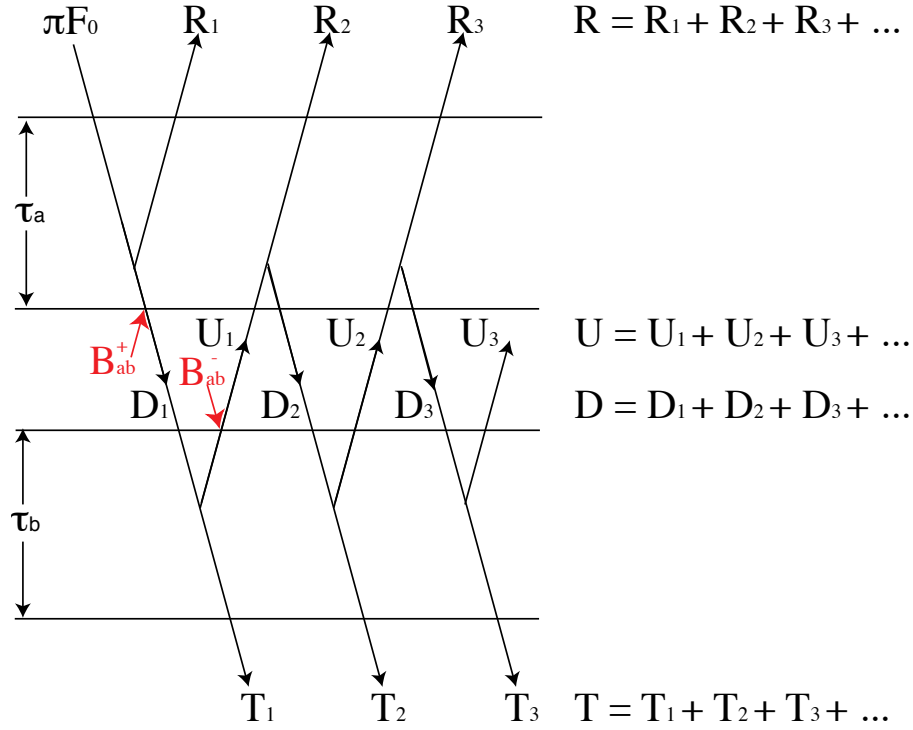


Figure 3.4.2-1. This figure show a schematic diagram of the interaction of photons with two atmospheric layers and how the multiple interaction terms in doubling/adding calculations are formed.

In what follows, we denote the scattering properties of the top and bottom layer by subscripts 'a' and 'b', respectively, and use superscripts ' \downarrow ' and ' \uparrow ' to indicate illumination from above and below, respectively. The reflection and transmission properties of the top layer are then described by the reflection and transmission matrices defined as follows. Let the top layer be illuminated from above in the direction of $s_0 = (\theta_0, \phi_0)$ by unpolarized, unidirectional light with Stokes vector I_0 , and let πF_0 be the flux of this light through a unit area perpendicular to s_0 . Denoting the Stokes vector of light reflected by this layer in the direction of $s_r = (\theta_r, \phi_r)$ by I_r , we write for the (4 x 4) reflection matrix of this layer:

$$I_r = \frac{\mu_0 \mathbf{R}_a^{\downarrow}(\mu_r, \mu_0, \varphi_r - \varphi_0) \mathbf{F}_0}{\pi} \quad 3.4.2-1$$

where μ_0 and F_0 are defined as in section 3.1, and where $\mu_r = |\cos \theta_r|$. Similarly, if I_t denotes the Stokes vector of light *diffusely* (i.e., by means of scattering) transmitted by this layer in the direction of $s_t = (\theta_t, \phi_t)$, we define its (4 x 4) transmission matrix as:

$$I_t = \frac{\mu_0 \mathbf{T}_a^{\downarrow}(\mu_t, \mu_0, \varphi_t - \varphi_0) \mathbf{F}_0}{\pi} \quad 3.4.2-2$$

where $\mu_t = |\cos \theta_t|$. The reflection and transmission matrices for this layer for illumination from below are defined in the same manner, except for substituting superscript ' \downarrow ' and ' \uparrow ', if I_0 is the Stokes vector of light incident from below. The reflection and transmission

matrices for the bottom layer can be defined in the same fashion, but substituting subscript 'a' with 'b'.

Consider now the combined layer illuminated from above. Let us introduce for any (4 x 4) matrices K , L , and M the notation

$$K = L \otimes M \equiv \frac{1}{\pi} \int_0^1 \mu'' d\mu'' \int_0^{2\pi} d\varphi'' \{ L(\mu, \mu'', \varphi - \varphi'') M(\mu'', \mu', \varphi'' - \varphi') \} = K(\mu, \mu', \varphi - \varphi'). \quad 3.4.2-3$$

Using τ_a to denote the optical thickness for the top layer and τ_b for the bottom layer, one can write for the reflection and transmission of the combined layer for illumination from above:

$$\mathbf{R}_{a+b}^\downarrow = \mathbf{R}_a^\downarrow + \exp(-\tau_a / \mu) \mathbf{U}^\downarrow + \mathbf{T}_a^\downarrow \otimes \mathbf{U}^\downarrow \quad 3.4.2-4$$

and

$$\mathbf{T}_{a+b}^\downarrow = \exp(-\tau_b / \mu_t) \mathbf{D}^\downarrow + \mathbf{T}_b^\downarrow \otimes \mathbf{D}^\downarrow + \mathbf{T}_b^\downarrow \exp(-\tau_a / \mu_0) \quad 3.4.2-5$$

respectively, where the exponential terms refer to direct transmission through layer a or b without scattering, and where \mathbf{U}^\downarrow and \mathbf{D}^\downarrow are the (4 x 4) matrices describing the upward and downward radiation field in between the layers when illuminating the combined layer from above. From figure 3.4-1, one can verify that

$$\begin{aligned} \mathbf{D}^\downarrow &= \mathbf{T}_a^\downarrow + \mathbf{Q}^\downarrow \exp(-\tau_a / \mu_0) + \mathbf{Q}^\downarrow \otimes \mathbf{T}_a^\downarrow \\ \mathbf{U}^\downarrow &= \mathbf{R}_b^\downarrow \exp(-\tau_a / \mu_0) + \mathbf{R}_b^\downarrow \otimes \mathbf{D}^\downarrow \end{aligned} \quad 3.4.2-6$$

where

$$\begin{aligned} \mathbf{Q}_1^\downarrow &= \mathbf{R}_a^\uparrow \otimes \mathbf{R}_b^\downarrow \\ \mathbf{Q}_n^\downarrow &= \mathbf{Q}_1^\downarrow \otimes \mathbf{Q}_{n-1}^\downarrow \\ \mathbf{Q}^\downarrow &= \sum_{n=1}^{\infty} \mathbf{Q}_n^\downarrow \end{aligned} \quad 3.4.2-7$$

accounts for the light reflected back and forth by the bottom and top layer for illumination from above, respectively.

If the combined layer is illuminated from below then one can obtain its transmission matrix from the one for illumination from above using symmetry relationships (Hovenier, 1969). The same holds for the reflection matrix for illumination from below only if the combined layer is homogeneous. However, since only the reflection matrix for illumination from below for layer 'a' is required in the construction of the combined reflection matrix, if an inhomogeneous atmosphere is constructed from the surface up it

is always possible to have layer 'a' be homogeneous by construction. It is not therefore generally necessary to calculate the combine layer reflection and transmission properties for illumination from below. If these matrices are required then one needs to evaluate

$$\mathbf{R}_{a+b}^{\uparrow} = \mathbf{R}_b^{\uparrow} + \exp(-\tau_b / \mu) \mathbf{U}^{\uparrow} + \mathbf{T}_b^{\downarrow} \otimes \mathbf{U}^{\uparrow} \quad 3.4.2-8$$

and

$$\mathbf{T}_{a+b}^{\uparrow} = \exp(-\tau_a / \mu) \mathbf{D}^{\uparrow} + \mathbf{T}_a^{\uparrow} \exp(-\tau_b / \mu) + \mathbf{T}_a^{\uparrow} \otimes \mathbf{D}^{\uparrow} \quad 3.4.2-9$$

for reflection and transmission by the combined layer. Here, \mathbf{U}^{\uparrow} and \mathbf{D}^{\uparrow} are the (4 x 4) matrices describing the *downward* and *upward* radiation field in between the layers when the combined layer is illuminated from below. Their respective equations are given by

$$\begin{aligned} \mathbf{D}^{\uparrow} &= \mathbf{T}_b^{\uparrow} + \mathbf{Q}^{\uparrow} \exp(-\tau_b / \mu_0) + \mathbf{Q}^{\uparrow} \otimes \mathbf{T}_b^{\uparrow} \\ \mathbf{U}^{\uparrow} &= \mathbf{R}_a^{\uparrow} \exp(-\tau_b / \mu_0) + \mathbf{R}_a^{\uparrow} \otimes \mathbf{D}^{\uparrow} \end{aligned} \quad 3.4.2-10$$

where

$$\begin{aligned} \mathbf{Q}_1^{\uparrow} &= \mathbf{R}_b^{\downarrow} \otimes \mathbf{R}_a^{\uparrow} \\ \mathbf{Q}_n^{\uparrow} &= \mathbf{Q}_1^{\uparrow} \otimes \mathbf{Q}_{n-1}^{\uparrow} \\ \mathbf{Q}^{\uparrow} &= \sum_{n=1}^{\infty} \mathbf{Q}_n^{\uparrow} \end{aligned} \quad 3.4.2-11$$

accounts for the light reflected back and forth by the top and bottom layer for illumination from below, respectively.

If the top and bottom layer are identical, then one refers to this method as the *doubling method*; if they are different then the method is referred to as the *adding method*. Any vertically inhomogeneous atmosphere can be subdivided into a collection of homogeneous sub-layers. The procedure followed is to first compute reflection and transmission by such sub-layers using the doubling method, and to then obtain the reflection and transmission properties of the entire atmosphere by stacking up the sub-layers with the adding method. The reflection and transmission properties of the initial layers in the doubling method are obtained by choosing the initial optical depth to be small enough that one may assume light to be scattered only once as it passes through each layer. The reflection and transmission matrices for such layer are given by

$$\mathbf{R}_1^{\downarrow}(\mu_r, \mu_0, \varphi_r - \varphi_0) = \frac{\varpi \Delta \tau}{4\mu_r \mu_0} \mathbf{Z}(-\mu_r, \mu_0, \varphi_r - \varphi_0) \quad 3.4.2-12$$

and

$$T_1^\downarrow(\mu_t, \mu_0, \varphi_t - \varphi_0) = \frac{\varpi \Delta \tau}{4\mu_t \mu_0} \mathbf{Z}(\mu_t, \mu_0, \varphi_t - \varphi_0) \quad 3.4.2-13$$

respectively, where as before \mathbf{Z} is the phase matrix for a volume element containing scattering particles. The properties of a combined layer with layers a and b being identical and using this single scattering approximation are calculated. This combined layer is then used to provide the reflectance and transmittance properties for a new pair of identical layers a and b and so forth with the optical depth of the resultant combined layer being double that at the previous step, hence the term ‘doubling’. Alternative initial values for the reflectance and transmittance in doubling calculations have been suggested (Wiscombe 1976) and a second order scattering approximation is used to increase the allowable initial optical depth value and to limit the number of Fourier terms that are required in the azimuthal decomposition that is used in the evaluation of integrals of the form 3.4-3 (Cairns *et al.* 1997).

The calculation of the functional derivatives required in the search for a statistically optimal retrieval (described in the next section) is the same as determining the effects of a pseudo-source imbedded in the model atmosphere (Box *et al.* 1988, 1989, Gerstl and Stacey 1973). Although this is generally done using the adjoint method the doubling/adding method provides the calculated internal fields (downwelling and upwelling) as part of the reflectance calculation. The perturbation calculation only requires the additional calculation of ‘escape’ (Twomey 1979) by photon emitted by the pseudo-source. We therefore now examine what the implications for remote sensing of a source \mathbf{B}_{ab} inserted between the layers a and b . Denoting the contribution of such sources to the radiation emerging from the top-of-the-atmosphere by $[\dots]_{\text{TOA}}$, we derive from figure 3.4-1:

$$\begin{aligned} [\mathbf{B}_{ab}^\uparrow]_{\text{TOA}} &= \exp(-\tau_a / \mu) \mathbf{B}_{ab}^\uparrow + \left(\mathbf{T}_a^\uparrow + \exp(-\tau_a / \mu) \mathbf{Q}^\uparrow + \mathbf{T}_a^\uparrow \otimes \mathbf{Q}^\uparrow \right) \otimes \mathbf{B}_{ab}^\uparrow \\ [\mathbf{B}_{ab}^\downarrow]_{\text{TOA}} &= \exp(-\tau_a / \mu) \mathbf{R}_b^\downarrow \otimes \mathbf{B}_{ab}^\downarrow + \left(\mathbf{T}_a^\uparrow + \exp(-\tau_a / \mu) \mathbf{Q}^\uparrow + \mathbf{T}_a^\uparrow \otimes \mathbf{S}^\uparrow \right) \otimes \mathbf{R}_b^\downarrow \otimes \mathbf{B}_{ab}^\downarrow \end{aligned} \quad 3.4.2-14$$

If we now consider the reciprocal (4 x 4) matrices of \mathbf{U}^\downarrow and \mathbf{D}^\downarrow and denote them by the subscript ‘rec’, i.e.,

$$\begin{aligned} \mathbf{D}_{\text{rec}}^\downarrow &= \mathbf{T}_a^\uparrow + \exp(-\tau_a / \mu) \mathbf{Q}^\uparrow + \mathbf{T}_a^\uparrow \otimes \mathbf{Q}^\uparrow \\ \mathbf{U}_{\text{rec}}^\downarrow &= \exp(-\tau_a / \mu) \mathbf{R}_b^\downarrow + \mathbf{D}_{\text{rec}}^\downarrow \otimes \mathbf{R}_b^\downarrow \end{aligned} \quad 3.4.2-15$$

then the upwelling at the top of the atmosphere can be written in terms of the source magnitudes and these terms as

$$\begin{aligned} [\mathbf{B}_{ab}^\uparrow]_{\text{TOA}} &= \exp(-\tau_a / \mu) \mathbf{B}_{ab}^\uparrow + \mathbf{D}_{\text{rec}}^\downarrow \otimes \mathbf{B}_{ab}^\uparrow \\ [\mathbf{B}_{ab}^\downarrow]_{\text{TOA}} &= \mathbf{U}_{\text{rec}}^\downarrow \otimes \mathbf{B}_{ab}^\downarrow \end{aligned} \quad 3.4.2-16$$

Thus, the reciprocal of the downwelling and upwelling diffuse fields can be used to calculate the effect of internal sources on the observed radiation fields. The only

additional term is the direct transmission of the upwelling source term to the top of the atmosphere. Symmetry allows most of the terms required in the calculation of these reciprocal fields to be evaluated with little additional effort as the adding process is performed and these fields can be calculated at every interface as the atmosphere is constructed in a manner analogous to that proposed by De Haan et al. (1987) for the usual downwelling and upwelling radiation fields. This approach has been used in scalar radiative transfer calculations to determine the contribution of the different vertical layers in a cloud to the observed radiance at cloud top (Platnick 2000).

3.4.3. Ocean modeling

To obtain the spectral and angular patterns of the underwater light contribution to the visible total and polarized TOA reflectance requires (i) the photo-polarimetric single-scattering properties of a volume element of the ocean body as a function of scattering angle Θ , wavelength λ and chlorophyll-C concentration [Chl], and (ii) vector radiative transfer computations for the entire ocean system (i.e., ocean body and surface). For the latter computations, we use the doubling/adding method described above where for the ocean surface we use the wind-speed dependent surface slope distribution obtained by Cox and Munk (1954). The scattering properties of a volume element of the ocean body are defined by the bulk scattering matrix \mathbf{P}_{blk} and bulk single-scattering albedo ϖ_{blk} . Noting that these properties originate from scattering by pure ocean water and particulate matter, one can write

$$\mathbf{P}_{\text{blk}}(\Theta, \lambda, \text{Chl}) = \frac{b_w(\lambda)\mathbf{P}_w(\Theta) + b_p(\lambda)\mathbf{P}_p(\Theta, \lambda, \text{Chl})}{b_w(\lambda) + b_p(\lambda, \text{Chl})} \quad 3.4.3-1$$

and

$$\varpi_{\text{blk}}(\lambda, \text{Chl}) = \frac{b_w(\lambda) + b_p(\lambda, \text{Chl})}{b_w(\lambda) + b_p(\lambda, \text{Chl}) + a_{\text{blk}}(\lambda, \text{Chl})} \quad 3.4.3-2$$

where \mathbf{P}_w and b_w are the scattering matrix and scattering coefficient of pure ocean water, respectively, and the same for \mathbf{P}_p and b_p except for particulate matter in the ocean. Furthermore,

$$a_{\text{blk}}(\lambda, \text{Chl}) = a_w(\lambda) + a_p(\lambda, \text{Chl}) \quad 3.4.3-3$$

where a_{blk} , a_w , and a_p are the absorption coefficients of the bulk ocean, pure ocean water, and particulate matter, respectively. To derive the dependence of these properties on Θ , λ , and [Chl], we review first statistical relationships for the albedo of the ocean body as a function of λ and [Chl]. Not only do these equations provide a_p and b_p , they also constrain the shape of the (1,1) element of \mathbf{P}_p – i.e., the scattering function P_p – as a function of λ and [Chl]. In what follows, we refer to the collective of these equations as the bio-optical model of the ocean. We then identify two components (referred to as hydrosol components) of the particulate matter based on in-situ measurements of refractive indices and size distributions obtained over the last three decades. Note that the existence of a multi-component particulate model is consistent with the prediction that P_p varies with [Chl]. Thirdly, we vary the parameters of each hydrosol component until the corresponding scattering matrix \mathbf{P}_{hyd} from Mie

computations reproduces the linear polarization signature that is typical for open ocean environments. This procedure ensures that mixtures of the two components always lead to the same, realistic linear polarization of underwater light. Finally, the two components are mixed as a function of [Chl] such that the shape of the resulting P_p agrees with the one predicted by the bio-optical model. Hence, our hydrosol mixture has the following characteristics: (i) the physical properties of its components are consistent with in-situ measurements; (ii) the scattering properties are consistent with empirical predictions; (iii) multiple scattering leads to realistic variations of the ocean albedo for a wide range of wavelengths ($400 \text{ nm} \leq \lambda \leq 600 \text{ nm}$) and Chlorophyll-C concentration $0.03 \text{ mg/m}^3 \leq [\text{Chl}] \leq 3 \text{ mg/m}^3$; and (iv) multiple scattering leads to realistic polarization signatures of underwater light.

3.4.3.1. Bio-optical model

The ansatz for bio-optical models of the ocean is to approximate the upwelling total radiance just below the ocean surface by a Lambertian reflector with albedo R_{blk} . That is, R_{blk} is equal to the ratio of the upwelling irradiance E_u to downwelling irradiance E_d at zero depth in the ocean:

$$R_{\text{blk}}(\lambda, \text{Chl}) = \frac{E_u(\lambda, \text{Chl})}{E_d(\lambda, \text{Chl})} \quad 3.4.3.1-1$$

Note that R_{blk} is independent of instrumental calibration and can therefore be measured relatively easy. Multiple scattering computations by Gordon et al. (1975) and by Morel and Prieur (1977) have shown that R_{blk} can be expressed in terms of the backscattering coefficient s_{blk} (m^{-1}) and absorption coefficient a_{blk} (m^{-1}) of bulk oceanic water according to

$$R_{\text{blk}}(\lambda, \text{Chl}) = \alpha \frac{s_{\text{blk}}(\lambda, \text{Chl})}{a_{\text{blk}}(\lambda, \text{Chl})}, \quad 3.4.3.1-2$$

where α is about 0.3 for oligotrophic waters and clear skies with the sun overhead. Variations of the factor α with decreasing solar zenith angles and increasing biomass concentrations are given by Morel and Gentili (1991). The bulk backscattering coefficient s_{blk} in equation 3.4.3.1-2 can be written as (Morel, 1988)

$$s_{\text{blk}}(\lambda, \text{Chl}) = 0.5 b_w(\lambda) + q_p(\lambda, \text{Chl}) b_p(\lambda = 550, \text{Chl}) \quad 3.4.3.1-3$$

where q_{bio} is the backscattering efficiency of the particulate matter scattering function P_p , i.e.,

$$q_p(\lambda, \text{Chl}) = 2\pi \int_{\pi/2}^{\pi} \frac{P_p(\Theta, \lambda, \text{Chl})}{4\pi} \sin(\Theta) d\Theta \quad 3.4.3.1-4$$

In situ measurements have shown b_p and q_p to be systematically correlated with [Chl] for open ocean waters according to (Morel and Maritonera, 2001)

$$b_p(\lambda, \text{Chl}) = 0.416 [\text{Chl}]^{0.766} (550/\lambda) \quad 3.4.3.1-5$$

and

$$q_p(\lambda, \text{Chl}) = 0.002 + 0.01 \{0.50 - 0.25^{10} \log[\text{Chl}]\} (\lambda/550)^k \quad 3.4.3.1-6$$

respectively, where

$$k = \begin{cases} 0.5(^{10}\log[\text{Chl}] - 0.3), & 0.02 \leq [\text{Chl}] \leq 2 \text{ mg m}^{-3} \\ 0, & \text{otherwise.} \end{cases} \quad 3.4.3.1-7$$

The variation of absorption coefficient a_{blk} with λ and $[\text{Chl}]$ has been studied by Bricaud et al. (1998) for suspended particular matter. They found similar non-linear relationships with $[\text{Chl}]$ as in equation 3.4.3.1-5 for both phytoplankton and non-algal particles, with the value of the exponent depending on λ . However, as pointed out by Morel and Maritonera (2001), such measurements do not account for absorption by colored dissolved organic matter (CDOM, or "yellow substance") which can be substantial in the blue. Instead, we retrieve a_{blk} and R_{blk} simultaneously by solving equation 3.4.3.1-2 together with

$$a_{\text{blk}}(\lambda, \text{Chl}) = K_{\text{d}}(\lambda, \text{Chl}) \{1 - R_{\text{blk}}(\lambda, \text{Chl})\} \frac{\mu_{\text{d}} \mu_{\text{u}}}{\mu_{\text{d}} R_{\text{blk}}(\lambda, \text{Chl}) + \mu_{\text{u}}} \quad 3.4.3.1-8$$

where μ_{d} and μ_{u} are the average cosine directions with respect to the vertical for the downward and upward underwater light flux, respectively, and

$$K_{\text{d}}(\lambda, \text{Chl}) = K_{\text{w}}(\lambda) + K_{\text{p}}(\lambda, \text{Chl}) \quad 3.4.3.1-9$$

is the attenuation coefficient (m^{-1}) for downward irradiance with

$$K_{\text{w}}(\lambda) = a_{\text{w}}(\lambda) + 0.5 b_{\text{w}}(\lambda) \quad 3.4.3.1-10$$

and

$$K_{\text{p}}(\lambda, \text{Chl}) = \chi(\lambda) ([\text{Chl}])^{e(\lambda)} \quad 3.4.3.1-11$$

In equation 3.4.3.1-11, $\chi(\lambda)$ and $e(\lambda)$ are the coefficients tabulated by Morel and Maritonera (2001) to fit observed spectra of the biogenic attenuation coefficient K_{bio} . Equation 3.4.3.1-8 is an exact relationship derived from Gershun's divergence law for irradiance in which the change of R_{blk} with depth is neglected (Morel, 1988, and references therein). It has the advantage of relating a_{blk} to *in situ* measurements of K_{blk} and incorporates thus absorption by all materials present, including yellow substance. Note that substituting R_{blk} by equation 3.4.3.1-2 leads to a second-order polynomial expression for a_{blk} , which can be handled analytically instead of using the iterative method proposed by Morel (1988). We solve this equation as a function of λ and $[\text{Chl}]$ using for μ_{d} and μ_{u} the values provided by Morel and Maritonera (2001). The absorption coefficient a_{w} and b_{w} in equations 3.4.3.1-3 and 3.4.3.1-10 are taken from Pope and Fry (1997).

3.4.3.2. Hydrosol components

The variation of q_{p} with $[\text{Chl}]$ suggests that there are at least two types of hydrosols present in the open ocean whose scattering matrices P_{hyd} contribute to P_{p} and whose mixing ratio varies with $[\text{Chl}]$. Laboratory measurements and analyses of light scattering show further that the real refractive index m_{hyd} (relative to seawater) of marine particulates is often bimodal, falling either between 1.02–1.09 or between 1.15–1.25

(Zaneveld et al., 1974; Spinrad and Brown, 1986). The former mode is typical for living plankton (Stramski and Mobley, 1997) and dead algae mass with high (>60%) water content (Aas, 1996). The latter mode is indicative of minerals from aeolian input (Sokolik and Toon, 1999) and dead algae mass with low (<25%) water content (Aas, 1996). We use the corresponding boundaries to define two particulate components of oceanic matter, phytoplankton ($1.02 \leq m_{\text{hyd}} \leq 1.09$) and high-refractive detritus ($1.15 \leq m_{\text{hyd}} \leq 1.25$), and denote the refractive index values of these components by m_{plk} and m_{det} , respectively. Because the imaginary part m'' of these refractive indices is usually less than 10^{-2} (Stramski et al., 2001) at which its impact on q_p becomes negligible (Ulloa et al., 1994), and because the bio-optical model already provides us with a_{blk} , we take m'' to be zero.

Measurements of the differential size distribution $n_{\text{hyd}}(r)$ of ocean particulates are often found to follow a power-law (or Junge-type) distribution (Stramski and Kiefer, 1991, and references therein), i.e.,

$$n_{\text{hyd}}(r) = C r^{-\gamma_{\text{hyd}}} \quad 3.4.3.2-1$$

where $dn_{\text{hyd}}(r)$ is the number of particles per unit volume with radius between r and $r+dr$, and the constant C is chosen such that

$$\int_0^{\infty} n_{\text{hyd}}(r) dr = 1 \quad 3.4.3.2-2$$

The value of the exponent γ_{hyd} in equation 3.4.3.2-1 varies in the majority of cases between 3.0–5.0 (Fig. 10 in Jonasz, 1983). Accordingly, we take $3.0 \leq \gamma_{\text{hyd}} \leq 5.0$ for each m_{plk} and m_{det} , and denote the corresponding values of γ_{hyd} by γ_{plk} and γ_{det} , respectively. Results obtained by Ulloa et al. (1994) show further that q_p becomes invariant for particles with $r_{\text{min}} \leq 0.025 \mu\text{m}$, and that particles with $r_{\text{max}} \geq 50 \mu\text{m}$ contribute less than 1% to q_p . We therefore set r_{min} and r_{max} to 0.01 and 100 μm , respectively.

3.4.3.3. Polarization constraints

Measurements of P_p performed for various open ocean samples (Kad'shevich and Lyubovtseva, 1973; Voss and Fry, 1984) and phytoplankton cultures (Fry and Voss, 1985; Volten et al., 1998) show that its degree of linear polarization $-P_{21}/P_{11}$ remains relatively stable, exhibiting a bell-shaped curve as a function of the scattering angle similar to that of Rayleigh-Gans scattering. The maximum value of this curve and its position were seen to vary between 0.6–0.8 and 87° – 97° , respectively. The corresponding numbers for pure seawater are 0.84 and 90° , i.e., the $-P_{21}/P_{11}$ values of P_w can be taken as an upper bound for those of P_p . These observations provide valuable constraints for $(m_{\text{plk}}, \gamma_{\text{plk}})$ and $(m_{\text{det}}, \gamma_{\text{det}})$ by requiring that the $-P_{21}/P_{11}$ values of the corresponding scattering matrices P_{plk} and P_{det} must be similar to those of P_w . Using Mie computations to fit $-P_{21}/P_{11}$, we obtain

$$\gamma_{\text{hyd}} = 6.63m_{\text{hyd}} - 3.25 \quad (\pm 0.05) \quad 3.4.3.3-1$$

for the range of $1.03 \leq m_{\text{hyd}} \leq 1.25$. The implication of this relation is that one may take arbitrary values for $m_{\text{plk}} \in [1.03, 1.09]$ and $m_{\text{det}} \in [1.15, 1.25]$, the choices of which then determine γ_{plk} and γ_{det} , respectively. We take:

$$\begin{cases} \text{plankton: } m_{\text{plk}} = 1.04 & \Rightarrow & \tilde{a}_{\text{plk}} = 3.7 \\ \text{detritus: } m_{\text{det}} = 1.15 & \Rightarrow & \tilde{a}_{\text{det}} = 4.4 \end{cases} \quad 3.4.3.3-2$$

The backscattering efficiencies q_{plk} and q_{det} corresponding to these $(m_{\text{plk}}, \gamma_{\text{plk}})$ and $(m_{\text{det}}, \gamma_{\text{det}})$ are 0.0026 and 0.0444, respectively.

3.4.3.4. Mixing ratios

The total particulate scattering matrix \mathbf{P}_p for a mixture of plankton and detritus particles is given by

$$\mathbf{P}_p(\Theta, \lambda, \text{Chl}) = \frac{[1 - f_{\text{det}}(\text{Chl})] C_{\text{plk}}(\lambda) \mathbf{P}_{\text{plk}}(\Theta, \lambda) + f_{\text{det}}(\text{Chl}) C_{\text{det}}(\lambda) \mathbf{P}_{\text{det}}(\Theta, \lambda)}{[1 - f_{\text{det}}(\text{Chl})] C_{\text{plk}}(\lambda) + f_{\text{det}}(\text{Chl}) C_{\text{det}}(\lambda)} \quad 3.4.3.4-1$$

where f_{det} is the fraction of the total number of particles that is detritus, and C_{plk} and C_{det} are the scattering cross sections (μm^2) obtained from Mie computations for $(m_{\text{plk}}, \gamma_{\text{plk}})$ and $(m_{\text{det}}, \gamma_{\text{det}})$, respectively. Note that

$$q_p(\lambda, \text{Chl}) = \frac{[1 - f_{\text{det}}(\text{Chl})] C_{\text{plk}}(\lambda) q_{\text{plk}}(\lambda) + f_{\text{det}}(\text{Chl}) C_{\text{det}}(\lambda) q_{\text{det}}(\lambda)}{[1 - f_{\text{det}}(\text{Chl})] C_{\text{plk}}(\lambda) + f_{\text{det}}(\text{Chl}) C_{\text{det}}(\lambda)} \quad 3.4.3.4-2$$

Hence, f_{det} can be determined from q_p given by the bio-optical model as function of $[\text{Chl}]$ and λ . A fit for our choice of $(m_{\text{plk}}, \gamma_{\text{plk}})$ and $(m_{\text{det}}, \gamma_{\text{det}})$ gives

$$f_{\text{det}}(\text{Chl}) = 1.49 - 0.91[\text{Chl}]^{-0.08} \quad 3.4.3.4-3$$

which states that the *relative* contribution of scattering by detritus particles decreases as $[\text{Chl}]$ increases.

3.4.4. Land surface models

The principal difficulties in retrieving aerosol loadings and microphysical properties using passive remote sensing measurements over land surfaces are the significant spectral and spatial variations in the observed intensities that are caused by the land surface. Indeed the unique and highly variable spectral signatures of land surfaces and their rapid spatial variations are of considerable value in geological prospecting and crop identification and evaluation [Asner 1998]. The polarized light reflected by surfaces may also be of use in remote sensing of the surface, being indicative of its roughness, or in the case of vegetation its leaf inclination distribution [Rondeaux and Herman 1991]. It is believed that this polarization is generated at the surface interface and this hypothesis has been used to develop theoretical models [Bréon et. al. 1995] for the polarized reflectance of vegetation and of bare soils. The fact that most surface polarization is generated at the surface interface and that the refractive index of natural targets varies little within the spectral domain of interest suggests that surface polarized reflectance will be spectrally neutral.

If this is the case, then the use of a measurement at a sufficiently long wavelength where the aerosol load is negligible can be used to characterize and correct for surface polarization effects at the shorter wavelengths. Such an approach has been suggested for use with intensity measurements [Kaufman et. al. 1997] based on the observation that surface reflectances at 440 and 670 nm are correlated with reflectances at 2250nm for many surface types. The shorter wavelengths can then be used to estimate the aerosol load and microphysical properties, for example size and refractive index. A theoretical examination of the retrieval of aerosol properties over land based on the assumption that the surface polarized reflectance is spectrally neutral has been performed elsewhere [Cairns et. al. 1997] and demonstrated the potential accuracy of this retrieval approach over land surfaces. Figure 3.2.2-1 demonstrates the validity of the assumption that the surface polarized reflectance is spectrally neutral and indicates some of the problems that may occur with the use of intensity only measurements.

In some cases it may be desirable to have a parametric model of the surface polarized reflectance that is estimated from the measurements at 2250 nm. This approach, using a parametric model, allows the aerosol retrieval over land to be iterated so that the 2250 nm measurements can be corrected for aerosol effects. A simple parametric model (I) of polarized surface reflectance that has been developed for the analysis of POLDER measurements [Nadal and Bréon 1999] is given by the expression

$$R_p(\theta_v, \theta_s, \varphi) = r \left[1 - \exp \left(-\beta \frac{F_p(\theta_v, \theta_s, \varphi)}{\mu_v + \mu_s} \right) \right] \quad 3.4.4-1$$

where F_p is the polarized Fresnel reflection coefficient for the given viewing geometry, θ_v is the viewing zenith [$\mu_v = \cos(\theta_v)$] and θ_s is the solar zenith angle. r and β are the empirical coefficients that are tuned to provide a good match to observations and that in the case of POLDER aerosol retrievals are then predicted based on surface type and NDVI. An alternative empirical model (II) for a vegetated surface is given by the formula

$$R_p(\theta_v, \theta_s, \varphi) = r \left[\frac{S(\beta, \theta_v) S(\beta, \theta_s) F_p(\theta_v, \theta_s, \varphi)}{\mu_v + \mu_s} \right] \quad 3.4.4-2$$

where the S functions allow for shadowing with β being an empirical coefficient that is indicative of surface roughness and r is an empirically tunable coefficient, which allows for the fraction of oriented facets to be adjusted. The empirical model I of Nadal and Breon, which is shown as a dashed line in Figure 3.4.4-1, is based on the empirical coefficients for a "low vegetation, high NDVI" case (a) and on the empirical coefficients for a "desert" case (b). Based on the preceding analysis the 2250nm polarized reflectance measurements are a reasonable approximation to the surface polarized reflectance. The empirical model I provides a reasonable fit for vegetation (a) and a somewhat worse fit for bare soil (b). This may simply be because a desert model is not appropriate for a bare soil field. The empirical model II (solid line) fits the data extremely well in both cases. This indicates that model II is an acceptable model that may explain some of the observed features of surface polarized reflectance using simple physical

mechanisms, e.g. shadowing [Saunders 1967] and fractional coverage of oriented surface facets.

The larger magnitude of observed surface polarized reflectance near the backscatter direction compared with simple physical models that was observed by Nadal and Bréon [1999], is also found in the data presented here. Higher orders of scattering may be responsible for this feature [Wolff 1980]. It should be noted that in the backscatter direction the polarization caused by Fresnel reflection is zero and so higher order scattering processes, that may have a spectral signature cause by the multiple interaction, are the source of surface polarized reflectance in this direction. Since this spectral signature is not known, backscattering directions are excluded from use in the

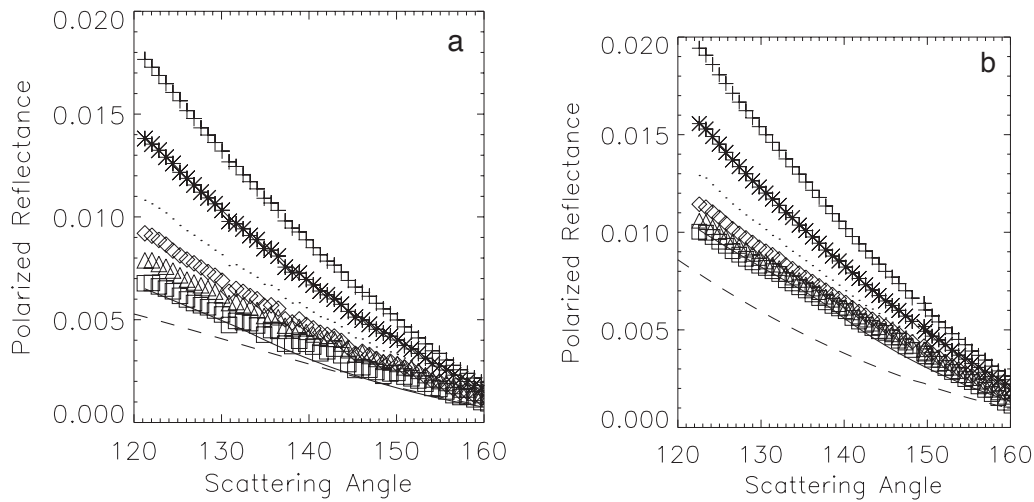


Figure 3. Polarized reflectance measurements at 410 (cross), 470 (star), 555 (dot), 670 (diamond), 865 (triangle) and 2250 (square) nm of a) a vegetated field and b) a bare soil field. retrieval of aerosols over land.

3.4.5. Spectral integrations and the correlated k distribution

The reflectance that is observed at the top of the atmosphere $R_E(obs)$ by an instrument with finite spectral bands is given by the expression

$$R_E(obs) = \frac{\int_{\Delta\lambda} r(\lambda) F_0(\lambda) R_E(\lambda) d\lambda}{\int_{\Delta\lambda} r(\lambda) F_0(\lambda) d\lambda} \quad 3.4.5-1$$

where $r(\lambda)$ is the (properly normalized) spectral response in this channel, F_0 is the solar flux at the top of the atmosphere, $R_E(\lambda)$ is the reflectance of the atmosphere-surface system and $\Delta\lambda$ is the spectral bandwidth. For the relatively narrow spectral bands used in the VNIR spectral domain it is possible to calculate the observed reflectance with

acceptable accuracy using a single calculation at a representative wavelength that is determined from the equation

$$\bar{\lambda} = \frac{\int_{\Delta\lambda} r(\lambda)F_0(\lambda)\lambda d\lambda}{\int_{\Delta\lambda} r(\lambda)F_0(\lambda)d\lambda} \quad 3.4.5-2$$

In the bands at 910 and 1378 nm that contain water vapor absorption and the SWIR bands at 1610 and 2250 nm that contain predominantly carbon dioxide and methane absorption respectively this type of approximation is not acceptable. Instead the band is broken down into smaller pieces of width $\delta\lambda$ that are typically of order 1 nm wide such that the spectral response of the instrument and continuum properties (refractive indices and solar spectrum) don't vary significantly. The observed reflectance can then be calculated using the approximation

$$\mathbf{R}_E(obs) = \frac{\sum r(j)F_0(j)\mathbf{R}_E(j)}{\sum r(j)F_0(j)} \quad 3.4.5-3$$

where the reflectance for the j th element of the passband is determined from the expression

$$\mathbf{R}_E(j) = \frac{1}{\delta\lambda} \int_{\delta\lambda} \mathbf{R}_E(\lambda) d\lambda \quad 3.4.5-4$$

The only atmospheric property that varies rapidly on a one nm spectral scale is absorption by gases. The most accurate calculations of atmospheric reflectance use calculations at a sufficiently high spectral resolution that the absorption lines of the gases are resolved. These are called line-by-line calculations. The k distribution is based on a reorganization of the spectral integral such that it becomes an integral over the fraction of lines with a given strength. The k distribution and its properties have been discussed at length elsewhere (Goody and Yung 1989, Lacis and Oinas 1991).

Evidently it is more accurate, given a limited number of discretization intervals, to discretize the distribution shown in Figure 3.4.5-1b), provided there is no sub-band variation of other atmospheric properties such as scattering. For polydisperse scatterers the spectral variation of scattering properties is smooth on a one nm scale and can be considered to be essentially constant within such a bandwidth. Thus, the spectral integration shown in equation 3.4.5-4 can be transformed into an integration over absorption strength.

As noted by Lacis and Oinas (1991) the k distribution can be tuned to provide exact transmission values for a particular absorber amount. The absorber amount for which the k distributions are exact in the APS calculations has an airmass of 2.5 (e.g. nadir viewing and solar zenith angle of 48°) a column absorber amount of 2 precipitable cm of water vapor and typical column amounts for the well mixed gases and carbon monoxide. The number of absorption intervals that is currently used is 15 that maintains an accuracy of better than 1% in the parts of the band that are absorbing and consequently allows band averaged accuracies of 0.2%, or better in radiance

calculations. It is straightforward to increase the accuracy of these calculations, if required, by recalculating the k -distributions from line-by-line calculations. The monotonic ordering of absorption coefficient strengths in the k distributions in each vertical layer implicitly preserves the monochromatic structure of the atmosphere at different pressure levels, thus simulating the monochromatic structure of the atmosphere at a fraction of the line-by-line computing cost. The reflectance of the atmosphere-surface system in the presence of line absorption can therefore be calculated using the equation

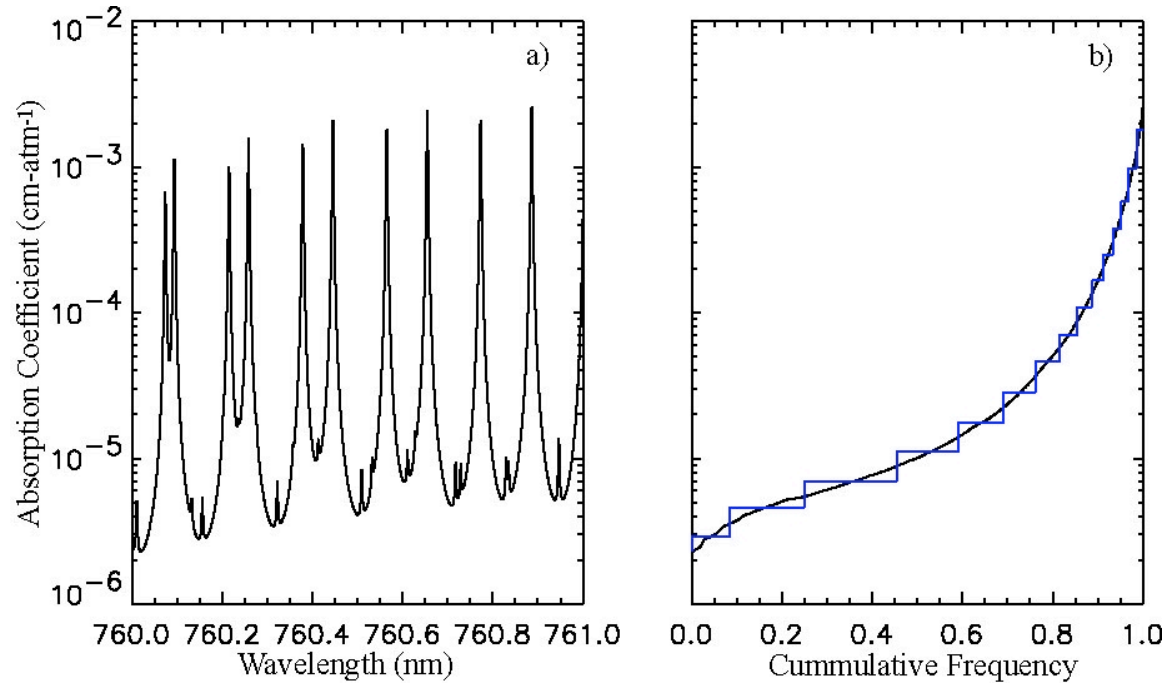


Figure 3.4.5-1. a) Variation of the O₂ absorption coefficient as a function of wavelength between 760 and 761 nm in the A-band and b) plotted as a cumulative histogram with a set of k values based on 15 discretization intervals.

$$\mathbf{R}_E(j) = \sum_i \left(\sum_z \mathbf{R}_E^z(k_i u, \lambda_j) \right) \Delta g_i \quad 3.4.5-5$$

where the summation over vertical layers (z) is a formalism indicating an adding calculation for each absorber interval i and λ_j indicates that all other properties of the atmosphere (single-scattering properties) are evaluated at the mean wavelength of the j th element of the passband.

3.5. Mathematical Implementation of Algorithm

The retrieval strategy that is used in the APS algorithms to retrieve aerosol and cloud EDRs is to search for the aerosol, or cloud model that best fits the complete set of observations for a given pixel. The best fit is statistically optimal in that it allows for the relative uncertainties in different measurements to appropriately weight the fit. In the

approach presented here a maximum posterior probability (MAP) estimate is used. This estimator is based on integrating the likelihood function over any known prior probability distributions to properly account not just for noise, but for radiometric, polarimetric, relative spectral and relative angular calibration accuracies.

The search for the statistically optimal solution can be implemented through the use of multidimensional look-up tables, iterative methods, neural networks or a combination of approaches. The mathematical description of the function that the algorithm must perform is described here. The actual implementation of the algorithm using look up tables that has been selected for processing APS data to EDRs is presented in Section 6.

The following mathematical description of the algorithm implementation is designed to be consistent with the formalism developed for the inversion of sounding data and general inversion approaches presented elsewhere. The description given here includes features, or interpretations, that are present in one, but not the other that are relevant to the particular problem of inverting the observed reflected polarized radiances to obtain aerosol and cloud EDRs from APS measurements.

The act of measurement is defined by the equation

$$\mathbf{y} = f(\mathbf{x}, \mathbf{b}) + \varepsilon \quad 3.5-1$$

Where f is identified as the “forward function” and represents the physics of the measurement including the characterization of the instrument and the radiative transfer process. The true atmospheric state is described by the vector \mathbf{x} and \mathbf{b} is a vector of “forward function parameters” which are quantities that affect the radiative transfer but which are not being retrieved. The error term is given by the vector ε with covariance matrix \mathbf{C} , that represents measurement noise. The “forward function parameters” can include both instrument calibration constants and “nuisance parameters” such as ocean color for aerosol retrieval algorithms. In Section 7 where an error analysis is performed we separate these terms into those associated with instrument uncertainties, i.e., calibration and characterization and those uncertainties associated with the atmospheric state that are not EDR requirements which, whether retrieved or not, are regarded as “nuisance parameters”. The forward model \mathbf{f} is used to calculate synthesized radiances \mathbf{y}' and can be represented by,

$$\mathbf{y}' = f(\mathbf{x}', \mathbf{b}') \quad 3.5-2$$

where \mathbf{x}' and \mathbf{b}' are estimation vectors for the state and model parameters, respectively. The effects of the approximation of the forward function f by the forward model and the uncertainties in calibration and “nuisance parameters” must be included in an analysis that provides a realistic estimate of inversion uncertainties. For example, a failure to allow for model errors caused significant problems in the initial aerosol retrieval process implemented for MISR data [Martonchik *et. al.* 2002]. We must therefore approximate the true forward transfer function f by the forward model \mathbf{f} and include a “forward model error” term, $\Delta \mathbf{f}$ to represent the resulting uncertainty. Similarly, the uncertainties in model parameters \mathbf{b} must be included in the analysis. A realistic model of the measurements is therefore given by the expression

$$\mathbf{y} = \mathbf{f}(\mathbf{x}, \mathbf{b}') + \frac{\partial \mathbf{f}(\mathbf{x}, \mathbf{b}')}{\partial \mathbf{b}} \Delta \mathbf{b} + \Delta \mathbf{f}(\mathbf{x}, \mathbf{b}) + \varepsilon. \quad 3.5-3$$

\mathbf{b} contains both calibration uncertainty and uncertainties in the atmospheric state including wind speed and ocean color over the ocean and refractive index variation of surface materials over land. $\Delta \mathbf{f}$ contains uncertainties in the forward modeling imposed by operational processing constraints. The latter errors can usually be mitigated by analysis, or improved numerical implementation whereas the former are imposed by the atmospheric state and the instrument calibration method. The error budget allocated to these different terms is discussed in further in Section 7. The basis for retrieving the EDRs from the measurements is the Likelihood function that can be written as

$$P(\mathbf{y} | \mathbf{x}) = \frac{\det(\mathbf{C}_\varepsilon)^{-1/2}}{(2\pi)^{m/2}} \exp \left[-\frac{1}{2} (\mathbf{y} - \mathbf{f})^T \mathbf{C}_\varepsilon^{-1} (\mathbf{y} - \mathbf{f}) \right] \quad 3.5-4$$

where \mathbf{C}_ε is the covariance matrix of measurement noise. The substitution of 3.5-3 into 3.5-4 and integration of the Likelihood function over prior probability distribution functions for forward model errors $\Delta \mathbf{f}$ and model parameters $\Delta \mathbf{b}$ and inclusion of a prior probability distribution for the state parameters \mathbf{x} allows us to derive the posterior probability distribution function

$$P(\mathbf{x} | \mathbf{y}, \mathbf{x}_a) = N \exp \left[-\frac{1}{2} (\mathbf{x} - \mathbf{x}_a)^T \mathbf{C}_a^{-1} (\mathbf{x} - \mathbf{x}_a) + (\mathbf{y} - \mathbf{f})^T \mathbf{C}_T^{-1} (\mathbf{y} - \mathbf{f}) \right] \quad 3.5-5$$

in which expression N is a constant that ensures the probability distribution is properly normalized. The total covariance \mathbf{C}_T is given by the expression

$$\mathbf{C}_T = \mathbf{C}_\varepsilon + \mathbf{C}_{\Delta \mathbf{f}} + \frac{\partial \mathbf{f}(\mathbf{x}, \mathbf{b})}{\partial \mathbf{b}}^T \mathbf{C}_b \frac{\partial \mathbf{f}(\mathbf{x}, \mathbf{b})}{\partial \mathbf{b}} \quad 3.5-6$$

where $\mathbf{C}_{\Delta \mathbf{f}}$ and \mathbf{C}_T are the covariance matrices of the model errors and the calibration/model parameter uncertainties respectively. The solution that maximizes this posterior probability is the maximum posterior probability (MAP) estimate that is similar to the more usual maximum likelihood estimate, although its behavior for small sample sizes is generally better. The maximization of probability is identical to the minimization of the exponential term

$$\Phi(\mathbf{x}) = (\mathbf{x} - \mathbf{x}_a)^T \mathbf{C}_a^{-1} (\mathbf{x} - \mathbf{x}_a) + (\mathbf{y} - \mathbf{f}(\mathbf{x}))^T \mathbf{C}_T^{-1} (\mathbf{y} - \mathbf{f}(\mathbf{x})) \quad 3.5-7$$

The first term in Eq. 3.5-7 is a penalty function which constrains the solution to lie “near” the a priori state where “near” is quantified by the a priori covariances. The second term is the familiar χ^2 -statistic that is a measure of the distance between the observed polarized radiances and the simulated polarized radiances with a weight that allows for noise, calibration and potential model errors. The minimization of Φ can be achieved by solving the expression

$$\nabla_{\mathbf{x}} \Phi(\mathbf{x}) = 0 = \mathbf{C}_a^{-1} (\mathbf{x} - \mathbf{x}_a) + \mathbf{K}^T \mathbf{C}_T^{-1} (\mathbf{y} - \mathbf{f}(\mathbf{x})) \quad 3.5-8$$

where

$$\mathbf{K} = \frac{\partial \mathbf{f}(\mathbf{x})}{\partial \mathbf{x}} \quad 3.5-9$$

is the weighting function matrix (commonly used in the analysis of sounding measurements) which represents the sensitivity of the forward model to the retrieved quantities. Rearranging Eq. 3.5-8 yields a nonlinear equation for the best estimate of \mathbf{x} ,

$$\hat{\mathbf{x}} = \mathbf{x}_a + \mathbf{C}_a \mathbf{K}^T \mathbf{C}_T^{-1} [\mathbf{y} - \mathbf{f}(\hat{\mathbf{x}})] \quad 3.5-10$$

The basic scheme for solving such a nonlinear system is the traditional Newton-Gauss procedure. In practice Newton-Gauss iterations may not converge and need to be modified. The most established modification is known as the Levenberg-Marquardt method which is implemented by the following iteration

$$\mathbf{x}^{(i+1)} = \mathbf{x}^{(i)} - [\mathbf{H}(\mathbf{x}^{(i)}) + \gamma \mathbf{I}]^{-1} \nabla_{\mathbf{x}} \Phi(\mathbf{x}^{(i)}) \quad 3.5-10$$

where \mathbf{I} is the identity matrix with the dimensionality of the state vector and \mathbf{H} is known as the Hessian matrix

$$\mathbf{H}(\mathbf{x}) = \nabla_{\mathbf{x}}^2 \Phi(\mathbf{x}) \approx \mathbf{C}_a^{-1} + \mathbf{K}^T \mathbf{C}_T^{-1} \mathbf{K} \quad 3.5-11$$

The value of γ controls the search strategy, for large values of γ the steepest descent dominates with a small step size viz.,

$$\mathbf{x}^{(i+1)} = \mathbf{x}^{(i)} - \gamma^{-1} \nabla_{\mathbf{x}} \Phi(\mathbf{x}^{(i)}) \quad 3.5-12$$

Conversely for small values of γ the inverse Hessian method dominates

$$\mathbf{x}^{(i+1)} = \mathbf{x}^{(i)} - \mathbf{H}(\mathbf{x}^{(i)})^{-1} \nabla_{\mathbf{x}} \Phi(\mathbf{x}^{(i)}) \quad 3.5-12$$

The prescription for changing the value of γ is dependent on the convergence behavior. If $\Phi(\mathbf{x}^{(i+1)}) > \Phi(\mathbf{x}^{(i)})$ then reject $\mathbf{x}^{(i+1)}$ and increase γ , whereas if $\Phi(\mathbf{x}^{(i+1)}) < \Phi(\mathbf{x}^{(i)})$ then accept $\mathbf{x}^{(i+1)}$ and decrease γ . This procedure starts out as a slow steepest descent method and as the iteration proceeds and the solution is approached more closely, the search turns to the faster inverse Hessian method.

In the equations presented above the prior probability of the state vector is used although it should be emphasized that prior probabilities may also be specified as functions of \mathbf{x} , the spectral smoothness of the refractive index being an example that is relevant to the APS algorithm. An extension of this formalism is to introduce prior probabilities that apply to the step sizes in the iterative search for the maximum of 3.5-5. This approach generalizes the Levenberg-Marquardt method but does not appear to have any significant advantages for the APS algorithm unless some prior information about the iterative steps is identified that has a covariance matrix with off-diagonal elements.

Stopping points for the algorithm are based on the χ^2 fits between observed data and values simulated for the retrieved aerosol model being consistent with the noise and calibration model of the instrument (i.e. χ^2 close to 1) and a limit on the allowed number of iterative steps that will be determined during the preliminary design phase.

A useful quantity in the analysis of the measurements that should be used in an algorithm is the 'information content' of the measurement. This is defined to be the difference in entropy before and after a measurement is made. The entropy of a probability density function $P(\mathbf{x}|\mathbf{y}, \mathbf{x}_a)$ is defined as

$$S(\mathbf{y}, \mathbf{x}_a) = - \int P(\mathbf{x}|\mathbf{y}, \mathbf{x}_a) \log_2 P(\mathbf{x}|\mathbf{y}, \mathbf{x}_a) d\mathbf{x} \quad 3.5-13$$

The information content of a measurement is defined as

$$I(\mathbf{y}) = S(\mathbf{x}_a) - S(\mathbf{y}, \mathbf{x}_a) \quad 3.5-14$$

Where $S(\mathbf{x}_a)$ is the entropy of the a priori probability density function of the unknown \mathbf{x} and $S(\mathbf{y}, \mathbf{x}_a)$ is the entropy of the probability density function after the measurement \mathbf{y}

has been made. If $P(\mathbf{x}|\mathbf{y},\mathbf{x}_a)$ and $P(\mathbf{x}|\mathbf{x}_a)$ are Gaussian distributions with covariances $\mathbf{C}_{\mathbf{y},\mathbf{x}_a}$, and $\mathbf{C}_{\mathbf{x}_a}$ then

$$I(\mathbf{y}) = \log_2 \left(\frac{|\mathbf{C}_{\mathbf{x}_a}|^{1/2}}{|\mathbf{C}_{\mathbf{y},\mathbf{x}_a}|^{1/2}} \right) \quad 3.5-15$$

which is the logarithm of the ratio of the ‘volumes of uncertainty’ before and after the measurement since the square root of the determinant of the covariance matrix is a measure of the volume of uncertainty in \mathbf{x} .

3.6. Robustness and Flexibility

The use of this type of algorithm provides flexibility against degradation of particular APS instrument channels and external inputs, by allowing the covariance matrix of uncertainties to be adjusted to allow for the best available information about the state of the instrument and the external data sources. For example, the required accuracy of the ozone column for APS to meet EDR requirements over land is ± 50 DU. This means that it is acceptable to use a climatology or to use recent measurements and assume persistence. Similarly the required accuracy for column nitrogen dioxide is ± 0.5 ppbv and so again use of climatology, or persistence is adequate. Nonetheless, since OMPS and GOME2 will be making measurements during the period when APS is operating it is desirable to be able to make use of either these measurements, or climatology. This is facilitated by the fact that these gaseous absorbers effectively act to increase the absolute radiometric calibration uncertainty of the spectral bands at 410, 490, 555 and 670 nm if their column amounts are not well know. It is therefore straightforward to perform APS retrievals with a covariance matrix of radiometric calibration uncertainties that reflects the source of the external data, OMPS and GOME2, or climatology.

The implementation of this algorithm using APS sensor data is also robust against loss of entire scan lines, or single CCSDS packets. Since each APS scene is synthesized from multiple scans the loss of a scan line simple means that data point is eliminated from used in the search outlined in Section 5. Since there are 194 view angles and 7 spectral bands used in each EDR retrieval the loss of a single scan line (view angle) does not significantly effect the retrieval.

4. SENSOR DESCRIPTION AND REQUIREMENTS

The APS instrument measures linear polarization components simultaneously at four polarization azimuths and in nine spectral bands. In the visible/near infrared (VNIR) spectral region blue enhanced silicon photodiodes provide scene measurements in six spectral bands centered at 412, 488, 555, 672, 865 and 910nm. Similarly, in the short wave infrared (SWIR) cooled HgCdTe detectors support measurements in three spectral bands centered at 1378, 1610 and 2250nm.

The optical system consists of six bore-sighted optical assemblies which define the instantaneous field of view (IFOV) and provide the spectral and polarimetric separation. In each optical assembly a telescope and field stop define the IFOV, a Wollaston prism provides the polarization separation, beamsplitters and bandpass filters produce the

spectral separation, and paired detectors sense the orthogonal polarizations. Three spectral bands are measured in each optical assembly, and identical optical assemblies are paired and mounted rotated by 45° in azimuth to each other. In this manner scene polarization is measured at azimuths of 0° (S1L) and 90° (S1R) and at 45° (S1L) and 135° (S1R) in the nine spectral bands (36 simultaneous measurements). In this configuration the Stokes parameters I, Q and U of the scene are measured simultaneously, Q by one optical assembly, U by the other and I independently by both. The actual evaluation of I, Q and U can be derived from the equations that define the effect of a polarizer on the Stokes vector. In the case of the APS measurements at the azimuths noted above this corresponds to

$$S1L = \frac{I+Q}{2}, \quad S1R = \frac{I-Q}{2}, \quad S2L = \frac{I+U}{2} \quad \text{and} \quad S2R = \frac{I-U}{2} \quad 4.0-1$$

The APS is oriented to scan in an along-track mode, and thus, as the spacecraft travels the same area is seen from multiple view angles. During the course of a scan 198 scene samples are taken plus ten dark reference samples. Also collected during each scan are calibration measurements obtained by sequential viewing of two inflight calibrators that effectively provide near 0% and 100% polarized outputs, respectively. These on-orbit calibration measurements are designed to assure that the predicted high polarimetric accuracy is achieved and maintained on orbit. The APS also incorporates an inflight radiometric calibrator that uses an aluminum mirror to provide solar illumination of a diffuse Spectralon reflector. This calibrator is deployed once a month to provide an evaluation of the radiometric calibration of APS. When the radiometric calibrator is closed it is protected from the space environment to mitigate against degradation of the reflective surfaces.

4.1. Simultaneous Measurements

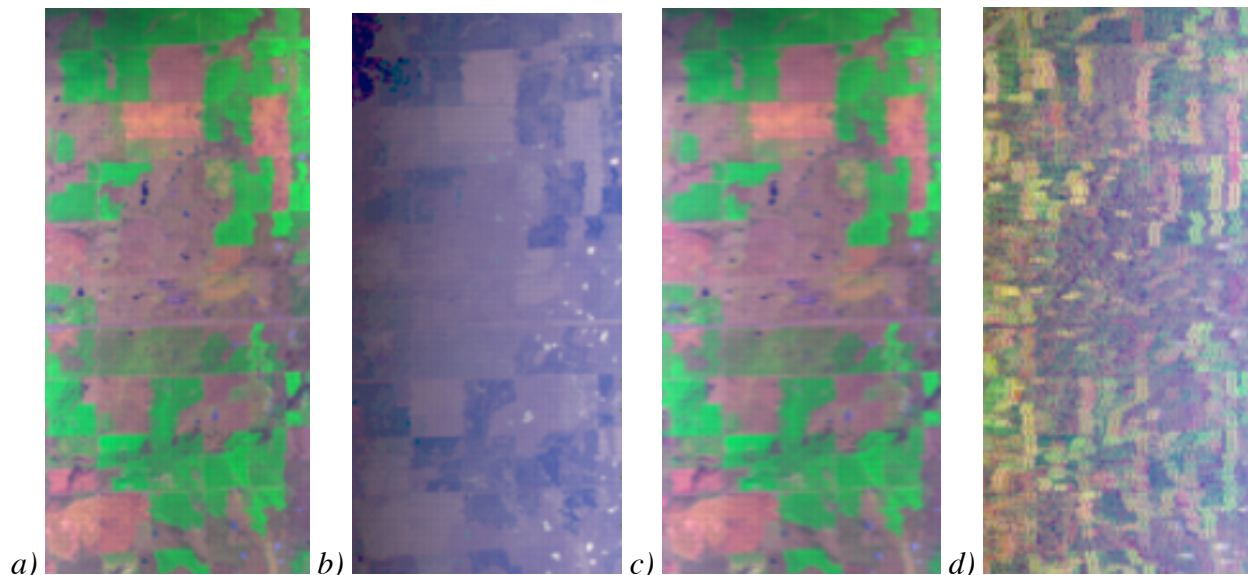


Figure 4.1-1 False color images utilizing RSP data showing “false polarization” effects

The orthogonal polarization component measurements made by APS in each telescope must be both simultaneous and collocated to achieve high accuracy over land. This is because Q and U are each determined by the difference of two measurements viz.,

$$Q = S1L - S1R \quad \text{and} \quad U = S2L - S2R \quad 4.1-1$$

Thus, if there is a change in intensity between the acquisition of the two measurements this will be erroneously inferred to be a polarization feature, or “false polarization”. An example of the results of such an error has been synthesized in Fig. 4.1-1. The RSP aircraft data [a) and b)] clearly has extremely well matched fields of view and temporal simultaneity since the high contrast between fields and bare soil does not show polarization features near their edges. This is a problem typical of polarization measurements that are made using a focal plane array (FPA). This is because a FPA must use either a polarizing beam splitter and two arrays, in which case spatial registration becomes difficult, a polarizing element is rotated in front of the FPA in which case temporal simultaneity is problematic, or approaches where the “effective” IFOV is subdivided with different portions being used to sense different components of the scene polarization (with consequent small, built-in spatial misregistration). The type of error that is observed under these conditions is simulated in Fig. 4.1-1d where the effect of spatial or temporal mismatch in the measurements is seen to create an extremely effective edge detection tool, but a poor polarimeter. This source of error is eliminated in the APS design by having measurements that are simultaneous temporally and having the measurements that are used in the differences shown in Eq. 4.1-1 made in the the same telescope.

4.1.1. Temporal Simultaneity

To ensure that worst case albedo contrasts when combined with non-simultaneous detector integration times in the APS measurement do not degrade the polarization accuracy beyond 0.1%, the timing of the detector integrations should be simultaneous to within 0.1% of the integration time. This requirement is derived from consideration of the error that an edge between a bright and a dark target would cause if properly (worst case/maximum error) aligned with the APS scan.

4.1.2. Spatial Simultaneity (IFOV Matching)

There are two different aspects to spatial registration for APS measurements. One is intra-telescope IFOV matching and uniformity which is crucial to accurate polarization measurements. The other is telescope boresight alignment, which is not crucial to polarimetric accuracy, since this is defined by the measurements within a telescope i.e., that determine Q, or U. However boresight alignment is important in the processing of APS measurements to EDR products this is because the processing must assume that any given scan sector has IFOVs in the different bands that observe the same scene.

4.1.2.1. Intra-telescope IFOV Uniformity

The constraints on intra-telescope field of view matching are driven by the need to ensure that the difference equations 4.1-1 are not contaminated by the measurements, of S1L and S1R for example, being of different scenes. This is straightforward to achieve when the IFOV is defined independently of the polarization separation of the polarization components, provided there is no vignetting at the detectors. The need for field of view response matching between the two measurements therefore becomes the main driver in defining the required performance, since any reasonable differential response matching will necessarily require an absence of vignetting. In the case of

IFOV response matching, polarization errors are caused when the differential responsivity of the two measurements within the IFOV combines with albedo variations that are then interpreted as “false polarization”. This integrated effect is dependent on both the magnitude and the spatial distribution of the responsivity mismatch and the convolution of this spatial distribution of the responsivity mismatch with the scene albedo variations. In the case when the spatial mismatch pattern coincides with a spatial albedo variation the integrated responsivity differences should be less than 1% for the 865 and 910 nm bands (for which albedo variability is typically highest) and should be less than 2% in all other channels in order to limit the contribution to polarimetric uncertainty from this source to less than 0.2% for typical magnitudes of albedo variation as APS threshold requirements. It is an objective requirement for the APS design to keep responsivity differences to less than 0.5% for the 865 and 910 nm bands and to less than 1% in all other channels.

4.1.2.2. *Inter-telescope Boresight Alignment*

The requirements on inter-telescope boresight alignment are driven by the need to be able to interpret the scene consistently across spectral bands. The main EDR driver for this derived requirement is that the surface polarized reflectance measurements at 2250 nm, which are used as a proxy for land surface polarized reflectance, be representative of the surface observed by all other bands. This need implies a required boresight alignment of all bands to within 10% of an IFOV as a threshold requirement and is based on the fact that surface polarized reflectance has relatively low contrast. With this boresight requirement, surface polarized reflectance “noise” in aerosol EDR retrievals over land is maintained at less than 1%. This requirement ensures that the nadir sample for the APS 9 mrad IFOV will have all IFOVs boresighted to better than 800 m. The objective requirement of the APS design is to provide boresight alignments to within 5% of an IFOV. In particular, this objective provides a useful reduction of surface polarized reflectance “noise” to less than 0.5% and this implies alignment of all the telescopes measuring Q to within 5% of an IFOV, alignment of all the telescopes measuring U to within 5% of an IFOV, and overall boresight matching of Q and U telescopes to within 10% of an IFOV.

4.2. *Spectral Band Selection*

It is important that bands used for the retrieval of aerosol and cloud EDRs be free from contamination by gaseous absorption, as far as is practical, to ensure that EDR accuracy requirements can be met. If gaseous absorption is to be allowed within the pass band of a channel, it is desirable that the absorber be a well mixed gas since the amounts and consequently the effects of well mixed gases are more straightforward to model and correct than the effects of water vapor. This is particularly an issue for spectral bands in the short wave infrared (SWIR) spectral domain where the atmospheric windows between strong water vapor absorption bands are contaminated by gaseous absorption, principally by methane and carbon dioxide. The requirement that bands not be contaminated by absorption significantly limits the possible location of spectral bands, and it is for this reason that the spectral bands of the APS sensor are almost identical to the VNIR and SWIR bands of VIIRS and MODIS. The prevalence of water vapor absorption across the solar spectrum and the contamination of the

atmospheric windows in the SWIR portion of the spectrum by weak water vapor continuum absorption means that, although the spectral band choices are made to limit the effects of water vapor, it is highly desirable to measure the amount of water vapor so that corrections can be performed if necessary.

A second consideration in band selection is the cloud size distribution EDRs. The size distribution of liquid water clouds can be retrieved using the rainbow feature in all of the APS spectral bands. For ice clouds there is no such well defined resonance feature, and it is necessary to have spectral bands where there is significant ice water absorption to determine particle size. The reason that absorption provides sensitivity to particle size is that the larger a particle is, the more efficiently it absorbs radiation. The spectral bands that have been selected to provide this capability are at 1610 and 2250 nm and have contrasting ice and liquid water absorption coefficients so that their relative spectral reflectance provides a secondary means for the identification of ice versus water clouds.

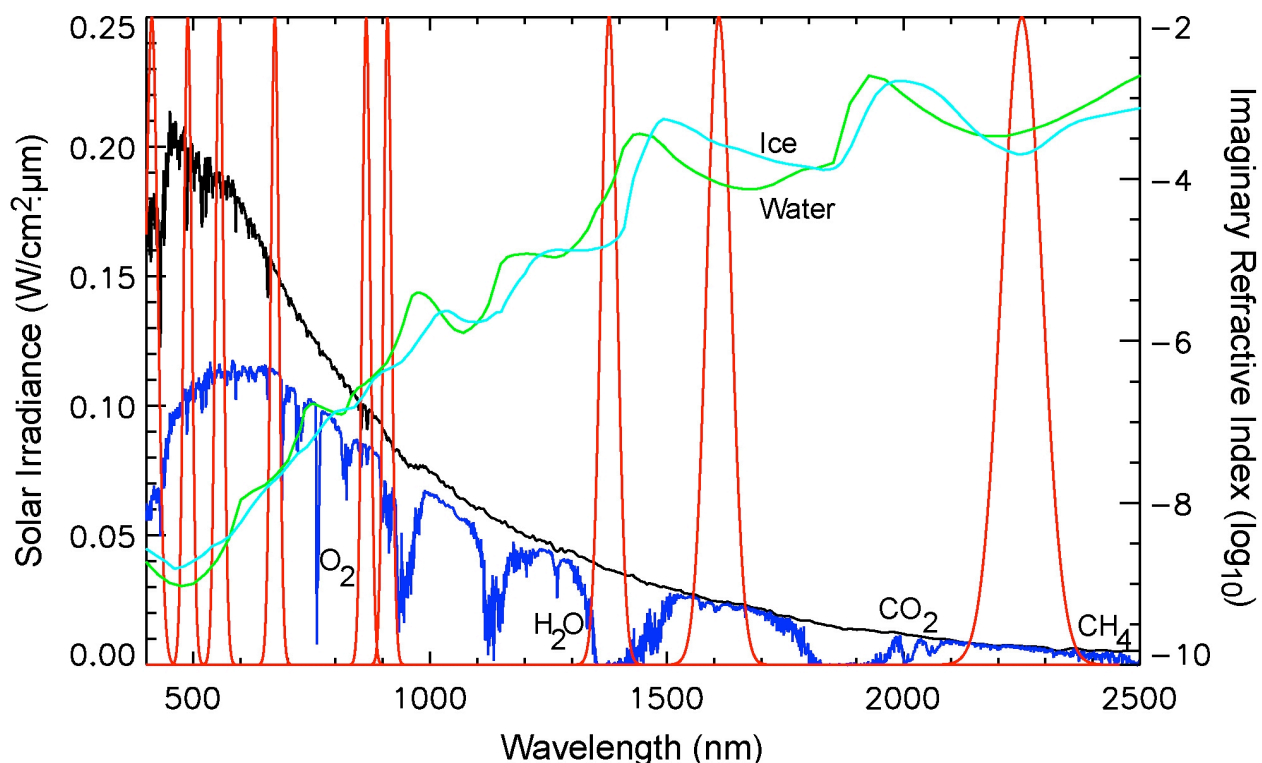


Figure 4.2-1. This figure shows the location of the APS spectral bands with respect to the solar spectrum (black curve) and atmospheric absorption features (solar spectrum reduced by two-pass direct beam transmission shown as a blue curve). The spectral variation of the imaginary refractive indices of ice (blue) and water (green) are also shown on a logarithmic scale.

4.2.1. Number of Spectral Bands

The number of bands specifically dedicated to aerosol remote sensing for the APS design baseline is seven. This decision was made based on an analysis of the

information content The information content as defined in section 3.5 of the measurement system as it applies to aerosol EDR retrievals.

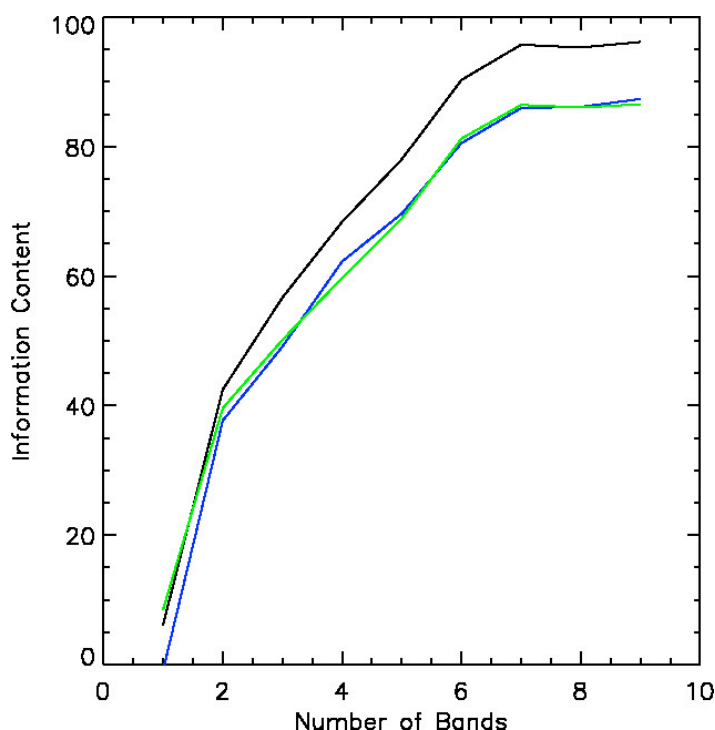


Figure 4.2.1-1. This figure shows how the EDR information content of APS measurements varies as a function of the number of bands.

In figure 4.2.1-1 the number of bands used is increased from one to nine. The order in which the bands are added to the analysis is 410, 488, 555, 670, 865, 1610, 2250, 747 and 1240 nm. It can be seen that the use of a 747 or 1240 nm band in addition to the first seven bands provides little or no additional information about the aerosol EDRs beyond what is already available in the first seven bands. The basic architectural approach selected for APS to meet the EDR performance requirements allows convenient groupings of bands in increments of 3 up to 12. There is a clear scientific justification for adding two bands dedicated to cirrus cloud screening (Section 3.3.2.1) and water vapor measurement (Section

4.2). Table 4.2.5-1 summarizes the APS band selections and compares them to the equivalent VIIRS bands.

4.2.2. Cirrus cloud screen

The purpose of having an APS band embedded in a strong water vapor absorption feature is to allow for screening of thin cirrus clouds and the potential to retrieve aerosol EDRs in the presence of sub-visible cirrus clouds. This requires that the band be located spectrally such that absorption by water vapor screens APS from detecting light scattered from the surface, or clouds in the lower troposphere. The current RSP instrument has a band located 1880 nm to perform this function. The advantage of this band compared to the 1378 nm band used by VIIRS and MODIS is that it is sensitive to ice particle size. However, since the primary task of APS is to produce aerosol EDRs on an operational basis, it is more important that this channel be capable of being used for correcting stratospheric aerosols, since the probability of there being a volcanic eruption at some point during the NPOESS era is extremely high. Thus, using a shorter wavelength band is preferable for greater sensitivity to stratospheric aerosols that typically have an effective radius of around 0.5 μm . Figure 4.2.2-1a) indicates why 1378 nm has been chosen as the location for such a band on VIIRS and MODIS. This figure also shows that although the VIIRS spectral band has a 15 nm bandwidth, the water

vapor absorption is similar, or lower over the spectral region from 1350-1400 nm than the 15 nm region around 1378 nm, which should allow a band centered near 1378 nm to be used with a width of 40 nm without compromising the capability to screen for cirrus clouds. The reason for desiring the broader width in this band for APS is to increase signal-to-noise ratio (SNR) so that these measurements can be used not only to detect thin cirrus, but also to characterize them down to an optical depth of 0.01. A high SNR is also desirable in this band for characterizing stratospheric aerosols, because of the typical size and loadings that this capability is required for.

There are two criteria that can be used to evaluate the performance of a band located in an absorption feature. One is the two-pass transmission from sun to surface to sensor and the other is the vertical weighting function, which provides a measure of how well lower levels of the atmosphere are screened from the sensor. The vertical weighting function in the single scattering approximation is defined in analogy with that used for infrared sounders viz.,

$$w(z,0) = \frac{d \exp(-m \int_0^z \sigma(z') dz')}{dz} \quad 4.2.2-1$$

where m is the air mass for two-pass transmission

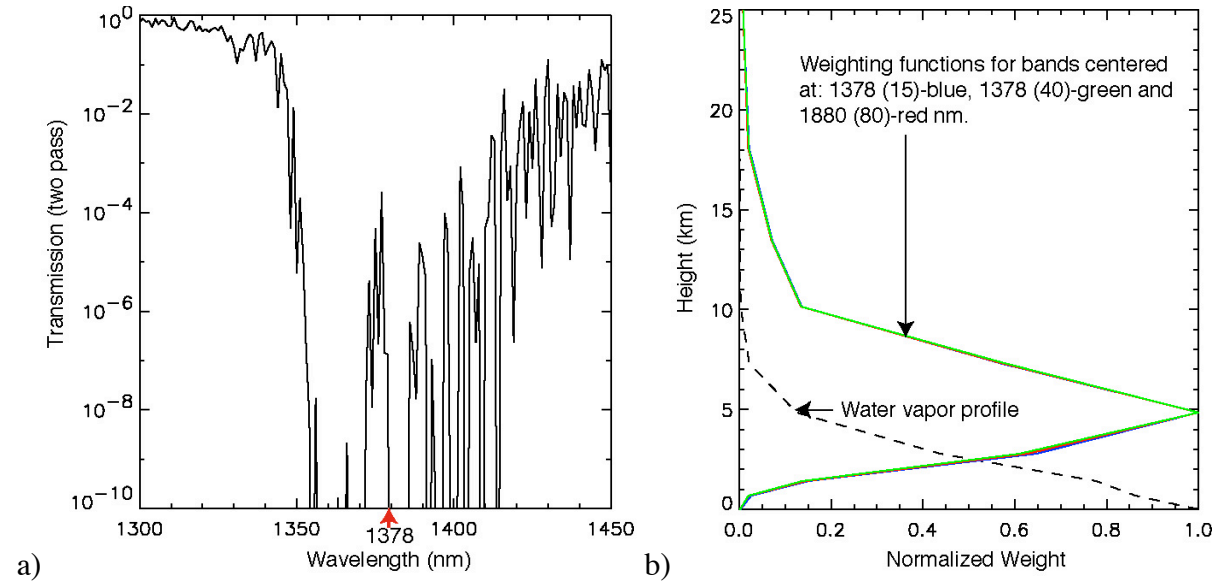


Figure 4.2.2-1 a) Two pass transmission in the spectral region of the 1378 nm VIIRS band. Water vapor profile is for a standard atmosphere and water vapor amount is 2 prec. cm. b) The vertical weighting function associated with candidate filter functions for a water vapor profile from the US standard atmosphere.

$$m = \frac{\mu + \mu_0}{\mu \mu_0} \quad 4.2.2-2$$

with μ and μ_0 the cosine of the view angle and solar zenith angle respectively. The reflectance in this formalism is given then by the expression

$$R(\mu, \mu_0, \phi) = \frac{1}{4(\mu + \mu_0)} \int_0^z \varpi(z') w(z', 0) P(\mu, \mu_0, \phi; z) dz' \quad 4.2.2-3$$

It should be emphasized that the weighting function is principally of use in evaluating how well the spectral band screens out the influence of the lower atmosphere. This is because the rapid decrease in water vapor amount with height means that although the weighting function is small in the upper troposphere the single scattering albedo will tend to increase with height for a given amount of scattering, since the amount of absorption is decreasing. The behavior of the weighting function is shown in Figure 4.2.2-1 b) for the VIIRS band parameters, candidate APS band parameters and the band parameters used for a similar type of band (at 1880 nm) on the RSP instrument. It can be seen that the atmosphere below about 5 km is screened from the sensor in all three cases with little difference between the vertical weighting functions. The water vapor profile (shape) is shown since this will also affect the weighting functions. Note, that the water vapor absorption for all three band specifications is sufficiently strong that the weighting function peaks above the majority of the water vapor. A more detailed comparison is presented in Table 4.2.2-1 below where the bandwidths have been varied by ± 5 nm from the nominal 5 and 15 nm values and the band center has also been varied by ± 5 nm from nominal values.

This table indicates that the 40 nm wide band provides similar performance to the 15 nm band specified for VIIRS. It should however be emphasized that this performance evaluation is for a rectangular filter function and that as can be seen from Figure 4.2.2-1 above the main source of contamination by the surface for a band located at 1378 nm will be from Out Of Band (OOB) contributions. It is therefore planned that the OOB performance of the filters for this band will be carefully evaluated and spectral blocking elements will be used to ensure that there is no short wavelength leak, since solar intensity is increasing rapidly in this spectral range.

Table 4.2.2-1: Effects of band location and bandwidth on the two pass transmission from sun to surface to satellite (Tsurf), the height (zbar) and the width of the weighting function.

Band Width 10 nm				Band Width 15 nm				Band Width 20 nm			
Band Center	Tsurf	zbar	zvar	Band Center	Tsurf	zbar	zvar	Band Center	Tsurf	zbar	zvar
1373	2.9E-05	5.15	2.99	1373	2.0E-05	5.30	3.05	1373	1.5E-05	5.49	3.12
1374	2.9E-05	4.90	2.86	1374	2.0E-05	5.26	3.02	1374	1.5E-05	5.52	3.13
1375	2.9E-05	5.04	2.99	1375	2.0E-05	5.41	3.13	1375	1.5E-05	5.48	3.09
1376	2.9E-05	4.99	2.95	1376	2.0E-05	5.41	3.12	1376	1.5E-05	5.39	3.06
1377	2.9E-05	5.11	3.13	1377	2.0E-05	5.32	3.07	1377	1.5E-05	5.40	3.08
1378	2.9E-05	5.21	3.16	1378	2.0E-05	5.35	3.08	1378	1.5E-05	5.35	3.06
1379	2.8E-05	5.26	3.15	1379	2.0E-05	5.24	3.04	1379	1.6E-05	5.21	3.04
1380	2.8E-05	5.34	3.18	1380	2.0E-05	5.19	3.06	1380	1.7E-05	5.13	3.02
1381	2.4E-05	5.40	3.15	1381	2.0E-05	5.19	3.06	1381	1.7E-05	5.00	2.97
1382	2.4E-05	5.40	3.17	1382	2.1E-05	5.14	3.08	1382	1.7E-05	5.06	3.04
1383	9.4E-08	5.61	3.15	1383	2.2E-05	5.06	3.07	1383	1.7E-05	5.01	3.02

Band Width 35 nm				Band Width 40 nm				Band Width 45 nm			
Band Center	Tsurf	zbar	zvar	Band Center	Tsurf	zbar	zvar	Band Center	Tsurf	zbar	zvar
1373	9.8E-06	5.42	3.07	1373	8.8E-06	5.36	3.05	1373	1.3E-05	5.27	3.03
1374	1.0E-05	5.36	3.05	1374	8.8E-06	5.37	3.05	1374	1.2E-05	5.32	3.05
1375	1.0E-05	5.44	3.10	1375	8.8E-06	5.40	3.06	1375	1.0E-05	5.32	3.05
1376	1.0E-05	5.39	3.08	1376	8.8E-06	5.41	3.07	1376	1.1E-05	5.31	3.05
1377	1.0E-05	5.38	3.08	1377	1.1E-05	5.39	3.09	1377	1.1E-05	5.32	3.05
1378	1.0E-05	5.40	3.09	1378	1.2E-05	5.32	3.08	1378	1.1E-05	5.35	3.07
1379	1.0E-05	5.42	3.11	1379	1.2E-05	5.32	3.08	1379	1.1E-05	5.35	3.07
1380	1.3E-05	5.31	3.09	1380	1.2E-05	5.34	3.10	1380	2.9E-05	5.31	3.09
1381	1.4E-05	5.20	3.05	1381	1.2E-05	5.34	3.10	1381	3.1E-05	5.25	3.08
1382	1.4E-05	5.23	3.07	1382	3.2E-05	5.23	3.08	1382	3.1E-05	5.27	3.08
1383	1.4E-05	5.22	3.06	1383	3.5E-05	5.14	3.05	1383	3.1E-05	5.24	3.08

4.2.3. Rayleigh measurements

The choice of whether to use a 440 nm or 490 nm band in place of the 470 nm band currently being used on the RSP instrument is dominated by the desire to minimize the effects of ocean color on at least one of the short wavelength visible bands so as to enhance sensitivity to aerosol single scattering albedo.

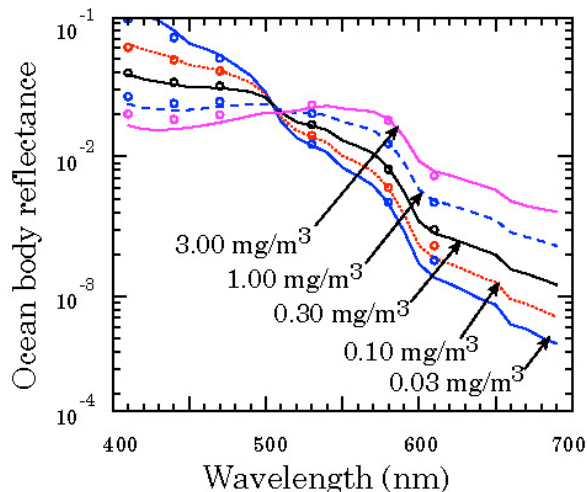


Figure 4.2.3-1. Spectral variation of ocean body reflectance as a function of Chlorophyll concentration.

In Figure 4.2.3-1 it can be seen that the variation of ocean body reflectance as a function of chlorophyll concentration is minimized at around 500 nm.

However, since the atmosphere is more opaque at 440 nm than 490 nm it is necessary to include the effects of atmospheric scattering in the evaluation of which band is least sensitive to ocean color.

Figure 4.2.3-2 shows polar plots of the errors in total reflectance and polarized reflectance that would be observed for a solar zenith angle of 45° and view angle range of ±60°. The azimuthal range from 60° to 120° is outlined in red. This viewing geometry is typical of the NPOESS 9:30 orbit.

Typical open ocean values of chlorophyll concentration are 0.1 mg/m^3 or less and have

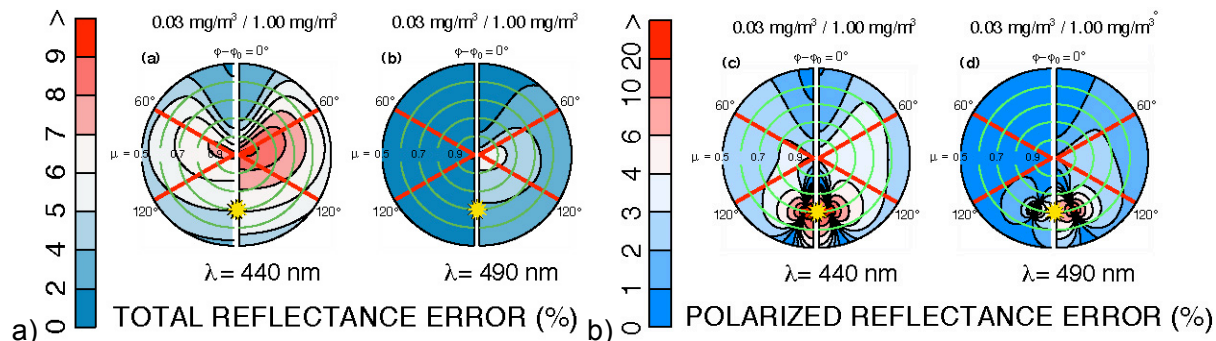


Figure 4.2.3-2. a) Reflectance errors and b) Polarized reflectance errors that would be made if the chlorophyll concentration used in a model calculation was 0.1 mg/m^3 but the actual concentration was 0.03 mg/m^3 (left side of each plot), or 1.0 mg/m^3 (right side of each plot) for spectral bands at 440 and 490 nm.

an upper limit of 1.0 mg/m^3 which suggests that the 490 nm band would be essentially insensitive to variations in ocean color. It is therefore planned that the 490 nm band corresponding to that used for VIIRS will be used in the APS instrument. The reduced uncertainty in lower boundary condition for this band over the oceans will provide an improved capability to estimate single-scattering albedo.

4.2.4. Water vapor estimation

The purpose of the spectral band at 910 nm is to provide a tool for atmospheric correction of APS measurements for water vapor. The only spectral band for which this is expected to be required is the 2250 nm band and in this band corrections only become relevant to meeting EDR specifications for water vapor amounts greater than two precipitable cm at extremes of the tolerances on the filter for this band.

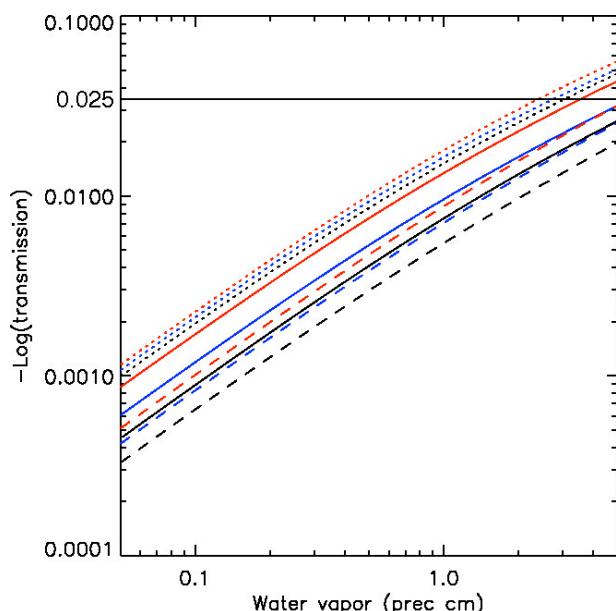


Figure 4.2.4-1. Demonstration of sensitivity of water vapor contamination of 2250 nm band to filter specifications. Horizontal black line corresponds to an effective optical depth of 0.01

Figure 4.2.4-1 shows how the negative log of two-pass transmission varies as a function of water vapor for the APS 2250 nm band with an air mass of 2.5. The negative log of two-pass transmission is effectively the optical depth (when divided by the airmass) of water vapor. Since the EDR requirements on aerosol optical depth have threshold accuracy requirements of 0.01, any water vapor effect of this order of magnitude needs to be corrected. The negative log transmission at 0.025 is therefore indicated since this corresponds to an effective optical depth of 0.01. The water vapor burden for which correction will become an issue is two

precipitable cm and greater and so the water vapor correction band needs to be chosen with a sensitivity that is optimized for this water vapor range.

The calculations shown here are for a band with a 90, 100 and 110 nm band width (black, blue and red respectively) and for 2240, 2250 and 2260 nm band centers (dotted, solid and dashed lines respectively). There are two conclusions that can be drawn from this figure: That tolerances should tend to be biased narrow with regard to bandwidth specification and long with regard to band center location. The need to maintain adequate signal to noise ratio at 2250 nm conflicts with the preference for a narrower band, since typical aerosol optical depths in this band are very low. A reasonable set of biased tolerances that account for the desire to eliminate the need for water vapor correction in the 2250 nm band altogether while maintaining good SNR are 2250 (+15-5) for band center and 100 (+5-15) nm for FWHM.

The discussion above indicates that the APS band used to retrieve water vapor should be designed to function effectively with large water vapor amounts, since it is under these conditions that the correction of the 2250 nm band for water vapor contamination may be necessary. The water vapor band that is typically used for remote sensing of water vapor in the Near Infra-Red (NIR) is that located between 890 and 1000 nm. This band effectively has two branches: one located between 890 and 920 nm (which we will term the 910 nm branch) and one located between 925 and 1000 nm (which we will term the 940 nm branch). We evaluated the capabilities of APS bands located in these two branches.

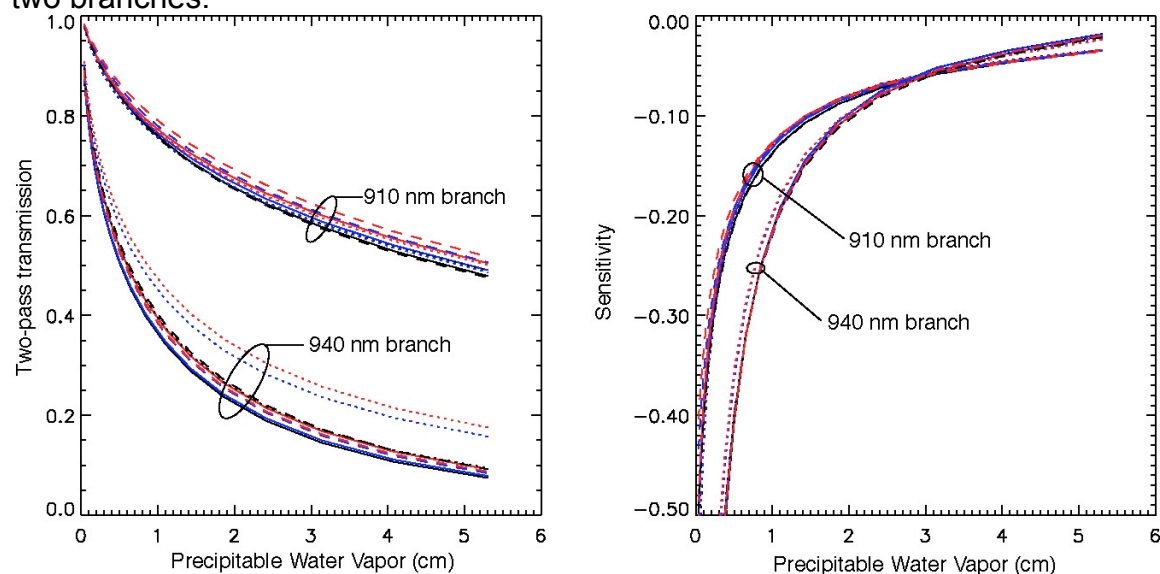


Figure 4.2.4-2. The left hand figure shows how the two-pass transmission of water vapor in the two branches of the water vapor band vary as a function of water vapor column amount for an air mass of 2.5 and a standard atmospheric water vapor profile. The right hand figure shows how the sensitivity (derivative of transmission as a function water vapor column amount) varies as a function of water vapor column amount. For the 910 nm branch the nominal center is 910 nm (solid lines) and variations from this value of 905 (dotted lines) and 915 (dashed lines) nm are shown. For each band center, bandwidths of 15, 20 and 25 nm (black, blue and red respectively) are shown.

The two-pass transmission indicates the magnitude of the signal that we may expect to be able to use in the water vapor estimate, while the sensitivity calculation indicates how rapidly the transmission is varying as a function of water vapor amount for a given water vapor amount. Based on the analysis of the 2250 nm band specification and tolerances we prefer the band with the greater sensitivity at high water vapor amounts which is the 910 nm branch. Moreover we can see that for water vapor amount more than one precipitable cm the two pass transmission for the 940 nm band is less than 0.4 decreasing to 0.1 at five precipitable cm. Thus, the sensitivity and the available signal are both greater in the 910 nm branch than the 940 nm branch. These figures indicate that tolerances of ± 5 nm on both the band width and the band center of this band may be allowed without affecting its behavior for a band center of 910 nm with a bandwidth of 20 nm.

4.2.5. Spectral Band Centers and Widths

Table 4.2.5-1 summarizes the locations and widths of the spectral bands selected for the APS instrument.

Table 4.2.5-1. Summary of APS spectral band parameters and comparison with VIIRS spectral band parameters.

APS			VIIRS		
Band ID	Wavelength (nm)	Bandwidth (nm)	Band ID	Wavelength (nm)	Bandwidth (nm)
VNIR1	412	30	M1	412	20
			M2	445	18
VNIR2	488	20	M3	488	20
VNIR3	555	20	M4	555	20
VNIR4	672	20	M5	672	20
			M6	747	15
VNIR5	865	20	M7	865	20
VNIR6	910 (1)	20			
			M8	1240	20
SWIR1	1378	40	M9	1378	15
SWIR2	1610	60	M10	1610	60
SWIR3	2250	100	M11	2250	50

Note 1: There is no comparable VIIRS band and the comparable on MODIS is located at 905 nm. The band used for APS is located at 910 nm to provide better sensitivity to slightly higher water vapor loads than the 905 nm band on MODIS.

4.3. Calibration

At the beginning of the sensor description section 4.0 idealized equations for the APS measurements were presented. Here we present a more realistic set of instrument

model equations that allow calibration issues to be addressed. The model presented here is not completely general (the plane of polarization of Q and U are not allowed to have an arbitrary reference direction), but does include all the sources of error and assumptions that are made in the analysis of APS measurements. The effects of small imperfections in instrument assembly that can be characterized prior to launch and reversed by simple linear transformations during RDR to SDR processing are discussed in section 5. The model equations for the Q and U telescopes are

$$C0 \times S1L = \frac{I + Q + q_{inst}I}{2}, \quad C0 \times K1 \times S1R = \frac{I - Q - q_{inst}I}{2} \quad 4.3-1$$

$$C0 \times C12 \times S2L = \frac{I + \cos(\Delta)(U + u_{inst}I) + \sin(\Delta)V}{2}, \quad 4.3-2$$

$$C0 \times C12 \times K2 \times S2R = \frac{I - \cos(\Delta)(U + u_{inst}I) - \sin(\Delta)V}{2}.$$

where these equations assume that the dark count has already been subtracted from the measurements. The radiometric calibration coefficient C0 and the radiometric relative calibration coefficient C12 are defined by these equations as are the relative gain coefficients K1 and K2 that are particularly relevant to polarimetric calibration. Instrumental polarization is introduced as being proportional to the observed intensity since this is a realistic model of the effect that non-ideal behavior of the scan mirror assembly would have. Retardance has been included in the model to allow for the potential effects of stress induced birefringence in the refractive optics and the circular polarization of light has been retained to indicate its role in the measurement process and conditions under which it can be neglected. In this model the effects of circular polarization and system retardance only affect the measurement of U. More generally these effects can project onto both Q and U depending on the reference plane in which they are measured. However all the necessary conclusions regarding measurement and calibration uncertainties can be drawn from these calibration equations.

4.3.1. Polarimetric Calibration

The polarimetric calibration of the APS can be separated from the radiometric calibration of the APS by restricting this form of calibration to be the determination of those constants required to ensure the accurate determination of the relative Stokes parameters $q=Q/I$ and $u=U/I$ and the degree of linear polarization $p=(q^2+u^2)^{0.5}$.

$$\frac{S1L - K1 \times S1R}{S1L + K1 \times S1R} = q_{scene} + q_{inst} \quad 4.3.1-1$$

$$\frac{S2L - K2 \times S2R}{S2L + K1 \times S2R} = \cos(\Delta)u_{scene} + \cos(\Delta)u_{inst} + \sin(\Delta)v_{scene} \quad 4.3.1-2$$

where $v=V/I$. Sources of error in the determination of q_{scene} and u_{scene} are the instrumental polarization q_{inst} and u_{inst} , the reduced scaling of u caused by retardance Δ and the coupling of retardance with circular polarization. Instrumental polarization can be characterized before flight and subtracted out. The effect of the introduction of instrumental polarization after launch is described in the following section. The effects of

retardance and other possible errors that have a mathematically identical effect on the determination of q and u are discussed in section 4.3.1.2. The magnitude of the circular v_{scene} polarization must be compared to that of the linear polarization component u_{scene} to determine its effect on the APS measurements. The value of v_{scene}/u_{scene} is small (typically of order 10^{-3}) and since the circular polarization only couples into the measurement of linear polarization in the presence of stress-induced birefringence, the effect of circular polarization on APS measurements is expected to be negligible. The use of air-spaced optical elements in the APS refractive telescopes is however considered a useful measure to limit the potential for the introduction of stress-induced birefringence into the APS measurements, since retardance also reduces the scale of u . The remaining unknowns in equations 4.3.1-1 and 4.3.1-2 are the relative gain coefficient $K1$ and $K2$ and it is the determination of these constants that discussed in the next section.

4.3.1.1. Onboard Polarimetric Calibrator (OPC–Primary)

The OPC-Primary will provide the essential calibration data required to maintain the inherent polarization accuracy of the APS on orbit. The OPC-Primary design was developed at SpecTIR and has been incorporated into the second RSP instrument (RSP2). The function of the OPC-Primary is to provide the means for determining the relative channel response between pairs of channels which measure orthogonal polarization components within each of the nine spectral bands, i.e., a total of 18 ratios. It consists of a specular reflector element and a polarization scrambler that is viewable on each scan after viewing of the scene portion of the scan has been completed. Thus, the scene that is viewed directly by the APS is also viewed through the OPC-Primary. The use of the scene radiance as the calibration source offers the following advantages: 1) the spectral content of the optical input has essentially the same spectral distribution within individual spectral bands as the directly viewed scene; 2) the overall spectral distribution of the optical input across the 400 to 2300 nm spectral range of the APS mimics the directly viewed scene; and 3) the dynamic range over which relative calibration measurements are made is automatically virtually the same as the dynamic range of the scene data. The availability of observations of the OPC-Primary on each scan means that the calibration can be tracked versus changes of instrument temperature, detector temperature, temperature gradients and contamination levels. Finally, the fact that the underlying scene will produce temporally and spectrally varying effective radiances should offer a superior *in situ* capability to assess any unexpected on-orbit performance changes.

The OPC-Primary allows the relative gain coefficients $K1$ and $K2$ to be determined by providing a source that is essentially unpolarized ($p < 0.05\%$). In this case, if we neglect instrumental polarization, the equations 4.3.1-1 and 4.3.1-2 reduce to

$$S1L = K1 \times S1R \quad 4.3.1.1-1$$

and

$$S2L = K2 \times S2R \quad 4.3.1.1-2$$

when viewing the OPC-Primary. The relative gain coefficients can therefore be determined simply from the ratio of measurements made using the OPC-Primary. If we allow for instrumental polarization that has been created on orbit degrading this

calibration process we obtain the following equations for the relationship of the observations q' and u' to the correct values of q_{scene} and u_{scene} , viz.,

$$q' = \frac{q_{scene}}{1 - q_{inst}(q_{scene} + q_{inst})} \quad 4.3.1.1-3$$

$$u' = \frac{\cos(\Delta)u_{scene}}{1 - \cos^2(\Delta)u_{inst}(u_{scene} + u_{inst})} \quad 4.3.1.1-4$$

where the relative gain coefficients have been determined using equations 4.3.1.1-1 and 4.3.1.1-2, but are contaminated by the presence of instrumental polarization and the effects of circular polarization are neglected. It is apparent that to first order the instrumental polarization is corrected by evaluating the relative calibration coefficients using the OPC-Primary. The effects of the OPC-Secondary on this correction are described in the following section.

4.3.1.2. Onboard Polarimetric Calibrator (OPC)– Secondary

The OPC-Secondary provides a near 100% polarized input to the APS during each scan prior to the start of the scene measurements. Such calibration data is used to verify that the absolute scaling of the degree of polarization determination is correct, e.g., if a 72% polarization is derived from the scene measurements, that the actual polarization is the same, and not say 73%, and to evaluate any variations in instrumental polarization. Thus, for the long design life and long term stability required for the NPOESS APS sensor, it has been deemed necessary to include this capability. With RSP the absolute scaling deviates from unity by less than 1% and no change in this scaling has been observed over time (4 years).

The OPC-Secondary is implemented by arranging to view the scene by reflection from a transparent plate at the Brewster angle where the reflected beam is 100% polarized. The preliminary choice for the plate material is to use Infrasil 302. Both particulate and film contamination can alter the observed polarization and so protective windows (analogous to those used on the scan mirror and OPC-Primary assemblies) will be used on the calibrator entrance and exit ports.

The measurements made with the OPC-Secondary are implemented in the processing of APS data by a rescaling of the values q' and u' obtained in equations 4.3.1.1-3 and 4.3.1.1-4 above viz.,

$$q'' = \alpha_q q' = \alpha_q \frac{q_{scene}}{1 - q_{inst}(q_{scene} + q_{inst})} \quad 4.3.1.2-1$$

$$u'' = \alpha_u u' = \alpha_u \frac{\cos(\Delta)u_{scene}}{1 - \cos^2(\Delta)u_{inst}(u_{scene} + u_{inst})} \quad 4.3.1.2-2$$

The coefficients α_q and α_u are determined from the requirement that the values of q'' and u'' match the values expected for observations of the calibrator.

$$\alpha_q = 1 - q_{inst}(q_{scene}^{cal} + q_{inst}) \quad 4.3.1.2-3$$

$$\alpha_u = \frac{1 - \cos^2(\Delta)u_{inst}(u_{scene}^{cal} + u_{inst})}{\cos(\Delta)} \quad 4.3.1.2-4$$

The calibration values will be close to $2^{-0.5}$, i.e., the polarization plane of the 100% polarized source will be at 22.5° to the planes of Q and U.

Scale errors can be caused not only by stress induced birefringence, but also by depolarization of radiation scattered at the input windows that remains within the optical field and scattering between the bandpass filters and the paired detectors for a given band (effectively a form of optical crosstalk). The main potential source of instrumental polarization is differential contamination of the scan mirror assembly, which is the reason for designing this unit so that it is effectively sealed to contaminants (sealed unit with porous plug for pressure relief).

Table 4.3.1.2-1. Errors in observed polarization caused by instrumental polarization and polarimetric scale factor uncertainty introduced after launch.

Scale Factor 1.0		Observed Polarization (Q/I, or U/I in %)											
		0.0	10.0	20.0	30.0	40.0	50.0	60.0	70.0	80.0	90.0	100.0	
Instrumental Polarization	0.1%	0.00%	0.01%	0.01%	0.01%	0.01%	0.01%	0.01%	0.00%	-0.01%	-0.02%	-0.03%	
	0.2%	0.00%	0.01%	0.02%	0.02%	0.02%	0.02%	0.01%	0.00%	-0.01%	-0.03%	-0.06%	
	0.5%	0.00%	0.03%	0.05%	0.06%	0.06%	0.05%	0.03%	0.00%	-0.04%	-0.09%	-0.15%	
	1.0%	0.00%	0.06%	0.10%	0.12%	0.12%	0.10%	0.06%	0.01%	-0.07%	-0.18%	-0.30%	
	2.0%	0.00%	0.12%	0.20%	0.25%	0.25%	0.21%	0.13%	0.01%	-0.15%	-0.35%	-0.60%	
	5.0%	0.00%	0.31%	0.51%	0.62%	0.63%	0.53%	0.33%	0.03%	-0.39%	-0.91%	-1.55%	
Scale Factor 0.99		Observed Polarization (Q/I, or U/I in %)											
		0.0	10.0	20.0	30.0	40.0	50.0	60.0	70.0	80.0	90.0	100.0	
Instrumental Polarization	0.1%	0.00%	0.01%	0.01%	0.01%	0.01%	0.01%	0.01%	0.00%	-0.01%	-0.02%	-0.03%	
	0.2%	0.00%	0.01%	0.02%	0.02%	0.02%	0.02%	0.01%	0.00%	-0.01%	-0.03%	-0.06%	
	0.5%	0.00%	0.03%	0.05%	0.06%	0.06%	0.05%	0.03%	0.00%	-0.04%	-0.09%	-0.14%	
	1.0%	0.00%	0.06%	0.10%	0.12%	0.12%	0.10%	0.06%	0.00%	-0.07%	-0.17%	-0.29%	
	2.0%	0.00%	0.12%	0.20%	0.24%	0.24%	0.21%	0.13%	0.01%	-0.15%	-0.35%	-0.59%	
	5.0%	0.00%	0.30%	0.50%	0.61%	0.62%	0.52%	0.33%	0.03%	-0.38%	-0.89%	-1.51%	
Scale Factor 0.95		Observed Polarization (Q/I, or U/I in %)											
		0.0	10.0	20.0	30.0	40.0	50.0	60.0	70.0	80.0	90.0	100.0	
Instrumental Polarization	0.1%	0.00%	0.01%	0.01%	0.01%	0.01%	0.01%	0.01%	0.00%	-0.01%	-0.02%	-0.03%	
	0.2%	0.00%	0.01%	0.02%	0.02%	0.02%	0.02%	0.01%	0.00%	-0.01%	-0.03%	-0.05%	
	0.5%	0.00%	0.03%	0.05%	0.06%	0.06%	0.05%	0.03%	0.00%	-0.03%	-0.08%	-0.13%	
	1.0%	0.00%	0.05%	0.09%	0.11%	0.11%	0.09%	0.06%	0.00%	-0.07%	-0.16%	-0.27%	
	2.0%	0.00%	0.11%	0.18%	0.22%	0.22%	0.19%	0.12%	0.01%	-0.14%	-0.32%	-0.54%	
	5.0%	0.00%	0.28%	0.46%	0.56%	0.57%	0.48%	0.30%	0.02%	-0.35%	-0.82%	-1.39%	

The effect of combinations of these problems on the accuracy of the APS measurements is shown in table Table 4.3.1.2-1. These calculations indicate that, as expected, scale factor changes are almost completely corrected as a result of the scale definition provided by the OPC-Secondary. Instrumental polarization up to a level of 2% is tolerable since the accuracy of the polarimetric observations is not degraded up to this level even without further correction.

4.3.2. Radiometric Calibration

There are three types of calibration that can be applied to satellite sensors: Hard, Soft and Vicarious. This terminology has been coined by the TOMS instrument team at NASA GSFC and seems to be a reasonable way to distinguish between the three different approaches. Hard calibration describes the traditional method whereby a source of known radiance is observed with the sensor and the calibration coefficient is determined by requiring that the intensity observed by the sensor match that which it is known to be observing. This approach allows for traceability of calibration to NIST standards and is described here. Soft calibration describes the use of the redundancy, or over completeness of a measurement set, to infer the calibration of a sensor, or identify sensor elements that should be discarded in the retrieval of data products. This approach cannot usually be traced to NIST standards, but is an important aspect of calibration validation and is described in Section 10. Vicarious calibration is the use of other instrumentation that has been calibrated and is therefore traceable to NIST standards to determine the calibration of the satellite sensor. This can include high altitude flights of instruments that match the spectral response of the satellite sensor, together with sufficient other instrumentation and measurements to allow the radiance at the top of the atmosphere to be accurately inferred. This approach is also described in Section 10.

Radiometric calibration is based on knowledge of the intensity that is being observed. The APS instrument make two measurements of intensity in each spectral band for which the formulae are

$$C0 \times (S1L + K1 \times S1R) = I \quad 4.3.2-1$$

and

$$C0 \times C12 (S2L + K2 \times S2R) = I \quad 4.3.2-2$$

C0 is the radiometric calibration coefficient. C12 is a coefficient that is used to track the relative gain stability in the two telescopes. Immediately after a calibration event C12 is unitary, but as gains drift the two determinations of intensity in equations 4.3.2-1 and 4.3.2-2 may no longer be the same. The value of C12 is determined from the ratio of the two intensity determinations

$$C12 = \frac{(S1L + K1 \times S1R)}{(S2L + K2 \times S2R)} \quad 4.3.2-3$$

and can be evaluated and tracked over 10-100 scans as a diagnostic of instrument stability.

4.3.2.1. Onboard Radiometric Calibrator (ORC)

The APS ORC consists of a mirror and a well-characterized Spectralon[®] diffuser. The ORC is mounted on the APS scanner housing so as to receive the direct solar view in the P-plane of the mirror at ~45° angle of incidence during satellite passage near the South Pole. (The mounting design of the ORC allows altering the orientation pre-flight to accommodate a different orbital equator crossing time.) When the solar diffuser is deployed into the “calibrate” position, the mirror is exposed and directs the solar beam onto the solar diffuser. During calibration the solar diffuser is viewed by the scanner in

a zone centered at ~62° from nadir between the end of the normal scene view and OPC-Primary portions of the scan.

During the intervals between the on-orbit radiometric calibrations, the diffuser element of the ORC is rotated to the “stowed” position such that the diffuser is positioned face-to-face with the mirror. The positioning of the ORC utilizes the same type of motor used by the APS aperture cover assembly. For enhanced reliability both primary and redundant drive electronics are provided for the ORC. The stowed position greatly minimizes the on-orbit exposure time and thereby the possibility of on-orbit degradation due to contamination, solarization, AO₂ or radiation effects. Vacuum-deposited aluminum is chosen as the ORC mirror coating for its inherent environmental stability and ruggedness. The Spectralon® solar diffuser material is processed specifically to avoid contaminants that could cause on-orbit degradation, and the diffuse polarized reflectance and BRDF is calibrated preflight using procedures and materials that are traceable to NIST, or NIST standards.

The radiance observed by the APS when viewing a calibrator of this type is

$$I(\lambda) = \frac{\cos(\theta_i)R_{\text{Spectralon}}(\lambda; \theta_i, \phi_i; \theta_v, \phi_v)R_{\text{Mirror}}(\lambda, \theta_M)F_0(\lambda)}{\pi SD^2} \quad 4.3.2.1-1$$

where θ_M is the angle of incidence of the solar beam on the mirror with respect to the mirror normal, θ_i and ϕ_i are the incident zenith and azimuth angles respectively with respect to the spectralon panel normal and θ_v and ϕ_v are the view zenith and azimuth angles respectively of the APS observations of the diffuser panel, again with respect to the panel normal. The remaining variables are the bidirectional reflectance function of the Spectralon® panel $R_{\text{Spectralon}}$, the reflectance of the mirror R_{Mirror} at its illumination angle θ_M , the exoatmospheric solar irradiance at 1 astronomical unit (AU) and the geocentric distance between the sun and the earth r_e in AU. The radiometric calibration constant $C0$ can then be determined from the formula

$$C0 = \frac{\cos(\theta_i)R_{\text{Spectralon}}(\lambda; \theta_i, \phi_i; \theta_v, \phi_v)R_{\text{Mirror}}(\lambda, \theta_M)F_0(\lambda)}{\pi SD^2(S1L_{\text{Cal}} + K1 \times S1R_{\text{Cal}})} \quad 4.3.2.1-2$$

where $S1L_{\text{Cal}}$ and $S1R_{\text{Cal}}$ are measurements made when the APS observes the ORC.

When the ORC calibration process is being performed the sectors where the Spectralon diffuser is located and those surrounding it will be observed continually for six hours prior to and six hours after the ORC deployment. These sectors view angles that scan through the limb of the Earth. Observations with this viewing geometry can be used post-launch as a natural calibration target, because the scattered radiation field is dominated by Rayleigh scattering by well mixed gases. The plane and magnitude of polarization are therefore well defined and provide a useful check on the presence of instrumental polarization and whether there has been any shift in the alignment of the telescope assemblies during launch.

4.3.2.2. Onboard Checkout Source (OCS)

As a means for verifying basic functioning of the APS, an onboard checkout source (OCS) is part of the APS design. The OCS provides optical stimulus signals that verify in a simple manner that the APS is functioning end-to-end. Redundant lamp sources (halogen-cycle tungsten filament) are located in the scanner housing and when commanded ON illuminate a diffuse strip located between the OPCA-Secondary and the start of the scene view portion of the scan. Although the principal function of this source is for “aliveness” testing while the APS is in storage, the type of lamp used generally has adequate color temperature stability for a given operating voltage and current that it can be used as a check of relative spectral calibration. This capability will be used, in addition to the ORC to check the relative spectral calibration between the 865 and 910 nm spectral bands that is crucial to the retrieval of water vapor column amounts from APS measurements.

4.3.3. Redundancy of Measurements

In the event that a single channel in a spectral band fails, it is still possible to determine I, Q and U. For example if there were no measurements of S2R, then based on equations 4.3-2 and 4.3.2-1 it is still possible to determine u using

$$\frac{2 \times C12 \times S2L}{(S1L + K1 \times S1R)} - 1 = \cos(\Delta) [u_{scene} + u_{inst}] \quad 4.3.3-1$$

The coefficient C12 cannot be determined from equation 4.3.2-3 in this case. The determination of C12 therefore follows in large part the discussion in section 4.3.1.1, since an unpolarized source must be used to compare the relative radiometric scale of the measurements from the two telescopes. The correction for scale effects such as $\cos(\Delta)$ can then use the OPC-Secondary as described in section 4.3.1.2. The principal source of error in the case of a channel failure is a mismatch in the scene radiance (not polarization) observed by the two telescopes. However, the determination of the calibration coefficient C12 has similar accuracy to the determination of K1 and K2 when averaged over suitably homogeneous scenes. However, in measurements over land the determination of u will be affected by a scene dependent noise as a result of differential albedo variations that are caused by the boresight misalignment of the telescopes measuring q and u . For most bands the allowed boresight misalignment of 10% should still allow u to be determined to within 0.5% over land, but the spectral bands at 865 and 910 nm may have more uncertainty than this because of the greater albedo variability that is typical of this spectral range. As noted in section 3.5, these measurements can still be used with an appropriate weighting for their increased uncertainty by adjusting the measurement covariance matrix.

4.4. Dynamic Range

The APS EDR requirements include both clouds and aerosols. This means that the maximum allowable Lambertian equivalent reflectance that the APS should be capable of measuring without saturating is unity. The principal determining factor in establishing the dynamic range is therefore the minimum detectable signal (resolved by a single bit)

that is required to detect the minimum expected aerosol signal. A secondary factor is the effect of quantization noise on polarimetric precision.

4.4.1. Primary Driver - Minimum Detectable Signal at 2250 nm

The radiance observed by a satellite sensor in the direction specified by the view zenith angle θ_v , the solar zenith angle θ_0 and the azimuth angle ϕ relative to the sun is given by the expression

$$I = \frac{\mu_0 R_{11}(\theta_v, \theta_0, \phi) F_0}{\pi r_E^2} \quad 4.4.1-1$$

where $\mu_0 = \cos(\theta_0)$, F_0 is the extra-terrestrial solar irradiance and r_E is the solar distance in AU. In analyzing the requirements on dynamic range and SNR the most appropriate quantity to use is the normalized radiance. This is because the effects of solar spectral irradiance variation are normalized which allows all channels to be treated uniformly in analyses, but the signal levels have the correct scale because the effects of solar elevation (μ_0) are still included. The normalized radiance is defined to be

$$\bar{I} = \frac{\pi r_E^2 I}{F_0} = \mu_0 R_{11}(\theta_v, \theta_0, \phi) \quad 4.4.1-2$$

As noted above, for the purposes of determining the required dynamic range of measurements we are interested in the lowest signal levels that must be resolved. Under these conditions single scattering provides a good approximation for the reflection of solar radiation by aerosols. In the single scattering approximation the normalized radiance is given by the expression

$$\bar{I} = \frac{\varpi_0 \tau P_{11}(\Theta)}{4\mu_v} \quad 4.4.1-3$$

in which Θ is the scattering angle (angle between the incident solar radiation and the angle of observation), ϖ_0 is the single scattering albedo, τ is the optical depth and $\mu_v = \cos(\theta_v)$. The normalized polarized radiance elements can be similarly defined although for simplicity we will assume that the particles are randomly oriented and macroscopically isotropic and mirror-symmetric [Mishchenko *et al.*, 2002], and that measurements are being made in the plane of scattering. Under these conditions the third Stokes vector element, U , is zero and the rotations between meridional plane and scattering plane are not required. The normalized polarized radiance in the single scattering approximation is then given by the expression

$$\bar{Q} = \frac{-\varpi_0 \tau P_{12}(\Theta)}{4\mu_v} \quad 4.4.1-4$$

The single scattering albedo typically varies between 0.8 and 1.0, while the phase function can vary by an order of magnitude and the optical depth can vary by several orders of magnitude (0.01-1.0 typically). For this analysis we generated a range of phase function values using a log normal size distribution (as defined in section 3) with effective radii of 0.1-10.0 μm and a fixed effective variance of 0.2. In Figure 4.4.1-1 we show the phase matrix elements P_{11} and $-P_{12}$ as a function of scattering angle.

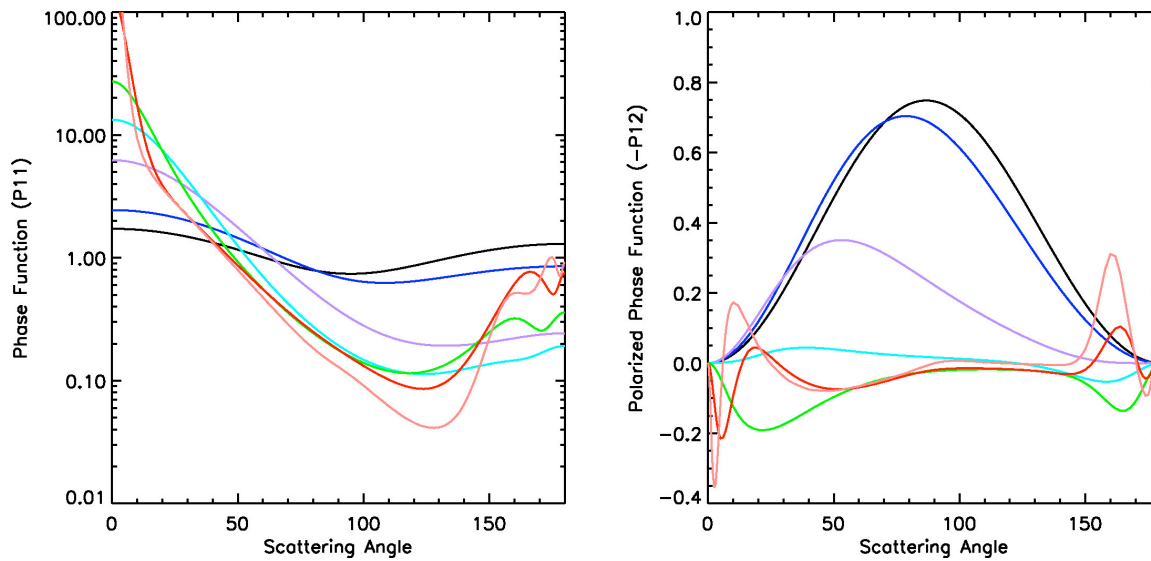


Figure 4.4.1-1. Phase function elements P11 and P12 calculated for a wavelength of 2250 nm with an effective variance of 0.2 and effective radii of 0.1, 0.2, 0.5, 1.0, 2.0, 5.0 and 10.0 μm (shown as black, blue, mauve, turquoise, green, red and orange respectively).

order to evaluate the required dynamic range we will examine the signal levels for the 2250 nm spectral band and their magnitude in digital numbers (DN) for 12, 13 and 14 bit resolution measurements. The 2250 nm channel is chosen since this is the band where the aerosol optical depth is expected to have its minimum value.

In the APS design the Stokes vector elements are not measured directly, but are related to the measurements, S1L and S1R, by the equations

$$S1L = \frac{\bar{I} + \bar{Q}}{2} \quad \text{and} \quad S1R = \frac{\bar{I} - \bar{Q}}{2} \quad 4.4.1-5$$

where we have assumed that the measurements are in units of normalized radiance.

It is planned that the full scale for APS bands will correspond to an unpolarized Lambertian equivalent reflectance of 1.2 ± 0.1 with the sun at zenith. This range is used to ensure that the APS instrument can be used unchanged on any NPOESS orbit, should that be necessary, and can be calibrated using the highly reflective ORC without saturating. Since half the signal is measured in each of the channels the upper limit on the full scale normalized radiance value for a particular channel is 0.6. The quantization step in each of the 1L and 1R channels is therefore 0.6×2^{-N} where N is the number of bits used to digitize the signal and the small effect of channel offset is ignored.

To provide reasonable minimum signal levels we need to determine values of view zenith, single scattering albedo, phase function elements P11 and P12 and optical depth to be used in equations 4.4.1-3 and 4.4.1-4. The phase function elements at an angle of 120° provide a conservatively low value for this component. An optical depth of

0.01 for the minimum detectable level is consistent with the EDR requirements on optical depth range, accuracy and precision. The single-scattering albedo is set to 1.0, although we note what the effect of reducing single scattering albedo to 0.8 would be in the discussion below. The cosine of the view zenith angle is given by the conservative value of 1.0 (reflectance is higher for non-nadir views). The signal levels corresponding to these assumed aerosol characteristics are given in Table 4.4.1-1 below.

Table 4.4.1-1. Calculation of signal levels using single scattering approximation.

Effective Radius	P11	P12	(P11-P12)/2	(P11+P12)/2	S1L	S1R	S1L+S1R
0.1	0.8620	-0.5286	0.6953	0.1667	1.74E-03	4.17E-04	2.16E-03
0.2	0.6443	-0.4200	0.5322	0.1121	1.33E-03	2.80E-04	1.61E-03
0.5	0.2017	-0.0952	0.1484	0.0532	3.71E-04	1.33E-04	5.04E-04
1.0	0.1140	-0.0019	0.0579	0.0560	1.45E-04	1.40E-04	2.85E-04
2.0	0.1153	0.0188	0.0483	0.0670	1.21E-04	1.68E-04	2.88E-04
5.0	0.0869	0.0174	0.0348	0.0522	8.69E-05	1.30E-04	2.17E-04
10.0	0.0456	0.0012	0.0222	0.0234	5.55E-05	5.84E-05	1.14E-04

Table 4.4.1-2. Signal levels in DN in the APS L and R channels for 12-,13- and 14-bit quantization.

Effective Radius	Number of bits: 12			Number of bits: 13			Number of bits: 14		
	Digitization step: 1.46E-04			Digitization step: 7.32E-05			Digitization step: 3.66E-05		
	S1L	S1R	S1L-S1R	S1L	S1R	S1L-S1R	S1L	S1R	S1L-S1R
0.1	11.87	2.85	9.02	23.73	5.69	18.04	47.47	11.38	36.09
0.2	9.08	1.91	7.17	18.16	3.83	14.34	36.33	7.65	28.67
0.5	2.53	0.91	1.62	5.07	1.82	3.25	10.13	3.63	6.50
1.0	0.99	0.96	0.03	1.98	1.91	0.07	3.96	3.82	0.13
2.0	0.82	1.14	-0.32	1.65	2.29	-0.64	3.29	4.58	-1.28
5.0	0.59	0.89	-0.30	1.19	1.78	-0.59	2.37	3.56	-1.19
10.0	0.38	0.40	-0.02	0.76	0.80	-0.04	1.51	1.60	-0.08

These signal levels can be converted into DN for 12-, 13- and 14-bit digitization levels to provide an evaluation of whether the signals are resolved with these different quantization levels. These values in DN are shown in Table 4.4.1-2. It is clear from this

table that 14-bit digitization is required to resolve the signal levels that are created by scattering of solar radiation on 10 µm particles with an optical depth of 0.01. This quantization level is also required to resolve the variation in polarization for particle sizes greater than 0.5 µm where there is a zero crossing and sign change that is only resolvable with 14-bit digitization.

4.4.2. Secondary Driver - Effect of quantization noise on polarization

The degree of linear polarization is constructed from the APS measurements of fractional Stokes parameters $q=Q/I$ and $u=U/I$, which are in turn related to the APS measurements by the equations

$$q = \frac{S1L - S1R}{S1L + S1R} \quad \text{and} \quad u = \frac{S2L - S2R}{S2L + S2R} \quad 4.4.2-1$$

For the sake of simplicity, in what follows it is assumed that the channels are well balanced so that the relative gain coefficients (K1 and K2) are equal to unity. In practice the gain select resistors will provide relative channel gains that are balanced to better than 3% at launch and the actual calculated relative gain values, determined by the OPC-Primary, will be used operationally. The assumption of identical gain is acceptable for the purposes of this analysis provided that the relative gains agree to within 10% and is used here to provide a quantitative indication of the effect of quantization on polarimetric precision. The effect of quantization on the precision of these determinations can be clearly seen for a worst case analysis of q where the S1L measurement is $+\Delta/2$ from its true value and the S1R measurement is $-\Delta/2$ from its true value where Δ is the quantization step. In this case the expression for q can be written as

$$q = \frac{S1L - S1R}{S1L + S1R} + \frac{\Delta}{S1L + S1R} = q_{True} + \frac{\Delta}{I} \quad 4.4.2-2$$

in which equation q_{True} is the actual value of q and the second term represents the effects of quantization on precision. This equation shows that a quantization dependent reflectance level determines the effects of quantization on polarimetric precision.

Table 4.4.2-1. Reflectance levels required for effects of digitization on polarimetric precision to be reduced to specified level.

Number of bits	Quantization Step	Precision Required 0.20%	Precision Required 0.50%
		Reflectance Level To Reach This Precision	
12	0.00014648	0.07324219	0.02929688
13	7.3242E-05	0.03662109	0.01464844
14	3.6621E-05	0.01831055	0.00732422

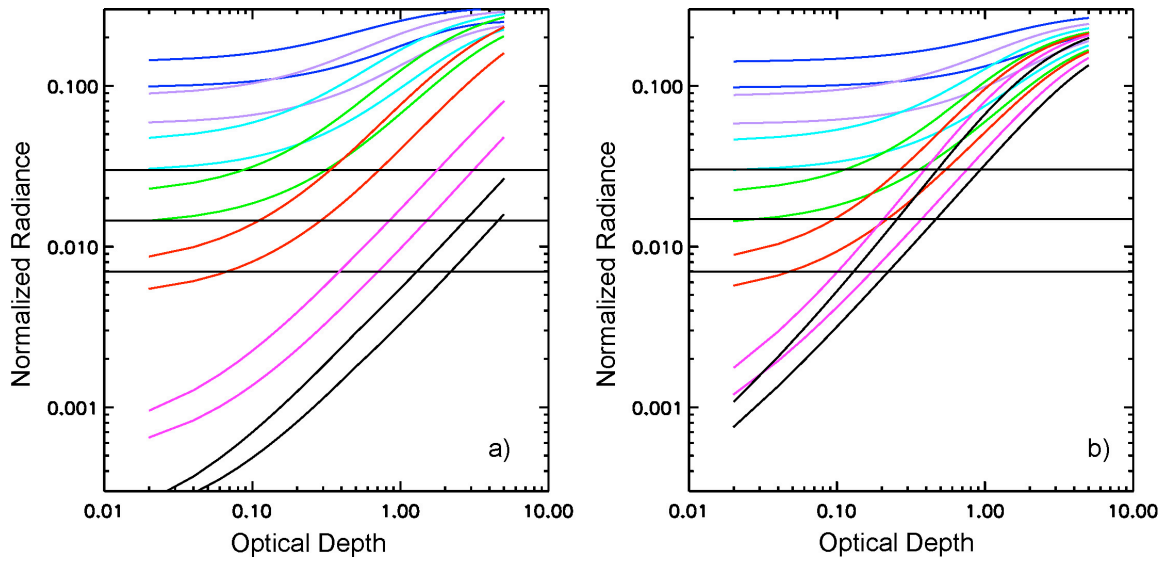


Figure 4.4.2-1 The horizontal solid black lines show the normalized radiance required to achieve 0.5% polarimetric precision. The colored lines are the normalized radiances at 410, 490, 555, 670, 865, 1610 and 2250 nm (blue, mauve, turquoise, green, red, cyan, black) for a fine mode (left hand figure; effective radius of 0.16 μm , effective variance of 0.21) and a coarse mode (right hand figure; effective radius of 1.13 μm , effective variance of 1.00) aerosol. For each spectral band the upper (lower) line is the maximum (minimum) radiance for a cross-principal plane measurement with a solar zenith angle of 45°.

It is clear from the Table 4.4.2-1 and Figure 4.4.2-1 that in order to have good precision for each measurement over the full scan range for all bands and for a realistic range of aerosol models and range of aerosol optical thicknesses it is necessary to have 14-bit digitization.

4.5. Signal-to-Noise

4.5.1. Intensity measurements

In the APS instrument the intensity is determined from the sum of the measurements of the intensity components in orthogonal polarizations. As in section 4.4.2, for the sake of simplicity it is assumed that the channels are well balanced so that the gains in the two channels are identical. The following analysis is valid provided that the relative gains agree to within 10% and is used here to provide a quantitative insight into how radiometric and polarimetric signal-to-noise ratio depends on the signal and noise of the APS instrument.

With the assumption noted above the intensity is given by the expression,

$$I = S1L + S1R \quad 4.5.1-1$$

in which S1L and S1R are the measurements after dark count subtraction and the dark count effects on noise are included in the following analysis. Since the noise in the independent detectors that measure the orthogonal polarizations is uncorrelated the expected variance in intensity measurements is given by the expression

$$\langle \Delta I^2 \rangle = \langle \Delta S1L^2 \rangle + \langle \Delta S1R^2 \rangle \quad 4.5.1-2$$

The signal to noise ratio (SNR) for intensity measurements is therefore defined to be

$$SNR_I = \sqrt{\frac{\langle I \rangle^2}{\langle \Delta S1L^2 \rangle + \langle \Delta S1R^2 \rangle}} \quad 4.5.1-3$$

4.5.2. Q and U measurements

The variances of the Stokes parameters Q and U for APS measurements are given by the following expressions

$$\langle \Delta Q^2 \rangle = \langle \Delta S1L^2 \rangle + \langle \Delta S1R^2 \rangle \quad \text{and} \quad \langle \Delta U^2 \rangle = \langle \Delta S2L^2 \rangle + \langle \Delta S2R^2 \rangle \quad 4.5.2-1$$

where the same simplifying assumption regarding relative gain coefficients has been made (see section 4.4.2). The SNRs for these two parameters are therefore given by the equations

$$SNR_Q = \sqrt{\frac{\langle Q^2 \rangle}{\langle \Delta S1L^2 \rangle + \langle \Delta S1R^2 \rangle}} \quad \text{and} \quad SNR_U = \sqrt{\frac{\langle U^2 \rangle}{\langle \Delta S2L^2 \rangle + \langle \Delta S2R^2 \rangle}} \quad 4.5.2-2$$

These equations can be written in the alternative form

$$SNR_Q = q \times SNR_I \quad \text{and} \quad SNR_U = u \times SNR_I \quad 4.5.2-3$$

where q (=Q/I) and u (=U/I) are the relative Stokes parameters. The formula 4.5.2-3 provides a simple link between the usual SNR formula and the SNR for the Stokes parameters Q and U.

4.5.3. Relative q (=Q/I) and u(=U/I) measurements

The normalized Stokes parameter q (=Q/I), with the same simplifying assumption regarding relative gain coefficients, is given by the expression

$$q = \frac{S1L - S1R}{S1L + S1R} = \frac{1 - r}{1 + r} \quad 4.5.2-1$$

where $r = S1R/S1L$ and the inverse of this relationship is

$$r = \frac{1 - q}{1 + q} \quad 4.5.3-2$$

The variation of q as a function S1L and S1R is therefore given by the equation

$$\Delta q = \frac{\partial q}{\partial S1L} \Delta S1L + \frac{\partial q}{\partial S1R} \Delta S1R \quad 4.5.3-3$$

where the partial derivatives are given by the expressions

$$\frac{\partial q}{\partial S1L} = \frac{2S1R}{(S1L + S1R)^2} = \frac{2}{I} \times \frac{S1R}{S1L + S1R} = \frac{1 - q}{I}$$

and

$$\frac{\partial q}{\partial S1R} = \frac{-2S1L}{(S1L + S1R)^2} = \frac{-2}{I} \times \frac{S1L}{S1L + S1R} = -\frac{(1+q)}{I} \quad 4.5.3-4$$

Since the noise in the independent detectors that measure the orthogonal polarizations is uncorrelated, the expected variance in intensity measurements is given by the expression

$$\langle \Delta q^2 \rangle = (1-q)^2 \frac{\langle \Delta S1L^2 \rangle}{I^2} + (1+q)^2 \frac{\langle \Delta S1R^2 \rangle}{I^2} \quad 4.5.3-5$$

The variance of u is given by a similar formula

$$\langle \Delta u^2 \rangle = (1-u)^2 \frac{\langle \Delta S2L^2 \rangle}{I^2} + (1+u)^2 \frac{\langle \Delta S2R^2 \rangle}{I^2} \quad 4.5.3-6$$

4.6. Field of View

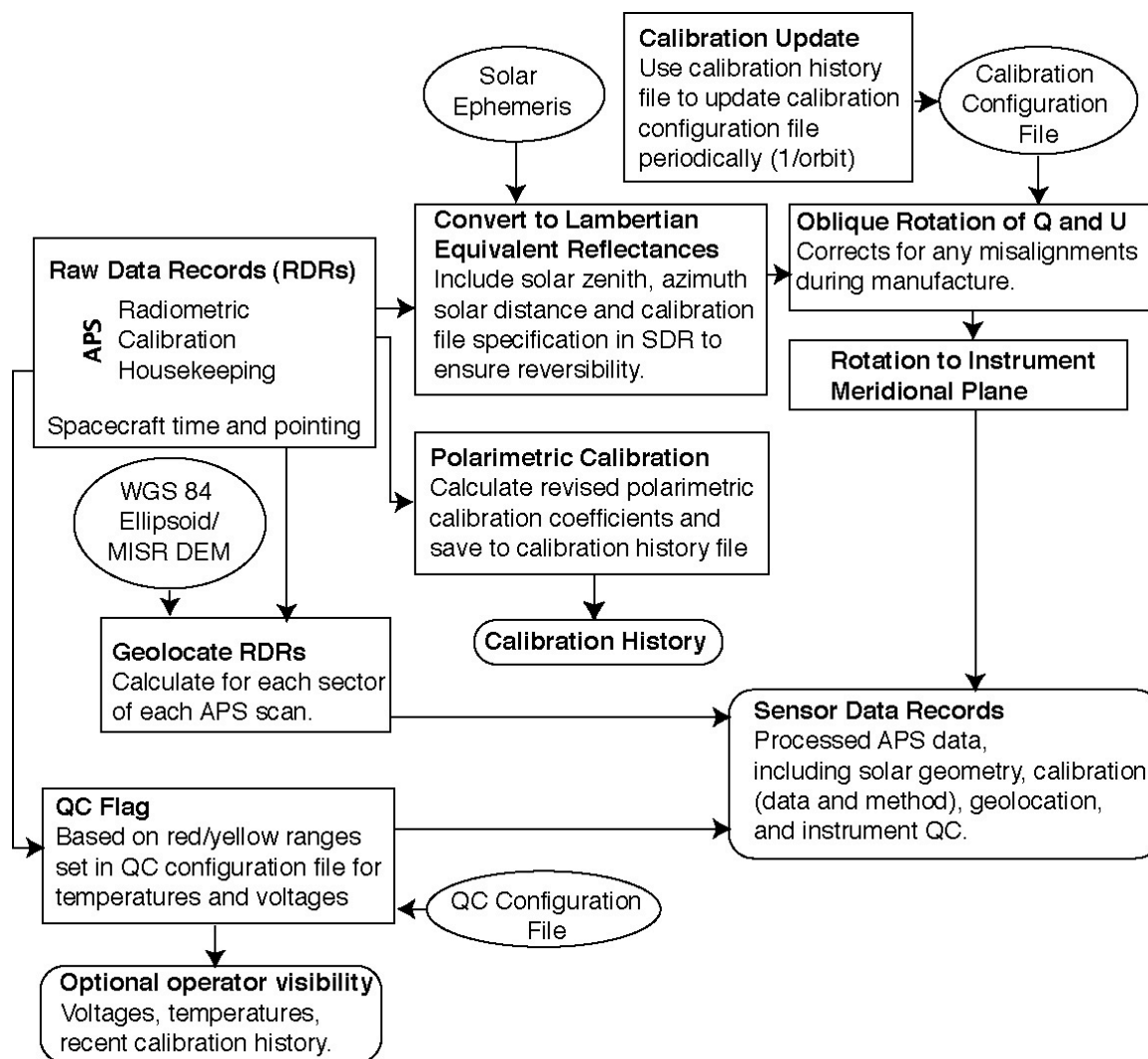
The instrument instantaneous field of view (IFOV) is 9 milliradians. This corresponds to a horizontal cell size (at nadir) of 7.5 km. This IFOV represents a balance between providing a small enough IFOV so that cloud contamination of scenes is reduced and having a large enough IFOV that instrument signal-to-noise ratio is adequate.

5. SDR (RDR to SDR) ALGORITHM DESCRIPTION

The principal data that are processed in the RDR to SDR algorithm are the raw data from the APS instrument. Operations that will be required to convert this data to the calibrated Stokes parameters I, Q and U that are the SDRs required to produce the APS EDRs are described in this section.

5.1. Processing Outline

An outline of the steps involved in processing the RDRs to SDRs is provided in figure 5.1-1. This figure shows operations as rectangular boxes, input files as ellipses and output files as rectangles with rounded corners.



5.1.1. Near Real-Time Processing

Sequential APS data processing:

1. Quality Control (QC): Convert the housekeeping data to physical units and check against set of yellow and red limits developed during APS instrument testing. Generate QC flags based on these tests as an indicator of instrument health.
2. Dark correction: Use mean of measured post DC-restore dark count values that are measured every scan (pre- and post- DC restore values available). Spread of post DC-restore dark counts and a comparison of pre- and post-DC restore values will also be used as instrument health indicators.
3. Relative calibration: Use current set of relative gain coefficients K1, K2 and C12 from Calibration Configuration file to convert quantities corrected for dark count to quantities corrected for relative gain in pairs of channels measuring orthogonal polarization elements.

4. Absolute radiometric calibration: Use current set of radiometric calibration coefficients from Calibration Configuration file to convert quantities corrected for relative calibration to radiometrically calibrated Stokes vector elements.
5. Absolute polarimetric scale: Use current set of polarimetric scale coefficients α_Q and α_U from Calibration Configuration file to correct scale of radiometrically calibrated Stokes vector elements Q and U .
6. Redundancy: Set redundant processing flag if a single channel of the two measuring Q , or U in a single band has failed. If this flag is set the following two rotations operations are not performed, but are instead applied to the synthetic data used in the EDR algorithm. This flag is used also used by the EDR algorithm to determine the appropriate measurement uncertainty to be used in the measurement covariance matrix. The final absolute reflectance calculation is still performed.
7. Correction for Wollaston orientation errors: Use current set of Wollaston prism orientation angles from Calibration Configuration file to perform an oblique rotation on Q and U such that they are correctly oriented with respect to one another and the instrument plane for the nadir view.
8. Rotation to standard reference plane: The rotation is proportional to the scan angle and is caused by the scan mirror assembly. It is removed by a simple geometric rotation of Q and U .
9. Absolute reflectance calibration: Use current set of spectrally integrated solar constant values for each APS band from Calibration Configuration together with solar zenith and solar distance from earth to calculate the Lambertian equivalent (polarized) reflectance for each Stokes vector element. This step is performed here at the end the processing sequence because it is the only step that requires external data input. Thus, its placement in this position allows the following two parallel ancillary data processing processes the maximum time to complete before their data is expected to be valid in order to perform this processing step.

Parallel ancillary data processing:

1. Geo-locate each IFOV sample to its location at the ground. Fixed external inputs are the WGS 84 ellipsoid and the digital elevation model (DEM) developed to process MISR data. Varying external inputs are the spacecraft ephemeris (location in earth centered co-ordinates, spacecraft orientation and time).
2. Calculate solar zenith angle at ground location of IFOV sample and solar distance from earth. Fixed external inputs are constants in astronomical ephemeris model which are included in program header file and are not expected to change. Varying external input are the IFOV location at the ground and the time. (Note: Solar distance from Earth will only be calculated once per orbit.)

5.1.2. Offline Processing

1. Relative calibration: The relative gain coefficients $K1$ and $K2$ are measured on every scan for each band using the OPC-Primary. The relative gain coefficient $C12$ is estimated on every scan for each band from scene data (see section 4.3.2) except when a channel fails when this coefficient is determined using the OPC-Primary (see section 4.3.3). Summary statistics (arithmetic mean, geometric mean, standard deviation and logarithmic standard deviation) are calculated for each orbit and are

saved in a separate Relative Calibration History. The coefficients in the Calibration Configuration file are updated using the geometric mean value. Change in the relative gain coefficients exceeding 0.2% per orbit are noted for further investigation by an operator.

2. Absolute radiometric calibration: The absolute radiometric calibration coefficients are evaluated once each month using measurements of the onboard radiometric calibrator (ORC) that is described in section 4.3.2.1. The radiometric calibration coefficients are saved in a Radiometric Calibration History and are used to update the Calibration Configuration file.
3. Absolute polarimetric scale: The polarimetric scale factor for each band is measured every scan using the OPC-Secondary. Summary statistics (arithmetic mean, geometric mean, standard deviation and logarithmic standard deviation) are calculated for each orbit and are saved in a separate Polarimetric Calibration History. The coefficients in the Calibration Configuration file are updated using the geometric mean value. Change in the polarimetric scale factor exceeding 0.2% per orbit are noted for further investigation by an operator.
4. Correction for Wollaston orientation errors: Data is taken for the sectors where the ORC is viewed for the entire day of the onboard radiometric calibration process. These view angles scan through the limb of the Earth and can be used post-launch to check for any drift in Wollaston orientation errors because scattering with this viewing geometry is dominated by Rayleigh scattering.

Periodic checking of the Radiometric and Polarimetric Calibration History is performed by a module of the EDR algorithm (Section 6.8) which controls any revisions to the Calibration Configuration file. This is done since the use of “soft” calibration will be implemented in the EDR algorithms to provide a check on radiometric calibration. In order to have a single point of control for the Calibration Configuration file it is therefore natural to allocate the merging and revision of all calibration coefficients into this module.

5.2. Algorithm Inputs

In this section we describe the APS data and non-APS data that is required as input to the SDR algorithm.

5.2.1. APS Data

As described in Section 3, the Aerosol Polarimetry Sensor (APS) makes four measurements to analyze the linear polarization state of the incident radiation in each spectral band at each view angle (sector). This measurement approach uses identical paired optical assemblies that are designated as “telescopes” for brevity. One telescope (labeled 1) in each pair makes simultaneous measurements of the linearly-polarized intensity at azimuths of 0° and 90° with respect to the APS meridional plane of the scan, while the other telescope (labeled 2) simultaneously measures equivalent intensities at 45° and 135°. These raw measurements are designated as R1L, R1R, R2L and R2R, respectively. The proposed APS design provides measurements in nine spectral bands and thus a sector data record consists of nine sets of these four measurements, i.e., from 36 signal channels. During the DC-restoration period each of

the 36 signal channels are DC-restored simultaneously to dark reference levels while the scanner views into a dark cavity. Following DC-restoration of the channels, measurement data are collected and stored while sequentially viewing: the dark reference cavity for pre-scene (post DC-restoration) dark reference samples designated as D1L, D1R, D2L and D2R; the secondary onboard polarimetric calibrator (OPC-Secondary); the scene over an angular swath of 120° (-55° to $+65^\circ$ about nadir); the primary onboard polarimetric calibrator (OPC-Primary); and the dark reference cavity for post-scene (pre-DC restoration for the next scan) dark reference samples designated as P1L, P1R, P2L and P2R.

5.2.2. Non-APS Data

The non-APS data required for construction of SDRs from APS RDRs is limited to spacecraft ephemeris, data sets required for geo-location and solar spectral irradiance as described below.

5.2.2.1. Spacecraft Ephemeris

The required spacecraft ephemeris includes spacecraft location, a time stamp for that location and the spacecraft orientation. These values are required for the geo-location of the APS data and for calculation of solar ephemeris. The solar ephemeris is necessary for conversion of APS radiometric measurements to reflectance values and for analysis of the APS SDRs to EDRs. In order to accurately locate the APS footprint in the surface of the earth the root mean square of the uncertainties in pointing in all three axes of the spacecraft should be less than 1 mrad. Synchronization of APS measurements with VIIRS is not required, since the higher resolution of VIIRS means that adequate timing knowledge of APS data acquisition can be used to identify VIIRS pixels that are within, or adjacent to an APS footprint. The threshold requirement on timing knowledge for APS data provided by the spacecraft is therefore ± 0.05 seconds, with an objective of ± 0.01 seconds. The threshold timing requirement corresponds to spacecraft location knowledge of approximately ± 350 m and the objective is for spacecraft location knowledge ± 70 m.

5.2.2.2. Surface Ellipsoid/Digital Elevation Model

Geo-location of the APS data uses the satellite ephemeris, the WGS 84 ellipsoid and the digital elevation model (DEM) developed to process MISR data to locate each APS IFOV at the surface of the earth.

5.3. Theoretical Description

1. Quality Control (QC): The measurements from temperature sensors are converted to temperature units and the logic and power measurements are converted to voltages.
2. Dark correction: Nine dark reference samples are collected and the mean value for each signal channel is used as the measurement of the dark offset (designated as D1Lm, D1Rm, D2Lm and D2Rm).
3. Relative calibration: There are two types of relative calibration coefficients required to transform dark-corrected measurements into the elements of the Stokes vector. The first is intra-telescope relative responsivity calibration, which is monitored during each scan using the primary onboard polarimetric calibrator, OPC-Primary. This

provides two calibration coefficients, K1 and K2 for each spectral band. K1 is a measure of the relative responsivity of the detector channels in telescope 1, while K2 is the equivalent for detector channels in telescope 2. The second is inter-telescope relative responsivity calibration that can be monitored using scene data. This provides a calibration coefficient, C12, which is a measure of the relative responsivity of the detector channels in telescopes 1 and 2.

4. Absolute radiometric calibration: This is a scaling of the observed dark, and relative gain corrected quantities to a traceable radiometric scale and is effected using the calibration coefficient C0. Thus, intensities are related to the original measurements by the following expressions

$$I(0) = C0 \times (R1L - D1Lm) \quad 5.3-1$$

$$I(90) = C0 \times K1 \times (R1R - D1Rm) \quad 5.3-2$$

$$I(45) = C0 \times C12 \times (R2L - D2Lm) \quad 5.3-3$$

$$I(135) = C0 \times C12 \times K1 \times (R2R - D2Rm) \quad 5.3-4$$

5. Absolute polarimetric scale: Use current set of polarimetric scale coefficients α_Q and α_U from Calibration Configuration file to correct scale of radiometrically calibrated Stokes vector elements Q and U. If instrumental polarization has been characterized as being present in the APS instrument prior to launch it is corrected as part of this step: q_{inst} and u_{inst} are the instrumental polarization coefficients in the telescopes measuring Q and U respectively.
6. Correction for Wollaston orientation errors: The angularly separated beams produced by a Wollaston prism are polarized orthogonally as a result of its material properties. However, the Wollaston prisms may not be perfectly aligned and the polarization azimuths at which measurements are made may therefore be at $0^\circ + \varepsilon_1$, $90^\circ + \varepsilon_1$, $45^\circ + \varepsilon_2$ and $135^\circ + \varepsilon_2$ where ε_1 and ε_2 are alignment errors. Provided these errors are characterized and are stable, there is no effect on the accuracy of the determination of the Stokes vector elements, but a further transformation between the RDRs and the calibrated measurements is required. This transformation can be derived from the following expression

$$I(\beta) = \frac{[I + Q \cos(2\beta) + U \sin(2\beta)]}{2} \quad 5.3-5$$

for the intensity observed after radiation has been analyzed by a polarizer in the plane β , where the circular polarization has been neglected since it is negligible for most naturally illuminated scenes (see section 4). By adding and subtracting the pairs of measurements made in each telescope, the following relationships between the measurements and the Stokes vector elements are obtained

$$I(0 + \varepsilon_1) + I(90 + \varepsilon_1) = I \quad 5.3-6$$

$$I(45 + \varepsilon_2) + I(135 + \varepsilon_2) = I$$

$$\begin{pmatrix} \alpha_Q(\Delta_1 - q_{inst}I) \\ \alpha_U(\Delta_2 - u_{inst}I) \end{pmatrix} = \begin{pmatrix} \alpha_Q[(I(0 + \varepsilon_1) - I(90 + \varepsilon_1)) - q_{inst}I] \\ \alpha_U[(I(45 + \varepsilon_2) - I(135 + \varepsilon_2)) - u_{inst}I] \end{pmatrix} = \begin{pmatrix} \cos 2\varepsilon_1 & \sin 2\varepsilon_1 \\ -\sin 2\varepsilon_2 & \cos 2\varepsilon_2 \end{pmatrix} \begin{pmatrix} Q' \\ U' \end{pmatrix} \quad 5.3-7$$

where the Stokes vector elements Q' and U' can be obtained by inverting the error matrix. This transformation is the same for all view angles and the operational use of

the polarimetric scale coefficients α_Q and α_U and the instrumental polarization coefficients q_{inst} and u_{inst} to obtain correct values of Q and U is demonstrated.

7. Rotation to standard reference plane: The Stokes vector elements Q' and U' are measured with respect to a reference plane that rotates with the rotation being proportional to the scan angle measured with respect to nadir. This rotation is caused by the scan mirror assembly, but is entirely reversible and predictable. The Stokes vector elements Q and U in a fixed meridional plane defined by the APS scan plane are obtained by a view angle dependent rotation of Q' and U' viz.,

$$\begin{pmatrix} Q \\ U \end{pmatrix} = \begin{pmatrix} \cos(2\theta + \varphi) & \sin(2\theta + \varphi) \\ -\sin(2\theta + \varphi) & \cos(2\theta + \varphi) \end{pmatrix} \begin{pmatrix} Q' \\ U' \end{pmatrix} \quad 5.3-8$$

where φ is determined from the expected orientation of the planes of polarization of the Wollaston prisms and is 45° in the case of the RSP instrument. Any errors have already been compensated in step 6.

8. Absolute reflectance calibration: This step requires the spectrally integrated solar constant values for each APS band, F_0 , from the Calibration Configuration file together with the solar zenith angle θ_0 and solar distance from the earth SD in AU. The radiances I , Q and U are converted to reflectances using the equation

$$\begin{pmatrix} R_I \\ R_Q \\ R_U \end{pmatrix} = \frac{\pi SD^2}{\cos(\theta_0) F_0} \begin{pmatrix} I \\ Q \\ U \end{pmatrix} \quad 5.3-9$$

5.4. Evaluation and Testing

The evaluation and testing of the SDR algorithm is straightforward since it simply implements the conversion of the raw data into calibrated Stokes vector elements I , Q and U . Once the APS instruments have been tested and calibrated a simple independent test is used to determine whether the SDR algorithm is being implemented correctly. The test uses a piece of glass in transmission, and reflection, that is mounted on a rotation stage so as to provide a source with varying magnitude and orientation of polarization.

5.5. Practical Considerations

The SDR algorithm is implemented using straightforward algebraic operations and no issues with regard to speed of the relatively few multiplication and additions that are required is expected. Precision of calculation must be adequate to maintain the instrumental precision, but with careful design the use of single precision floating point arithmetic will be adequate. It is noted that many current and planned computers use hardware for which double precision is the natural representation and so compiler flags will be used so as to allow the use of double precision arithmetic when the hardware platform indicates that it is appropriate.

5.6. SDR Algorithm Development Schedule

The basic operations required of the SDR algorithm already exist and represent less than a hundred source lines of code. Implementation of exception handling and geo-location will be additional tasks that will require implementing and the input and output modules will need to be redesigned to reflect the requirements implemented through the software interface control documents (ICD). It is expected that a complete version of the SDR algorithm will be available at time of the Preliminary Design Review, with any further modifications being determined by any updates to the ICDs and consequent changes to the data structure provided by the flight software.

6. EDR (SDR to EDR) ALGORITHM DESCRIPTION

The principal data that will be processed in the SDR to EDR algorithm is the calibrated (polarized) radiance data that are contained in the SDRs produced by the SDR algorithm. Operations that will be required to analyze this data into the APS aerosol and cloud EDRs are described in this section.

All the processes described in this section will use similar data transformations and so these transformations and the reasons for using them are presented here. First we repeat the equation defining the measurement process

$$\mathbf{y} = f(\mathbf{x}, \mathbf{b}) + \varepsilon \quad 6-1$$

that was introduced in Section 3. f can be any function of the measurements, or simply the measurements themselves. It has generally been found advantageous in the analysis of intensity data to use a logarithmic transformation, f , of the measurements viz.,

$$\ln \mathbf{y} = \ln [I(\mathbf{x}, \mathbf{b}) + \varepsilon] \quad 6-2$$

For measurements with useful SNR this equation can be approximated by

$$\ln \mathbf{y} = \ln [f(\mathbf{x}, \mathbf{b})] + \frac{\varepsilon}{I(\mathbf{x}, \mathbf{b})} \quad 6-3$$

If we now include the effect of calibration on the intensity measurements through the calibration constant c which has an expected value of unity and standard deviation determined by the calibration so that the underlying radiance $f'(\mathbf{x}, \mathbf{b})$ is related to a noise free measurement process $f(\mathbf{x}, \mathbf{b})$ by the expression

$$f(\mathbf{x}, \mathbf{b}) = cf'(\mathbf{x}, \mathbf{b}) \quad 6-4$$

The combined uncertainties in $\ln \mathbf{y}$ can then be written as

$$\ln \mathbf{y} = \ln [f'(\mathbf{x}, \mathbf{b})] + \ln c + \frac{\varepsilon}{I(\mathbf{x}, \mathbf{b})} \quad 6-5$$

where, since it is a scale coefficient, the natural distribution of c is log normal (Jaynes 1968) so the difference between the log of the measurements and the log of the true underlying radiance is well modeled by a log normal distribution. Although the probability distribution of the calibration coefficient is the most important statistical reason for using a log-normal probability distribution practical experience also indicates that this transformation is appropriate for the analysis of intensity measurements (Dubovik and King 2000).

A logarithmic transformation is not appropriate for the analysis for the relative Stokes parameters q and u , since they can be negative. Although the use of a complex number for the log of q and u could be used, an analysis of the sources of uncertainty in q and u suggests the use of a z-transformation. This transformation is typically used in the analysis of correlation coefficients that also lie on the interval $(-1,1)$ similar to q and u . There are three elements to the calculation of these relative Stokes vector elements, the dark count subtraction, the relative gain coefficient and the polarimetric scale factor. We shall ignore the effects of uncertainty in the dark count determination since this is a small random effect. In the following analysis we are concentrating on the accuracy with which the polarization can be determined for a given accuracy in the determination of the relative gain coefficients and the polarimetric scale factor and an appropriate variance stabilizing transformation for comparing measurements with observations that takes these uncertainties into account. The equation used to construct the normalized Stokes parameter q is:

$$q = \alpha_Q \left(\frac{S1L - K1 \times S1R}{S1L + K1 \times S1R} \right) \quad 6-6$$

where S1L and S1R are the dark corrected instrument digital numbers (DN) for a given band, K1 is the relative gain coefficient between the two detectors sensing orthogonal polarizations and α_Q is the polarimetric scale factor that corrects for any small depolarization, or optical cross-talk effects.

As a result of uncertainties in the relative gain coefficient and the polarimetric scale factor there are uncertainties in the determination of the relative Stokes parameter q . Since both the relative gain coefficient K1 and the polarimetric scale factor α_Q are scale parameters it is appropriate to assume that their probability distribution functions are log normal (Jaynes 1968). This means that the probability distribution function for the Stokes parameter q is given by the expression

$$p(q | \hat{q}) = N \int_0^\infty \exp \left\{ - \frac{\left[\ln \left(\frac{1 - \alpha_Q \hat{q}}{1 + \alpha_Q \hat{q}} \right) - \ln \left(\frac{1 - q}{1 + q} \right) \right]^2}{2\sigma_K^2} \right\} \exp \left[- \frac{(\ln \alpha_Q)^2}{2\sigma_\alpha^2} \right] d\alpha_Q \quad 6-6$$

The z-transformations, z_q and z_u are defined by the expression

$$\begin{aligned} z_q &= \ln \left(\frac{1 - q}{1 + q} \right) \\ z_u &= \ln \left(\frac{1 - u}{1 + u} \right) \end{aligned} \quad 6-7$$

and these variables are used in the analysis of APS measurements of q and u over the ocean.

Over land because the surface reflectance is quite uncertain while the surface polarized reflectance is much better known, the APS algorithm will use the measurements of Q and U in the retrieval of EDR parameters not q and u . A logarithmic transformation is

not applied to Q and U since these parameters are not constrained to be positive. Such a transformation could be used if necessary by extending the variable into the complex plane and would provide a straightforward means of identifying the influence of zero crossings on the APS EDR retrievals, but at present, given the additional programming and mathematical complexity and lack of any obvious benefits, the use of such a transformation is not regarded as necessary.

6.1. Processing Outline

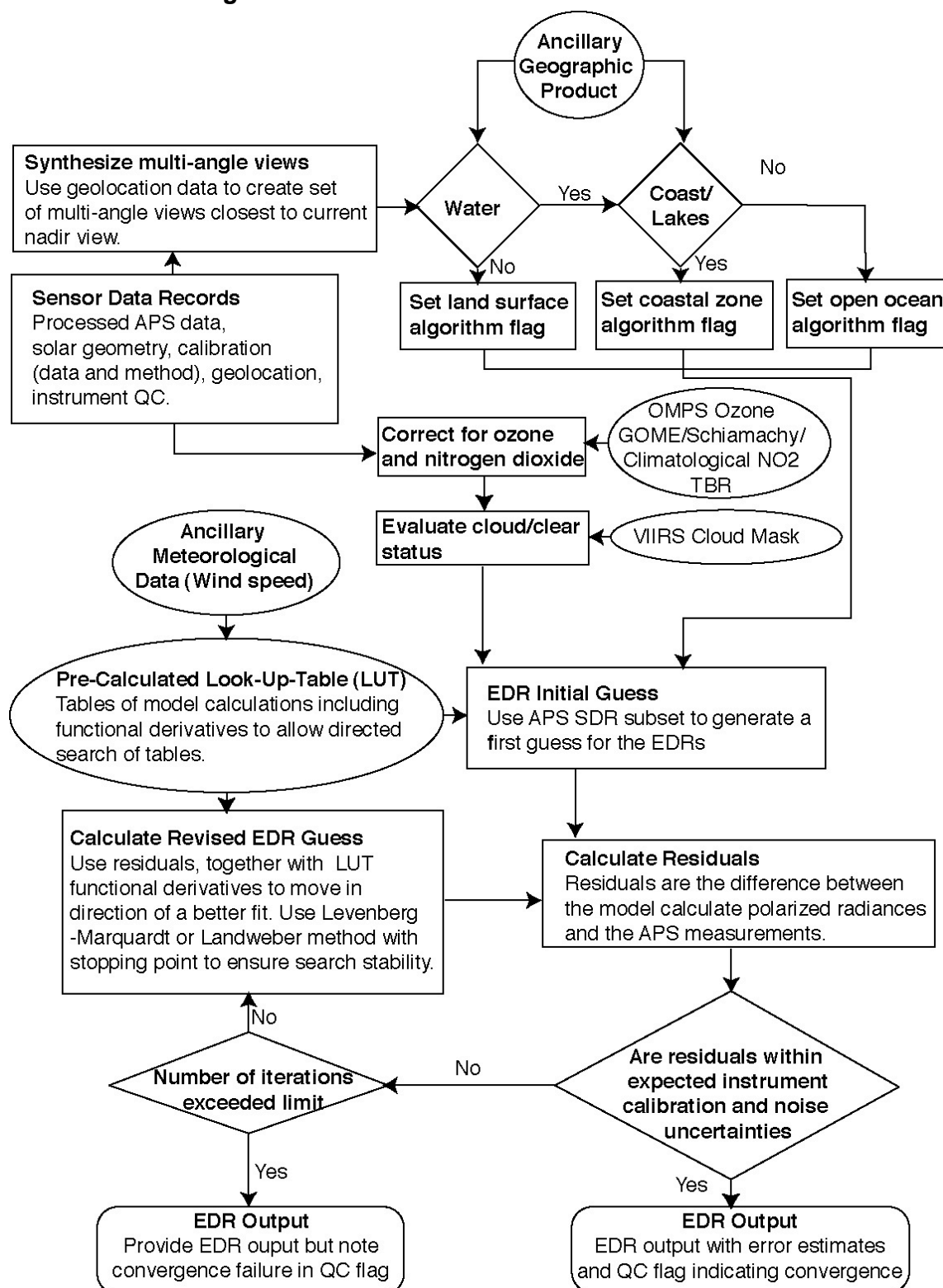


Figure 6.1-1 Flow of algorithmic tasks required to process SDRs to EDRs

In Figure 6-1 the data flow for the planned algorithmic approach for converting the SDRs to aerosol and cloud EDRs is shown. Key elements of the processing approach are discussed in this section together with the mathematical implementation, while unique details of the implementation of the aerosol and cloud EDR algorithms are outlined in succeeding sections.

1. As the spacecraft flies overhead, the along track scanning APS instrument sees the same surface location from different directions during successive scans. The scene-level data for the APS EDR algorithm is created by providing all the APS measurements that view the same surface location from different angles during an orbit. The view angles that match the ground location of the nadir view can be found using a simple view angle dependent time-offset from the nadir view acquisition time. Any small corrections to the predicted time-offset that may be caused by satellite orientation variations can be corrected by searching the immediate vicinity and using the IFOV geo-location information to find the APS scan that is physically closest to the nadir for a given view angle.
2. Use the location of the nadir pixel to check the type of underlying surface to set switch for lower boundary condition (i.e. select which look-up table [LUT] will be used). This process uses an ancillary geographic product that is one of the elements in the VIIRS clouds mask. A backup source for this information is the land surface type database used in the processing of MODIS data that is of a higher spatial resolution than is required for APS data processing.
3. Correct radiances for stratospheric gaseous absorption by ozone and nitrogen dioxide. The location of the majority of ozone and nitrogen dioxide above much of the molecular and aerosol scattering in the atmosphere means that it is possible to correct the observed (polarized) reflectances for this source of extinction and use these corrected reflectance values in the EDR algorithms. This correction is implemented using the following expression

$$\begin{pmatrix} R'_I \\ R'_Q \\ R'_U \end{pmatrix} = \exp(\tau_{O_3} M_{O_3} + \tau_{NO_2} M_{NO_2}) \begin{pmatrix} R_I \\ R_Q \\ R_U \end{pmatrix} \quad 6.1-1$$

where the primed quantities are the reflectances from the SDR algorithm that have been corrected for stratospheric gaseous absorption. The airmass factors are given by the following expressions

$$M = \frac{\int_{P_1} \int_{P_2} m(\xi_V \mathbf{s}_V + \xi_0 \mathbf{s}_0) d\xi_V d\xi_0}{\int_P m(\xi \mathbf{z}) d\xi} \quad 6.1-2$$

where m is the density distribution of the absorber, \mathbf{s}_V and \mathbf{s}_0 are unit direction vectors for the view and solar angles respectively, \mathbf{z} is the unit vector in the vertical direction, P_1 is the downward path from sun to surface, P_2 is the upward path from surface to satellite and P is a vertical path. For view and solar zenith angles that are less than 60° this expression has the usual form

$$M = \frac{1}{\mu_0} + \frac{1}{\mu_V} \quad 6.1-3$$

The more general form of 6.1-2 is necessary for larger view and solar zenith angles because of the spherical geometry of the earth and the consequent effect that the altitude distribution of the absorbers has on the path length that the solar beam follows. The equations defining the optical depths are

$$\begin{aligned} \tau_{O_3} &= \bar{k}_{O_3} X_{O_3} \\ \tau_{NO_2} &= \bar{k}_{NO_2} X_{NO_2} \end{aligned} \quad 6.1-4$$

with X being the absorber amount. The band averaged absorption coefficients \bar{k} are evaluated with an appropriate climatological temperature profile and integrated over the spectral response of the APS instrument viz.,

$$\bar{k} = \frac{\int r(\lambda) F_0(\lambda) k(\lambda) d\lambda}{\int r(\lambda) F_0(\lambda) d\lambda} \quad 6.1-5$$

where $r(\lambda)$ is the instrument spectral response and $F_0(\lambda)$ is the exo-atmospheric solar irradiance.

This simple correction is not valid in the event of a volcanic eruption that injects large amounts of aerosol into the stratosphere. In this event the aerosol and cloud EDR algorithms use LUTs that are parameterized by stratospheric aerosol optical depth, size distribution and amounts of the gaseous absorbers ozone and nitrogen dioxide. That is, a particular LUT table that matches the stratospheric conditions is selected for the subsequent estimation of the tropospheric aerosol and cloud EDRs. The retrieval of stratospheric aerosol conditions using APS measurements is described in Section 6.7.

4. Select ocean, or land surface processing.
5. Evaluate cloud contamination likelihood using VIIRS clouds mask and APS measurements.
6. Estimate water vapor amount (Section 6.6).
7. Make initial guess of aerosol, or cloud model.
8. Search look up tables (LUTs) for best fit. We repeat here the relevant equations from section 3 that are used to implement the search for a best fit. The next step in the iterative search for the EDR product is given by the equation

$$\mathbf{x}^{(i+1)} = \mathbf{x}^{(i)} - [\mathbf{H}(\mathbf{x}^{(i)}) + \gamma \mathbf{I}]^{-1} \nabla_{\mathbf{x}} \Phi(\mathbf{x}^{(i)}) \quad 6.1-6$$

where the terms in this equation are defined as follows:

$$\nabla_{\mathbf{x}} \Phi(\mathbf{x}) = \mathbf{C}_a^{-1} (\mathbf{x} - \mathbf{x}_a) + \mathbf{K}^T \mathbf{C}_T^{-1} (\mathbf{y} - \mathbf{f}(\mathbf{x})) \quad 6.1-7$$

$$\mathbf{K} = \frac{\partial \mathbf{f}(\mathbf{x})}{\partial \mathbf{x}} \quad 6.1-8$$

$$\mathbf{H}(\mathbf{x}) = \nabla_{\mathbf{x}}^2 \Phi(\mathbf{x}) \approx \mathbf{C}_a^{-1} + \mathbf{K}^T \mathbf{C}_T^{-1} \mathbf{K} \quad 6.1-9$$

It is therefore necessary to have the functional derivatives \mathbf{K} included in the LUTs both to implement this search and also to interpolate between tabulated values of \mathbf{x} . The LUTs are stored as one set for coarse and one set for fine mode aerosols. This approach makes the required size of the tables substantially smaller. This does

have accuracy implications, since interactions between coarse and fine mode aerosols are not being properly accounted for. Appropriate mixing rules must therefore be used to combine the (polarized) radiances from the two sets of tables (Abdou *et al.* 1997). The scheme for adjusting γ as the iteration proceeds is described in Section 3. The use of the log of the EDR parameters is not required in the algorithm since any positivity constraints are enforced by the use of appropriate numerical methods (Stoer 1971).

9. The iteration process must be stopped at a suitable point which prevents (i) over-running the iteration, resulting in time-wasting computational effort, and (ii) under-running the iteration and therefore not converging on an answer lying within a negligible difference from the optimal solution. A practical convergence test is to stop the iteration when the difference between the last two iterates of the state vector are smaller than a pre-defined set of tolerances, ϵ_j , i.e. $|x_j^{(i)} - x_j^{(i+1)}| < \epsilon_j$. An upper limit on the number of iterations must also be set to prevent the algorithm running away.
10. Make a radiative transfer calculation for the final value of \mathbf{x} obtained using the LUTs and use this to calculate a refinement to the aerosol model. This step is designed to correct the model retrieved from the LUTs for any inaccuracies in using separate tables for coarse and fine mode. As such, this step is implemented as an optional final processing step that is performed if there is sufficient processing time available. The EDR retrieval has a set of QC flags, one of which indicates whether this final processing step occurred.

6.2. Algorithm Input

The APS EDR algorithms use look-up tables (LUTs) that are pre-calculated and are required inputs to the algorithm. These tables need to be built before the algorithm is used and are constructed using the radiative transfer methods described in Section 3. The correction of absorption by stratospheric gases requires the absorption coefficients for ozone and nitrogen dioxide integrated over the APS spectral bandpasses with appropriate climatological vertical profiles and temperatures. The imposition of a smooth prior probability on the spectral variation of the refractive index requires specification of the spectral slope and its covariance.

6.2.1. APS Data

The required APS data is the calibrated and geo-located Stokes parameters I, Q and U in all the spectral bands, 410, 488, 555, 670, 865, 910, 1378, 1610 and 2250 nm.

6.2.2. Non-APS Data

The following data is required in the processing of APS SDR data to EDR products:

- VIIRS cloud mask is required for the particular scene being viewed and VIIRS near nadir radiances for periodic radiance histogram comparisons. VIIRS is a cross-track scanner and so the highest view angle forward view of the APS will see a point near the satellite ground track approximately 170 seconds before the nadir view sees the same location. Similarly the highest view angle backward view will see a point near the satellite ground track approximately 170 seconds after the nadir view sees the same location. The VIIRS clouds mask will

therefore be supplemented by analysis of APS data, particularly for the higher view angles for which APS and VIIRS data will not be simultaneous.

- OMPS ozone column and GOME2 nitrogen dioxide column are required but there are no timing, or synchronization requirements on this data since their column amounts are dominated by the stratospheric contribution which has relatively slow time scales and large spatial scales for variations relevant to the APS products. If these products are not available then they can be replaced by climatological values since the required accuracy to meet the EDR requirements on optical depth with a margin of 50% is that the ozone column amount is known to ± 50 DU and the nitrogen dioxide product is known to within ± 0.5 ppbv.
- NCEP wind speed data products are required in order to determine the lower boundary condition over oceans, i.e., specular reflectance due to sun glint and diffuse reflectance due to ocean foam. This product is desirable to simplify the EDR algorithm, but in general the APS data can itself be used to determine wind speed when the wind speed is high enough that an estimate is required. This estimate is made by evaluating the reflectance and polarization measurements at 2250 nm in the angular range where the sunglint is predicted to be for a range of wind speeds using a Cox-Munk model of Fresnel reflectance by the ocean. The best fit is then used as an estimate for wind speed. Under many viewing geometries the sunglint will not be visible at all for low wind speeds, however under these viewing conditions knowledge of wind speed is not required since the contributions of foam and glint to the observed polarized radiances are negligible.

6.3. APS Cloud Mask Generation

The APS cloud mask will use the VIIRS cloud mask to evaluate the presence of sub-pixel cloud in the APS IFOV. Similar tests to those used by VIIRS will also be evaluated using the APS measurements to determine cloud mask consistency between the two instruments. These cloud mask tests will be supplemented by an evaluation of the APS radiances and polarization for the extreme view angles which are acquired with the greatest time difference from the VIIRS data and angular smoothness tests to evaluate whether cloud contaminates some of the APS view angles.

1. APS measurements at 1378 nm are sensitive to thin cirrus clouds and if a scene has an increased radiance in this band it is identified as being contaminated by cirrus clouds. Extreme view angles are particularly sensitive to thin cirrus because of the long pathlength which enhances the cloud signature and reduces the surface contribution.
2. Measurements at 410 nm are relatively stable over both land and ocean and are not typically significantly reduced by anything other than clouds, or snow and ice. Threshold tests of
 - a. the magnitude of the degree of linear polarization at 410 nm
 - b. the magnitude of the radiance at 410 nm
 - c. angular smoothness of the degree of linear polarization at 410 nm
 - d. angular smoothness of the radiance at 410 nm

will therefore serve as a general test for the presence of clouds. This threshold will be adjusted for viewing geometry using calculations for a cloud and aerosol free atmosphere.

3. Over snow and ice the radiance in the 1610 nm band will be used to test for the presence of clouds because snow albedo is very low in this band.
4. When the cloud tests at 410 and 1610 nm and the VIIRS cloud tests all indicate the absence of clouds other than thin cirrus clouds the pixel is regarded as only having cirrus clouds, stratospheric aerosols. The angular variation of the 1378 nm measurements is then tested to determine whether stratospheric aerosols (small spherical particles), or ice particles (large non-spherical particles) are the principal contributor to the observed radiance and polarization signature.
 - a. If the particles are identified as spherical a stratospheric aerosol retrieval is attempted, Section 6.7.
 - b. If the particles are identified as non-spherical and the radiance at 1378 nm is sufficiently low the cloud mask estimates an optical depth and ice-crystal phase function that is consistent with these measurements and that is then used in the path radiance corrections of thin cirrus clouds described in section 6.4.2.

Each cloud detection test returns a confidence level that the pixel is clear ranging in value from 1 (high confidence clear) to 0 (low confidence) clear. A final mask is determined as the product of the results from the APS specific test, the APS VIIRS-type tests and the VIIRS cloud mask tests themselves. This final mask is classified into categories, confident clear, probably clear, probably cloudy and confident cloudy.

6.4. Aerosol EDR Implementation

Two sets of tables are required for aerosol EDR processing, one for ocean retrievals and one for retrievals over land. The tables are calculated using Mie-Lorentz theory for spherical particles and T-matrix for shape-size mixtures of nonspherical particles (Mishchenko *et al.* 2000). The initial retrieval uses only spherical particles.

The tables for the ocean retrievals have an ocean surface that is roughened depending on the windspeed (Cox and Munk 1954) and parameterized ocean upwelling radiance calculations (Section 3.4.3). The Chlorophyll concentration on which this parameterization is based is estimated as part of the EDR retrieval (Section 7.2).

The tables for land retrievals use a black Lambertian surface.

The basis for aerosol retrievals over ocean is that the ocean system reflectance can be well modeled if wind speed and Chlorophyll concentration are known. The wind speed can be estimated from APS measurements when required (Section 6.2) and the Chlorophyll concentration is included in the retrieved state vector.

The basis for aerosol retrievals over land is the observation that the land surface polarized reflectance is grey and that the observations at 2250 nm can therefore be used to estimate the surface polarized reflectance in all spectral bands. If a model of

surface polarization is used it is a parametric model (Section 3.4.4) estimated from the 2250 nm APS measurements. A simple model for the reflectance of the atmosphere-surface system is

$$\mathbf{R}_{tot}(\lambda) = \mathbf{R}_{atm}(\lambda) + T(\lambda)\mathbf{R}_{surf}(\lambda) \quad 6.4-1$$

where we are neglecting multiple reflections between the surface and atmosphere, $\mathbf{R}_{tot}(\lambda)$ is the total reflectance observed at the top of the atmosphere, $\mathbf{R}_{atm}(\lambda)$ is the polarized reflectance for an atmosphere above a black surface and $\mathbf{R}_{surf}(\lambda)$ is the surface polarized reflectance. The initial estimate of $\mathbf{R}_{surf}(\lambda)$ is $\mathbf{R}_{tot}(2250)$. In subsequent processing steps a modified estimate that is corrected for aerosols effects viz.,

$$\mathbf{R}_{surf}(\lambda) = \frac{\mathbf{R}_{tot}(2250) - \mathbf{R}_{atm}(2250)}{T(2250)} \quad 6.4-2$$

is used.

The fact that the surface can be well characterized, for both ocean and land, allows the contribution to the observed signal from the atmosphere to be accurately estimated. It is this atmospheric signal that provides the information which is used in the aerosol EDR retrieval.

The starting point for initializing the search for the aerosol EDRs in both cases uses a short wavelength (865 nm for oceans and 670 nm for land surfaces) to estimate the fine mode aerosol EDRs and a long wavelength (2250 nm for oceans and 1610 nm for land surfaces) to estimate the coarse mode aerosol EDRs. The search for a best fit model then continues as described in Section 6.1 using all spectral bands.

Identification of non-spherical particles is based on an analysis of the residual errors between the observations and EDR retrieved polarized radiances both for successful retrievals and also when a retrieval fails to converge to within the required tolerances. We have determined (Cairns et al. 1998) that it is possible to match the angular distribution of radiances scattered by non-spherical particles using strongly absorbing spherical particles. It is not possible to simultaneously match the polarized radiances, nor is it possible to match the polarized radiances when the fitting procedure emphasizes this measurement. Thus, when residual errors between the observations and EDR retrieved polarized radiances are greater than expected based on APS sensor calibration and noise characteristics the aerosol is classified as non spherical.

When the aerosols are identified as non-spherical the aerosol EDR retrieval is then continued using a shape-size distribution of nonspherical particles as one mode of the aerosol size distribution and spherical particles as the other mode.

6.4.1. Confident Clear Sky

Under clear skies no special processing, or operations are performed.

6.4.2. Cirrus Contamination

An aerosol retrieval is attempted when thin cirrus contamination is identified using the 1378 nm APS band, provided the estimated cirrus optical depth is less than 0.1 and that

the only cloud test that has identified the cloud as being present uses the 1378 nm measurements. The aerosol retrieval is attempted using radiances that are corrected for the cirrus path radiance. This correction is performed using a single scattering approximation for the effects of cirrus cloud to simplify the correction process and maintain processing speed. For higher cirrus optical depths only a cloud EDR retrieval is performed. The exact cirrus optical depth below which this path radiance correction will be used will be resolved using data that was acquired with the RSP instrument during the IHOP and CRYSTAL-FACE field experiments. This data has provided a preliminary indication of the capability to retrieve bimodal aerosol properties below thin cirrus clouds.

6.4.3. Probably Clear Sky

When the cloud mask estimate is that the sky is probably clear the standard aerosol EDR retrieval is performed. If no convergence is reached, or the goodness of fit between the observations and model is unacceptable (χ^2 statistic does not satisfy the 95% confidence interval) we allow for a fractional filling of cloud. This fractional filling of cloud estimate uses the cloud EDR tables and is implemented similarly to the cloud EDR retrievals, but effectively uses the residual radiances from the initial aerosol EDR retrieval.

6.5. Cloud EDR Production

Four sets of look-up tables are required for cloud EDR processing, two for ocean retrievals for low optical depth clouds and two for retrievals over ocean and land that are calculated for all optical depths. Each pair of tables consists of one set of calculations for water clouds and one set of calculations for ice clouds. The tables are calculated using Mie-Lorentz theory for spherical water cloud particles and T-matrix and geometrical ray tracing for shape-size mixtures of ice crystal particles (Mishchenko *et al.* 2000).

The tables for the low cloud optical depth ocean retrievals have an ocean surface that is roughened depending on the windspeed (Cox and Munk 1954). This lower boundary condition is only calculated for cloud optical depths less than 5. For higher optical depths all retrievals use the same set of look-up tables for which the lower boundary condition is a black Lambertian surface.

The following approach is used to provide a good starting point in the cloud EDR iterative retrieval.

1. The starting point for initializing the search for the cloud EDRs uses a pair of nadir radiances (670 nm and 865 nm over ocean, 410 and 678 nm over land) to estimate the cloud optical depth (assumes 10 μm effective radius liquid water cloud).
2. If the optical depth estimate is less than 5 then the 1378 nm band and polarized reflectances in the vicinity of the rainbow, if available, (from bands at 678 nm over land and 865 nm over ocean) are initially used to determine cloud phase.
3. If the optical depth estimate is greater than 5 then the ratio of reflectances at 1610 and 2250 nm and polarized reflectances in the vicinity of the rainbow are used to determine cloud phase (ice clouds are darker at 1610 nm than at 2250 nm with the converse being true for water clouds).

4. Once cloud phase has been estimated a set of nadir radiances (410, 678, 1610 and 2250 nm over land and 865, 1610 and 2250 nm over ocean) are used to provide a revised estimate of optical depth and effective radius as the starting point for the iterative retrieval (Nakajima and King 1990).
5. If the 1378 nm band indicates the presence of a thin cirrus cloud (i.e. angular signature of ice – no rainbow), but the cloud phase estimates from the other tests indicate the presence of liquid water clouds then the cloud EDR retrieval is attempted using radiances that are corrected for the cirrus path radiance. This correction is performed using a single scattering approximation for the effects of cirrus cloud to simplify the correction process and maintain processing speed.

Once a starting point and cloud phase has been established the algorithm iterates as outlined in Section 6.1 using the spectral bands at 410, 678, 1610 and 2250 nm over land and 865, 1610 and 2250 nm over ocean. For clouds with an optical depth less than 5.0 the log of the radiances and the polarized radiances will be used in the clouds retrievals. For clouds with an optical depth greater than 5.0 the log of the radiances and the z-transformed parameters z_q and z_u will be used in the cloud retrievals. Over snow and ice the retrieval will be restricted to the use of measurements at 1610 and 2250 nm because the snow and ice albedoes are low in these bands.

6.5.1. Cloudy Sky

Under cloudy skies no special processing, or operations are performed.

6.5.2. Probably Cloudy Sky

When the cloud mask estimate is that the sky is probably clear the standard cloud EDR retrieval is performed. If no convergence is reached, or the goodness of fit between the observations and model is unacceptable (χ^2 statistic does not satisfy the 95% confidence interval) we allow for a fractional filling of aerosol. This fractional filling of aerosol estimate uses the aerosol EDR tables and is implemented similarly to the aerosol EDR retrievals, but effectively uses the residual radiances from the initial cloud EDR retrieval.

6.6. Water Vapor Estimation

The APS estimate of water vapor uses two spectral bands one of which has water vapor absorption, 910 nm and one of which does not, 865 nm. The transmission functions for these two bands are given by the expressions

$$T(865) = \exp[-M\tau(865)] \quad 6.6-1$$

and

$$T(910) = T_w(Mu) \times \exp[-M\tau(910)] \quad 6.6-2$$

Using the simple model of reflectance from the atmosphere-surface system, equation 6.4-1, if the surface is bright then the surface contribution to the reflectance dominates and the ratio of the 910 to 865 nm reflectance is given approximately by the expression

$$\frac{R_{tot}(910)}{R_{tot}(865)} \approx T_w(Mu) \times \exp\{-M[\tau(910) - \tau(865)]\} \frac{R_{surf}(910)}{R_{surf}(865)} \quad 6.6-3$$

Provided the spectral variation in aerosol optical depth and surface albedo are not too great the ratio of the 910 to 865 nm reflectance provides an estimate of the water vapor transmission function. This water vapor transmission is tabulated as a function of water vapor amount and a simple one dimensional tabular search with linear interpolation is used to provide an initial estimate of the water vapor amount. This initial water vapor amount estimate only uses reflectance measurements.

It should be noted that the spectral variation of surface albedo for snow, vegetation and soil tends to cause biases in this water vapor estimate if the pixel is clear (Gao and Goetz 1990). This is not the case for clouds and so if the pixel is cloudy this estimate is the final one generated and it is used in the subsequent iteration of the cloud EDR processing. If the pixel is clear then the initial aerosol EDR retrieval is used to determine the polarized reflectance ratio including the effects of the surface (using 2250 nm polarized reflectance), aerosol and atmospheric polarized reflectance. The ratio of polarized reflectance at 910 to 865 nm is then tabulated as a function of water vapor amount and a simple one dimensional tabular search used to determine the observed water vapor amount. This revised water vapor amount estimate is then used in the subsequent iteration of the aerosol EDR processing. This estimate reduces the uncertainties in the water vapor estimate caused by surface spectral reflectance variations because the surface polarized reflectance tends to be grey. Over the clear skies over the ocean the estimate water vapor estimate will be noisy, unless there is sunglint present, because the reflectance and polarized reflectance in the 910 nm are very low as the aerosols are being used as the source of reflectance.

6.7. Stratospheric Aerosols

Stratospheric aerosol retrievals are performed based on the results of the cloud mask. This retrieval uses only the 1378 nm APS measurements in order to limit the contamination of the retrieval by tropospheric aerosols, or low level thin/broken clouds. The retrieval uses climatological water vapor profiles with the aerosols located in a vertical layer (that varies with latitude) in the lower stratosphere. This layer is located based on the retrievals of the vertical distribution of stratospheric aerosol optical depth from SAGE measurements during the Pinatubo eruption. The retrieval is of optical depth, effective radius, effective variance and refractive index for a mono-modal aerosol. The refractive index retrieval is included for generality and to allow the retrieval to behave reasonably when retrieving PSC properties,

6.8. Calibration Analysis and Synthesis

The use of “soft” calibration to provide a continuous check on the ORC is based on using the radiometric calibration of each channel as one of the retrieved state vector elements over the ocean with an appropriate prior probability distribution reflecting how recently the ORC and/or vicarious calibrations have been performed. The current estimate of the radiometric calibration coefficient is used as the estimated prior value of this state vector element. The radiometric calibration coefficient will be updated monthly based on ORC measurements, unless the “soft” calibration evaluation exceeds a 3% deviation from that expected based on the ORC with 90% confidence. Tracking trends in this divergence provides a tool for evaluating radiometric gain changes between ORC

calibrations and bootstrapping the radiometric calibration to the in-flight polarimetric calibration process. This process also provides a cross check of the Spectralon diffuser stability that is independent of the VIIRS radiance histogram comparison and VIIRS lamp stability. The calibration analysis and synthesis module of the EDR algorithm will also analyse the Radiometric and Polarimetric calibration history files and control the update and revision of the Calibration Configuration file.

6.9. *Evaluation and Testing*

Pre-launch evaluation and testing activities will include further development of the algorithms and verification over a wide range of surface types that will allow us to better characterize retrieval uncertainties. The pre-launch algorithm validation objectives will be accomplished principally by conducting ground-based measurements coordinated with further overflights of the aircraft simulator instruments and by analyzing existing data. These data sets include acquisitions at the DoE's ARM SGP CART site in Oklahoma and during the ferry trip between Santa Barbara, CA and Oklahoma, during the CLAMS field experiment and during the ferry trip between Santa Barbara and NASA Wallops Flight Facility and during the CRYSTAL-FACE field experiment and during the ferry trip between Mojave and Key West. The SGP site has a well characterized surface and extensive ground-based instrumentation, while the ferry trip includes data over the highly inhomogeneous surface of the Los Angeles area as well as farmlands and deserts. The CLAMS data set demonstrated the ability of APS-like measurements to provide good estimates of single-scattering albedo, optical depth and aerosol vertical extent under conditions of high aerosol loading. The CRYSTAL-FACE data set provides the first data set for which high accuracy multispectral polarimetric measurements of cirrus clouds have been made and the first measurement of aerosols from high altitude (58 kft) using the Proteus aircraft platform.

6.10. *Practical Considerations*

The use of input-output modules that are separate from the science code itself is designed to insulate the science code from the burdens of the production environment and provide a single code unit where changes in interface definitions external to the code, or data structures internal to the code can be captured and controlled.

The APS EDR algorithms will be developed on a Unix cluster and will make use of parallel processing where feasible. This processing will be structured so as not to prevent the use of the algorithm on a single processor machine.

Error exception handling will be implemented to identify and capture the existence of missing input data files, programming errors, instrument status anomalies, system failure (I/O failure, disk space full etc.) and user errors (user set-up prevents normal execution).

6.11. EDR Algorithm Development Schedule

The EDR algorithm schedule shows the following development of the SDRLs which constitute the ATBD, the algorithm performance specification and the algorithm software and its required documentation.

Table 6.11-1. Schedule of status of the APS EDR SDRL documents.

Document/Code	Status			
	Skeleton	Initial	Preliminary (PDR)	Final (Prior to CDR)
SDRL 020		1/17/2003	5/1/2004	7/30/2004
SDRL 021	4/30/2003	10/30/2003	5/1/2004	10/30/2004
SDRL 022a, b		10/30/2003	5/1/2004	1/31/2005
SDRL 023a, b	7/31/2003	1/31/2004	5/1/2004	4/30/2005

7. RETRIEVAL CHARACTERIZATION AND ERROR ANALYSIS

In this section we discuss the sensitivity of the retrieval to the true state and how the various error sources are propagated into the retrieved product. In Section 3.5 we presented an analysis in which both uncertainties in model parameters and uncertainties in the forward model were integrated over under the assumption that the uncertainties in these properties were included in the statistical optimization procedure. This may not always be done in practice, particularly in the case of errors in the forward model which may themselves be highly dependent on the state vector \mathbf{x} . Those model parameters and model errors that are not used in the statistical optimization of the estimate of \mathbf{x} do nonetheless contribute to uncertainties, or errors in the retrieval.

One set of model parameters that do properly belong in the set of prior probabilities over which we integrate is the set of instrument calibration coefficients. This approach ensures that the correct covariance structure of the calibration of the APS instrument measurements is used in the statistically optimum estimate of \mathbf{x} . It is important that this structure be used in the estimation process because both relative angular calibration and relative spectral calibration of APS measurements are much more accurate than the absolute radiometric calibration of the sensor.

A useful separation of the retrieval error, which is the difference between the true underlying state \mathbf{x} and its estimate, into its different terms is the expression

$$\begin{aligned}
 \hat{\mathbf{x}} - \mathbf{x} = & (\mathbf{A} - \mathbf{I})(\mathbf{x} - \mathbf{x}_a) \quad \dots \text{smoothing error} \\
 & + \mathbf{D}_y \frac{d\mathbf{f}(\mathbf{x}, \mathbf{b})}{d\mathbf{b}} (\mathbf{b} - \hat{\mathbf{b}}) \quad \dots \text{model parameter error} \\
 & + \mathbf{D}_y \Delta \mathbf{f}(\mathbf{x}, \mathbf{b}) \quad \dots \text{forward model error} \\
 & + \mathbf{D}_y \varepsilon_y \quad \dots \text{retrieval noise}
 \end{aligned} \tag{7-1}$$

that is used commonly used in atmospheric sounding. In this expression the contribution function that is defined to be

$$\mathbf{D}_y = \frac{\partial \hat{\mathbf{x}}}{\partial \mathbf{y}} = \left(\mathbf{C}_a^{-1} + \mathbf{K}^T \mathbf{C}_T^{-1} \mathbf{K} \right)^{-1} \mathbf{K}^T \mathbf{C}_T^{-1} \tag{7-2}$$

and the averaging kernel matrix

$$\mathbf{A} = \frac{\partial \hat{\mathbf{x}}}{\partial \mathbf{x}} = \left(\mathbf{C}_a^{-1} + \mathbf{K}^T \mathbf{C}_T^{-1} \mathbf{K} \right)^{-1} \mathbf{K}^T \mathbf{C}_T^{-1} \mathbf{K} \quad 7-3$$

are introduced. Both of these expressions can be derived by differentiating expression 3.5-10. In these expressions the total covariance of the measurement \mathbf{y} includes the effects of calibration, but we are now excluding forward model errors and model parameter uncertainties, other than calibration from the the search for a statistically optimum EDR retrieval. In this case the total covariance matrix is given by the expression

$$\mathbf{C}_T = \mathbf{C}_\varepsilon + \frac{d\mathbf{f}(\mathbf{x}, \mathbf{b})}{d\mathbf{b}_{cal}}^T \mathbf{C}_{b_{cal}} \frac{d\mathbf{f}(\mathbf{x}, \mathbf{b})}{d\mathbf{b}_{cal}} \quad 7-4$$

The solution covariance is then given by the sum of the error covariance matrices and can be written as

$$\mathbf{C}_x = \left[\mathbf{C}_a^{-1} + \mathbf{K}^T \left(\mathbf{C}_\varepsilon + \frac{d\mathbf{f}(\mathbf{x}, \mathbf{b})}{d\mathbf{b}_{cal}}^T \mathbf{C}_{b_{cal}} \frac{d\mathbf{f}(\mathbf{x}, \mathbf{b})}{d\mathbf{b}_{cal}} \right)^{-1} \mathbf{K} \right]^{-1} + \mathbf{D}_y \mathbf{C}_{\Delta t}^{-1} \mathbf{D}_y^T \quad 7-5$$

where the first term is the uncertainty caused by the prior, the second is caused by measurement error (precision) the third is caused by instrument calibration uncertainty (accuracy) and the fourth term (which may have parameter uncertainties other than calibration lumped in it) is the uncertainty due to the algorithm. The covariance matrix of the measurement errors is diagonal with the magnitude of the elements determined from calculations of the APS instrument signal and noise. The calibration covariance matrix is not diagonal and has a structure of the form

$$\mathbf{C}_\theta = \begin{pmatrix} 1 & \rho_\theta & \rho_\theta^2 & \rho_\theta^3 \\ \rho_\theta & 1 & \rho_\theta & \rho_\theta^2 \\ \rho_\theta^2 & \rho_\theta & 1 & \rho_\theta \\ \rho_\theta^3 & \rho_\theta^2 & \rho_\theta & 1 \end{pmatrix} \quad 7-6$$

with 194x194 elements for multiple angle measurements in a single spectral band and a covariance matrix of the form

$$\frac{d\mathbf{f}(\mathbf{x}, \mathbf{b})}{d\mathbf{b}_{cal}}^T \mathbf{C}_{b_{cal}} \frac{d\mathbf{f}(\mathbf{x}, \mathbf{b})}{d\mathbf{b}_{cal}} = \mathbf{C}_{cal} = \begin{pmatrix} \mathbf{C}_\theta & \rho_\lambda \mathbf{C}_\theta & \rho_\lambda^2 \mathbf{C}_\theta \\ \rho_\lambda \mathbf{C}_\theta & \mathbf{C}_\theta & \rho_\lambda \mathbf{C}_\theta \\ \rho_\lambda^2 \mathbf{C}_\theta & \rho_\lambda \mathbf{C}_\theta & \mathbf{C}_\theta \end{pmatrix} \quad 7-7$$

for the combination of multiple spectral bands and multiple angles. It is important that the correlations in the calibration accuracy of the sequential APS view-angle and of the sequential APS spectral bands is used in the estimate of \mathbf{x} to ensure that those combinations of measurements that are most accurate are correctly weighted in the retrieval process. In the next section we present the results of some calculations of the error covariance matrix of \mathbf{x} for the accuracy and precision of the APS instrument based on expression 7-5. No forward model errors are included in this analysis, but a discussion of some potential forward model errors and mitigations is presented in Section 7.2. It should be noted that the strong coupling between EDR retrievals means that any retrieval characterization and error analysis that treats the EDRs separately to establish a performance margin is not valid.

A strawman error budget allocation of EDR accuracy and precision between instrument and algorithm was 50% to each. In the following sections it is apparent that the predicted APS instrument performance allows EDR accuracy and precision requirements to be met with some margin. It is therefore expected that the principal source of uncertainty in EDR products will be caused by uncertainties in the algorithm. Specifically fractional cloud coverage of APS pixels that is not well approximated by the fractional mixing approach used in the algorithm, incorrect modeling of surface properties and forward model approximations that are required to meet the Algorithm Performance Specification of EDR production latency which is 20 minutes.

7.1. Accuracy and Precision

Calculations were performed for a set of realistic bimodal aerosol distributions and the corresponding accuracy and precision for each model were calculated. It was assumed for this analysis that absorption was only present in the fine mode aerosol. This assumption was made since it is probably the case that in real observations there will be a third “very fine” mode of soot particles the effects of which will have to be included in the APS fine mode EDR single scattering albedo. It is therefore particularly important to understand the accuracy and precision of single scattering albedo retrievals for the fine mode. In the tables below a single value is presented for the accuracy and precision of the optical depth at a reference wavelength of 550 nm since the retrieval of a detailed specification of the particle size distribution allows the spectral variation of optical depth at all APS sensor wavelengths to be determined. A single value is also presented for the accuracy and precision of the refractive indices of the fine and coarse modes and the single scattering albedo. This is done since the spectral smoothness of these parameters imposed by their prior probability distribution means that the dominant form of uncertainty in the retrievals of these parameters is in their overall magnitude. A final parameter for which the accuracy and precision are determined is the fraction of the particles that are in the coarse mode since this parameter effectively determines the optical depth accuracy and precision for the longest APS wavelengths (1610 and 2250 nm).

Table 7.1-1 Spectral refractive indices used in model calculations of accuracy and precision.

	Wavelength of APS band						
Mode	410	488	555	670	865	1610	2250
Fine	1.46	1.44	1.43	1.42	1.41	1.40	1.39
Coarse	1.41	1.41	1.39	1.39	1.39	1.39	1.39

The parameters of five models used to evaluate the accuracy and precision of APS aerosol EDR retrievals are presented in Table 7.1-2. These analyses allow the effects of coupling between the retrieval of the EDR parameters to be evaluated, but do not explore the full range of EDR parameters. The results presented here provide a sample for which the signal magnitudes are representative of the type of conditions expected in practice, i.e. the optical depth range is from 0.1 to 0.5, that represent the most difficult conditions for the APS instrument. The retrieval of aerosol EDRs under higher aerosol

optical depth loads is less subject to measurement precision errors since the signal is higher and forward modeling errors since the surface contribution is smaller. The observation geometry used in the analyses assumes a relative solar azimuth angle of 90° and a solar zenith angle of 45° this provides a conservative estimate of the APS measurement sensitivity to aerosols since the scattering angle range is minimum for this geometry.

Table 7.1-2 Model parameters used in the accuracy and precision calculations.

Model Parameter							
Model	τ_{550}	$r_{\text{eff, fine}}$	$V_{\text{eff, fine}}$	$r_{\text{eff, coarse}}$	$V_{\text{eff, coarse}}$	ϖ	f_{coarse}
A	0.3	0.2	0.2	1.0	1.0	0.9	0.1
B	0.1	0.2	0.2	1.0	1.0	0.9	0.05
C	0.1	0.1	0.2	1.0	1.0	0.9	0.05
D	0.1	0.2	0.2	1.0	1.0	0.9	0.1
E	0.5	0.2	0.2	1.0	1.0	0.9	0.1

7.1.1. Aerosol EDR Accuracy

Using APS predicted instrument performance the accuracy of all EDR retrievals except the refractive index of the fine mode for model C meets threshold performance requirements. The reason for this is that small particles ($r_{\text{eff, fine}}=0.1 \mu\text{m}$) have similar scattering characteristics to Rayleigh scatterers and so the sensitivity of APS measurements to refractive index for these small particles is reduced. This reduced sensitivity is inherent in polarimetric measurements with a shortest wavelength measurement of 400 nm, or greater. Other analyses of RSP data (not shown) have found adequate sensitivity to refractive index for particles larger than 0.15 μm . Although this one EDR retrieval fails to meet threshold accuracy requirements it should be emphasized that most other parameters are retrieved with accuracies that meet the EDR objective performance requirements. In this analysis all the APS data is used simultaneously and the correlations between measurement accuracies imply a 1% relative radiometric calibration accuracy for a single band across the angular range for which scene data is being obtained and 0.5% relative spectral radiometric calibration accuracy between spectral bands.

Table 7.1.1-1. Accuracy of APS EDR retrievals for a range of aerosol models using predicted APS radiometric (5%) and polarimetric (0.2-0.5%) accuracy.

Ocean									
Model	τ_{550}	$r_{\text{eff, fine}}$	$V_{\text{eff, fine}}$	$r_{\text{eff, coarse}}$	$V_{\text{eff, coarse}}$	$m_{\text{eff, fine}}$	$m_{\text{eff, coarse}}$	ϖ	f_{coarse}
A	2.15E-03	1.17E-03	7.96E-03	6.13E-03	4.04E-02	4.33E-03	1.17E-03	5.86E-03	9.71E-03
B	1.28E-03	1.32E-03	1.18E-02	5.40E-03	4.52E-02	5.71E-03	1.31E-03	1.08E-02	5.56E-03
C	2.06E-03	1.55E-02	4.44E-03	9.25E-02	2.36E-02	6.68E-02	6.96E-04	1.45E-02	2.59E-02
D	1.16E-03	1.77E-03	9.49E-03	8.20E-03	4.39E-02	7.35E-03	1.05E-03	9.50E-03	1.13E-02
E	3.28E-03	1.17E-03	7.57E-03	6.06E-03	4.46E-02	3.99E-03	1.28E-03	4.83E-03	1.00E-02
Land									
Model	τ_{550}	$r_{\text{eff, fine}}$	$V_{\text{eff, fine}}$	$r_{\text{eff, coarse}}$	$V_{\text{eff, coarse}}$	$m_{\text{eff, fine}}$	$m_{\text{eff, coarse}}$	ϖ	f_{coarse}
A	1.98E-03	1.54E-03	4.17E-02	6.22E-03	1.23E-01	2.68E-03	2.82E-03	1.79E-03	1.59E-02

B	1.80E-03	2.92E-03	1.66E-01	1.14E-02	4.54E-01	4.85E-03	1.16E-02	5.73E-03	3.40E-02
C	2.22E-03	9.54E-03	4.05E-02	5.65E-02	1.73E-01	4.89E-02	3.80E-03	1.09E-02	1.84E-02
D	1.80E-03	3.86E-03	1.05E-01	1.45E-02	2.92E-01	6.35E-03	7.17E-03	4.86E-03	4.15E-02
E	2.22E-03	1.06E-03	2.96E-02	4.81E-03	9.34E-02	1.98E-03	1.97E-03	1.18E-03	1.13E-02

Using APS predicted instrument performance for polarimetric accuracy and a degraded radiometric accuracy of 5% all EDR retrievals except the refractive index of the fine mode for model C again meet threshold performance requirements. The reduced radiometric accuracy is indicative of the expected radiometric accuracy of the APS instrument if flying without VIIRS for radiometric calibration cross checks. In this analysis all the APS data is used simultaneously and the correlations between measurement accuracies imply a 1% relative radiometric calibration accuracy for a single band across the angular range for which scene data is being obtained and 0.5% relative spectral radiometric calibration accuracy between spectral bands.

Table 7.1.1-2. Accuracy of APS EDR retrievals for a range of aerosol models using reduced APS radiometric accuracy (5%) and predicted polarimetric (0.2-0.5%) accuracy.

Ocean									
Model	τ_{550}	$r_{\text{eff, fine}}$	$V_{\text{eff, fine}}$	$r_{\text{eff, coarse}}$	$V_{\text{eff, coarse}}$	$m_{\text{eff, fine}}$	$m_{\text{eff, coarse}}$	ϖ	f_{coarse}
A	5.35E-03	2.93E-03	1.99E-02	1.53E-02	1.01E-01	1.08E-02	2.92E-03	1.46E-02	2.43E-02
B	3.19E-03	3.28E-03	2.95E-02	1.35E-02	1.13E-01	1.42E-02	3.26E-03	2.70E-02	1.39E-02
C	5.13E-03	3.86E-02	1.11E-02	2.31E-01	5.89E-02	1.66E-01	1.74E-03	3.61E-02	6.46E-02
D	2.90E-03	4.40E-03	2.37E-02	2.05E-02	1.10E-01	1.83E-02	2.61E-03	2.37E-02	2.83E-02
E	8.16E-03	2.91E-03	1.89E-02	1.51E-02	1.11E-01	9.96E-03	3.19E-03	1.20E-02	2.50E-02
Land									
Model	τ_{550}	$r_{\text{eff, fine}}$	$V_{\text{eff, fine}}$	$r_{\text{eff, coarse}}$	$V_{\text{eff, coarse}}$	$m_{\text{eff, fine}}$	$m_{\text{eff, coarse}}$	ϖ	f_{coarse}
A	2.83E-03	2.20E-03	5.96E-02	8.89E-03	1.76E-01	3.82E-03	4.03E-03	2.55E-03	2.27E-02
B	2.58E-03	4.17E-03	2.37E-01	1.63E-02	6.48E-01	6.92E-03	1.66E-02	8.19E-03	4.86E-02
C	3.17E-03	1.36E-02	5.79E-02	8.08E-02	2.47E-01	6.99E-02	5.43E-03	1.56E-02	2.63E-02
D	2.58E-03	5.52E-03	1.50E-01	2.07E-02	4.17E-01	9.07E-03	1.02E-02	6.94E-03	5.92E-02
E	3.17E-03	1.51E-03	4.23E-02	6.87E-03	1.33E-01	2.83E-03	2.82E-03	1.69E-03	1.62E-02

7.1.2. Aerosol EDR Precision

Using APS predicted instrument performance the precision of all EDR retrievals meets threshold performance requirements. It should be emphasized that all the APS data is used simultaneously in the retrieval process and that the precision using any single channel is less than that presented here.

Table 7.1.2-2. Precision with APS predicted signal and noise.

Ocean									
Model	τ_{550}	$r_{\text{eff, fine}}$	$V_{\text{eff, fine}}$	$r_{\text{eff, coarse}}$	$V_{\text{eff, coarse}}$	$m_{\text{eff, fine}}$	$m_{\text{eff, coarse}}$	ϖ	f_{coarse}
A	2.52E-04	5.14E-04	4.91E-03	1.57E-03	1.54E-02	5.01E-04	3.20E-04	1.44E-04	2.98E-03
B	2.50E-04	1.11E-03	2.14E-02	3.24E-03	6.55E-02	1.09E-03	1.38E-03	4.76E-04	6.68E-03
C	2.46E-04	1.34E-03	4.05E-03	1.64E-02	2.25E-02	4.42E-03	3.67E-04	1.64E-03	4.78E-03

D	2.34E-04	1.47E-03	1.35E-02	4.29E-03	4.28E-02	1.45E-03	8.72E-04	4.43E-04	8.48E-03
E	2.69E-04	3.09E-04	3.18E-03	1.05E-03	1.02E-02	3.02E-04	2.15E-04	8.50E-05	1.94E-03
Land									
Model	τ_{550}	$r_{\text{eff, fine}}$	$V_{\text{eff, fine}}$	$r_{\text{eff, coarse}}$	$V_{\text{eff, coarse}}$	$m_{\text{eff, fine}}$	$m_{\text{eff coarse}}$	ϖ	f_{coarse}
A	7.97E-04	1.40E-03	3.52E-02	4.83E-03	9.90E-02	1.49E-03	1.06E-03	6.01E-04	1.24E-02
B	6.97E-04	2.72E-03	1.37E-01	7.12E-03	3.29E-01	2.11E-03	4.20E-03	1.94E-03	2.53E-02
C	1.04E-03	4.12E-03	2.44E-02	3.12E-02	1.16E-01	1.75E-02	8.99E-04	4.77E-03	1.16E-02
D	6.69E-04	3.55E-03	8.36E-02	8.84E-03	2.10E-01	2.56E-03	2.49E-03	1.64E-03	2.98E-02
E	1.01E-03	8.68E-04	2.33E-02	4.10E-03	7.86E-02	1.27E-03	6.99E-04	3.52E-04	9.47E-03

Using APS predicted instrument noise performance and a signal strength reduced by a factor of 10 the precision of EDR retrievals over the ocean still generally meets threshold performance requirements. However it is clear from the precision of the coarse mode effective variance retrievals, precision greater than model values, that the retrieval of coarse mode aerosol over land would effectively be eliminated under these low signal condition. It should again be emphasized that all the APS data is used simultaneously in the retrieval process and that the precision using any single channel is less than that presented here.

Table 7.1.2-2. Precision with APS predicted noise and signal reduced by a factor of 10.

Ocean									
Model	τ_{550}	$r_{\text{eff, fine}}$	$V_{\text{eff, fine}}$	$r_{\text{eff, coarse}}$	$V_{\text{eff, coarse}}$	$m_{\text{eff, fine}}$	$m_{\text{eff coarse}}$	ϖ	f_{coarse}
A	2.31E-03	4.66E-03	4.46E-02	1.44E-02	1.37E-01	4.50E-03	2.96E-03	1.23E-03	2.57E-02
B	2.33E-03	1.04E-02	1.98E-01	3.05E-02	5.98E-01	1.01E-02	1.29E-02	4.22E-03	5.92E-02
C	2.17E-03	1.16E-02	3.81E-02	1.45E-01	2.05E-01	4.00E-02	3.46E-03	1.41E-02	4.19E-02
D	2.18E-03	1.37E-02	1.25E-01	4.03E-02	3.90E-01	1.33E-02	8.19E-03	3.93E-03	7.51E-02
E	2.42E-03	2.74E-03	2.83E-02	9.43E-03	9.01E-02	2.65E-03	1.96E-03	7.09E-04	1.64E-02
Land									
Model	τ_{550}	$r_{\text{eff, fine}}$	$V_{\text{eff, fine}}$	$r_{\text{eff, coarse}}$	$V_{\text{eff, coarse}}$	$m_{\text{eff, fine}}$	$m_{\text{eff coarse}}$	ϖ	f_{coarse}
A	7.16E-03	1.26E-02	3.15E-01	4.25E-02	8.79E-01	1.27E-02	9.41E-03	5.09E-03	1.10E-01
B	6.46E-03	2.51E-02	1.25E+00	6.51E-02	2.99E+00	1.83E-02	3.84E-02	1.69E-02	2.31E-01
C	9.11E-03	3.56E-02	2.36E-01	2.75E-01	1.09E+00	1.51E-01	8.62E-03	4.03E-02	1.05E-01
D	6.21E-03	3.27E-02	7.63E-01	8.09E-02	1.91E+00	2.22E-02	2.27E-02	1.44E-02	2.72E-01
E	8.82E-03	7.53E-03	2.02E-01	3.54E-02	6.85E-01	1.07E-02	6.07E-03	2.90E-03	8.24E-02

7.1.3. Cloud EDR Accuracy and Precision

Cloud accuracy and precision calculations were performed for water clouds with an optical depth at a reference wavelength of 550 nm of 20, effective radii of 5, 10 and 15 μm and for an effective variance of 0.1. This type of cloud with a narrow size distribution was regarded as the most severe test of whether the APS sensor can meet the cloud EDR accuracy and precision requirements. This is because of the nature of the specification of the requirements as a fraction of their value which means that for ice clouds, with very broad size distributions and large effective radii, the accuracy and precision required is not particularly burdensome. The observation geometry used in the analyses assumes a relative solar azimuth angle of 90° and a solar zenith angle of 45° this provides a conservative estimate of the APS measurement sensitivity to water

clouds since the scattering angle range is minimum for this geometry and does not transect the entire rainbow and glory scattering angle range.

Table 7.1.3-1. Accuracy and precision with APS predicted radiometric and polarimetric calibration accuracy and noise and signal levels.

Model	Accuracy		Precision	
	V_{eff}	$r_{\text{eff}} (\mu\text{m})$	V_{eff}	$r_{\text{eff}} (\mu\text{m})$
5 μm	0.004	0.04	0.00004	0.00012
10 μm	0.005	0.09	0.00014	0.00061
15 μm	0.008	0.12	0.00028	0.00077

Table 7.1.3-2. Accuracy and precision with APS radiometric calibration accuracy of 5% and polarimetric calibration accuracy of 5% with predicted noise levels and signal levels reduced by a factor of 10.

Model	Accuracy		Precision	
	V_{eff}	$r_{\text{eff}} (\mu\text{m})$	V_{eff}	$r_{\text{eff}} (\mu\text{m})$
5 μm	0.008	0.08	0.0003	0.0010
10 μm	0.012	0.18	0.0010	0.0047
15 μm	0.017	0.25	0.0020	0.0053

These tables indicate that the APS sensor will meet cloud EDR and accuracy requirements with considerable margin, even when sensor performance is degraded. This is not unexpected as the aerosol EDR requirements are much more stressing of the instrument measurements because the material that the scatterer is made of is unknown.

7.2. Forward Model Uncertainties – Ocean Surface

Accumulation-mode ($0.1 \mu\text{m} \leq r_{\text{eff}} \leq 1.0 \mu\text{m}$) aerosols have the largest potential of all aerosols to change the radiative budget of the atmosphere because of their large efficiency in the scattering of sunlight (“direct climate forcing”), and because of their role in the formation of cloud droplets (“indirect climate forcing”). Evaluating these climate forcings requires accurate retrievals of the size, shape distributions and complex refractive index of these particles (Hansen *et al.*, 1995). However, unlike coarse-mode aerosols ($r_{\text{eff}} > 1.0 \mu\text{m}$) which have sufficiently large size parameters $x_{\text{eff}} = 2\pi r_{\text{eff}}/\lambda$ to show scattering patterns in the near-infrared that vary with particle properties, accumulation-mode particles are often too small for near infrared reflectances ($x_{\text{eff}} \leq 1$) to differ much from Rayleigh scattering patterns (Mishchenko and Travis, 1997). Only in the visible part of the spectrum does light scattered by such small particles begin reveal sufficient information to retrieve useful information on in particular real refractive indices (Chowdhary *et al.*, 2002a). Another advantage of using visible wavelength observations to monitor accumulation mode aerosols is that their optical thickness becomes then sufficiently large to dominate that of coarse mode particles. In other words, except for extreme cases such as the transport of desert dust, one can then also ignore the scattering contribution of large particles.

Including visible wavelength observations to retrieve aerosols over the ocean poses a new challenge not encountered in near-infrared retrievals, i.e., the presence of water-leaving radiances. The contribution of these radiances to space-borne observations can as large as 15% for $\lambda \leq 450$ nm, where absorption by pure ocean water is least. Such large magnitudes in a wavelength regime where sunlight reflected by the atmosphere is most sensitive to accumulation-mode aerosols necessitates evaluating the uncertainty in these radiances and their impact on aerosol retrieval.

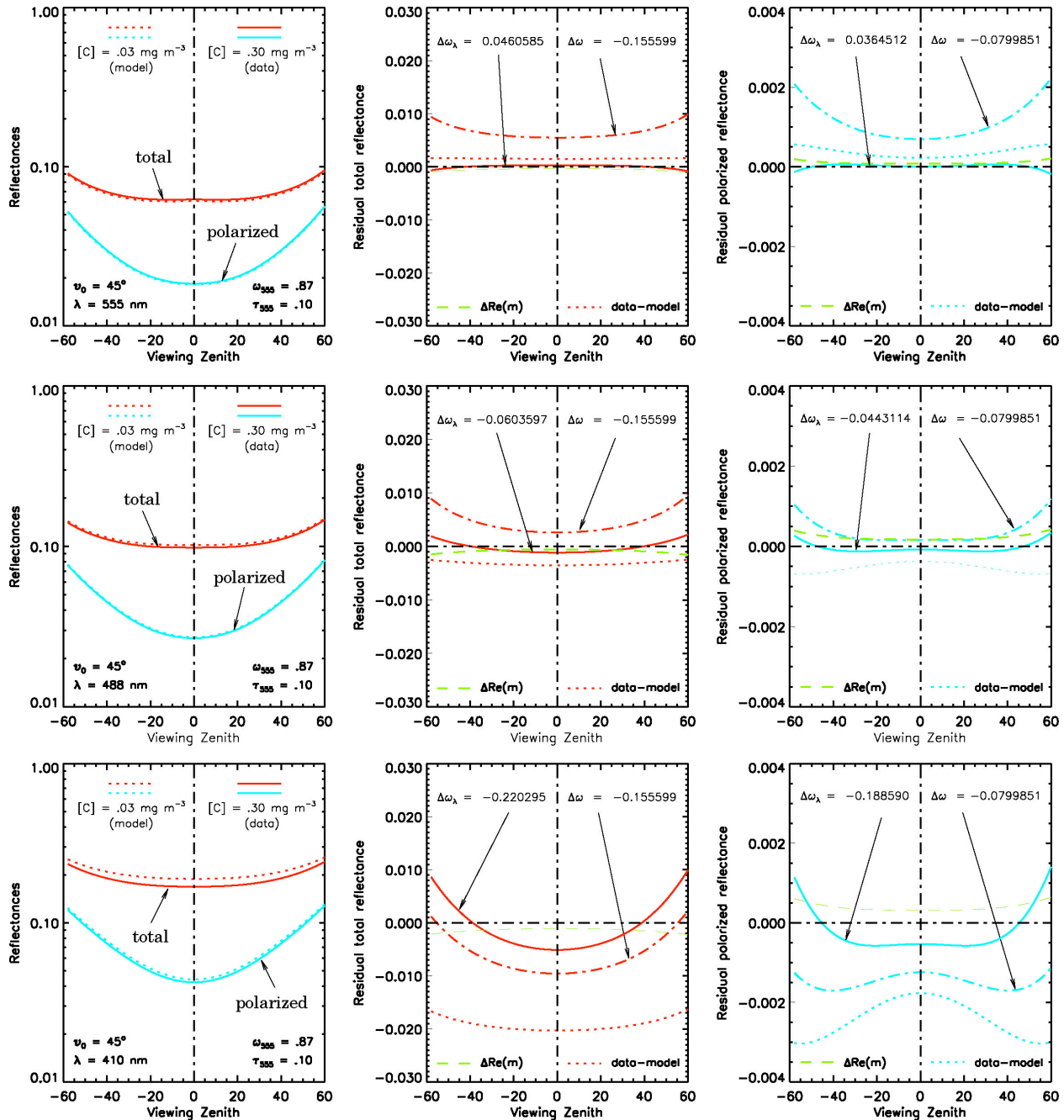


Figure 7.2-1. The effect of uncertainties in ocean color on APS observations and APS single-scattering albedo retrievals.

The uncertainty can be related to variations in [Chl], the Chlorophyll-C pigment concentration in the ocean (Maritonera and Morel, 2001), which cause these radiances to vary by a factor of four. Satellite instruments dedicated to the retrieval of [Chl] such as the Sea-viewing Wide Field-of-view Sensor (SeaWiFS) and the Ocean Color and Temperature Sensor (OCTS) separate the ocean signal from atmospheric scattering by estimating the latter contribution from near-infrared ($\lambda \geq 700$ nm) reflectances (Gordon, 1997). Such estimations, called *atmospheric correction*, will evidently be biased towards scattering by coarse mode particles because of the relatively large optical thickness of these particles in the near infrared. In addition, the estimates are often based on analyses of total rather than polarized reflectances, which significantly decreases the ability of even distinguishing monomodal from bimodal aerosols (Chowdhary *et al.*, 2001, 2002a). The result is an error in atmospheric correction, which propagates in the estimate of [Chl]. Of importance to note is that the accuracy listed for such estimates, 30%-40%, do *not* include errors resulting from atmospheric correction but are based on surface measurements of water-leaving radiances (e.g., O'Reilly *et al.*, 1998). Hence, rather than using ancillary [Chl] data with uncertain accuracies to estimate the contribution of water-leaving radiances, we simultaneously constrain these radiances and retrieve the properties of accumulation-mode particles by employing differences in the spectral *and* angular patterns of oceanic and atmospheric contributions to the visible total *and* polarized remote sensing reflectance.

Figure 7.2-1 illustrates the sensitivity of total and polarized reflectance to changes in water-leaving radiances. The results are from simulations performed for top-of-the-atmosphere (TOA) observations of a two-layer atmosphere in which aerosol particles are homogeneously mixed with molecules below 12000 ft, and which is bounded from below by a rough ocean surface and a homogeneous ocean body. The properties of the aerosol resemble those actually retrieved by the airborne Research Scanning Polarimeter (RSP) instrument off the coast of California except for including absorption (*cf.* Chowdhary *et al.*, 2001). Note that this aerosol is also capable of reproducing many of the multi-angle total reflectances observed over the ocean by the Multi-angle Imaging SpectroRadiometer (MISR) on the Earth Observation Science (EOS) Terra platform (Martonchik *et al.*, 2002). The ocean surface roughness follows the wind-speed-dependent surface slope distribution measured by Cox and Munk (1954), and it contains foam whose albedo is given by Koepke (1984) and whose wind-dependent coverage is taken from Monahan and O'Muircheartaigh (1986). The bidirectional scattering properties of the ocean body depend on [Chl] and λ (see Section 3.4.3). The sun angle for this figure is 45 degrees, and viewing occurs along the cross-principal plane.

The panels in the first column show the total (red lines) and polarized (blue lines) reflectance at 555 nm (first row), 488 nm (second row), and 410 nm (third row). The dotted and solid lines in this column are for an ocean body with [Chl] = 0.03 mg/m³ and 0.30 mg/m³, and are referred to as our base model and data model, respectively. Hence, these lines illustrate a realistic case in which a wrong ocean model is used to analyze TOA reflectance data. The differences are shown by the dotted lines in the second column and third column for the total and polarized reflectance, respectively.

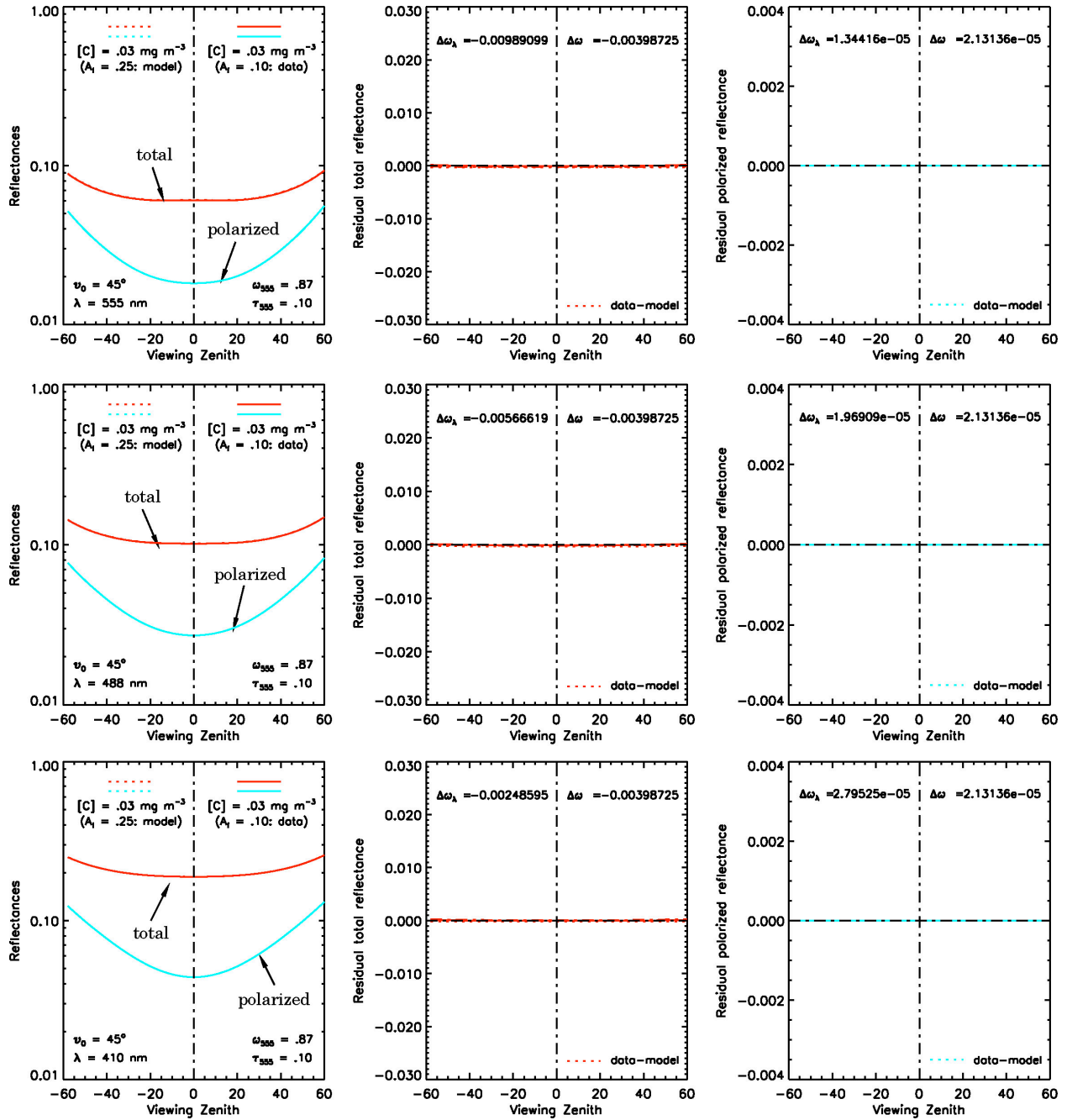


Figure 7.2-2. The effect of uncertainties in ocean foam albedo on measurements in the UV/VIS spectral domain.

Note first that underestimating $[Chl]$ causes both the total and polarized reflectance to be larger than observed for $\lambda \leq 488$ nm, and lower for $\lambda = 555$ nm. This is because Chlorophyll-C pigments exhibit an absorption peak at 443 nm, which for $\lambda \leq 510$ nm decreases the ocean albedo with increasing $[Chl]$ and *vice versa* for larger wavelengths. Secondly, the differences in reflectance will be similar in magnitude for $\lambda = 488$ and 555 nm, and several factors larger for $\lambda = 410$ nm which again can be uniquely related to the

absorption peak of Chlorophyll-C. Thirdly, the angular pattern of difference in polarized reflectance is the same for all wavelengths, and derives from Rayleigh-Gans polarization of the underwater light. These trends provide fingerprints for identifying the ocean model rather than the aerosol model as the cause for discrepancies between model results and observations. To illustrate this point we show what happens if one attempts to fit the data by adjusting the aerosol single scattering albedo ω , which can cause differences in TOA reflectances that are comparable in magnitude to those resulting from variations in water-leaving radiances (Chowdhary *et al.*, 2002b). The solid lines in the second and third columns correspond to the residual reflectances resulting from a band-by-band least square fit of ω , with the change in single scattering albedo $\Delta\omega$, given in the upper left corner for each wavelength. Note that the residual reflectances can still be large especially for 410 nm because of angular differences between light scattered by the aerosol and light scattered by hydrosol particles. Furthermore, the sign and magnitude in change of single scattering albedo follow the pattern discussed above for water-leaving radiances. If one attempts to fit the differences in a broadband least square fit of ω , (see resulting change $\Delta\omega$, in upper right corners), then the residual reflectances (given by the dashed-dotted lines) can become even larger than the original differences. Another potential source of uncertainty in TOA reflectance that can be confused with differences in ocean model is the albedo of surface foam. However, the contribution of light reflected by such foam to TOA reflectance is too small in the visible part of the spectrum to cause large variations. This is shown in Figure 7.2-2 which is the same as Figure 7.2-1 except for changing the albedo of oceanic foam from 25% to 10% rather than [Chl] in the data model.

For comparison, we also included in Figure 7.2-1 differences in reflectance when the real refractive index m of the observed aerosol differs by $\Delta m = -0.04$ from the one used for retrieval (green dashed lines). Note that these differences are now *opposite* in sign for the total reflectance and polarized reflectance for *all* wavelengths, the signature of which will be especially evident in the degree of polarization. Changes in the aerosol size distribution result in yet other signatures in the degree of polarization that can be distinguished from those resulting from variations in the ocean color (not shown here). Finally, we remark that the conclusions drawn from these figures become even more prominent for scattering geometries close to the backscattering direction as demonstrated by Chami *et al.* (2001) and by Chowdhary *et al.* (2001).

8. CONSTRAINTS, LIMITATIONS AND ASSUMPTIONS

8.1. Spectral refractive index

The spectral refractive indices for an aerosol mode (a given material, or mixture of materials) are not independent since they must satisfy causality and consequently a dispersion relationship. Although in principal 9 independent spectral refractive indices could be retrieved for each mode, this is neither useful, nor computationally effective. Potential approaches that have been identified are:

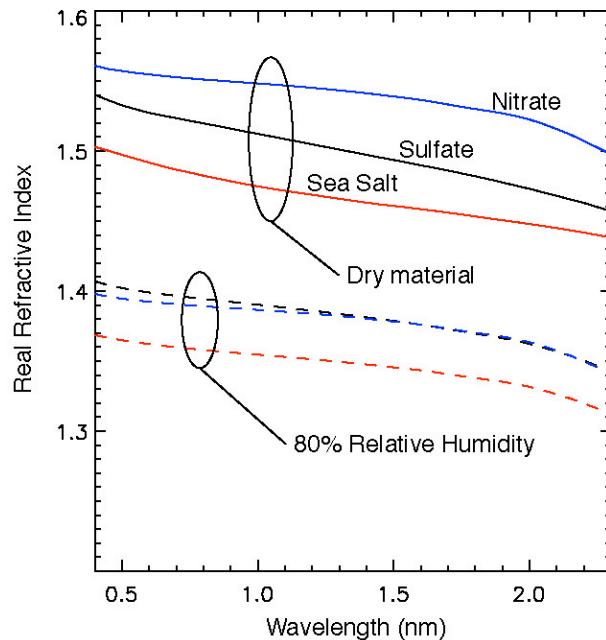


Figure 8.1-1. Variation of refractive index of some typical materials for aerosols, for dry material and material in presence of 80% humidity.

constraint on the spectral variation of the refractive index. All three approaches should have the same effect on the retrieval, i.e., that of imposing spectral smoothness on the refractive index retrieved. However, the smoothness constraint imposes no constraint on the absolute value of the complex refractive index, does not impose a particular functional form and does not have the computational overhead required for parameterizing the spectral variation of refractive index in terms of a simplified dispersion relationship. This approach is being successfully used with the AERONET sunphotometer network (Dubovik and King, 2000) and therefore has the benefit of having already been tested on real data from an extensive network of operational sunphotometers. The smoothness constraint corresponds to approach 3, where the covariance matrix is diagonal and is applied to derivative, not actual refractive indices. An indication of why this type of approach is expected to work can be gained from examining some typical spectral refractive indices over the spectral range of APS measurements as shown in Figure 8.1-1. It is clear the absolute refractive index varies dependent on material and state of hydration while the spectral variation does not show such large variability.

8.2. Specification of uncertainty

The measurement uncertainty for the EDR products will be specified by providing the diagonal elements of the EDR covariance matrix. The true uncertainty in a retrieval requires information about off-diagonal elements of the EDR covariance matrix. However, the correlation structure is not induced by correlations of the measurement uncertainties, but by correlations between the measurement sensitivities (Jacobians). This means that the off-diagonal elements can be reconstructed (from the diagonal elements of the EDR covariance matrix and the EDR parameters that are retrieved) by

- Retrieve a base wavelength refractive index, a spectral slope and possibly spectral curvature.
- Use a simplified dispersion relationship parameterized on the location and strength of a UV and SWIR absorption feature.
- Develop prior probability distributions for spectral refractive indices, or more simply estimate the covariance matrix for spectral refractive indices and use this as a constraint in the retrieval.

As a result of surveying the literature and evaluating the effect on the retrieval algorithm of the different forms of specification we have decided to impose a smoothness

calculation if they are required. This choice is made for simplicity in packaging the EDR products. However, the complete covariance matrix can be provided as part of the APS data product in a straightforward implementation at any point up to and including the Critical Design Review, if this is regarded as desirable.

8.3. Solar Zenith Angle

There are four effects that may degrade EDR production at high solar zenith angles.

- Reduction in reflected radiance caused by cosine solar zenith angle dependence.
- Observed radiances are sensitive to actual vertical structure of atmosphere rather than some simple approximation.
- Plane parallel approximation is not valid and must be corrected using a pseudo-spherical approximation (next order approximation for a spherical atmosphere).
- Most pixels are cloud contaminated

The first effect causes a reduced signal level as a result of the reduced solar intensity incident on a horizontal surface which is proportional to the cosine of the solar zenith angle dependence, but this reduction is compensated for by the increased pathlength which causes more scattering to occur.

The second effect causes the degree of linear polarization at 410 nm to be greater for a homogeneously mixed aerosol between 1000 and 700 mbar than for an otherwise identical layer located between 800 and 700 mbar. Thus if the retrieval algorithm assumes that the aerosol vertical distribution is homogeneous, when it is not, the retrieval will have to find a model with a higher polarization than it should. This corresponds to an error in single scattering albedo retrieval with the retrieved value being lower than it should (increased absorption increases the degree of linear polarization at 410 nm).

The third effect can be controlled by using an appropriate forward model. If necessary model calculations at high solar zenith angles will use a pseudo-spherical calculation to calculate the reflected Stokes vector elements. The pseudo-spherical approximation calculates the single scattering source term using the actual spherical geometry and vertical profile of aerosols and gases and then calculates the multiple scattering using a plane parallel calculation with this exact single scattering calculation as a source term.

The fourth effect will necessarily impact the frequency of aerosol EDR retrievals since the longer the solar pathlength the more likely it is that a cloud transects the path. However, very low solar zenith angles, are principally an issue at or near the poles and so provide ideal conditions for the retrieval of PSC properties, even when the sun is below the horizon provided it is illuminating the atmospheric layer at 15-25 km.

Because of the increase in cloud contamination daytime conditions for APS retrievals are defined as being for solar zenith angles greater than 70°. APS data will be taken and the standard processing path used to retrieve both aerosol and cloud EDRs for non-daytime solar zenith angles from 70° to 85°, but with the expectation that most

retrievals will be mixtures of cloud and aerosols. Data will be acquired for solar zenith angles from 85° to 92° but a special processing path will be followed that restricts the algorithm to the retrieval of stratospheric aerosol and cirrus clouds if they are identified as present.

8.4. Neglect of circular polarization

Circular polarization, V (sometimes referred to as S3) is neglected in the APS EDR algorithms. The rationale for this is presented in Section 4.3.1.

9. CALIBRATION AND VALIDATION

The APS team has conducted a comprehensive assessment of all its science data products, including algorithm validation and specification of the uncertainties in the retrieved geophysical quantities derived from the calibrated Stokes vector elements. Validation activities will be conducted in coordination with other NASA, NSF, NOAA, and DoE programs. Airborne measurements from existing and planned instruments and ground-based observations from AERONET, NASA's Solar Irradiance Research Network (SIRN) and the DoE-ARM program each play an essential role in post-launch validation studies.

The principal validation and vicarious calibration tool is the use of RSP instruments on high (and low) altitude aircraft. The use of two RSP instruments at low and high altitude allows for a better characterization of the surface and simultaneous measurement of radiances (radiometrically) close to the space environment. Consequently a better vicarious calibration for an instrument with a relatively large footprint such as the APS instrument can be obtained i.e. surface reflectance sampling error can be reduced. The Research Scanning Polarimeter (RSP) has already been developed and aerosol and cloud property retrieval algorithms have been demonstrated on data obtained from field experiments performed over agricultural lands and the Pacific Ocean near Santa Barbara.

Post-launch activities include refinement of algorithms and confirmation of uncertainty estimates based on comparisons with correlative measurements. Three components are planned: 1) field experiment activities, 2) life-of-mission comparisons to ground-based observations from the ARM sites, AERONET sites, SIRN sites and USDA UVB measurement network and 3) extensive comparisons to other instruments especially VIIRS and any other satellite platforms that have UV, or polarization measurements. 4) Evaluation of APS calibration using targets of opportunity.

The field experiment component provides detailed validation information on the physical basis and implementation of the algorithms including test of retrieved geophysical parameters. Utilization of a Proteus platform for an NPOESS Airborne Simulator Testbed – APS (NAST-A) experiment in the post-launch period would provide a high-quality benchmark validation of the radiance calibration for the APS instrument and is the best platform to validate the ice crystal EDR objectives of the mission, but will depend on the funding of flight hours from sources other than the APS EMD program.

The APS-retrieved geophysical parameters will be compared with independent retrievals from ground-based measurements of cloud and aerosol properties, *in situ* microphysical observations of clouds and aerosols, and similar measurements from other satellites, both operational and experimental. APS aerosol optical depth, particle size and index of refraction will be validated by comparison with a worldwide network (AERONET) of ground-based sunphotometer measurements and US networks (NASA's SIRN network and USDA's UVB measurement network) that provide a denser set of measurements. Validation of the single-scatter albedo retrieval relies on a limited number of ground-based observations and experimental remote sensing retrievals, both of which are themselves quite uncertain. Deposition measurements and ground-based sampling will be used to evaluate the validity of refractive index retrievals and their use in speciation.

The NPOESS 9:30 am orbit includes a VIIRS instrument and so intercomparisons of APS retrievals and radiances with VIIRS retrievals will be of great interest both for calibration evaluation and for VIIRS algorithm evaluation and validation. This is because VIIRS is on all the NPOESS polar orbiting instruments and so the detection and correction of any errors in the aerosol and cloud algorithms used by VIIRS are a key element in the synergy between VIIRS and APS. It is expected that many of the prior assumptions used in VIIRS retrievals over cirrus clouds (shape distribution) and aerosols (size and refractive index) can be substantially based on the APS EDR retrievals. This provides enormous synergies since although APS is only on one of the NPOESS orbital planes and only samples along the satellite groundtrack, improving the products from VIIRS impacts data sets that are produced three times a day globally.

The principal surfaces of interest for evaluating and checking APS UV/VIS radiometric stability are the snow surfaces of the high plateaus of East Antarctica and Greenland ice sheets. In this spectral region snow has a very high albedo (>97%) that is invariant with grain size and incidence angle. On the high plateaus the temperatures are always far below freezing so the surface consists of cold fine-grained snow, and there is negligible contamination. The ice sheets are flat and uniform across large areas. Ozone is the only significant variable absorber and its absorption can be accounted for if the ozone amount is known. Cloud detection and removal is not necessary because the thin clouds over the high ice sheets apparently do not alter the near nadir reflectance, as they do over darker surfaces. Measurements over these surfaces can therefore be used to track variations in radiometric gain, although not the absolute value of radiometric gain.

10. POTENTIAL SCIENCE OPPORTUNITIES

There are a number of scientific opportunities that are provided by the measurements made by the APS instrument. The six principal opportunities that have been identified are to use the sensitivity of polarimetric measurements to:

- Determine aerosol mixed layer depth and cloud top height
- Identify predominant ice crystal shapes
- Determine in cloud absorption

- Determine surface BRDF
- Determine water vapor column
- Determine ocean color

10.1. *Aerosol mixed layer depth and cloud top height*

The aerosol mixed layer depth and cloud top height estimates are based on the use of the APS bands at 412 and 488 nm to determine aerosol absorption (single-scattering albedo) and aerosol vertical extent (mixed layer depth) simultaneously, or the cloud top height when a cloud is present. The physical mechanism that provides this sensitivity is the absolute and differential effect on the polarization and reflectance generated by Rayleigh scattering of absorbing aerosols and clouds at different heights in the atmosphere.

10.2. *Identify predominant ice crystal shapes*

The identification of the predominant ice-crystal shapes (habits) in cirrus clouds uses the fact that the polarized scattering phase function is sensitively dependent on particle shape. RSP data from NASA's CRYSTAL-FACE experiment has already demonstrated the capability of measurements in a strong water vapor absorption band such as 1378 nm to screen surface and aerosol contributions to the observed radiance so that thin cirrus can be unambiguously identified and their shape classified between fractal polycrystals (proxy for aged/damaged crystals), hexagonal plates and hexagonal columns.

10.3. *In Cloud Absorption*

The cloud physical thickness estimate is based on the use of the degree of linear polarization measurements at 910 nm. The increase in the polarization of clouds between 865 and 910 nm is caused by absorption of solar radiation by water vapor within the cloud, since the degree of linear polarization is insensitive to absorption above the cloud. Once a cloud EDR retrieval is complete the retrieved cloud model for the 910 nm measurement can be used to generate a table of values of degree of linear polarization across the scan as a function of water vapor amount. A least mean square best fit of the observed degree of linear polarization to the model table is then used to determine the water vapor amount.

10.4. *Surface Polarized BRDF*

A direct result of the retrieval of aerosols over land and ocean is that the APS measurements can be atmospherically corrected to provide surface polarized BRDF measurements. These will be of use in improving BRDF models of the land surface to allow better vegetation characterization and to improve the types of leaf orientation models that are used in detailed land-vegetation surface models (Asner 1998).

10.5. *Water vapor column*

The retrieval of water vapor column is described in Section 6.6. This retrieval provides a complement and synergy with the water vapor retrieval performed by VIIRS, because the shortwave reflectance method used is sensitive to water vapor in the warm boundary layer air that infrared methods cannot detect.

10.6. Ocean Color

As outlined in Section 7.2 the ocean color can (and should) be retrieved as part of the aerosol EDR processing over oceans. The Chlorophyll concentration that is estimated will therefore be provided as an additional APS product.

11. REFERENCES

1. W. A. Abdou, J. V. Martonchik, R. A. Kahn, R. A. West, and D. J. Diner, 1997: A modified linear-mixing method for calculating atmospheric path radiances of aerosol mixtures, *J. Geophys. Res.*, **102**, 16,883-16,888.
2. M. O. Andrea, 1995: Climatic effects of changing atmospheric aerosol layers, in *World survey of climatology, Vol. 16, Future climates of the world*, A. Henderson-Sellers, Ed., Elsevier, Amsterdam.
3. G. P. Asner, 1998: Biophysical and biochemical sources of variability in canopy reflectance, *Remote Sens. Environ.*, **64**, 234-253.
4. I. J. Barton, 1983: Upper level cloud climatology from an orbiting satellite, *J. Atmos. Sci.*, **40**, 435-447.
5. M. A. Box, S. A. W. Gerstl, and C. Simmer, 1988: Application of the adjoint formulation to the calculation of atmospheric radiative effects, *Beitr. Phys. Atmos.*, **61**, 303-311.
6. M. A. Box, S. A. W. Gerstl, and C. Simmer, 1989: Computation of atmospheric radiative effects via perturbation theory, *Beitr. Phys. Atmos.*, **62**, 193-199.
7. M. A. Box, P. E. Loughlin, and M. Samaras, 1997: Application of radiative perturbation theory to changes in absorbing gas, *J. Geophys. Res.*, **102**, 4333-4342.
8. F.-M. Bréon, Tanré, P. Lecomte and M. Herman, 1995: Polarized reflectance of bare soils and vegetation: Measurements and models, *IEEE Trans. Geo. Rem. Sens.*, **33**, 487-499.
9. A. Bricaud, A. Morel, M. Babin, K. Allili, and H. Claustre, 1998: Variations of light absorption by suspended particles with chlorophyll a concentration in oceanic (case 1) waters: Analysis and implications for bio-optical models, *J. Geophys. Res.*, **103**, 31,033-31,044.
10. B. Cairns, B.E. Carlson, A.A. Lacis and E.E. Russell, 1997: An analysis of ground-based polarimetric sky radiance measurements, *Proc. SPIE*, **3121**, 383-393.
11. B. Cairns, L.D. Travis and E.E. Russell, 1999: Research Scanning Polarimeter: Calibration and ground-based measurements, *Proc. SPIE*, **3754**, 186-197, Denver.
12. B. Cairns, L.D. Travis and J. Chowdhary, 2001: Aerosol retrievals over land surfaces (The Advantages of Polarization), presented at AMS Annual Meeting, Albuquerque, NM, January 2001.
13. T. N. Carlson, 1979: Atmospheric turbidity in Saharan dust outbreaks as determined by analyses of satellite brightness data, *Mon. Wea. Rev.*, **107**, 322-335.
14. T. N. Carlson and J. M. Prospero. 1972: The large-scale movement of Saharan dust air outbreaks over the Northern Equator Atlantic, *J. Appl. Meteor.*, **11**, 283-297.
15. T. N. Carlson and P. Wendling, 1977: Reflected radiance measured by NOAA 3 VHRR as a function of optical depth for Saharan dust, *J. Appl. Meteor.*, **16**, 1368-1371.
16. B. E. Carlson and B. L. Lutz, 1989: Time-variable Phenomena in the Jovian System, R. A. West, and J. Rahe, Eds., NASA-SP-494.
17. M. R. Chami, R. Santer, and E. Dillegaard, 2001: Radiative transfer model for the computations of radiance and polarization in an atmosphere-ocean system: polarization properties of suspended matter for remote sensing, *Appl. Opt.*, **40**, 2398-2416.

18. H. Chepfer, G. Brogniez, P. Goloub, et al, 1999a: Observations of horizontally oriented ice crystals in cirrus clouds with POLDER-1/ADEOS-1, *J. Quant. Spectrosc. Radiat. Transfer*, **63**, 521–543.
19. H. Chepfer, G. Brogniez, L. Sauvage, P.H. Flamant, V. Trouillet and J. Pellon, 1999b: Remote sensing of cirrus radiative parameters during EUCREX '94. Case study of 17 April 1994. Part II: Microphysical models, *Mon. Wea. Rev.*, **127**, 504-519.
20. H. Chepfer, P. Goloub, J. D. Spinhirne, P. H. Flamant, L. Laverato, L. Sauvage G. Brogniez and J. Pellon, 2000: Cirrus cloud properties derived from POLDER/ADEOS-1 polarized radiances: First validation using a ground-based lidar network, *J. Appl. Meteorol.*, **39**, 154-168.
21. J. Chowdhary, B. Cairns, M. Mishchenko, and L. Travis, 2001: Retrieval of aerosol properties over the ocean using multispectral and multiangle photopolarimetric measurements from the Research Scanning Polarimeter, *Geophys. Res. Lett.*, **28**, 243-246.
22. J. Chowdhary, B. Cairns, and L. D. Travis, 2002a: Case studies of aerosol retrievals over the ocean from multiangle, multispectral photopolarimetric remote sensing data, *J. Atm. Sci.*, **59**, 383-397.
23. J. Chowdhary, B. Cairns, J. Laveign, and L. D. Travis, 2002b: Evaluation of ocean color and its effect on the polarization of water-leaving radiances during the Chesapeake Lighthouse and Aircraft Measurements for Satellites (CLAMS) experiment, *11th Conference on Atmospheric Radiation*, Proc. American Meteorological Society, 86-89.
24. D. L. Coffeen, 1979: Polarization and scattering characteristics in the atmospheres of the Earth, Venus and Jupiter, *J. Opt. Soc. Am.*, **69**, 1051-1064.
25. D. L. Coffeen and T. Gehrels, 1969: Wavelengths dependence of polarization, XV. Observations of Venus, *Astron. J.*, **74**, 433-445.
26. C. Cox, and W. Munk, 1954: Statistics of the sea-surface derived from sun glitter, *J. Mar. Res.*, **13**, 198-227.
27. J. F. de Haan, 1987: Effects of aerosols on the brightness and polarization of cloudless planetary atmospheres, Thesis, Vrije Universiteit, Amsterdam.
28. J. F. de Haan, P. B. Bosma and J. W. Hovenier, 1987: The adding method for multiple scattering calculations of polarized light. *Astronom. Astrophys.*, **183**, 371-391.
29. D.J.Debrestian, J.D.Lumpe, E.P.Shettle, R.M.Bevilacqua, J.J.Olivero, J.S.Hornstein, W.Glaccum, D.W.Rusch and M.D.Fromm, 1997: Preliminary Analysis of Southern Hemisphere POAM II Observations of Polar Mesospheric Clouds, *J. Geophys. Res.*, **102**, 1971-1981.
30. T. DelGenio, 1993: Accuracy measurements, in Long-Term monitoring of Global Climate Forcings and Feedbacks, J. Hansen, W. Rossow, and I. Fung (eds.), NASA Conf. Publ. 3234, NASA/GSFC, Greenbelt, MD.
31. D. J. Diner, and Coauthors, 1991: A multi-angle Imaging SpectroRadiometer for terrestrial remote sensing from the Earth Observing System, *Int. J. Imaging Syst. Techhnol.*, **3**, 92-107.
32. A. Dollfus, S. Ebisawa, and E. Bowel, 1984a: Polarimetric analysis of the Martian dust storms and clouds in 1971, *Astron. Astrophys.*, **131**, 123-136.
33. A. Dollfus, S. Ebisawa, and E. Bowel, 1984b: The Martian dust storms of 1973: a polarimetric analysis, *Astron. Astrophys.*, **134**, 343-353.
34. O. Dubovik and M. D. King, 2000: A flexible inversion algorithm for retrieval of aerosol optical properties from Sun and sky radiance measurements, *J. Geophys. Res.*, **105**, 20673-20696.
35. L. W. Espesito and L. D. Travis, 1982: Polarization studies of the Venus UV contrasts: Cloud height and haze variability, *Icarus*, **51**, 374-390.
36. R. A. Ferrare, R. S. Fraser, and Y. J. Kaufman, 1990: Satellite measurements of large scale air pollution: Measurements of forest fire smoke, *J. Geophys. Res.*, **92**, pp. 9911–9925.
37. J. S. Foot, 1988: Some observations of the optical properties of clouds. II: Cirrus, *Quart. J. Royal Meteorol. Soc.*, **114**, 145-164.

38. P. N. Francis, 1995: Some aircraft observations of the scattering properties of ice crystals. *J. Atmos. Sci.*, **52**, 1142–1154.
39. R. S. Fraser, 1976: Satellite measurements of mass Sahara dust in the atmosphere, *Appl. Opt.*, **15**, 2471–2479.
40. R. S. Fraser and Y. J. Kaufman, 1985: The relative importance of aerosol scattering and absorption in remote sensing, *IEEE Trans. Geosci. Remote Sensing*, **GE-23**, 625–633.
41. E. S. Fry and K. J. Voss, 1985: Measurement of the Mueller matrix for phytoplankton, *Limnol. Oceanogr.*, **30**, 1322–1326.
42. B.-C. Gao and A. F. H. Goetz, Column atmospheric water vapor and vegetation liquid water retrievals from airborne imaging spectrometer data. *J. Geophys. Res.*, **95**, 3549–3564, 1990
43. N.-C. Gao and Y.J. Kaufman, 1992: Selection of the 1.375- μ m MODIS Channel for Remote Sensing of Cirrus Clouds and Stratospheric Aerosols from Space. *J. Atmos. Sci.*, **52**, 4231–4237.
44. C. K. Gatebe, M. D. King, S.-C. Tsay, Q. Ji, G. T. Arnold, and J. Y. Li, 2001: Sensitivity of Off-Nadir Zenith Angles to Correlation between Visible and Near-Infrared Reflectance for Use in Remote Sensing of Aerosol over Land, *IEEE Trans. Geosci. Remote Sensing*, **39**, 805–819.
45. J.-F. Gayet, G. Febvre, G. Brogniez, H. Chepfer, W. Renger and P. Wendling, 1996: Microphysical and optical properties of cirrus and contrails: cloud field study on 13 October 1989, *J. Atmos. Sci.*, **53**, 126–138.
46. S. A. W. Gerstl, and W. M. Stacey, 1973: A class of second order approximate formulations of deep penetration radiation transport problems, *Nucl. Sci. Eng.*, **51**, 339–343.
47. P. Goloub, D. Tanré, M. Herman, A. Marchand, and F.-M. Bréon, 1999: Validation of the first algorithm applied for deriving aerosol properties over the ocean using the POLDER/ADEOS measurements, *EEE Trans. Geosci. Remote Sens.*, **37**, 1586–1596.
48. R. M. Goody and Y. L. Yung, 1989: *Atmospheric Radiation: Theoretical Basis*. pp.125–188, Oxford University.
49. H. R. Gordon, O. B. Brown, and M. M. Jacobs, 1975: Computed relationships between the inherent and apparent optical properties of a flat homogeneous ocean body, *Appl. Opt.*, **14**, 417–427
50. H. R. Gordon, 1997: Atmospheric correction of ocean color imagery in the Earth Observing System era, *J. Geophys. Res.*, **102**, 17,081–17,106.
51. M. Griggs, 1975: Measurements of atmospheric aerosol optical thickness over water using ERTS-1 data, *J. Air. Pollut. Control Assoc.*, **25**, 622–625.
52. Griggs, M. 1977: Comment on “Relative atmospheric aerosol content from ERTS-1 data, *J. Geophys. Res.*, **82**, 4972.
53. M. Griggs, 1979: Satellite observations of atmospheric aerosols during the EOMET cruise, *J. Atm. Sci.*, **36**, 695–698.
54. J. Hallet, 1994: *Cirrus ice crystals nucleation and growth*, in 74th AMS Annual Meeting Am. Meteorol. Soc., Boston, Mass.
55. J. E. Hansen and A. Arking, 1971: Near-infrared scattering by terrestrial clouds, *Science*, **171**, 669–672.
56. J. E. Hansen and L. D. Travis, 1974: Light scattering in planetary atmospheres, *Space Sci. Rev.*, **16**, 527–610.
57. J. E. Hansen, W. Rossow, B. Carlson, A. Lacis, L. Travis, A. DelGenio, I. Fung, B. Cairns, M. Mishchenko, and M. Sato, 1995: Low-cost long-term monitoring of global climate forcings and feedbacks, *Clim. Change*, **31**, 247–271.
58. S. Havemann and A. J. Baran, 2001: Extension of *T*-matrix to scattering of electromagnetic plane waves by non-axisymmetric dielectric particles: Application to hexagonal ice cylinders, *J. Quant. Spectrosc. Radiat. Transfer* **70**, 139–158.

59. A. J. Heymsfield, and C. M. R. Platt, 1984: A parameterization of the particle size spectrum of ice clouds in terms of the ambient temperature and ice water content, *J. Atmos. Sci.* **41**, 846-855.
60. A. J. Heymsfield, and J. Iaquinta, 2000: Cirrus crystal terminal velocities, *J. Atmos. Sci.*, **57**, 916-938.
61. P. V. Hobbs, 1993: Aerosol-cloud interactions, in *Aerosol-Cloud-Climate Interactions*, Chapter 2, Academic Press, New York.
62. J. W. Hovenier, 1969: Symmetry relationships for scattering of polarized light in a slab of randomly oriented particles, *J. Atm. Sci.*, **26**, 488-499.
63. J. W. Hovenier, 1971: Multiple scattering of polarized light in planetary atmospheres, *Astron. Astrophys.*, **13**, 7-29.
64. J. W. Hovenier, and C. V. M. van der Mee, 1983: Fundamental relationships relevant to the transfer of polarized light in a scattering atmosphere, *Astron. Astrophys.*, **128**, 1-16.
65. B. Hu, W. Lucht and A.H. Strahler, 1999: The interrelationship of atmospheric correction of reflectances and surface BRDF retrieval: A sensitivity study, *IEEE Trans. Geo. Rem. Sens.*, **37**, 724-738.
66. D. J. Jacob, M. O. Andrea, E. K. Bigg, R. A. Duce, I. Fung, G. M. Hidy, M. Legrand, J. M. Prospero, F. Raes, S. G. Warren, and A. Wiedensohler, 1995: What factors influence atmospheric aerosols, how have they changed in the past, and how might they change in the future?, in *Aerosol forcing of the climate*, Chapter 2, R. J. Charlson and J. Heintzenberg, Eds., Wiley, Chichester.
67. E. T. Jaynes, 1968: Prior Probabilities, *IEEE Transactions on Systems Science and Cybernetics*, **SSC-4**, 227-241.
68. M. Jonasz, 1983: Particle-size distributions in the baltic, *Tellus*, **35B**, 346-358.
69. Y. J. Kaufman, 1987: Satellite sensing of aerosol absorption, *J. Geophys. Res.*, **92**, 4307-4317.
70. Y. J. Kaufman, A. E. Wald, L. A. Remer, B. C. Gao, R. R. Li, and L. Flynn, 1997: The MODIS 2.1- μ m channel-correlation with visible reflectance for use in remote sensing of aerosol, *IEEE Trans. Geosci. Remote Sensing*, **35**, 1286-1298.
71. Y. A. Kadyshevich, and Y. S. Lyubovtseva, 1973: Certain characteristics of ocean hydrosols from scattering matrices, *Izv. Acad. Sci. USSR Atmos. Oceanic Phys.*, **9**, 659-663.
72. F. M. Kahnert, J. J. Stamnes, and K. Stamnes, 2001: Application of the extended boundary condition method to homogeneous particles with point-group symmetries, *Appl. Opt.*, **40**, 3110-3123.
73. K. Kawabata, D. L. Coffeen, J. E. Hansen, W. A. Lane, M. Sato, and L. D. Travis, 1980 :Cloud and haze properties from Pioneer Venus polarimetry, *J. Geophys. Res.*, **85**, 8129-8140.
74. M. D. King, Y. J. Kaufman, W. P. Menzel, and D. Tanre, 1992: Remote sensing of cloud, aerosol, and water vapor properties from the MODerate maging Spectroradiometer, *IEEE Trans. Geosci. Remote Sens*, **30**, 2-27.
75. M. D. King, S.-C. Tsay, S. E. Platnick, M. Wang and K. N. Liou, 1997: Cloud retrieval algorithms for MODIS: Optical thickness, effective particle radius and thermodynamic phase, in *MODIS Algorithm Theoretic Basis Document ATBD-MOD-05, MOD-06 - Cloud Product, Version 5*, NASA GSFC, Greenbelt, MD.
76. S. Kinne, T. P. Ackerman, A. J. Heymsfield, F. P. J. Valero, K. Sassen and J. D. Spinhirne, 1992: Cirrus microphysics and radiative transfer: Cloud field study on 28 October 1986, *Mon. Wea. Rev.*, **120**, 661-684.
77. S. Kinne, 2000: Personal communication.
78. W. J. Knibbe, J. F. de Haan, J. W. Hovenier, and L. D. Travis, 1997: A biwavelength analysis of Pioneer Venus polarization observations, *J. Geophys. Res.*, **102**, 10,945-10,957.
79. W. J. Knibbe, J. F. de Haan, J. W. Hovenier, and L. D. Travis, 1998: Analyses of

- temporal variations of the polarization of Venus as observed by Pioneer Venus Orbiter, *J. Geophys. Res.*, **103**, 8557-8574.
80. P. Koepke., 1984: Effective reflectance of oceanic whitecaps, *Appl. Opt.*, **23**, 1816-1842.
 81. L. C.-Labonnote, G. Brogniez, J.-C. Buriez and M. Doutriaux-Boucher, 2001: Polarized light scattering by inhomogeneous hexagonal mono-crystals: Validation with ADEOS-POLDER measurements. *J. Geophys. Res.*, **106**, 12,139-12,153.
 82. A. A. Lacis and V. Oinas, 1991: A description of the correlated k distribution method for modeling nongray gaseous absorption, thermal emission and multiple scattering in vertically inhomogeneous atmospheres, *J. Geophys. Res.*, **96**, 9027-9063.
 83. A. A. Lacis and M. I. Mishchenko, 1995: Climate forcing, climate sensitivity, and climate response: a radiative modeling perspective on atmospheric aerosols, in *Aerosol forcing of the climate*, Chapter 2, R. J. Charlson and J. Heintzenberg, Eds., Wiley, Chichester.
 84. N.-H. Lin and V. K. Saxena, 1992: Characteristics of Antarctic stratospheric aerosols during the 1987 ozone depletion episode based on SAGE II satellite observations, *J. Geophys. Res.*, **97**, 7635-7649.
 85. K. N. Liou, Y. Takano, and P. Yang, 2000: Light scattering and radiative transfer in ice crystal clouds: Applications to climate research. In *Light Scattering by Nonspherical Particles: Theory, Measurements, and Applications*, eds. M. I. Mishchenko, J. W. Hovenier, and L. D. Travis, pp. 417-449, Academic Press, San Diego.
 86. A. Macke, J. Mueller and E. Raschke, 1996a: Single scattering properties of atmospheric ice crystals. *J. Atmos. Sci.*, **53**, 2,813-2,825.
 87. A. Macke, M. I. Mishchenko and B. Cairns, 1996b: The influence of inclusions on light scattering by large ice particles, *J. Geophys. Res.*, **101**, 23,311-23,316.
 88. J. V. Martonchik, D. J. Diner, K. A. Crean and M. A. Bull, 2002: Regional aerosol retrieval results from MISR, *IEEE Trans. Geosci. Remote Sensing*, **40**, pp. 1520-1531.
 89. K. Masuda, and Takashima, T., 1992: Feasibility study of derivation of cirrus information using polarimetric measurements from satellite, *Remote Sens. Environ.* **39**, 45-59.
 90. G. M. McFarquhar and A. J. Heymsfield, 1996: Microphysical characteristics of three cirrus anvils sampled during the central equatorial Pacific experiment (CEPEX), *J. Atmos. Sci.*, **52**, 4,143-4,158.
 91. Y. Mekler, H. Quenzel, G. Ohring, and I. Marcus, 1977: Relative atmospheric aerosol from ERTS observations, *J. Geophys. Res.*, **82**, 967-970.
 92. Mergenthaler, J. L., J. B. Kumer, A. E. Roche and S. T. Massie, 1997: Distribution of Antarctic polar stratospheric clouds as seen by the CLAES experiment. *J. Geophys. Res.*, **102**, 19161-19171.
 93. Meywerk, J. and V. Ramanathan, 1999: Observations of the Spectral Clear-Sky Aerosol Forcing over the Tropical Indian Ocean. *J. Geophys. Res.*, **104**, 24,359-24,370.
 94. P. Minnis, K.-N. Liou, and Y. Takano, 1993: Inference of cirrus cloud properties using satellite-observed visible and infrared radiances. I. Parameterization of radiance fields, *J. Atmos. Sci.* **50**, 1279-1304.
 95. M. I. Mishchenko, 1990: Physical properties of the upper tropospheric aerosols in the equatorial region of Jupiter, *Icarus*, **84**, 296-304.
 96. M. I. Mishchenko, W. B. Rossow, A. Macke and A. Lacis, 1996: Sensitivity of cirrus cloud albedo, bidirectional reflectance and optical thickness retrieval accuracy to ice-particle shape, *J. Geophys. Res.*, **101**, 16,973-16,986.
 97. M. I. Mishchenko and L. D. Travis, 1997a: Satellite retrieval of aerosol properties over the ocean using polarization as well as intensity of reflected sunlight, *J. Geophys. Res.*, **102**, 16,989-17,013.
 98. M. I. Mishchenko and L. D. Travis, 1997b: Satellite retrieval of aerosol properties over ocean using measurements of reflected sunlight: Effect of instrumental errors and aerosol absorption, *J. Geophys. Res.*, **102**, 13,543-13,553.

99. M. I. Mishchenko, L. D. Travis, W. B. Rossow, B. Cairns, B. E. Carlson, and Q. Han, 1997: Retrieving CCN column density from single-channel measurements of reflected sunlight over the ocean: A sensitivity study, *Geophys. Res. Lett.*, **24**, 2655-2658.
100. M. I. Mishchenko, J. W. Hovenier, and L. D. Travis, eds., 2000: *Light Scattering by Nonspherical Particles: Theory, Measurements, and Applications*, 690 p. Academic Press, San Diego.
101. M. I. Mishchenko, L. D. Travis, A. A. Lacis, eds., 2002: *Scattering, Absorption, and Emission of Light by Small Particles*, 445 p., Cambridge University Press.
102. E. C. Monahan and I. G. O'Muircheartaigh, 1986: Whitecaps and the passive remote sensing of the ocean surface, *Int. J. Rem. Sens.*, **7**, 627-642.
103. K. Muinonen, 2000: Light scattering by stochastically shaped particles, In *Light Scattering by Nonspherical Particles: Theory, Measurements, and Applications*, eds. M. I. Mishchenko, J. W. Hovenier, and L. D. Travis, pp. 323-352, Academic Press, San Diego.
104. A. Morel, 1988: Optical modeling of the upper ocean in relation to its biogenous matter content (case I waters), *J. Geophys. Res.*, **93**, 10,749-10,768.
105. A. Morel, and I. Prieur, 1977: Analysis of variations in ocean color, *Limnol. Oceanogr.*, **22**, 709-722.
106. A. Morel, and B. Gentili, 1991: Diffuse reflectance of oceanic waters: its dependence on sun angle as influenced by the molecular scattering contribution, *Appl. Opt.*, **30**, 4427-4438.
107. A. Morel and Maritorena, S., 2001: Bio-optical properties of oceanic waters: A reappraisal, *J. Geophys. Res.*, **106**, 7163-7180.
108. F. Nadal and F. M. Bréon, 1999: Parameterization of surface polarized reflectance derived from POLDER spaceborne measurements, *IEEE Trans. Geo. Rem. Sens.*, **37**, 1709-1718.
109. T. Nakajima and M. D. King, 1996: "Determination of the optical thickness and effective particle radius of clouds from reflected solar radiation measurements. Part I: Theory," *J. Atmos. Sci.*, vol. 47, pp. 1878-1893.
110. K. B. Noone, K. J. Noone, J. Heintzenberg, J. Strom and J. A. Ogren, 1993: In situ observations of cirrus cloud microphysical properties using the Counterflow Virtual Impactor, *J. Atmos. Oceanic Technol.*, **10**, 294-303.
111. C. C. Norton, F. R. Moshier, B. Hinton, D. W. Martin, D. Santek, and W. Kuhlow, 1980: A model for calculating desert dust turbidity over the oceans from geostationary data, *J. Appl. Meteor.*, **11**, 633-644.
112. J. E. O'Reilly, S. Maritorena, B. G. Mitchell, D. A. Siegel, K. L. Carder, S. A. Garver, M. Kahru, and C. McClain, 1998: Ocean color chlorophyll algorithm for SeaWiFS, *J. Geophys. Res.*, **103**, 24,937-24,953.
113. J. M. Ortega and W. C. Reinholdt, 1970: *Iterative Solutions of Nonlinear Equations in Several Variables*, 504 pp., Academic, San Diego, CA.
114. W. Pan, M. A. Tatang, G. J. McRae, and R. G. Prinn, 1998: uncertainty analyses of indirect radiative forcing by anthropogenic aerosols, *J. Geophys. Res.*, **103**, 3815-3823.
115. S. Platnick, 2000: Vertical photon transport in cloud remote sensing problems, *J. Geophys. Res.*, **105**, 22,919-22,935.
116. C. M. R. Platt, 1978: Lidar backscatter from horizontal ice crystal plates, *J. Appl. Meteorol.*, **17**, 482-488.
117. R. M. Pope and E. S. Fry, 1997: Absorption spectrum (380-700 nm) of pure water. II. Integration cavity measurements, *Appl. Opt.*, **36**, 8710-8723.
118. P. Posse, and W. von Hoyningen-Huene, 1995: Information about scattering properties and particle characteristics of a stratiform cloud at Heligoland by remote optical measurements, *Contr. Atmos. Phys.*, **68**, 359-366.
119. J. M. Prospero and T. N. Carlson, 1972: Vertical and areal distribution of Saharan dust over the western equatorial North Atlantic Ocean, *J. Geophys. Res.*, **77**, 5255-5265.

120. F. Raes, J. Wilson, and R. van Dingenen, 1995: Aerosol dynamics and its implication for the global aerosol climatology, in *Aerosol forcing of the climate*, Chapter 8, R. J. Charlson and J. Heintzenberg, Eds., Wiley, Chichester.
121. C. R. N. Rao, L. L. Stowe, and E. P. McClain, 1989: Remote sensing of aerosols over the ocean using AVHRR data. Theory, practice, and Application, *Int. J. Remote Sensing*, **10**, 743-749.
122. L. A. Remer, A. E. Ward, and Y. J. Kaufman, 2001: Angular and seasonal variation of spectral ratios: Implications for the remote sensing of aerosol over land, *IEEE Trans. Geosci. Remote Sensing*, **39**, 275-283.
123. C. D. Rodgers, 1976: Retrieval of atmospheric temperature and composition from remote measurements of thermal radiation, *Rev. Geophys. Space Phys.*, **14**, 609-624.
124. J. Riedi, M. Doutriaux-Boucher, P. Goloub, P. Couvert, 2000: Global distribution of cloud top phase from POLDER/ADEOS I, *Geophys. Res. Lett.*, **27**, 1707-1710.
125. Rolland, K. N. Liou, M. D. King, S. C. Tsay and G. M. McFarquhar, 2000: Remote sensing of optical and microphysical properties of cirrus clouds using the Moderate Resolution Imaging Spectroradiometer channels: Methodology and sensitivity to physical assumptions, *J. Geophys. Res.*, **105**, 11,721-11,738.
126. G. Rondeaux and M. Herman, 1991: Polarization of light reflected by crop canopies, *Remote Sens. Environ.*, **38**, 63-75.
127. W. A. de Rooij, and C. C. A. H. van der Stap, 1984: Expansion of Mie scattering matrices in generalized spherical functions, *Astron. Astrophys.*, **131**, 237-248.
128. R. Santer and M. Herman, 1979: Wavelength dependence of the polarization. XXXVII. Analyses of ground-based observations of Venus, *Astron. J.*, **84**, 1802-1810.
129. R. Santer, M. Deschamps, L. V. Ksanfomality, and A. Dollfus, 1985: Photopolarimetric analysis of the Martian atmosphere by the Soviet MARS-5 orbiter, *Astron. Astrophys.*, **150**, 217-228.
130. R. Santer, M. Deschamps, L. V. Ksanfomality, and A. Dollfus, 1986: Photopolarimetry of Martian aerosols. II. Limb and terminator measurements, *Astron. Astrophys.*, **158**, 247-258.
131. R. Santer, M. Herman, D. Tanre, and J. Lenoble, 1988: Characterization of stratospheric aerosol from polarization measurements, *J. Geophys. Res.*, **93**, 14,209-14,221.
132. K. Sassen, N. C. Knight, Y. Takano, and A. J. Heymsfield, 1994: Effects of ice-crystal structure on halo formation: Cirrus cloud experimental and ray-tracing modeling studies, *Appl. Opt.*, **33**, 4590-4601.
133. K. Sassen, 2000: Lidar backscatter depolarization technique, In *Light Scattering by Nonspherical Particles: Theory, Measurements, and Applications*, eds. M. I. Mishchenko, J. W. Hovenier, and L. D. Travis, pp. 393-416, Academic Press, San Diego.
134. K. Sassen, J. M. Comstock, Zh. Wang and G. G. Mace, 2001: Cloud and aerosol research capabilities at FARS: The Facility for Atmospheric Remote Sensing, *Bull. Am. Meteorol. Soc.*, **82**, 1119-1138.
135. M. Sato, L. D. Travis, and K. Kawabata, 1996: photopolarimetry analysis of the Venus atmosphere in polar regions, *Icarus* **124**, 569-585.
136. P. M. Saunders 1967: Shadowing on the ocean and the existence of the horizon, *J. Geophys. Res.*, **72**, 4643-4649.
137. L. Sauvage, H. Chepfer, V. Trouillet, P. H. Flamant, G. Brogniez, J. Pellon and F. Albers, 1999: Remote sensing of cirrus radiative parameters during EUCREX '94. Case study of 17 April 1994. Part I: Observations, *Mon. Wea. Rev.*, **127**, 504-519.
138. Schulz, F. M., K. Stamnes, and F. Weng, 1999: VDISORT: An improved and generalized discrete ordinate radiative transfer model for polarized (vector) radiative transfer computations, *J. Quant. Spectrosc. Radiat. Transfer*, **61**, 105-122.
139. W. L. Smith, S. Ackerman, H. Revercomb, H. G. Huang, D. H. DeSlover, W. Feltz, L. Gumley and A. Collard, 1998: Infrared spectral absorption of nearly invisible cirrus clouds,

- Geophys. Res. Letts.*, **25**, 1137-1140.
140. I. N. Sokolik, and O. B. Toon, 1999: Incorporation of mineralogical composition into models of the radiative properties of mineral aerosol from UV to IR wavelengths, *J. Geophys. Res.*, **104**, 9423-9444.
 141. J. D. Spinhirne, W. D. Hart & D. L. Hlavka, 1996: Cirrus infrared parameters and shortwave reflectance relations from observations, *J. Atmos. Sci.*, **53**, 1438-1458.
 142. R. W. Spinrad and J. F. Brown, 1986: Relative real refractive index of marine microorganisms: a technique for flow cytometric estimation, *Appl. Opt.*, **25**, 1930-1934.
 143. G. L. Stephens, S.-C. Tsay, P. W. Stackhouse, Jr., and P. J. Flatau, 1990: The relevance of the microphysical and radiative properties of cirrus clouds to climate and climatic feedback, *J. Atmos. Sci.* **47**, 1742-1753.
 144. J. Stoer, 1971: On the numerical solution of constrained least square problems, *SIAM J. Num. Anal.*, **8**, 382-421.
 145. D. Stramski and D. A. Kiefer, 1991: Light scattering by microorganisms in the open ocean, *Prog. Oceanogr.*, **28**, 343-381.
 146. D. Stramski and C. D. Mobley, 1997: Effects of microbial particles on ocean optics: A database of single-particle optical properties, *Limnol. Oceanogr.*, **42**, 538-549.
 147. D. Stramski, A. Bricaud, and A. Morel, 2001: Modeling the inherent optical properties of the ocean based on the detailed composition of the planktonic community, *Appl. Opt.*, **40**, 2929-2945.
 148. B. Strauss, R. Meerketter, B. Wissinger, P. Wendling and M. Hess, 1997: On the regional climatic impact of contrails: Microphysical and radiative properties of contrails and cirrus, *Ann. Geophys.*, **15**, 1457-1467, 1997.
 149. Y. Takano, and K. N. Liou, 1995: Radiative transfer in cirrus clouds. Part III: Light scattering by irregular ice crystals, *J. Atmos. Sci.*, **52**, 818-837.
 150. Y. Takano, K. N. Liou and P. Minnis, 1992: The effects of small ice crystals on cirrus infrared radiative properties, *J. Atmos. Sci.*, **49**, 1487-1493.
 151. M. G. Tomasko and P. H. Smith, 1982: Photometry and polarimetry of Titan: Pioneer 11 observations and their implications for aerosol properties, *Icarus*, **51**, 65-95.
 152. M. G. Tomasko, R. A. West, and N. D. Castillo, 1978: Photometry and polarimetry of Jupiter at large phase angles. I. Analysis of imaging data of prominent belt and a zone from Pioneer 10, *Icarus*, **33**, 558-592.
 153. O. B. Toon, 1995: Modeling the relationships between aerosol properties and the direct and indirect effects of aerosols on climate, in *Aerosol forcing of the climate*, Chapter 11, R. J. Charlson and J. Heintzenberg, Eds., Wiley, Chichester.
 154. H. H. Tynes, G. W. Kattawar, E. P. Zege, I. L. Katsef, A. S. Prikhach, and L. I. Chaikovskaya, 2001: Monte Carlo and multicomponent approximation methods for vector radiative transfer by use of effective Mueller matrix calculations, *Appl. Opt.*, **40**, 400-412.
 155. O. Ulloa, Sathyendranath, S., and T. Platt, 1994: effect of the particle-size distribution on the backscattering ratio in seawater, *Appl. Opt.*, **33**, 7070-7077.
 156. H. C. van de Hulst, H. C., 1957: *Light Scattering by Small Particles*, 470 pp, John Wiley, New York.
 157. H. Volten, J. F. de Haan, J. W. Hovenier, R. Schreurs, W. Vassen, A. G. Dekker, H. J. Hoogenboom, and F. Charlton, 1998: Laboratory measurements of angular distributions of light scattering by phytoplankton and silt, *Limnol. Oceanogr.*, **43**, 1180-1197.
 158. K. J. Voss, and Fry, 1984: Measurement of the Mueller matrix for ocean water, *Appl. Opt.*, **23**, 4427-4439.
 159. G. Wen, S.-C. Tsay, R. F. Cahalan, L. Oreopoulos, 1999: Path radiance technique for retrieving aerosol optical thickness over land, *J. Geophys. Res.*, **104**, 31,321-31,332.
 160. R. A. West, A. L. Lane, H. Hart, K. E. Simmons, C. W. Hord, D. L. Coffeen, L. W. Esposito, M. Sato, and R. B. Pomphrey, 1983: Voyager 2 photopolarimeter observations of

- Titan, *J. Geophys. Res.*, **88**, 8699-8708.
161. B. A. Wielicki, J. T. Suttles, R. M. Heymsfield, et al, 1990: The 27-28 October 1986 FIRE IFO cirrus case study: Comparison of radiative transfer theory with observations by satellite and aircraft, *Mon. Weather Rev.*, **118**, 2356–2376.
162. W. J. Wiscombe, 1976: On initialization, error and flux conservation in the doubling method, *J. Quant. Spectrosc. Radiat. Transfer*, **16**, 637-658.
163. M. Wolff, 1980: Theory and application of the polarization-albedo rules, *Icarus*, **44**, 780-792.
164. P. Yang, and K. N. Liou, 2000: Finite Difference Time Domain Method for Light Scattering by Nonspherical and Inhomogeneous Particles, In *Light Scattering by Nonspherical Particles: Theory, Measurements, and Applications*, eds. M. I. Mishchenko, J. W. Hovenier, and L. D. Travis, pp. 173–221, Academic Press, San Diego.
165. J. R. Zaneveld, D. M. Roach, and H. Pak, 1974: The determination of the index of refraction distribution of oceanic particles, *J. Geophys. Res.*, **79**, 4091-4095.

APPENDIX A – Evaluation of required tolerances on spectral bands in order to limit contamination by gaseous absorption

Effects of line absorption and water vapor continuum on deviations of band locations and widths from nominal values. Gases included are CO₂, CO, N₂O, CH₄, H₂O, O₂ and O₂-O₂. O₃ and NO₂ are not included because the broad continuum nature of these absorption features means that within reasonable limits of deviations from nominal values the absorption caused by these gases in any given band is small. Transmission values are based on cosine solar zenith of 0.75, nadir view, 2 precipitable cm of water vapor and climatological values for all the well mixed gases. The method used takes line by line calculations (at 0.001 cm⁻¹) that are then converted into k distributions with 1nm resolution. Errors in the transmission calculated from the k distribution compared with line by line calculations are less than 0.5% even in strongly absorbing bands. For the absorber amount and geometry used here errors are substantially less than that since the transmission was tuned (see Lacis and Oinas) to be exact for a similar geometry and water vapor amount.

Nominal center	412.0 and width 20.0										
Delta	Delta Width										
Center	-5.0	-4.0	-3.0	-2.0	-1.0	0.0	1.0	2.0	3.0	4.0	5.0
-5.0	0.99991	0.99991	0.99990	0.99990	0.99989	0.99989	0.99989	0.99989	0.99988	0.99988	0.99987
-4.0	0.99992	0.99991	0.99991	0.99990	0.99990	0.99989	0.99989	0.99989	0.99988	0.99988	0.99987
-3.0	0.99992	0.99991	0.99991	0.99990	0.99990	0.99989	0.99989	0.99989	0.99988	0.99988	0.99988
-2.0	0.99991	0.99991	0.99991	0.99990	0.99990	0.99990	0.99989	0.99989	0.99989	0.99988	0.99988
-1.0	0.99991	0.99991	0.99991	0.99990	0.99990	0.99990	0.99989	0.99989	0.99989	0.99988	0.99988
0.0	0.99991	0.99991	0.99990	0.99990	0.99990	0.99990	0.99989	0.99989	0.99989	0.99989	0.99988
1.0	0.99991	0.99991	0.99990	0.99990	0.99990	0.99990	0.99989	0.99989	0.99989	0.99989	0.99988
2.0	0.99991	0.99991	0.99990	0.99990	0.99990	0.99989	0.99989	0.99989	0.99989	0.99989	0.99988
3.0	0.99991	0.99991	0.99990	0.99990	0.99990	0.99989	0.99989	0.99989	0.99989	0.99989	0.99988
4.0	0.99990	0.99990	0.99990	0.99990	0.99990	0.99989	0.99989	0.99989	0.99989	0.99989	0.99988
5.0	0.99989	0.99989	0.99990	0.99990	0.99990	0.99989	0.99989	0.99989	0.99989	0.99989	0.99988

Nominal center 445.0 and width 18.0												
Delta		Delta Width										
Center	-5.0	-4.0	-3.0	-2.0	-1.0	0.0	1.0	2.0	3.0	4.0	5.0	
-5.0	0.99847	0.99848	0.99849	0.99853	0.99857	0.99861	0.99865	0.99870	0.99874	0.99878	0.99882	
-4.0	0.99832	0.99838	0.99842	0.99848	0.99853	0.99858	0.99863	0.99868	0.99873	0.99877	0.99881	
-3.0	0.99825	0.99832	0.99838	0.99845	0.99851	0.99857	0.99862	0.99868	0.99872	0.99877	0.99881	
-2.0	0.99820	0.99829	0.99837	0.99844	0.99851	0.99857	0.99862	0.99867	0.99872	0.99876	0.99880	
-1.0	0.99818	0.99828	0.99836	0.99844	0.99850	0.99857	0.99862	0.99867	0.99872	0.99876	0.99880	
0.0	0.99817	0.99827	0.99836	0.99844	0.99850	0.99857	0.99862	0.99867	0.99872	0.99876	0.99880	
1.0	0.99817	0.99827	0.99836	0.99844	0.99850	0.99857	0.99862	0.99867	0.99872	0.99876	0.99880	
2.0	0.99818	0.99828	0.99836	0.99844	0.99850	0.99857	0.99862	0.99867	0.99872	0.99876	0.99880	
3.0	0.99820	0.99829	0.99837	0.99844	0.99851	0.99857	0.99862	0.99867	0.99872	0.99876	0.99880	
4.0	0.99829	0.99834	0.99838	0.99845	0.99851	0.99857	0.99862	0.99867	0.99872	0.99876	0.99880	
5.0	0.99854	0.99850	0.99847	0.99850	0.99853	0.99858	0.99863	0.99868	0.99872	0.99876	0.99880	

Nominal center 488.0 and width 20.0												
Delta		Delta Width										
Center	-5.0	-4.0	-3.0	-2.0	-1.0	0.0	1.0	2.0	3.0	4.0	5.0	
-5.0	0.99405	0.99410	0.99414	0.99423	0.99431	0.99442	0.99452	0.99463	0.99474	0.99486	0.99497	
-4.0	0.99484	0.99475	0.99468	0.99469	0.99470	0.99475	0.99480	0.99488	0.99495	0.99504	0.99512	
-3.0	0.99583	0.99559	0.99538	0.99527	0.99518	0.99516	0.99515	0.99518	0.99521	0.99527	0.99532	
-2.0	0.99685	0.99653	0.99625	0.99602	0.99581	0.99569	0.99559	0.99556	0.99553	0.99555	0.99556	
-1.0	0.99773	0.99743	0.99716	0.99687	0.99660	0.99637	0.99617	0.99605	0.99594	0.99589	0.99585	
0.0	0.99840	0.99816	0.99795	0.99767	0.99742	0.99714	0.99689	0.99667	0.99646	0.99633	0.99620	
1.0	0.99886	0.99870	0.99855	0.99833	0.99813	0.99787	0.99763	0.99735	0.99710	0.99684	0.99660	
2.0	0.99916	0.99906	0.99897	0.99881	0.99867	0.99845	0.99825	0.99795	0.99768	0.99733	0.99702	
3.0	0.99934	0.99928	0.99922	0.99911	0.99901	0.99881	0.99863	0.99833	0.99807	0.99748	0.99694	
4.0	0.99943	0.99938	0.99934	0.99923	0.99912	0.99892	0.99874	0.99823	0.99775	0.99730	0.99689	
5.0	0.99947	0.99938	0.99929	0.99915	0.99902	0.99855	0.99812	0.99775	0.99741	0.99716	0.99694	

Nominal center 555.0 and width 20.0												
Delta		Delta Width										
Center	-5.0	-4.0	-3.0	-2.0	-1.0	0.0	1.0	2.0	3.0	4.0	5.0	
-5.0	0.99615	0.99601	0.99589	0.99587	0.99586	0.99591	0.99595	0.99599	0.99603	0.99606	0.99609	
-4.0	0.99644	0.99637	0.99630	0.99615	0.99601	0.99596	0.99592	0.99594	0.99595	0.99597	0.99598	
-3.0	0.99678	0.99664	0.99652	0.99642	0.99633	0.99616	0.99601	0.99594	0.99587	0.99585	0.99583	
-2.0	0.99695	0.99684	0.99675	0.99660	0.99646	0.99635	0.99624	0.99605	0.99587	0.99577	0.99567	
-1.0	0.99713	0.99698	0.99684	0.99672	0.99661	0.99643	0.99628	0.99612	0.99599	0.99575	0.99554	
0.0	0.99741	0.99716	0.99694	0.99676	0.99660	0.99644	0.99630	0.99608	0.99588	0.99565	0.99545	
1.0	0.99737	0.99721	0.99707	0.99680	0.99656	0.99634	0.99614	0.99590	0.99569	0.99520	0.99475	
2.0	0.99719	0.99704	0.99691	0.99670	0.99652	0.99618	0.99587	0.99536	0.99489	0.99436	0.99387	
3.0	0.99691	0.99672	0.99656	0.99633	0.99612	0.99560	0.99513	0.99448	0.99388	0.99346	0.99308	
4.0	0.99646	0.99623	0.99602	0.99550	0.99502	0.99445	0.99393	0.99352	0.99314	0.99273	0.99236	
5.0	0.99581	0.99525	0.99476	0.99416	0.99362	0.99323	0.99287	0.99256	0.99227	0.99182	0.99141	

Nominal center 672.0 and width 20.0												
Delta		Delta Width										
Center	-5.0	-4.0	-3.0	-2.0	-1.0	0.0	1.0	2.0	3.0	4.0	5.0	
-5.0	0.99997	0.99997	0.99997	0.99996	0.99994	0.99994	0.99995	0.99994	0.99993	0.99993	0.99993	
-4.0	0.99997	0.99997	0.99997	0.99997	0.99997	0.99996	0.99995	0.99995	0.99994	0.99993	0.99992	
-3.0	0.99997	0.99997	0.99997	0.99997	0.99997	0.99997	0.99997	0.99997	0.99995	0.99993	0.99992	
-2.0	0.99997	0.99997	0.99997	0.99997	0.99997	0.99996	0.99995	0.99993	0.99992	0.99989	0.99986	
-1.0	0.99997	0.99997	0.99997	0.99996	0.99995	0.99993	0.99991	0.99989	0.99987	0.99986	0.99984	
0.0	0.99997	0.99996	0.99995	0.99993	0.99991	0.99988	0.99986	0.99985	0.99984	0.99980	0.99976	

1.0	0.99994	0.99992	0.99990	0.99987	0.99985	0.99984	0.99982	0.99978	0.99975	0.99973	0.99971
2.0	0.99989	0.99986	0.99984	0.99982	0.99981	0.99976	0.99973	0.99971	0.99969	0.99841	0.99724
3.0	0.99982	0.99980	0.99979	0.99974	0.99970	0.99968	0.99966	0.99828	0.99701	0.98858	0.98081
4.0	0.99976	0.99971	0.99967	0.99965	0.99963	0.99811	0.99674	0.98759	0.97921	0.97733	0.97559
5.0	0.99965	0.99961	0.99959	0.99791	0.99641	0.98641	0.97732	0.97535	0.97355	0.97026	0.96722

Nominal center 865.0 and width 20.0

Delta	Delta Width										
Center	-5.0	-4.0	-3.0	-2.0	-1.0	0.0	1.0	2.0	3.0	4.0	5.0
-5.0	0.99626	0.99591	0.99559	0.99551	0.99543	0.99536	0.99529	0.99510	0.99493	0.99510	0.99525
-4.0	0.99710	0.99687	0.99667	0.99633	0.99603	0.99593	0.99583	0.99575	0.99567	0.99549	0.99532
-3.0	0.99762	0.99751	0.99741	0.99719	0.99698	0.99666	0.99637	0.99627	0.99618	0.99608	0.99600
-2.0	0.99843	0.99813	0.99786	0.99775	0.99765	0.99744	0.99725	0.99695	0.99667	0.99656	0.99645
-1.0	0.99892	0.99874	0.99858	0.99831	0.99807	0.99796	0.99787	0.99765	0.99746	0.99715	0.99686
0.0	0.99906	0.99905	0.99904	0.99887	0.99872	0.99846	0.99822	0.99809	0.99797	0.99777	0.99758
1.0	0.99954	0.99934	0.99916	0.99913	0.99910	0.99892	0.99875	0.99851	0.99829	0.99810	0.99793
2.0	0.99956	0.99956	0.99956	0.99934	0.99915	0.99913	0.99910	0.99886	0.99864	0.99844	0.99825
3.0	0.99970	0.99960	0.99951	0.99951	0.99951	0.99924	0.99900	0.99899	0.99898	0.99876	0.99855
4.0	0.99963	0.99963	0.99963	0.99946	0.99930	0.99932	0.99934	0.99909	0.99887	0.99879	0.99871
5.0	0.99968	0.99952	0.99939	0.99941	0.99943	0.99927	0.99913	0.99907	0.99902	0.99875	0.99850

Nominal center 1610.0 and width 60.0

Delta	Delta Width										
Center	-5.0	-4.0	-3.0	-2.0	-1.0	0.0	1.0	2.0	3.0	4.0	5.0
-5.0	0.96071	0.96040	0.96009	0.96040	0.96069	0.96037	0.96006	0.95974	0.95943	0.95850	0.95759
-4.0	0.96197	0.96176	0.96157	0.96111	0.96068	0.96095	0.96122	0.96080	0.96039	0.96009	0.95979
-3.0	0.96347	0.96298	0.96250	0.96229	0.96208	0.96153	0.96100	0.96127	0.96153	0.96119	0.96086
-2.0	0.96439	0.96416	0.96393	0.96334	0.96277	0.96257	0.96238	0.96191	0.96146	0.96128	0.96111
-1.0	0.96576	0.96517	0.96461	0.96439	0.96417	0.96368	0.96320	0.96255	0.96191	0.96154	0.96118
0.0	0.96600	0.96597	0.96594	0.96546	0.96498	0.96430	0.96364	0.96324	0.96285	0.96217	0.96151
1.0	0.96654	0.96644	0.96634	0.96583	0.96533	0.96494	0.96457	0.96386	0.96317	0.96278	0.96240
2.0	0.96636	0.96612	0.96589	0.96588	0.96586	0.96532	0.96479	0.96442	0.96405	0.96385	0.96365
3.0	0.96549	0.96568	0.96587	0.96559	0.96531	0.96530	0.96529	0.96526	0.96524	0.96437	0.96352
4.0	0.96520	0.96505	0.96491	0.96509	0.96527	0.96552	0.96575	0.96522	0.96470	0.96464	0.96459
5.0	0.96420	0.96441	0.96461	0.96500	0.96538	0.96502	0.96467	0.96487	0.96507	0.96510	0.96513

Nominal center 1378.0 and width 15.0

Delta	Delta Width										
Center	-5.0	-4.0	-3.0	-2.0	-1.0	0.0	1.0	2.0	3.0	4.0	5.0
-5.0	0.00017	0.00016	0.00015	0.00014	0.00013	0.00012	0.00011	0.00011	0.00011	0.00010	0.00009
-4.0	0.00017	0.00016	0.00015	0.00014	0.00013	0.00012	0.00011	0.00011	0.00011	0.00010	0.00009
-3.0	0.00017	0.00016	0.00015	0.00014	0.00013	0.00012	0.00011	0.00011	0.00011	0.00010	0.00009
-2.0	0.00017	0.00016	0.00015	0.00014	0.00013	0.00012	0.00011	0.00011	0.00011	0.00010	0.00009
-1.0	0.00017	0.00016	0.00015	0.00014	0.00013	0.00012	0.00011	0.00011	0.00011	0.00010	0.00009
0.0	0.00017	0.00016	0.00015	0.00014	0.00013	0.00012	0.00011	0.00011	0.00011	0.00010	0.00009
1.0	0.00017	0.00016	0.00015	0.00014	0.00013	0.00012	0.00011	0.00011	0.00011	0.00010	0.00010
2.0	0.00017	0.00015	0.00014	0.00014	0.00013	0.00012	0.00011	0.00011	0.00011	0.00011	0.00011
3.0	0.00015	0.00015	0.00014	0.00013	0.00013	0.00012	0.00012	0.00013	0.00012	0.00012	0.00012
4.0	0.00013	0.00012	0.00013	0.00013	0.00013	0.00014	0.00014	0.00014	0.00013	0.00013	0.00012
5.0	0.00007	0.00012	0.00013	0.00013	0.00014	0.00015	0.00014	0.00014	0.00013	0.00013	0.00012

Nominal center 2250.0 and width 50.0

Delta	Delta Width										
Center	-5.0	-4.0	-3.0	-2.0	-1.0	0.0	1.0	2.0	3.0	4.0	5.0
-5.0	0.91690	0.91479	0.91277	0.91357	0.91434	0.91437	0.91439	0.91494	0.91547	0.91525	0.91504

-4.0	0.91228	0.91291	0.91351	0.91291	0.91233	0.91305	0.91374	0.91335	0.91297	0.91356	0.91412
-3.0	0.91169	0.91177	0.91185	0.91240	0.91292	0.91191	0.91094	0.91168	0.91240	0.91295	0.91347
-2.0	0.90946	0.91032	0.91115	0.91078	0.91042	0.91100	0.91157	0.91155	0.91153	0.91012	0.90876
-1.0	0.91074	0.90937	0.90807	0.90896	0.90981	0.91044	0.91105	0.90940	0.90782	0.90732	0.90683
0.0	0.90850	0.90894	0.90936	0.90908	0.90882	0.90737	0.90599	0.90609	0.90620	0.90646	0.90672
1.0	0.90859	0.90894	0.90927	0.90729	0.90540	0.90462	0.90387	0.90440	0.90491	0.90562	0.90631
2.0	0.90743	0.90593	0.90450	0.90430	0.90410	0.90420	0.90430	0.90418	0.90406	0.90531	0.90651
3.0	0.90137	0.90176	0.90212	0.90277	0.90339	0.90385	0.90430	0.90516	0.90599	0.90486	0.90378
4.0	0.89903	0.89970	0.90035	0.90140	0.90241	0.90382	0.90518	0.90457	0.90399	0.90443	0.90486
5.0	0.89860	0.89903	0.89945	0.90092	0.90233	0.90225	0.90216	0.90311	0.90403	0.90345	0.90289

Nominal center 905.0 and width 30.0

Delta	Delta Width										
Center	-5.0	-4.0	-3.0	-2.0	-1.0	0.0	1.0	2.0	3.0	4.0	5.0
-5.0	0.76965	0.76613	0.76286	0.76661	0.77012	0.76886	0.76767	0.77084	0.77382	0.77273	0.77171
-4.0	0.74565	0.75043	0.75486	0.75372	0.75267	0.75650	0.76009	0.75941	0.75877	0.76094	0.76299
-3.0	0.73710	0.73651	0.73596	0.74073	0.74518	0.74464	0.74414	0.74686	0.74942	0.75304	0.75646
-2.0	0.71703	0.72272	0.72800	0.72799	0.72798	0.73149	0.73478	0.73879	0.74256	0.74807	0.75328
-1.0	0.70825	0.70907	0.70983	0.71409	0.71805	0.72283	0.72731	0.73370	0.73972	0.74284	0.74579
0.0	0.68914	0.69425	0.69900	0.70486	0.71033	0.71756	0.72435	0.72810	0.73163	0.73728	0.74261
1.0	0.67769	0.68467	0.69115	0.69934	0.70699	0.71163	0.71598	0.72233	0.72832	0.73242	0.73630
2.0	0.67245	0.68039	0.68777	0.69330	0.69845	0.70559	0.71229	0.71721	0.72184	0.72493	0.72786
3.0	0.67365	0.67778	0.68161	0.68838	0.69471	0.70042	0.70578	0.70937	0.71274	0.71777	0.72253
4.0	0.67182	0.67715	0.68209	0.68646	0.69055	0.69351	0.69629	0.70204	0.70745	0.71185	0.71601
5.0	0.67939	0.68080	0.68210	0.68340	0.68462	0.68909	0.69327	0.69711	0.70071	0.70477	0.70860

Nominal center 936.0 and width 10.0

Delta	Delta Width										
Center	-5.0	-4.0	-3.0	-2.0	-1.0	0.0	1.0	2.0	3.0	4.0	5.0
-5.0	0.29258	0.30511	0.31452	0.33246	0.34682	0.35774	0.36684	0.36945	0.37168	0.37676	0.38122
-4.0	0.22721	0.24108	0.25149	0.27062	0.28592	0.29974	0.31126	0.32286	0.33281	0.35093	0.36679
-3.0	0.18697	0.20201	0.21330	0.22140	0.22788	0.24524	0.25971	0.28911	0.31431	0.33032	0.34432
-2.0	0.15057	0.16372	0.17359	0.18624	0.19636	0.22307	0.24534	0.26578	0.28330	0.30007	0.31474
-1.0	0.13387	0.14028	0.14508	0.17859	0.20539	0.22124	0.23445	0.24588	0.25568	0.27166	0.28563
0.0	0.13030	0.16073	0.18356	0.19327	0.20105	0.21363	0.22412	0.23487	0.24409	0.25268	0.26020
1.0	0.19810	0.20144	0.20395	0.20753	0.21040	0.21447	0.21786	0.22644	0.23379	0.23639	0.23867
2.0	0.24169	0.23387	0.22801	0.22553	0.22354	0.22377	0.22396	0.21936	0.21542	0.22231	0.22834
3.0	0.26127	0.25869	0.25675	0.24787	0.24077	0.22930	0.21975	0.21942	0.21914	0.22037	0.22144
4.0	0.28514	0.27586	0.26890	0.25593	0.24555	0.23835	0.23234	0.22893	0.22601	0.22412	0.22246
5.0	0.31406	0.28548	0.26405	0.25800	0.25317	0.25065	0.24856	0.24085	0.23425	0.23217	0.23036

Nominal center 940.0 and width 50.0

Delta	Delta Width										
Center	-5.0	-4.0	-3.0	-2.0	-1.0	0.0	1.0	2.0	3.0	4.0	5.0
-5.0	0.41550	0.41891	0.42218	0.42145	0.42074	0.42298	0.42512	0.42740	0.42960	0.42992	0.43022
-4.0	0.40908	0.41007	0.41102	0.41410	0.41705	0.41937	0.42160	0.42320	0.42475	0.42739	0.42993
-3.0	0.40581	0.40503	0.40428	0.40837	0.41230	0.41468	0.41697	0.41966	0.42224	0.42445	0.42659
-2.0	0.39740	0.40249	0.40736	0.40601	0.40471	0.40910	0.41333	0.41630	0.41916	0.42189	0.42452
-1.0	0.39855	0.39834	0.39813	0.40349	0.40862	0.40803	0.40746	0.41182	0.41602	0.41908	0.42204
0.0	0.38894	0.39471	0.40023	0.40076	0.40126	0.40653	0.41160	0.41123	0.41088	0.41652	0.42197
1.0	0.39084	0.39172	0.39257	0.39823	0.40366	0.40437	0.40505	0.41161	0.41793	0.42004	0.42208
2.0	0.38448	0.38975	0.39480	0.39585	0.39686	0.40384	0.41055	0.41377	0.41687	0.42334	0.42958
3.0	0.38078	0.38512	0.38928	0.39593	0.40231	0.40596	0.40946	0.41631	0.42290	0.42633	0.42964
4.0	0.37061	0.38010	0.38919	0.39608	0.40269	0.40920	0.41546	0.41929	0.42297	0.42905	0.43491
5.0	0.37130	0.37847	0.38535	0.39455	0.40339	0.41032	0.41698	0.42269	0.42819	0.43172	0.43512

The following sensitivity analysis uses only water vapor absorption since it is typically easier to correct for absorption contamination by well mixed gases than water vapor.

Nominal center 412.0 and width 20.0

Delta	Delta Width										
Center	-5.0	-4.0	-3.0	-2.0	-1.0	0.0	1.0	2.0	3.0	4.0	5.0
-5.0	0.99999	0.99999	0.99998	0.99998	0.99997	0.99997	0.99997	0.99997	0.99996	0.99996	0.99995
-4.0	1.00000	0.99999	0.99999	0.99999	0.99998	0.99998	0.99998	0.99998	0.99997	0.99997	0.99996
-3.0	1.00000	1.00000	1.00000	0.99999	0.99999	0.99999	0.99999	0.99999	0.99998	0.99998	0.99997
-2.0	1.00000	1.00000	1.00000	1.00000	1.00000	1.00000	0.99999	0.99999	0.99999	0.99998	0.99998
-1.0	1.00000	1.00000	1.00000	1.00000	1.00000	1.00000	1.00000	1.00000	1.00000	0.99999	0.99999
0.0	1.00000	1.00000	1.00000	1.00000	1.00000	1.00000	1.00000	1.00000	1.00000	1.00000	0.99999
1.0	1.00000	1.00000	1.00000	1.00000	1.00000	1.00000	1.00000	1.00000	1.00000	1.00000	1.00000
2.0	1.00000	1.00000	1.00000	1.00000	1.00000	1.00000	1.00000	1.00000	1.00000	1.00000	1.00000
3.0	1.00000	1.00000	1.00000	1.00000	1.00000	1.00000	1.00000	1.00000	1.00000	1.00000	1.00000
4.0	1.00000	1.00000	1.00000	1.00000	1.00000	1.00000	1.00000	1.00000	1.00000	1.00000	1.00000
5.0	1.00000	1.00000	1.00000	1.00000	1.00000	1.00000	1.00000	1.00000	1.00000	1.00000	1.00000

Nominal center 445.0 and width 18.0

Delta	Delta Width										
Center	-5.0	-4.0	-3.0	-2.0	-1.0	0.0	1.0	2.0	3.0	4.0	5.0
-5.0	0.99912	0.99915	0.99917	0.99922	0.99926	0.99929	0.99932	0.99936	0.99939	0.99941	0.99944
-4.0	0.99906	0.99911	0.99916	0.99921	0.99925	0.99929	0.99932	0.99936	0.99939	0.99941	0.99944
-3.0	0.99904	0.99910	0.99916	0.99921	0.99925	0.99929	0.99932	0.99936	0.99939	0.99941	0.99944
-2.0	0.99904	0.99910	0.99916	0.99921	0.99925	0.99929	0.99932	0.99936	0.99939	0.99941	0.99944
-1.0	0.99904	0.99910	0.99916	0.99921	0.99925	0.99929	0.99932	0.99936	0.99939	0.99941	0.99944
0.0	0.99904	0.99910	0.99916	0.99921	0.99925	0.99929	0.99932	0.99936	0.99939	0.99941	0.99944
1.0	0.99904	0.99910	0.99916	0.99921	0.99925	0.99929	0.99932	0.99936	0.99939	0.99941	0.99944
2.0	0.99904	0.99910	0.99916	0.99921	0.99925	0.99929	0.99932	0.99936	0.99939	0.99941	0.99944
3.0	0.99905	0.99911	0.99916	0.99921	0.99925	0.99929	0.99932	0.99936	0.99939	0.99941	0.99944
4.0	0.99913	0.99915	0.99917	0.99921	0.99925	0.99929	0.99932	0.99936	0.99939	0.99941	0.99944
5.0	0.99935	0.99929	0.99924	0.99925	0.99926	0.99929	0.99933	0.99936	0.99939	0.99941	0.99944

Nominal center 488.0 and width 20.0

Delta	Delta Width										
Center	-5.0	-4.0	-3.0	-2.0	-1.0	0.0	1.0	2.0	3.0	4.0	5.0
-5.0	0.99976	0.99977	0.99977	0.99977	0.99977	0.99977	0.99976	0.99976	0.99975	0.99975	0.99974
-4.0	0.99975	0.99976	0.99978	0.99978	0.99979	0.99979	0.99979	0.99979	0.99978	0.99978	0.99977
-3.0	0.99975	0.99976	0.99978	0.99979	0.99980	0.99980	0.99981	0.99981	0.99981	0.99980	0.99980
-2.0	0.99975	0.99976	0.99978	0.99979	0.99980	0.99981	0.99982	0.99982	0.99983	0.99982	0.99982
-1.0	0.99975	0.99976	0.99978	0.99979	0.99980	0.99981	0.99982	0.99982	0.99983	0.99983	0.99983
0.0	0.99975	0.99976	0.99978	0.99979	0.99980	0.99981	0.99982	0.99982	0.99982	0.99981	0.99981
1.0	0.99975	0.99976	0.99978	0.99979	0.99980	0.99980	0.99980	0.99980	0.99979	0.99975	0.99971
2.0	0.99975	0.99976	0.99977	0.99978	0.99978	0.99978	0.99977	0.99973	0.99969	0.99960	0.99952
3.0	0.99975	0.99975	0.99976	0.99976	0.99975	0.99970	0.99966	0.99956	0.99948	0.99913	0.99881
4.0	0.99973	0.99973	0.99972	0.99967	0.99962	0.99952	0.99943	0.99906	0.99871	0.99845	0.99820
5.0	0.99972	0.99965	0.99958	0.99947	0.99938	0.99897	0.99859	0.99831	0.99805	0.99794	0.99783

Nominal center 555.0 and width 20.0

Delta	Delta Width										
Center	-5.0	-4.0	-3.0	-2.0	-1.0	0.0	1.0	2.0	3.0	4.0	5.0
-5.0	0.99751	0.99739	0.99729	0.99730	0.99732	0.99740	0.99748	0.99757	0.99765	0.99773	0.99781
-4.0	0.99787	0.99782	0.99778	0.99766	0.99755	0.99755	0.99754	0.99761	0.99768	0.99775	0.99782

-3.0	0.99829	0.99819	0.99810	0.99804	0.99798	0.99787	0.99776	0.99775	0.99774	0.99779	0.99784
-2.0	0.99858	0.99852	0.99846	0.99836	0.99827	0.99821	0.99816	0.99804	0.99793	0.99791	0.99789
-1.0	0.99892	0.99881	0.99872	0.99866	0.99861	0.99850	0.99841	0.99835	0.99829	0.99816	0.99804
0.0	0.99938	0.99919	0.99903	0.99892	0.99883	0.99877	0.99871	0.99859	0.99849	0.99839	0.99830
1.0	0.99958	0.99950	0.99943	0.99925	0.99910	0.99898	0.99888	0.99878	0.99868	0.99834	0.99803
2.0	0.99969	0.99964	0.99960	0.99950	0.99942	0.99922	0.99903	0.99867	0.99835	0.99799	0.99766
3.0	0.99978	0.99971	0.99965	0.99956	0.99948	0.99912	0.99879	0.99832	0.99789	0.99767	0.99747
4.0	0.99979	0.99970	0.99963	0.99926	0.99894	0.99855	0.99819	0.99799	0.99781	0.99763	0.99747
5.0	0.99970	0.99932	0.99898	0.99857	0.99820	0.99802	0.99785	0.99778	0.99771	0.99751	0.99732

Nominal center 672.0 and width 20.0

Delta	Delta Width										
Center	-5.0	-4.0	-3.0	-2.0	-1.0	0.0	1.0	2.0	3.0	4.0	5.0
-5.0	0.99997	0.99997	0.99997	0.99996	0.99994	0.99994	0.99994	0.99995	0.99994	0.99993	0.99993
-4.0	0.99997	0.99997	0.99997	0.99997	0.99997	0.99997	0.99996	0.99995	0.99995	0.99994	0.99992
-3.0	0.99997	0.99997	0.99997	0.99997	0.99997	0.99997	0.99997	0.99997	0.99995	0.99993	0.99992
-2.0	0.99997	0.99997	0.99997	0.99997	0.99997	0.99997	0.99996	0.99995	0.99993	0.99992	0.99989
-1.0	0.99997	0.99997	0.99997	0.99996	0.99995	0.99993	0.99991	0.99989	0.99987	0.99986	0.99984
0.0	0.99997	0.99996	0.99995	0.99993	0.99991	0.99988	0.99986	0.99985	0.99984	0.99980	0.99976
1.0	0.99994	0.99992	0.99990	0.99987	0.99985	0.99984	0.99982	0.99978	0.99975	0.99973	0.99971
2.0	0.99989	0.99986	0.99984	0.99982	0.99981	0.99976	0.99973	0.99971	0.99969	0.99968	0.99967
3.0	0.99982	0.99980	0.99979	0.99974	0.99970	0.99968	0.99966	0.99965	0.99964	0.99965	0.99965
4.0	0.99976	0.99971	0.99967	0.99965	0.99963	0.99962	0.99961	0.99962	0.99962	0.99963	0.99964
5.0	0.99965	0.99962	0.99959	0.99958	0.99958	0.99958	0.99959	0.99960	0.99961	0.99960	0.99959

Nominal center 865.0 and width 20.0

Delta	Delta Width										
Center	-5.0	-4.0	-3.0	-2.0	-1.0	0.0	1.0	2.0	3.0	4.0	5.0
-5.0	0.99636	0.99600	0.99569	0.99560	0.99552	0.99544	0.99537	0.99518	0.99500	0.99517	0.99532
-4.0	0.99720	0.99697	0.99676	0.99642	0.99611	0.99601	0.99591	0.99582	0.99574	0.99556	0.99538
-3.0	0.99772	0.99761	0.99751	0.99728	0.99707	0.99674	0.99645	0.99635	0.99625	0.99615	0.99607
-2.0	0.99853	0.99823	0.99796	0.99784	0.99774	0.99753	0.99733	0.99703	0.99675	0.99662	0.99651
-1.0	0.99903	0.99884	0.99868	0.99840	0.99816	0.99805	0.99794	0.99773	0.99753	0.99721	0.99692
0.0	0.99917	0.99915	0.99913	0.99896	0.99881	0.99854	0.99830	0.99816	0.99804	0.99783	0.99765
1.0	0.99964	0.99944	0.99926	0.99922	0.99919	0.99900	0.99883	0.99859	0.99836	0.99817	0.99799
2.0	0.99967	0.99966	0.99965	0.99943	0.99924	0.99921	0.99918	0.99894	0.99872	0.99850	0.99831
3.0	0.99980	0.99970	0.99960	0.99960	0.99959	0.99932	0.99908	0.99907	0.99905	0.99882	0.99861
4.0	0.99973	0.99973	0.99972	0.99955	0.99939	0.99940	0.99942	0.99917	0.99894	0.99885	0.99878
5.0	0.99977	0.99962	0.99948	0.99950	0.99952	0.99935	0.99921	0.99915	0.99909	0.99882	0.99857

Nominal center 1610.0 and width 60.0

Delta	Delta Width										
Center	-5.0	-4.0	-3.0	-2.0	-1.0	0.0	1.0	2.0	3.0	4.0	5.0
-5.0	0.99558	0.99560	0.99562	0.99562	0.99562	0.99562	0.99565	0.99567	0.99568	0.99568	0.99574
-4.0	0.99555	0.99558	0.99561	0.99561	0.99561	0.99561	0.99562	0.99563	0.99569	0.99574	0.99579
-3.0	0.99560	0.99557	0.99554	0.99558	0.99562	0.99565	0.99568	0.99571	0.99574	0.99561	0.99548
-2.0	0.99554	0.99557	0.99561	0.99561	0.99562	0.99568	0.99573	0.99558	0.99542	0.99545	0.99547
-1.0	0.99551	0.99557	0.99562	0.99567	0.99573	0.99554	0.99535	0.99540	0.99546	0.99546	0.99547
0.0	0.99554	0.99559	0.99563	0.99549	0.99534	0.99539	0.99544	0.99542	0.99540	0.99542	0.99545
1.0	0.99564	0.99545	0.99526	0.99530	0.99534	0.99537	0.99539	0.99541	0.99543	0.99544	0.99544
2.0	0.99536	0.99535	0.99534	0.99532	0.99531	0.99532	0.99533	0.99539	0.99544	0.99549	0.99554
3.0	0.99535	0.99538	0.99541	0.99537	0.99533	0.99535	0.99536	0.99540	0.99545	0.99530	0.99516
4.0	0.99531	0.99533	0.99535	0.99540	0.99546	0.99545	0.99545	0.99526	0.99508	0.99506	0.99504
5.0	0.99545	0.99540	0.99536	0.99541	0.99547	0.99531	0.99516	0.99509	0.99503	0.99503	0.99503

Nominal center 1378.0 and width 15.0

Delta	Delta Width										
Center	-5.0	-4.0	-3.0	-2.0	-1.0	0.0	1.0	2.0	3.0	4.0	5.0
-5.0	0.00017	0.00016	0.00015	0.00014	0.00013	0.00012	0.00011	0.00011	0.00010	0.00009	0.00009
-4.0	0.00017	0.00016	0.00015	0.00014	0.00013	0.00012	0.00011	0.00011	0.00010	0.00009	0.00009
-3.0	0.00017	0.00016	0.00015	0.00014	0.00013	0.00012	0.00011	0.00011	0.00010	0.00009	0.00009
-2.0	0.00017	0.00016	0.00015	0.00014	0.00013	0.00012	0.00011	0.00011	0.00010	0.00009	0.00009
-1.0	0.00017	0.00016	0.00015	0.00014	0.00013	0.00012	0.00011	0.00011	0.00010	0.00010	0.00009
0.0	0.00017	0.00016	0.00015	0.00014	0.00013	0.00012	0.00011	0.00011	0.00010	0.00010	0.00009
1.0	0.00017	0.00016	0.00015	0.00014	0.00013	0.00012	0.00011	0.00011	0.00010	0.00010	0.00010
2.0	0.00017	0.00015	0.00014	0.00014	0.00013	0.00012	0.00011	0.00011	0.00011	0.00011	0.00011
3.0	0.00015	0.00015	0.00014	0.00013	0.00013	0.00012	0.00012	0.00013	0.00012	0.00012	0.00012
4.0	0.00013	0.00012	0.00013	0.00013	0.00013	0.00014	0.00014	0.00014	0.00013	0.00013	0.00012
5.0	0.00007	0.00012	0.00013	0.00013	0.00014	0.00015	0.00014	0.00014	0.00013	0.00013	0.00012

Nominal center 2250.0 and width 50.0

Delta	Delta Width										
Center	-5.0	-4.0	-3.0	-2.0	-1.0	0.0	1.0	2.0	3.0	4.0	5.0
-5.0	0.98598	0.98612	0.98626	0.98627	0.98627	0.98611	0.98595	0.98586	0.98578	0.98585	0.98593
-4.0	0.98666	0.98636	0.98608	0.98622	0.98635	0.98640	0.98645	0.98626	0.98608	0.98600	0.98591
-3.0	0.98690	0.98682	0.98674	0.98650	0.98627	0.98638	0.98648	0.98652	0.98656	0.98638	0.98621
-2.0	0.98687	0.98697	0.98706	0.98696	0.98686	0.98662	0.98639	0.98650	0.98660	0.98663	0.98666
-1.0	0.98928	0.98811	0.98699	0.98707	0.98716	0.98706	0.98696	0.98673	0.98651	0.98662	0.98672
0.0	0.98939	0.98933	0.98928	0.98817	0.98709	0.98717	0.98725	0.98716	0.98707	0.98685	0.98663
1.0	0.98932	0.98936	0.98940	0.98934	0.98929	0.98823	0.98720	0.98728	0.98735	0.98726	0.98717
2.0	0.98919	0.98926	0.98932	0.98937	0.98942	0.98937	0.98932	0.98829	0.98730	0.98736	0.98742
3.0	0.98913	0.98918	0.98922	0.98928	0.98935	0.98939	0.98943	0.98937	0.98931	0.98831	0.98735
4.0	0.98905	0.98911	0.98917	0.98920	0.98924	0.98929	0.98934	0.98938	0.98941	0.98931	0.98922
5.0	0.98894	0.98901	0.98908	0.98912	0.98917	0.98920	0.98922	0.98923	0.98924	0.98927	0.98930

Nominal center 905.0 and width 30.0

Delta	Delta Width										
Center	-5.0	-4.0	-3.0	-2.0	-1.0	0.0	1.0	2.0	3.0	4.0	5.0
-5.0	0.76965	0.76613	0.76286	0.76661	0.77012	0.76886	0.76767	0.77084	0.77382	0.77273	0.77171
-4.0	0.74565	0.75043	0.75486	0.75372	0.75267	0.75650	0.76009	0.75941	0.75877	0.76094	0.76299
-3.0	0.73710	0.73651	0.73596	0.74073	0.74518	0.74464	0.74414	0.74686	0.74942	0.75304	0.75646
-2.0	0.71703	0.72272	0.72800	0.72799	0.72798	0.73149	0.73478	0.73879	0.74256	0.74807	0.75328
-1.0	0.70825	0.70907	0.70983	0.71409	0.71805	0.72283	0.72731	0.73370	0.73972	0.74284	0.74579
0.0	0.68914	0.69425	0.69900	0.70486	0.71033	0.71756	0.72435	0.72810	0.73163	0.73728	0.74261
1.0	0.67769	0.68467	0.69115	0.69934	0.70699	0.71163	0.71598	0.72233	0.72832	0.73242	0.73630
2.0	0.67245	0.68039	0.68777	0.69330	0.69845	0.70559	0.71229	0.71721	0.72184	0.72493	0.72786
3.0	0.67365	0.67778	0.68161	0.68838	0.69471	0.70042	0.70578	0.70937	0.71274	0.71777	0.72253
4.0	0.67182	0.67715	0.68209	0.68646	0.69055	0.69351	0.69629	0.70204	0.70745	0.71185	0.71601
5.0	0.67939	0.68080	0.68210	0.68340	0.68462	0.68909	0.69327	0.69711	0.70071	0.70477	0.70860

Nominal center 936.0 and width 10.0

Delta	Delta Width										
Center	-5.0	-4.0	-3.0	-2.0	-1.0	0.0	1.0	2.0	3.0	4.0	5.0
-5.0	0.29258	0.30511	0.31452	0.33246	0.34682	0.35774	0.36684	0.36945	0.37168	0.37676	0.38122
-4.0	0.22721	0.24108	0.25149	0.27062	0.28592	0.29974	0.31126	0.32286	0.33281	0.35093	0.36679
-3.0	0.18697	0.20201	0.21330	0.22140	0.22788	0.24524	0.25971	0.28911	0.31431	0.33032	0.34432
-2.0	0.15057	0.16372	0.17359	0.18624	0.19636	0.22307	0.24534	0.26578	0.28330	0.30007	0.31474
-1.0	0.13387	0.14028	0.14508	0.17859	0.20539	0.22124	0.23445	0.24588	0.25568	0.27166	0.28563
0.0	0.13030	0.16073	0.18356	0.19327	0.20105	0.21363	0.22412	0.23487	0.24409	0.25268	0.26020
1.0	0.19810	0.20144	0.20395	0.20753	0.21040	0.21447	0.21786	0.22644	0.23379	0.23639	0.23867

2.0	0.24169	0.23387	0.22801	0.22553	0.22354	0.22377	0.22396	0.21936	0.21542	0.22231	0.22834
3.0	0.26127	0.25869	0.25675	0.24787	0.24077	0.22930	0.21975	0.21942	0.21914	0.22037	0.22144
4.0	0.28514	0.27586	0.26890	0.25593	0.24555	0.23835	0.23234	0.22893	0.22601	0.22412	0.22246
5.0	0.31406	0.28548	0.26405	0.25800	0.25317	0.25065	0.24856	0.24085	0.23425	0.23217	0.23036

Nominal center 940.0 and width 50.0

Delta	Delta Width										
Center	-5.0	-4.0	-3.0	-2.0	-1.0	0.0	1.0	2.0	3.0	4.0	5.0
-5.0	0.41550	0.41891	0.42218	0.42145	0.42074	0.42298	0.42512	0.42740	0.42960	0.42992	0.43022
-4.0	0.40908	0.41007	0.41102	0.41410	0.41705	0.41937	0.42160	0.42320	0.42475	0.42739	0.42993
-3.0	0.40581	0.40503	0.40428	0.40837	0.41230	0.41468	0.41697	0.41966	0.42224	0.42445	0.42659
-2.0	0.39740	0.40249	0.40736	0.40601	0.40471	0.40910	0.41333	0.41630	0.41916	0.42189	0.42452
-1.0	0.39855	0.39834	0.39813	0.40349	0.40862	0.40803	0.40746	0.41182	0.41602	0.41908	0.42204
0.0	0.38894	0.39471	0.40023	0.40076	0.40126	0.40653	0.41160	0.41123	0.41088	0.41652	0.42197
1.0	0.39084	0.39172	0.39257	0.39823	0.40366	0.40437	0.40505	0.41161	0.41793	0.42004	0.42208
2.0	0.38448	0.38975	0.39480	0.39585	0.39686	0.40384	0.41055	0.41377	0.41687	0.42334	0.42958
3.0	0.38078	0.38512	0.38928	0.39593	0.40231	0.40596	0.40946	0.41631	0.42290	0.42633	0.42964
4.0	0.37061	0.38010	0.38919	0.39608	0.40269	0.40920	0.41546	0.41929	0.42297	0.42905	0.43491
5.0	0.37130	0.37847	0.38535	0.39455	0.40339	0.41032	0.41698	0.42269	0.42819	0.43172	0.43512
